Growth Mechanisms and Microstructure Evolution of MAX phases Thin Films and of Oxide Scales on High Temperature Materials

Von der Fakultät für Georessourcen und Materialtechnik der
Rheinisch -Westfälischen Technischen Hochschule Aachen

zur Erlangung des akademischen Grades eines

Doktors der Ingenieurwissenschaften

genehmigte Dissertation

vorgelegt von **Magister der Physik**

Mohamad Riza Iskandar

aus Jakarta, Indonesien

Berichter: Univ.-Prof. Dr.rer.nat. Joachim Mayer
Univ.-Prof. Jochen M. Schneider, Ph.D.

Tag der mündlichen Prüfung: 15. November 2011

Diese Dissertation ist auf den Internetseiten der Hochschulbibliothek online verfügbar

To my beloved wife, Lia

Acknowledgments

I could have never reached the heights and explored the depths without the wholehearted support and generous help of a lot of genuinely inspiring people. They have made the successful completion of this dissertation possible and because of them my Ph.D. study has been an unforgettable experience.

I am deeply grateful to Univ.-Prof. Dr. Joachim Mayer for his continuous support, inspiration, fruitful discussions, valuable suggestions and encouragement during my Ph.D. study. I feel fortunate to have the opportunity to work with him.

My special gratitude goes to my second supervisor Prof. Jochen M. Schneider, Ph.D. for his willingness to be my co-supervisor.

I give my hearty thanks to my colleagues from Material Chemistry RWTH Aachen University and from Institute of Microstructure and Properties of Materials (IEK-2) at Jülich Research Centre for a very conducive team work which surely without their contribution, this work could not have been possible to accomplish.

I would like to extend my gratitude to all my GFE’s friends and colleagues for the friendship and creating a very warm work atmosphere with I had pleasure working together.

I would gratefully acknowledge the DAAD (German Academic Exchange Service) for the financial support through the time period of my PhD study at the RWTH Aachen University. Without their support, the implementation of this dissertation would not have been possible.

Finally, and most importantly, my heartfelt thanks go to my family Ayah, Ibu, Kakak, Bang Niko, Salma, Vania, my beloved family in laws in Cibadak especially Papi and Mami. Their unconditional love, unwavering support, great understanding, continuous encouragement, and endless patience were undeniably the bedrock upon which my study in Germany has been built. Last but not least, thanks to my beloved wife Lia, whose understanding, encouragement, love and passion during the work enabled me to complete this dissertation. To them, I would like to dedicate this work and all of my achievements.

Abstract

The knowledge of the exact conditions under which a material forms a microstructure with optimum physical and chemical properties is essential for any technological application. Beyond this, it is also often crucial for reliable and save operation to know how a particular material changes its microstructure under long-term working conditions, e.g. at high-temperature and oxidising atmosphere.

Recently, the class of MAX-phases and some Fe-Cr-Al model alloys have gained increasing interest in materials research due to their promising properties for future applications in the high-temperature regime. In order to shed some light on the hitherto unknown growing mechanism of MAX-phases, thin-films of the prominent phases Ti-Al-C and Cr-Al-C were synthesised by magnetron sputtering at various temperatures and their microstructure was subsequently characterised in great detail. Moreover, the effect of oxidation time on the microstructure was studied using thin-film samples with nominal composition Cr_2AlC. These investigations were completed by a study on the changes in the microstructure of Fe-Cr-Al model alloys for different thickness and high-temperature oxidation conditions.

The microstructural characterisation was performed in all cases using analytical transmission electron microscopy (TEM) on focused ion-beam (FIB) machined cross section specimens.

The investigation on as-deposited thin films resulted in several new findings. At high deposition temperatures (850°C), Ti-Al-C thin films form a porous microstructure with many faults and contain some minor phases such as TiC and Ti_3AlC_2 in addition to Ti_2AlC. On the contrary, the microstructure of Cr-Al-C thin-films is free of pores and consists only of Cr_2AlC, despite a significant lower deposition temperature (650°C) than used in the Ti-Al-C system. On the other hand, specimens deposited at 450°C and 550°C are not found any longer as single-phase and decompose into Cr_2AlC and $Cr_{23}C_6$ as main constituents.

The obtained results confirm that magnetron sputtering of MAX-phases is a complex process which can yield entirely different microstructures depending on the chemistry of the system. However, was possible to prove that good quality Cr-Al-C thin-films can be obtained at temperatures much lower than required to synthesise thin-films in the Ti-Al-C system. This indicates that the nature of the M element likely has the greatest effect on the deposition temperature of a particular MAX-phase and the developed microstructure.

Investigations on the oxidation performance of the MAX-phases were carried out using Cr_2AlC thin-films as a model system. Notably changes in the microstructure upon oxidation for periods of 4 min, 39 min and 282 min are a rise of the thickness of the upper alumina scale, the increase in the porosity underneath the oxide scale and growing of a Cr-C interlayer at the boundary between substrate and thin-film. In particular the formation of voids and pores below the upper oxide scale appears to be a special feature of the thin-films that is unknown for oxidation of bulk Cr_2AlC. Despite the observation that the Cr_2AlC thin-film samples undergo decomposition into Cr_3C_2 and Cr_7C_3 under oxidation conditions, they still show a fairly good overall oxidation resistance.

The series of oxidation studies was completed by a detailed investigation on Fe-Cr-Al alloys doped with Y and Zr. Since incorporation of Zr in the oxide scale became evident during in the early stages of the investigations, specimen with thickness of 0.3 mm and 1.3 mm were later used for studying the effect of the available Zr on the oxidation rate. As a main result it was found that the amount of precipitates in the oxide scale is different only for long oxidation periods. Moreover, EDX analysis revealed that thin specimens always contain more Y-rich precipitates, especially under high-temperature oxidation conditions. The varying thickness of the alumina scale thickness and the finding of Zr-rich precipitates indicates that the extended oxidation life time of the alloy must be directly linked with the presence of a Zr reservoir in the specimen. Based on this a modified model was developed, which describes the mechanism of Zr incorporations into the alumina scale upon oxidation for specimen with finite thickness.

Kurzfassung

Die Kenntnis der Bedingungen, bei denen ein Material eine Mikrostruktur mit optimalen physikalischen und chemischen Eigenschaften ausbildet ist für jede technologische Anwendung von großer Bedeutung. Darüber hinaus ist es für zuverlässige und sichere Arbeitsabläufe oftmals wichtig zu wissen, wie ein bestimmtes Material seine Mikrostruktur unter Langzeit-Arbeitsbedingungen verändert, z.B. unter Hochtemperatur-Bedingungen oder oxidierender Atmosphäre.

In der letzten Zeit ist in der Materialforschung das Interesse an der Klasse der so genannten MAX-Phasen und einigen Fe-Cr-Al-Modell-Legierungen aufgrund ihrer viel versprechenden Eigenschaften für zukünftige Hochtemperatur-Anwendungen gestiegen. Um Erkenntnisse über den bisher unbekannten Wachstumsmechanismus der MAX-Phasen zu erlangen wurden zunächst dünne Schichten der beiden bedeutenden Phasen Ti-Al-C und Cr-Al-C mittels Magnetronsputtern bei verschiedenen Temperaturen hergestellt und anschließend ihre jeweilige Mikrostruktur detailliert charakterisiert. Des Weiteren wurde an dünnen Cr_2AlC-Schichten der Einfluss der Oxidationszeit auf die Mikrostruktur untersucht. Zuletzt wurden die Untersuchungen abgeschlossen, indem die Änderung der Mikrostruktur von Fe-Cr-Al-Modell-Legierungen durch Variationen der Schichtdicke und der Hochtemperatur-Oxidationsbedingungen untersucht wurde.

Zur Charakterisierung der jeweiligen Mikrostruktur wurden Probenquerschnitte, die zuvor mittels fokussierten Ionenstrahl (FIB) hergestellt wurden, in einem analytischen Transmissionselektronenmikroskop (TEM) untersucht.

Die Untersuchung der abgeschiedenen dünnen Schichten lieferte einige neue Erkenntnisse. Bei hohen Abscheidungstemperaturen (850°C) bilden die Ti-Al-C-Dünnschichten eine poröse Mikrostruktur mit vielen Fehlstellen aus, die zusätzlich zu der hauptsächlich auftretenden Ti_2AlC-Phase noch weitere Phasen, wie beispielsweise TiC und Ti_3AlC_2, aufweist. Im Gegensatz dazu, weist die Mikrostruktur der Cr-Al-C-Dünnschicht, trotz geringerer Abscheidungstemperatur (650°C), keine Poren und ausschließlich die Cr_2AlC-Phase auf. Auf der anderen Seite sind die Schichten, die bei 450°C und 550°C abgeschieden wurden nicht mehr einphasig, sie haben sich in Cr_2AlC und $Cr_{23}C_6$ zersetzt.

Die Ergebnisse bestätigen, dass das Magnetronsputtern der MAX-Phasen ein komplexer Prozess ist, der abhängig von der Chemie des Systems zur Ausbildung verschiedener Mikrostrukturen führen kann. Allerdings konnte gezeigt werden, dass Cr-Al-C-Dünnschichten mit guten Eigenschaften bei viel geringeren Abscheidungstemperaturen hergestellt werden können, als zur Herstellung von Dünnschichten im Ti-Al-C-System benötigt werden. Dies deutet darauf hin, dass bei den MAX-Phasen das M-Element den größten Einfluss auf die Abscheidungstemperatur und die ausgebildete Mikrostruktur hat.

Das Korrosionsverhalten der MAX-Phasen wurde an dem Modellsystem Cr_2AlC untersucht. Zu den nennenswerten Veränderungen der Mikrostruktur bei Oxidationszeiten von 4 min, 39 min und 282 min zählen die Dickenzunahme der Al_2O_3-Deckschicht, die Verstärkung der Porosität in der Schicht unterhalb der Al_2O_3-Deckschicht und die Ausbildung einer Cr-C Zwischenschicht an der Grenzfläche zwischen dem Substrat und der Dünnschicht. Insbesondere die Ausbildung von gasgefüllten und nicht gefüllten Poren unterhalb der Al_2O_3-Deckschicht stellt vermutlich eine Besonderheit der Dünnschichten dar, da diese bei der Oxidation des Cr_2AlC-Bulkmaterials nicht beobachtet wird. Abgesehen davon, dass sich die Cr_2AlC-Schichten in oxidierender Atmosphäre in Cr_3C_2 und Cr_7C_3 zersetzen, weisen sie im Großen und Ganzen dennoch eine relativ gute Korrosionsbeständigkeit auf.

Die Reihe der Oxidationsuntersuchungen wurde durch die detaillierte Untersuchung der mit Y und Zr dotierten Fe-Cr-Al-Legierungen abgeschlossen. Schon zu Beginn der Untersuchungen hat sich gezeigt, dass sich das Zr in die Al_2O_3-Deckschicht einbaut. Daher wurden anschließend Proben mit Dicken von einerseits 0,3 mm und andererseits 1,3 mm verwendet, um den Einfluss des vorhandenen Zr auf die Oxidationsrate zu untersuchen. Das Hauptergebnis der Untersuchungen ist, dass sich die Menge der Ausscheidungen in der Oxid-Deckschicht lediglich bei langen Oxidationszeiten unterscheidet. Darüber hinaus hat die EDX-Analyse ergeben, dass dünne Proben vor allem bei Hochtemperatur-Oxidationsbedingungen stets mehr Y-reiche Ausscheidungen aufweisen. Die variierende Dicke der Al_2O_3-Deckschicht und die Zr-reichen Ausscheidungen deuten darauf hin, dass die vergrößerte Oxidationsbeständigkeit der Legierung von der Existenz eines Zr-Reservoirs in der Probe abhängt. Darauf basierend wurde ein modifiziertes Modell entwickelt, das den Mechanismus des Zr-Einbaus in die Al_2O_3-Deckschicht während der Oxidation von Proben endlicher Dicke beschreibt.

This page is intended to be blank

Table of Contents

1 Introduction

From simple commodities to advanced technology, ceramics and metals are the most common materials being used, despite the fact that the two of them have almost opposite properties. Ceramics are good insulators, have good corrosion resistance, but are extremely brittle. On the other hand, metals are known as good electrical and thermal conductors, machinable, have high elastic moduli, but frequently show poor corrosion resistance. The search for materials which have the combination of both metal and ceramic properties is becoming more important in the 21st century. In the framework of the present thesis, the MAX-phases and Fe-Cr-Al model alloys, which both have been known for their low brittleness and high corrosion resistance respectively, have been selected as the best representative materials of both ceramics and metals.

Transition Metal Carbides and Nitrides, developed by Jeitschko and Nowotny in 1960's, are ceramics which also have metal properties [1]. This new class of materials is called the MAX phases because of its compositions, where M stands for an early transition metal, A is an A-group element (mostly 13 or 14) and X is either C and/or N. MAX phases are a good electrical and thermal conductors, machinable, and exhibit good corrosion resistance. They have high elastic moduli, good damage tolerance, and excellent thermal shock resistance [2].

In the last 20 years, many research activities have been focused on investigating this new class materials, which mostly were performed on the bulk form of the material. Only a few experiments have been reported which have been performed on thin films. Wilhemsson et al. have successfully deposited epitaxial and phase pure films of the Ti-Al-C system by DC magnetron sputtering [3, 4]. Another promising method to deposit thin films in large areas by using single targets for Cr_2AlC, and Ti_2AlC and Ti_2AlN was reported by Walter et al. [5]. In their experiments, the Cr-Al-C system was deposited successfully in a large area and at low substrate temperatures. Furthermore, several theoretical calculations investigating the properties of MAX phases have also been reported. Schneider et al. determined the elastic properties of Cr_2AlC thin films and compared them with *ab initio* calculations [6]. Additionally, some theoretical calculations for the electronic structure and thermodynamic properties of other MAX phases have also been performed [7-9]. As thin film systems have several application advantages compared to bulk systems, a thorough investigation of their microstructure to understand the film growth of these phases has very interesting prospects.

One of the promising applications of this new material class in thin film systems is by using it as high-temperature coatings. For application in high-temperature environments, the materials need to meet at least two main requirements. Firstly, they must exhibit good hot corrosion resistance. Secondly, they must not only be as resistant as possible to the effects produced by reaction with oxygen, but also show resistance to attack by other oxidants in the environment. Depending on the temperature and environment, materials ranging from metal to ceramics are used for high-temperature coatings. For temperatures above 1100°C, ceramics are favourable. In the group of MAX phases, both Cr_2AlC and Ti_2AlC bulk materials are reported to have a good corrosion resistance [10-12].

Based on the description above, the objective of this work is to develop a more detailed understanding of MAX phase thin film processes, their microstructure and properties, and to obtain more insight in their physical and chemical properties. This research also prepares the basis for their technological application in industry, especially for high-temperature applications. To achieve the first goal, thin films of Ti_2AlC and Cr_2AlC MAX phases were synthesised. Systematic characterisations by analytical and high-resolution transmission electron microscopy were performed. It has been reported that bulk Cr_2AlC has better oxidation resistance than Ti_2AlC[10], therefore detailed electron microscopy investigations of selected MAX phase thin films for high temperature applications were only performed on the oxidation of Cr_2AlC thin films.

To get a deeper understanding on the oxidation of high-temperature materials, microstructural characterization of Fe-Cr-Al model alloys was performed after corrosion tests. They have very good oxidation resistance and are being used in various high temperature applications. The resistance against high temperatures oxidation relies on the formation of an alumina scale, which forms on the component surface during high temperature service. The two technologically most relevant properties of the alumina scale are low growth rate and an optimum adherence to the metallic substrate. Those two properties are strongly affected by minor alloying addition of reactive elements [13-15] . In the present work, the microstructure of the oxide scale due the alloying addition of reactive elements, especially the dependency of RE reservoir in the alloy, was investigated.

In the present dissertation, the state of the art and the background of the work are discussed in this introduction chapter. Chapter two and three will discuss the theoretical background of thin film deposition and the basics of oxidation. The growth mechanisms of both MAX phases will be discussed in chapter four. As one of the main topics of this work, the isothermal oxidation behaviour and the microstructural evolution of high temperature oxidation resistant materials, i.e. Cr_2AlC thin films and Fe-Cr-Al alloys, will be presented in chapter five, while the experimental details will be given in chapter six. Chapter seven will present the results of the electron microscopy characterization, while the discussion of the corresponding results will be given in chapter eight. Conclusions will be presented in chapter nine along with several possibilities for technological applications and future work. References and appendices will be presented in the last part of this dissertation.

2 Thin film deposition

2.1. Growth mechanisms

Thin films are formed on a substrate by a process of nucleation and growth of individual islands or clusters on the substrate from the vapour phase of the materials. This process starts by the arrival of atoms on the substrate which in a second step will adhere on the substrate or will be re-evaporated from the substrate. Those atoms which have stayed on the substrate later build some clusters as nuclei for the final phases. Furthermore, when additional atoms arrive, some of them will be deposited directly or diffuse across the substrate to join stable nuclei while the others will be re-evaporated from the clusters. In the last process, the nuclei will start to grow. There are three basic models which explain the initial stage of film growth, namely island, layer and layer-island combination models. A detailed description about these models can be found in [16].

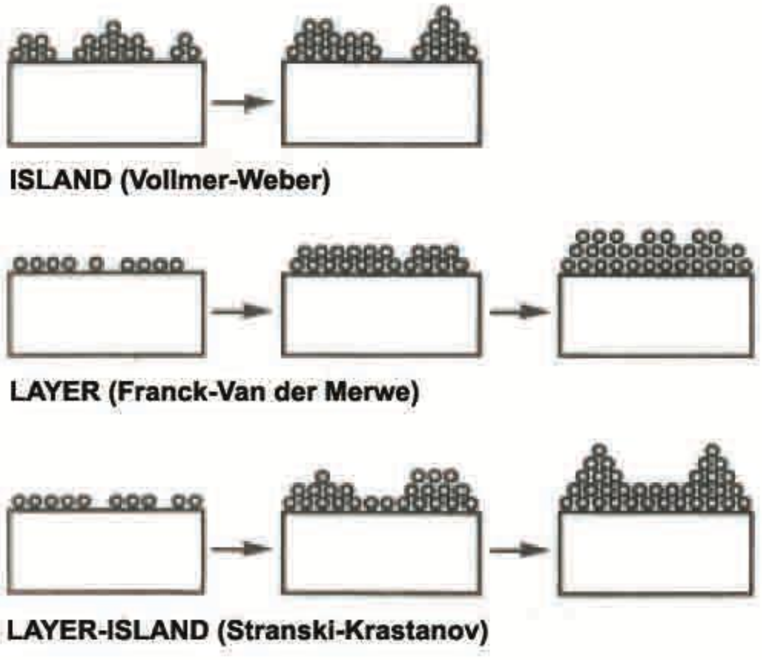

Figure 2.1 Basic model of thin-film growth [16].

2.2. Deposition

In thin film growth, different techniques can be applied for depositing a thin film of a given material onto a substrate or previously deposited layers. Depending on the process, the deposition techniques can be divided into chemical and physical deposition. In chemical deposition, a solid material is deposited from a vapour by chemical reaction occurring on or in the vicinity of a heated substrate surface. Different materials with different properties can be grown by varying the experimental conditions such as substrate material, substrate temperature, composition of the reaction gas mixture, total pressure gas flows, etc.

As seen in figure 2.2 (a), gaseous reactants are admitted into reactor and near or on a heated surface, chemical reactions will occur. There are five important reaction zones which are developed during the CVD process (see Fig. 2.2(b)). The interacting processes which occur in these zone will affect the properties of CVD materials. Detailed explanation of every process occurring in the different zones can be read in [17-19].

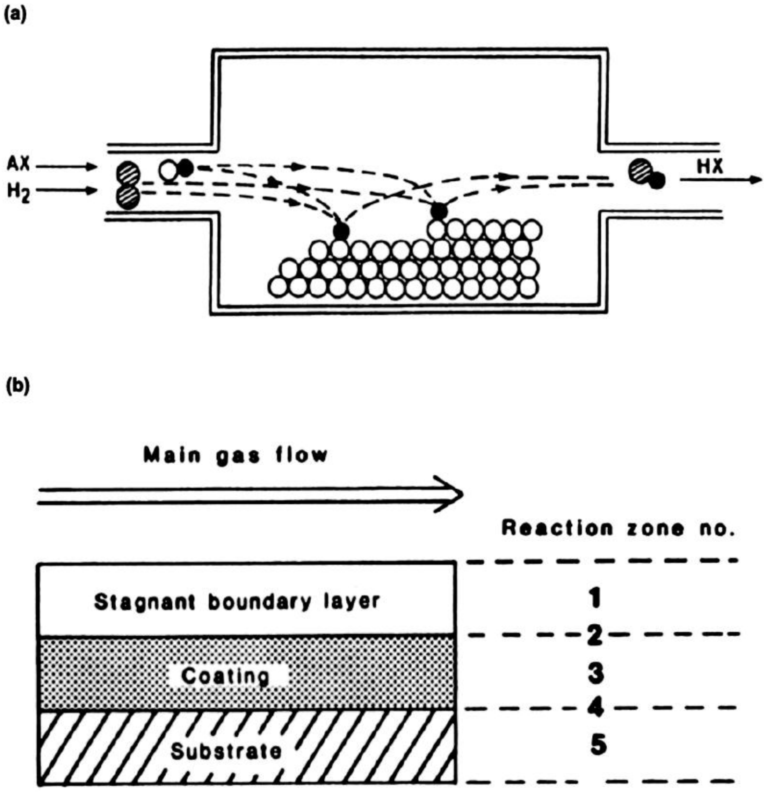

Figure 2.2 (a) A schematic CVD process and (b) Five important reaction zones in CVD [19].

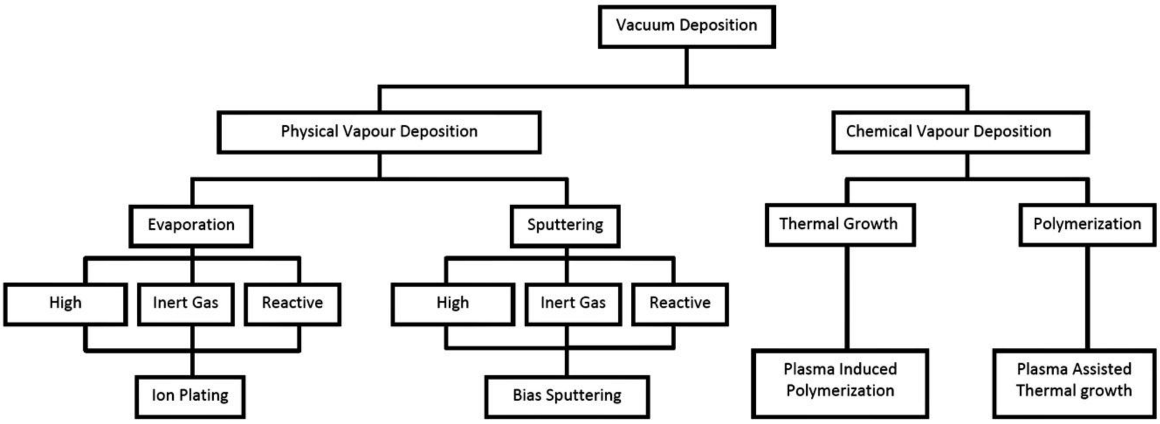

Figure 2.3 Type of vacuum deposition techniques [18].

A process called Physical Vapour Deposition (PVD), which is the basic deposition process used in this experiment, is an atomistic deposition process in which materials are vaporised from a solid or liquid source in the form of atoms or molecules, transported in the form of a vapour through a vacuum or low pressure gaseous (or plasma) environment to the substrate where they condense [20]. Evaporation and sputtering are two PVD techniques which are already well known. Additionally, in some literature the ion platting process is also known as hybrid technique in PVD [17, 18].

Sputtering can be defined as the ejection of particles from a condensed matter target due to the collision of energetic projectile particles. The kinetic energy from sputter-ejected species is higher than their thermal energy. From a statistical point of view, sputtering can also be defined as a statistical process which occurs as a result of a momentum exchange in collision cascade processes initiated near the target surface by an incident energetic particle. From the computer simulations of Cu bombardment by 600 eV Ar^+ ions, it is known that the radius of a collision cascade under such conditions is of the order of 10 nm and that the fraction of collisions sequences which actually intersect the surface and transfer sufficient momentum resulting in the sputtering is quite low. Most of the energy transferred to the lattice during ion bombardment is lost as heat.

In general, a sputtering system mainly consists of a target and a substrate. The target, known as cathode, is a plate of the material from which a film is synthesised and on which several kilovolts are typically applied. The substrate or anode that faces the cathode may be grounded or electrically floating, biased positively or negatively, heated, cooled or some combination of them. The process starts firstly by evacuation of the chamber. After that, an inert gas, which is typically argon, is introduced and serves as the medium in which a discharge is initiated and sustained. The use of inert-gas ions avoids chemical reactions in the target and the substrate. Accordingly, argon is often used because of its mass compatibility with materials of engineering interest and its low cost. After a visible glow discharge is maintained between the electrodes, the current flows and a film condenses on the substrate (anode).

Microscopically, positive ions in the discharge strike the cathode plate and eject neutral target atoms through momentum transfer. These atoms enter and pass through the discharge region to be eventually deposited on the growing film. In addition, other particles (secondary electrons, desorbed gases, and negative ions) as well as radiation (X-rays and photons) are emitted from the target. In the electric field, the negatively charged ions are accelerated towards the substrate to bombard the growing film.

The sputtering processes allow any inorganic material to be deposited. Generally DC discharge methods are used for most sputtering process. For sputtering of non conducting materials, an RF potential must be applied to the target. The deposition can be initiated by several processes:

- Using a target which contains several materials
- Using several targets simultaneously to obtain an alloy film
- Using several targets sequentially to create compositionally layered coatings
- Providing ion bombardment of the growing film during deposition by biasing the substrate electrically, in order to modify the film microstructure.
- Introducing a gas (e.g., O_2, N_2, H_2S, etc) into the chamber for coating materials which is known as reactive sputtering.

2.3. DC magnetron sputtering

Magnetron sputtering, which is performed by applying magnetic field in a PVD system, is known as a deposition technique which has several advantages compared with other techniques. The technique provides (i) relatively high deposition rates, (ii) large deposition areas and (iii) low substrate heating [21]. Magnetron sputtering sources can be defined as diode devices in which magnetic fields are used in concert with the cathode surface to form electron traps which are configured so that the $\vec{E}\times\vec{B}$ electron drift currents close upon them.

In DC diode sputtering, the electrons that are ejected from the cathode are accelerated away from the cathode and are not efficiently used for sustaining the discharge. This discharge is important for the sputtering rate. Increasing the discharge can be done by increasing the argon pressure at a given voltage. Since a significant number of the sputtered atoms cannot get through the dense working gas atmosphere and is deflected back to the cathode by collisions with gas atoms, increasing the pressure doesn't solve the problem completely. By a suitable application of the magnetic field, the electrons can be deflected to stay near the target surface and by an appropriate arrangement of the magnets, the electrons can be made to circulate on a closed path above the target surface. These high flux electrons create a high density plasma from which a high rate of ions can be extracted to sputter the target material. In other words, by forcing the migration of the electrons, an effective sputtering discharge can be maintained in the cavity. A detailed description of the magnetron sputtering process can be found in the article by Thornton [22].

There are several magnetron sources used for these applications, details of which can be found in the following references, for example the cylindrical [23], planar [24-27] and sputter or S-gun magnetron [28-30].

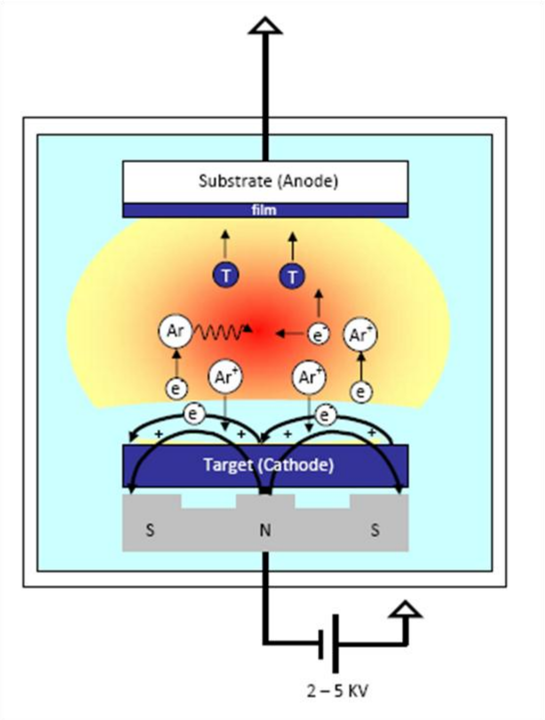

Figure 2.4 Schematic drawing of the deposition process using dc magnetron sputtering.

3 Basics of oxidation

Corrosion is the degradation of a material's properties or mass over time due to environmental effects. It is caused by the natural tendency of the material's compositional elements to return to their most thermodynamically stable state. For most metallic materials, corrosion means the formation of oxides or sulphides as a passivating film on the surface.

Corrosion processes are based on the basic laws of thermodynamics. One can measure or repeat the process, and predict the result under controlled conditions. Because they are governed by reactions on an atomic level, corrosion processes can act on isolated regions and uniform surface areas, or result in subsurface microscopic damage. Because of its uniformity, the corrosion rate of metals is often expressed in terms of metal or alloy thickness loss per unit time. This rate of uniform attack is reported in various units such as mils per year (mpy) or millimetre per year. To understand the corrosion phenomena, both thermodynamics and kinematic process have to be used.

3.1. Thermodynamic considerations

The chemical reaction between pure divalent metal, M, and an oxidizing gas, X_2 (oxygen, sulphur, and others), will result metal oxide, M_aX_b as the reaction product (oxide, sulphide, etc). This condition is expressed by the chemical reaction:

$$aM + \frac{b}{2} X_2 = M_a X_b \tag{3.1}$$

In this process, the thermodynamic laws play a very important role. The Second Law of Thermodynamics, which describes the Gibbs energy change, is used to determine whether the oxidation process of specific metal may occur at a given temperature and oxidant gas pressure [31]. The Gibss energy change, ΔG, is written as:

$$\Delta G = \Delta H - T\Delta S \tag{3.2}$$

where

ΔH = the enthalpy of reaction

T = the absolute temperature

ΔS = the entropy change.

The reaction can be divided into there conditions based on the sign of ΔG: spontaneous reaction ($\Delta G<0$), non spontaneous reaction ($\Delta G>0$) and equilibrium ($\Delta G=0$). The Gibbs energy change of the chemical reaction given by Eq (3.1) equals to the sum of the chemical potentials, μ, of all components present in the system (M, X_2, M_aX_b):

$$\Delta G = \mu_{M_aX_b} - a\mu_M - \frac{b}{2}\mu_{X_2} \tag{3.3}$$

The chemical potential, μ, and the activity, a_i, of a given component i are interrelated as follows:

$$\mu_i = \mu_o^i + RT\ln a_i \tag{3.4}$$

where

R = the gas constant

μ_0^i = the chemical potential of a given i-component in standard state.

Generally, the activity of pure solid components (such as metals and oxides) are equal to unity, and therefore $\mu_{\mathrm{M}} = \mu_M^o$ and $\mu_{M_aX_b} = \mu_{M_aX_b}^o$. The activity of a gaseous component X_2 can be approximated by its pressure:

$$\mu_{X_2} = \mu_{X_2}^o + RT\ln p_{X_2} \tag{3.5}$$

Thus, Eq 3.3 can be writen in the following form:

$$\Delta G = \mu_{M_aX_b}^o - a\mu_M^o - \frac{b}{2}\mu_{X_2}^o - \frac{b}{2}RT\ln p_{X_2} \tag{3.6}$$

Since the sum of the standard chemical potentials is the standard of Gibbs energy change, ΔG^0, the previous equation can be written as:

$$\Delta G = \Delta G^o - \frac{b}{2} RT \ln p_{X_2} \tag{3.7}$$

Where $\Delta G = 0$, Eq (3.7) can be presented in the form:

$$\Delta G^o = \frac{b}{2} RT \ln p_{X_2}^{eq} \tag{3.8}$$

In the previous equation, $p_{X_2}^{eq}$ denotes the dissociation pressure of the M_aX_b compound and can be calculated from the following relation:

$$p_{X_2}^{eq} = \exp\left(\frac{2\Delta G^o}{bRT}\right) \tag{3.9}$$

From thermodynamic point of view, if the oxidant pressure is lower than the calculated value of the equilibrium dissociation pressure of the M_aX_b compound, then the metal, M, is not oxidised. In the opposite case, the spontaneous oxidation reaction may occur.

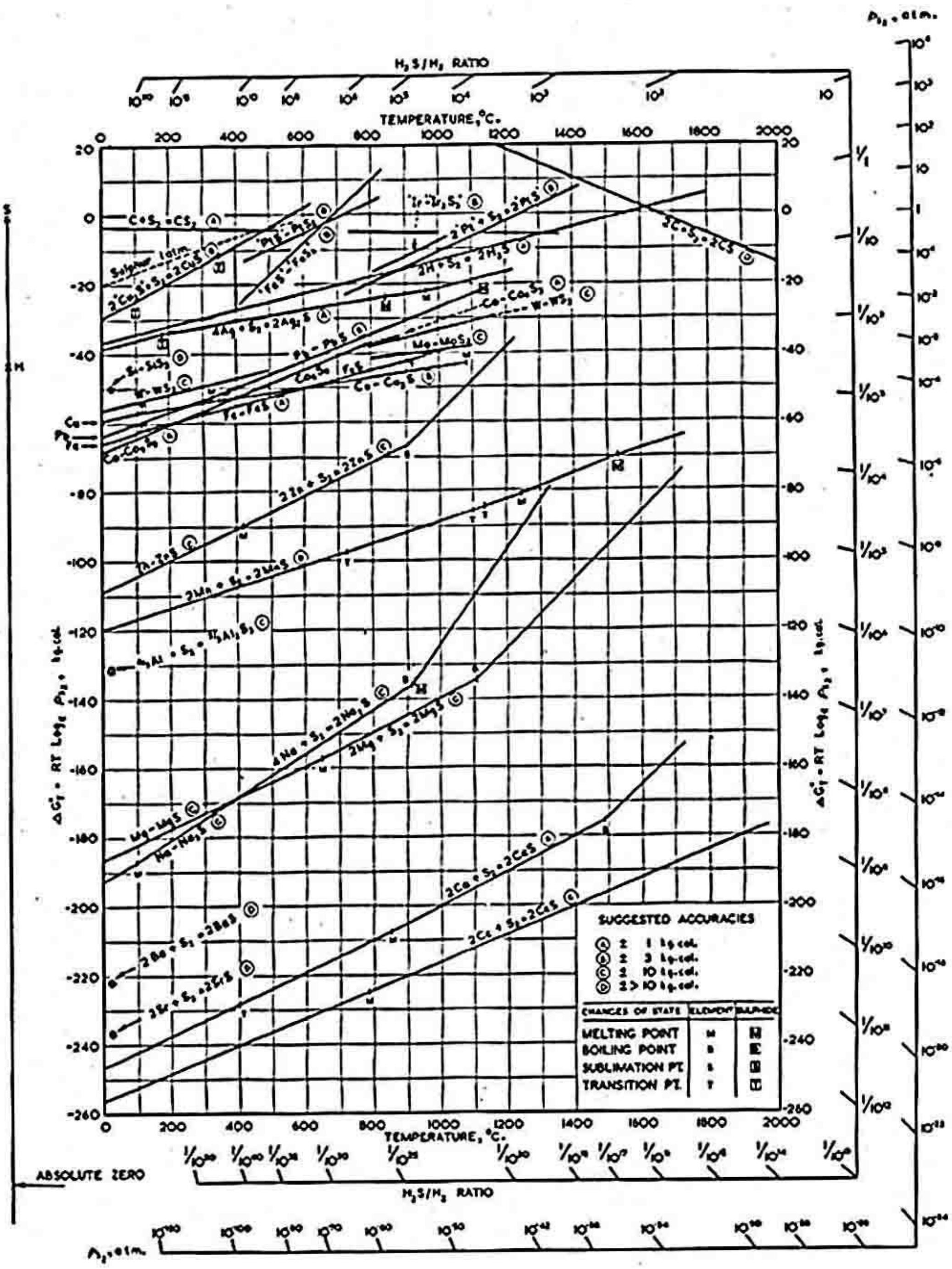

Figure 3.1 Richardson-Jeffes diagram [32].

The standard Gibbs energy change of formation of oxides as well as the corresponding dissociation pressure of the oxide as a function of temperature without any calculation can be known from the Richardson-Jeffes diagram. It plots standard Gibbs energies of formation of the oxides per mole oxygen, O_2, versus temperature. A more detail explanation about this diagram can be found in [32].

3.2. Kinetics of oxidation

In contrast to thermodynamics which predicts which reactions are possible, in kinetics of oxidation one explains how fast these possible reactions will be proceeded. The reaction rate is affected by a number of complex interactions between material and environment during the test such as [33]:

- Temperature
- Time/thermal cycle conditions
- Corrosive species and their activity (concentration)
- Chemisorption and dissociation characteristics
- Stress states and cycle strains

Corrosion products start to form at the interface between two reactants under high temperature exposure and thermodynamically favourable conditions. The reactants, i.e. the metal and the oxidant, are separated when dense oxide films or scales are formed. At this time, the reaction may only proceed through solid state diffusion of reactants through the scale. In general, diffusion occurs due to the differences in chemical potential to the extent that a component always diffuses down its potential gradient. In solids, diffusion plays a key role in oxidation and other gaseous reactions with metals. Metal ion diffusion may result in mass transfer from a metal surface through the oxide, nitride, sulphide, or chloride (and other such metal compounds) layer to the surface, whereas the absorbed anions diffuse inward through the scale to the metal or alloy. Diffusion and transport of electrical charges in solids take place because of the occurrence of defects in solids [34].

We can use two Fick’s law to understand the diffusion process:

$$J = -D\frac{\partial \phi}{\partial x} \tag{3.10}$$

and

$$\frac{\partial \phi}{\partial t} = D\frac{\partial^2 \phi}{\partial x^2} \tag{3.11}$$

where

J = the diffusion flux [(amount of substance) length^{-2} time^{-1}]
D = the diffusion coefficient or diffusivity [length^{2} time^{-1}]
ϕ = the concentration [(amount of substance) length^{-3}]
x = the position [length]

Fick's first law relates the diffusive flux to the concentration field by postulating that the flux goes from regions of high concentration to regions of low concentration, with a magnitude that is proportional to the concentration gradient (spatial derivative). In one (spatial) dimension, Fick's second law predicts how diffusion causes the concentration field to change with time.

There are many theories which explain the underlying oxidation mechanism. The Cabrera-Mott theory is known as the best theory of thin-film oxidation and applies to films of up to 10 nm thickness [35]. For thicker film, the Hauffe-Ilschner theory has been proposed [36]. The Grimley-Trapnell theory uses a different approach from the Cabrera-Mott theory by assuming a constant electric field instead of a constant potential [37]. All previous theories apply at low temperatures. The Uhlig theory, developed by Uhlig and extended by Fromhold, predicts logarithmic kinetics at temperatures of up to 600 K and explains oxidation rate changes at crystal and magnetic transformations [38]. Last but not least, the Wagner theory of oxidation explains very well the oxidation process for high temperature and thick films [39].

Wagner proposed that during the oxidation process the two reactants are separated by an oxide layer. For this theory several conditions need to be met:

- One type of defect is dominant in the oxide
- The thermodynamic equilibrium is established on both metal/scale and scale/oxidant interfaces
- The oxide scale shows small deviations from stochiometry
- The oxidant solubility in the metal, the oxide evaporation, and any other processes at interfaces are negligible.
- The scale is thick compared to the distance over which space charge effects occur (electrical double layer)

From the assumption of low nonstoichiometry, it follows that the metal and oxidant concentration in the growing scale is constant and does not depend on the position. Consequently, when the metal (eg., interstitial cations M_{ej}) diffusion is dominant, Eq. (3.10) reduces to:

$$\frac{\partial}{\partial x} = J_{Me_i} = 0 \tag{3.12}$$

from which it follows that the flux of metals does not depend on the position in the scale and only depends on time. The rate of growth of the oxide scale, dX/dt, is then proportional to the flux of metal ions J_{Me} by Fick first law:

$$J_{Me} = J_{Me_i} = -D_{Me_i}\frac{\partial C_{Me_i}}{\partial_x} \tag{3.13}$$

When the diffusion coefficient does not depend on defect concentration, from the two previous equations it follows that the gradient of metal concentration in the growing scale is constant. This allows further simplification of the flux formulas:

$$J_{Me} = -D_{Me_i}\frac{\Delta C_{Me_i}}{X} \tag{3.14}$$

where both flux and the scale thickness X are unknown. The last necessary equation relates the flux of metal at the oxidant interface to the rate of scale formation. This is the mass balance at the scale/oxidant interface and is often called the Stefan condition:

$$J_{Me} = C_{Me}\frac{dX}{dt} \tag{3.15}$$

Combining both equations, the differential form of the parabolic rate law is as follows:

$$\frac{dX}{dt} = \left(D_{Me_i}\frac{\Delta C_{Me_i}}{C_{Me}} \right)\frac{1}{X} = \frac{k^{'}}{X} \tag{3.16}$$

where the parabolic rate constant (term in the brackets) depends on the diffusivity of defects and their concentrations. By integrating with the limit at time $t = 0$ and the oxide thickness $X = 0$, the integral form of the parabolic equation is:

$$X^2 = k' \cdot t \tag{3.17}$$

Below is the diagram of the scale formation according to the Wagner's model

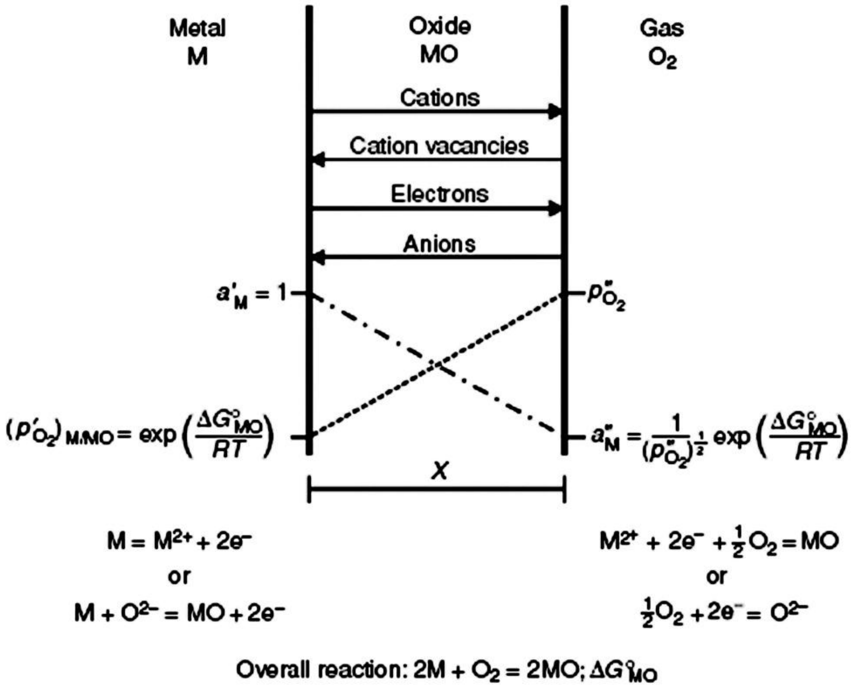

Figure 3.2 The Diagram of the scale formation according to Wagner's model [40].

Beside parabolic oxidation rates (Eq. 3.17), there are three other oxidation rates classified for high-temperature corrosion: linear, logarithmic and cubic. The theory about those rates can be read in reference [41].

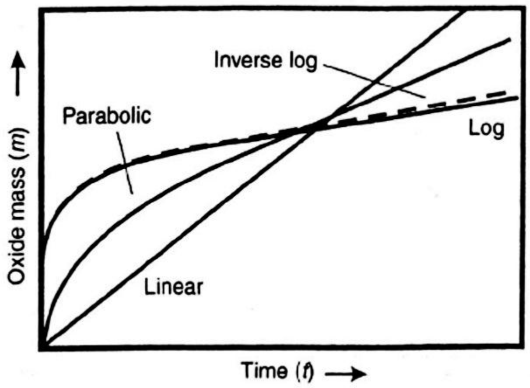

Figure 3.3 Types of the oxidation kinetics [42].

3.3. Protective Al_2O_3 scales

Alloys intended for high-temperature applications are designed to possess the capability of forming protective oxide scales which is very essential for high temperature resistance. The scale must be dense, slow growing, relatively chemical inert and adherent. There are several protective scales that are known and used in technical applications: Cr_2O_3 (chromia), Al_2O_3 (alumina) and SiO_2 (silicon dioxide). Al_2O_3 and Cr_2O_3 are known to be better protective scales compared to other scales. Al_2O_3 is widely used for applications above 1000°C and Cr_2O_3 for applications between 800°C and 1000°C. This research mainly investigates the protective properties of Al_2O_3 scales.

Al_2O_3 exists in several phases both as metastable and stable crystal structure. Several investigations reported that meta-stable Al_2O_3 scales such as, γ, δ and θ are formed in the temperature range of 800 to 1200°C [14, 43-45]. The γ-Al_2O_3 phase may be initiated in the early stages; it transforms to the intermediate θ-Al_2O_3 phase, possibly via the δ-Al_2O_3 modification and finally, to α-Al_2O_3.

Most studies of Al_2O_3-forming alloys have concentrated on ternary M-Cr-Al alloys, where M is Fe, Ni or Co and binary intermetallics based on nickel aluminides and iron aluminides since they form the basis of the current and possible future oxidation-resistant systems. The Al_2O_3 scale is thermodynamically very stable with respect to the metal and grows relatively slowly, even at 1300°C. Reports show the susceptibility to cracking and spalling as the main weakness of α-Al_2O_3 scales [14]. Scale failure can be caused by stress applied in service, growth stress or temperature changes that give rise to compressive stress in the scale due to the mismatch of the thermal expansion between alloy and oxide. In almost every study of alumina-formers, the formation of voids or cavities at the scale-alloy interface has been mentioned [14]. Several experiments have been made to improve the quality of Al_2O_3 scale such as by adding refractive elements. Wukusick and Collins showed that addition of yttrium to Fe-Cr-Al alloy resulted in improved oxidation resistance under cyclic conditions. The details of the effect of reactive element addition can be found elsewhere in this work [46].

4 Growth mechanisms of Ti_2AlC and Cr_2AlC MAX phases

4.1. MAX phases

In the 1960's Nowotny and Jetschiko have synthesised a large number of nitrides and carbides, amongst them were more than thirty so called H-phases or Hägg-phases. The H-phase has a special chemistry labelled as M_2AX, where M is an early transition metal, A is an A-group element (mostly 13 or 14) and X is either C and/or N. More generally, this chemical component has $M_{n+1}AX_n$ composition.

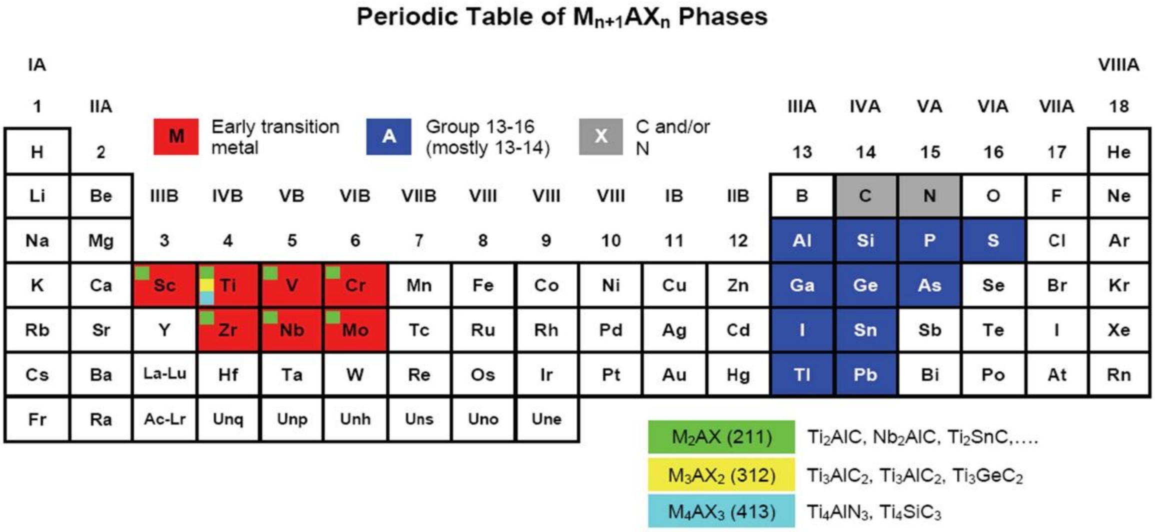

Figure 4.1 An early transition metal M (red), an element from the A groups, mostly 13 and 14 (blue, in modern IUPAC notation), and a third element, X, which is either nitrogen or carbon (grey) form the MAX phases. With the general formula $M_{n+1}AX_n$, where n is 1, 2 or 3, three groups of MAX phases, 211, 312, 413 are known [2].

The $M_{n+1}AX_n$ phases are layered hexagonal solids with two formula units per unit cell, in which near close-packed layers of M are interleaved with layers of pure group A-elements and where the X-atoms are filling the octahedral sites between M layers (fig 4.2). The A group elements are located at the centres of trigonal prisms which are slightly larger than the octahedral sites. This site condition makes it better to accommodate the larger A-atoms [47]. This specific structure is believed to be the cause of their interesting properties such as their machinability [48]. Furthermore, it has also been known that their structure is characterised by a bond between M-C which is stronger than the bond between M-A.

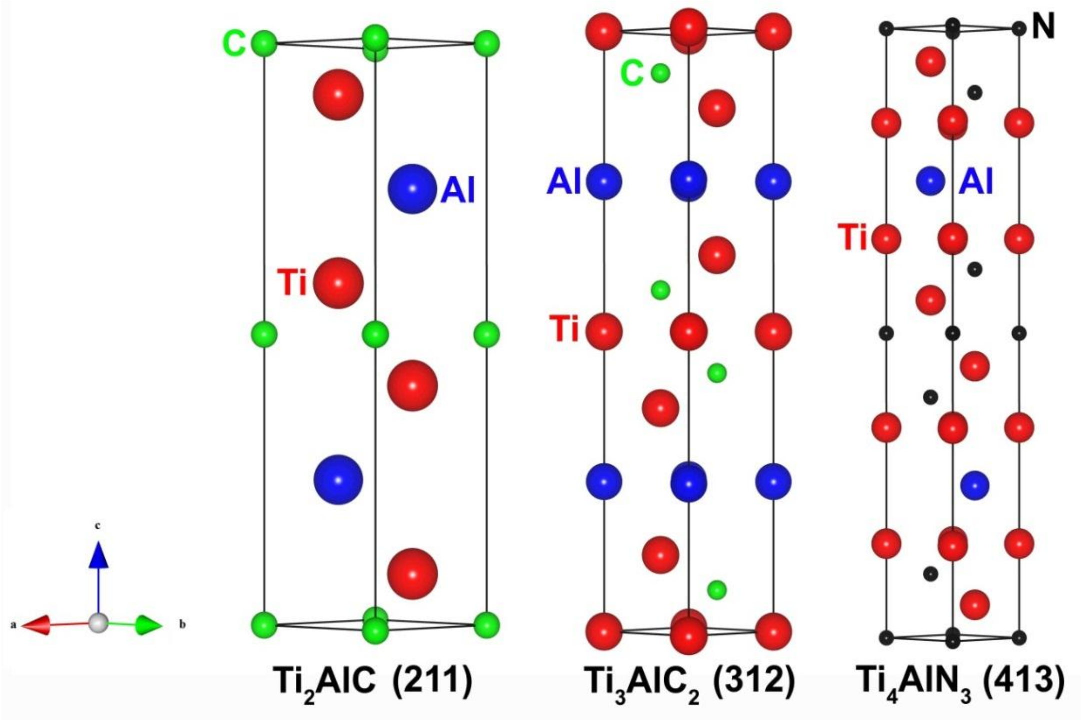

Figure 4.2 The crystal structure of the common MAX phase systems. The transition metal carbide or nitride layers are interleaved with layers of pure A-group element. An A-group element is located in the third layer (211 compounds), the fourth layer (312 compounds) and the fifth layer (413 compounds) [48].

These materials have unusual and sometimes unique combinations of properties which are in between the properties of ceramics and metals [1, 3-5]. On one hand, they behave as metals in terms of their machinability, electrical and thermal conductivity. On the other hand, they behave as ceramics in terms of their specific stiffness. Additionally, they are also damage-tolerant and thermal-shock resistant [49, 50]. These properties give rise to potential applications of MAX phases for instance as wear and corrosion resistant coatings of electrical contacts.

In bulk systems, MAX phases have several technological applications. For example, Ti_2AlC and Cr_2AlC demonstrated remarkable tribiological performance when tested against several counterparts [51, 52]. Ti_3SiC_2 has an oriented grain structure which is very important for high temperature applications such as jet engines for aircraft.

4.2. Ti_2AlC MAX phases

In the mid 70's Ivchenko and coworkers have reported their work on synthesising Ti_2AlC and Ti_2AlN, together with several properties of these materials [53-55]. But to date, the most complete scientific report about the Ti_2AlC bulk system such as the mechanical, thermal and electrical properties was made by Barsoum et al. and Radovic et al. [47, 55]. Furthermore, stress-strain curves of this material and its oxidation behaviour have also been investigated [56-58].

Unlike the bulk system, a thin film synthesis for Ti_2AlC has rarely been attempted. The most detailed investigation was done by Wilhelmson et al. who have deposited an epitaxial Ti_2AlC thin films with magnetron sputtering from individual targets [3]. Wilhemsson et al. have reported the physical properties of the thin films and compared it to the bulk system. Another deposition of Ti_2AlC films was reported by Walter who has deposited $Ti_{2.}AlC$ thin films from a single target [58]. Additionally several theoretical calculations have also been done [9, 59, 60].

To fulfil industrial needs, the film synthesis of MAX phases should address three things: (i) single phase growth of MAX phases, (ii) large area deposition and (iii) low substrate temperature. Until now, a detail study about the deposition process especially to achieve these three things has not been done. For that purpose a microstructural investigation is needed to be performed.

4.3. Cr_2AlC MAX phases

The first synthesis of the Cr_2AlC phase was reported by Nowotny [61]. In 1980 Schuster et al. have reported the phase relationship in the ternary system M-Al-C (M=Ti, Al and V) with their lattice parameters [62]. Several simulation studies try to complete the understanding of Cr_2AlC. For example Hallstedt et al. have calculated a thermodynamic evaluation of Al-Cr-C system [63]. Ab initio calculations to investigate the effect of composition on the structure of Cr_2AlC was reported by Martens et al. [64] and furthermore, Lofland et al. have also calculated elastic and electronic properties of the Cr_2AlC phase [65].

Table 4.1 Physical properties of Ti_2AlC Max phases in bulk and thin films.

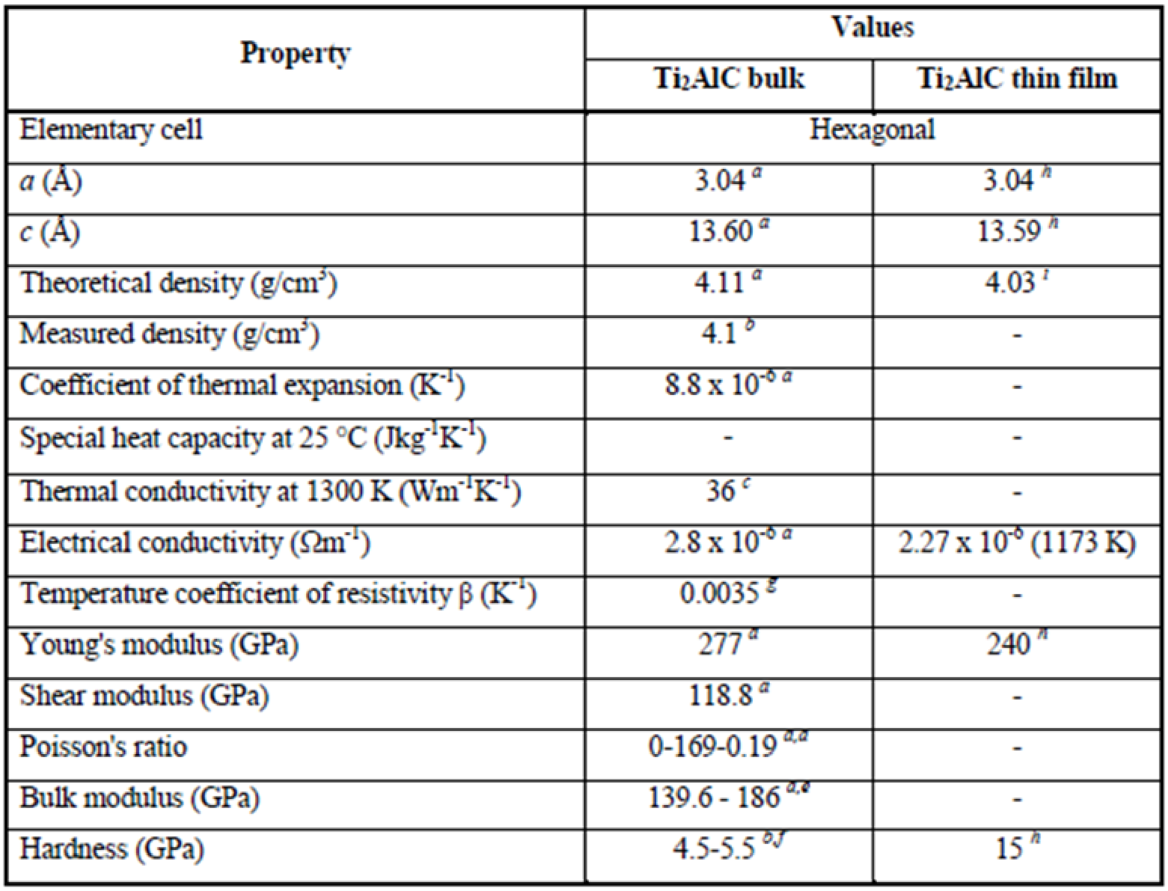

Property	**Values**	
	Ti_2AlC bulk	**Ti_2AlC thin film**
Elementary cell	Hexagonal	
a (Å)	3.04^{a}	3.04^{h}
c (Å)	13.60^{a}	13.59^{h}
Theoretical density (g/cm^3)	4.11^{a}	4.03^{i}
Measured density (g/cm^3)	4.1^{b}	-
Coefficient of thermal expansion (K^{-1})	$8.8 \times 10^{-6\ a}$	-
Special heat capacity at 25 °C (Jkg^{-1}K^{-1})	-	-
Thermal conductivity at 1300 K (Wm^{-1}K^{-1})	36^{c}	-
Electrical conductivity (Ωm^{-1})	$2.8 \times 10^{-6\ a}$	2.27×10^{-6} (1173 K)
Temperature coefficient of resistivity β (K^{-1})	0.0035^{g}	-
Young's modulus (GPa)	277^{a}	240^{h}
Shear modulus (GPa)	118.8^{a}	-
Poisson's ratio	$0\text{-}169\text{-}0.19^{a,a}$	-
Bulk modulus (GPa)	$139.6 - 186^{a,e}$	-
Hardness (GPa)	$4.5\text{-}5.5^{b,f}$	15^{h}

Reference a = [47], b = [66], c = [49], d = [55], e = [65], f = [67], g = [68], h = [3], i = [60]

The first successful Cr_2AlC thin film deposition by magnetron sputtering was reported by Schneider et al. [7]. Two years later, Walter et al. have successfully deposited Cr_2AlC thin films in large areas [5]. Some physical properties of the Ti_2AlC and Cr_2AlC Max phases are presented in table 4.1 and 4.2.

Tabel 4.2 Physical properties of Cr_2AlC Max phases in bulk and thin films.

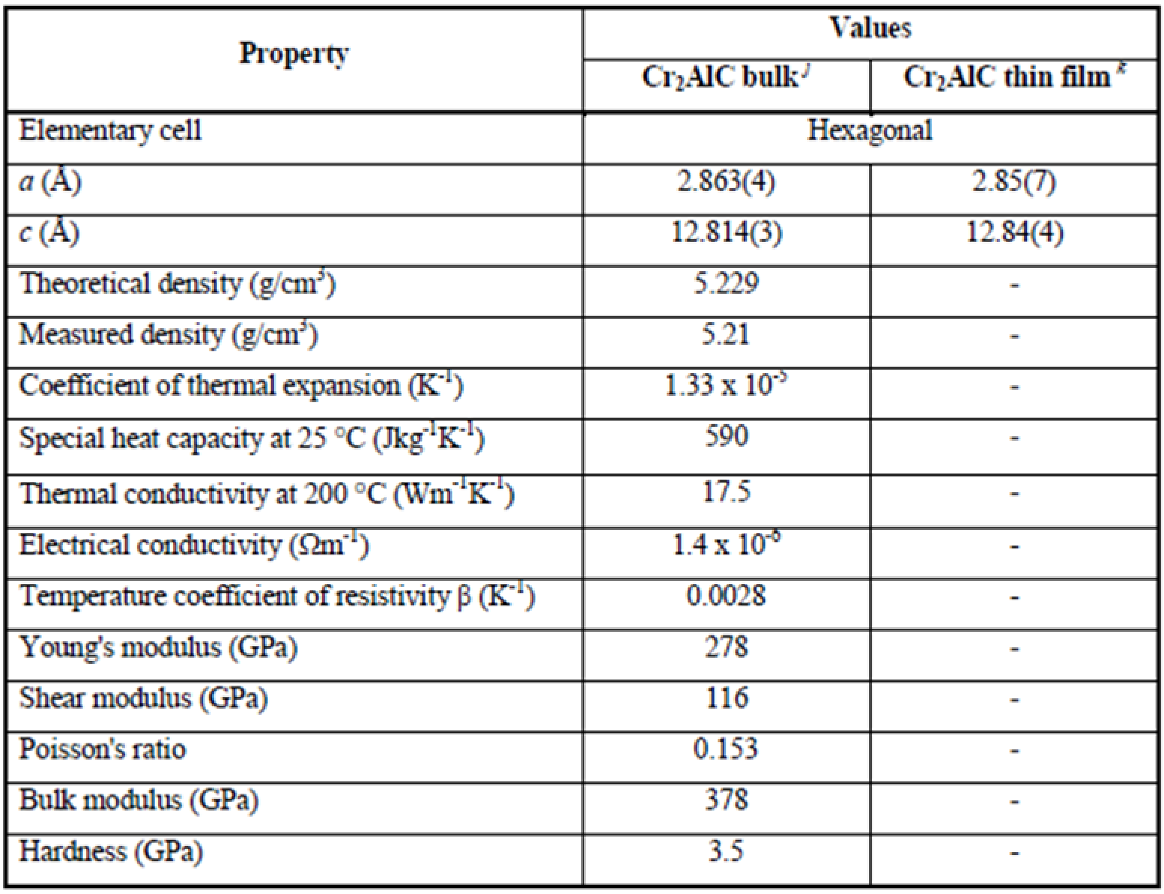

Property	Values	
	Cr_2AlC bulk^j	Cr_2AlC thin film^k
Elementary cell	Hexagonal	
a (Å)	2.863(4)	2.85(7)
c (Å)	12.814(3)	12.84(4)
Theoretical density (g/cm^3)	5.229	-
Measured density (g/cm^3)	5.21	-
Coefficient of thermal expansion (K^{-1})	1.33×10^{-5}	-
Special heat capacity at 25 °C (Jkg^{-1}K^{-1})	590	-
Thermal conductivity at 200 °C (Wm^{-1}K^{-1})	17.5	-
Electrical conductivity (Ωm^{-1})	1.4×10^{-6}	-
Temperature coefficient of resistivity β (K^{-1})	0.0028	-
Young's modulus (GPa)	278	-
Shear modulus (GPa)	116	-
Poisson's ratio	0.153	-
Bulk modulus (GPa)	378	-
Hardness (GPa)	3.5	-

Reference j = [68], k = [7]

4.4. Ti_2AlC and Cr_2AlC thin film growth and characterization

4.4.1. Physical vapour deposition (PVD) by Magnetron sputtering

All thin film deposition experiments were done at the Institute of Material Chemistry, RWTH Aachen University. Both Ti_2AlC and Cr_2AlC thin films were deposited using DC Magnetron sputtering. A high vacuum with a base pressure $\leq 5 \times 10^{-6}$ mbar was used. During the deposition, argon gas with 99.999% purity was introduced and a deposition pressure of 5×10^{-3} mbar was adjusted. As substrates, polished single crystal (0001) sapphire wafers were used. Both cathode and substrate have distance of ≈ 75 mm and the cathode was tilted approximately 40° with respect to the substrate's normal. The method was adopted from the experiment performed by Walter et al., in which MAX phase thin films have successfully been deposited in a large area [5, 69]. As seen in figure 4.3 (a), we used two targets from which, one was a compound target during the deposition. Additionally, for Ti_2AlC deposition the compound target was cut into 16 slices, 12 Ti_2AlC slices and 4 Ti slices. The use of target slices was due to the lack of Ti concentration in the deposited films [69]. Furthermore, the substrate was rotated at 10 rotations per minute during deposition.

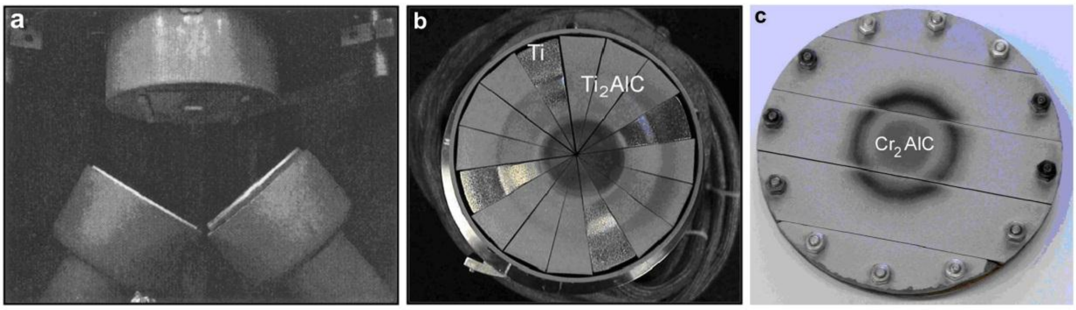

Figure 4.3 (a) Cathode and substrate position used in this work, (b) Target material for deposition of Ti_2AlC made by 16 slices of Ti_2AlC and Ti and (c) Target material for deposition of Cr_2AlC [70].

Based on previous results [69], the deposition of Ti_2AlC was done at a deposition temperature of 850°C. For Cr_2AlC, the deposition temperature was varied and values of 450°C, 550°C and 650°C were chosen.

4.4.2. Phase identification by X-ray diffraction

X-rays are produced when a high-energy electron strikes a material target and causes the electrons of core shells to be ejected, leaving holes in the inner shell. The excited state of the atom presents an unstable condition. To return to its ground state, electrons from the outer shells are transferred to the inner shells, in the process giving off characteristic X-rays whose energy is the difference between the binding energy of the corresponding shells. A schematic drawing of the X-ray production of K-lines can be seen in fig. 4.4. These X-rays can be used to identify the phase and crystal structure of the corresponding materials. The method is known as X-ray diffraction and a detailed description about this method can be found in [71]. Generally, when the incoming beams of X-rays are coming and passing into material, they scatter with the atoms. Each scattered beam will re-radiate a small portion of its intensity as a spherical wave. If scattered beams are arranged symmetrically with a separation *d*, these spherical waves will be in synchronization (add constructively) only in the direction where their path-length difference obeys Bragg's law [71]:

$$2d\sin\theta = n\lambda \tag{4.1}$$

where

d = the spacing between two lattice planes

θ = half of diffraction angle

n = an integer number and λ is the wavelength of X-ray beam.

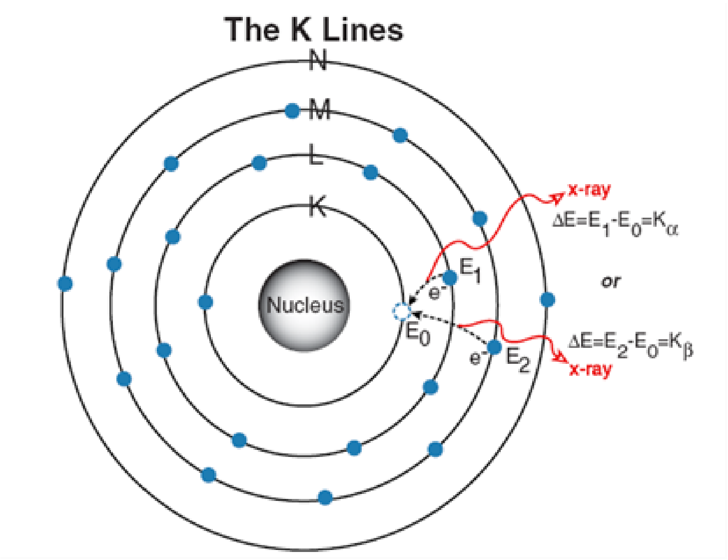

Figure 4.4 Schematic diagram of X-ray production.

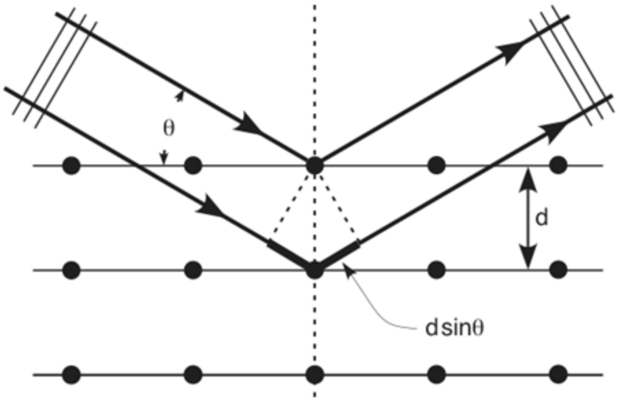

Figure 4.5 Schematic diagram of elastic X-ray scattering (Bragg diffraction) in crystalline matter.

In that case, a part of the incoming beam is deflected by an angle of 2θ, producing a reflection spot in the diffraction pattern. X-rays are used to produce diffraction patterns because their wavelength λ (0.1-1Å) is typically at the same order of magnitude as the spacing d between planes in the crystal.

Both the Ti_2AlC and Cr_2AlC target and all deposited films were investigated by X-ray diffraction. As seen in figure 4.6 (a), the X-ray diffractogram shows that the compound target of Ti_2AlC contains a small amount of Ti_3AlC_2. On other hand for the Cr_2AlC compound target ≥ 90 pct peak intensity can be attributed to Cr_2AlC phase (figure 4.6(b)).

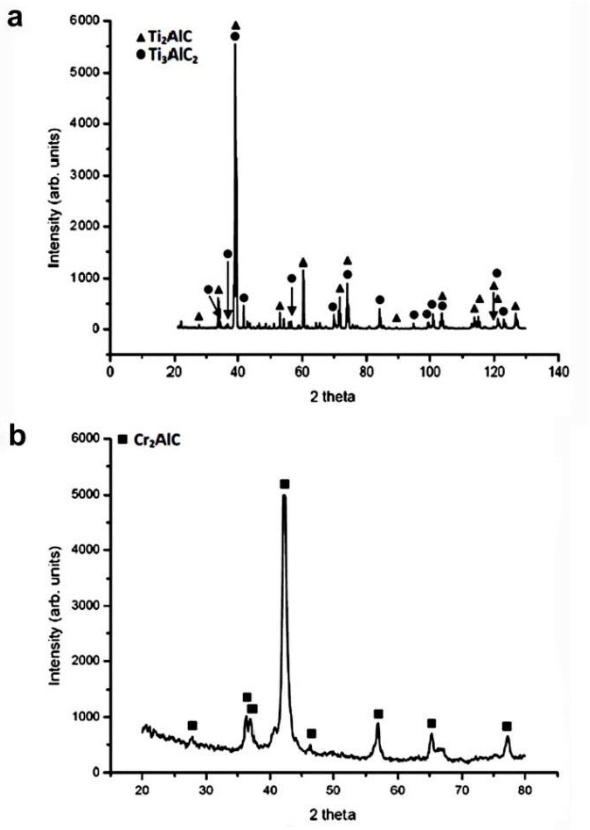

Figure 4.6 X-ray diffractograms of (a) Ti_2AlC and (b) Cr_2AlC target material.

X-ray diffractogram of the Ti_2AlC deposited film shows that the film contains Ti_2AlC as the major phase and a small amount of TiC (see fig 4.7 (a)). Furthermore, XRD diffractograms of all Cr_2AlC thin films indicate that a single phase Cr_2AlC with a purity of more than 90% has successfully been deposited. Peaks belonging to Cr_2AlC which have been detected for the thin film deposited at 450°C show that the thin film can be deposited at a very low deposition temperature (figure 4.7 (b)).

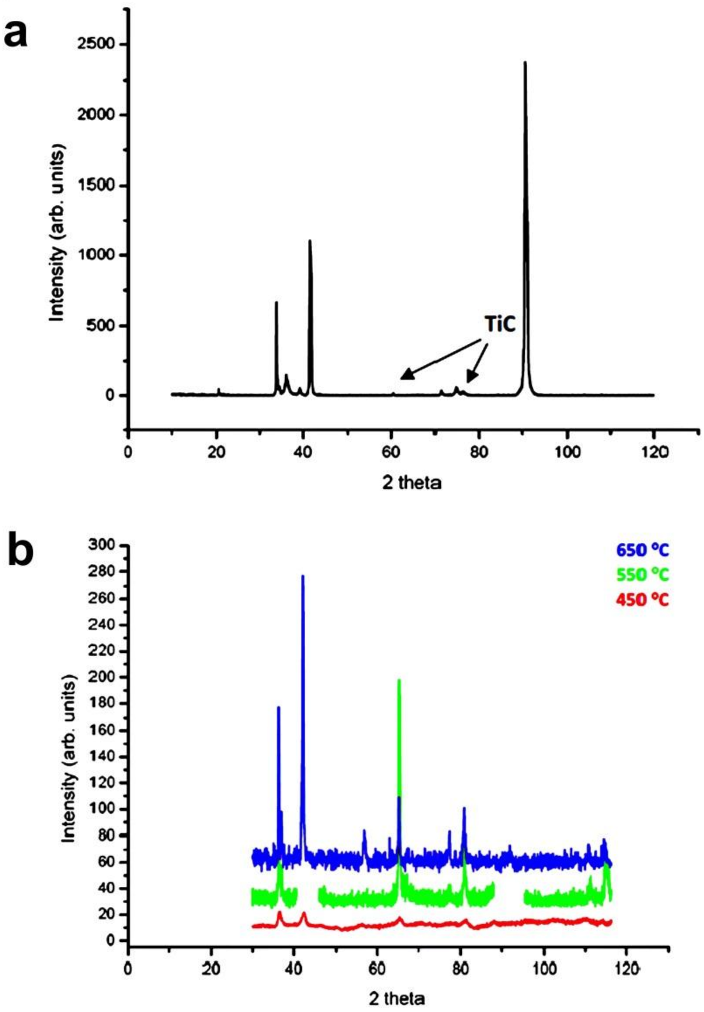

Figure 4.7 XRD data for (a) Ti_2AlC film deposited at 850°C temperature substrate and (b) Cr_2AlC films deposited at different substrate temperatures.

4.4.3. Nanoindentation

Special instruments and methods to measure mechanical properties of thin films are needed. There are two methods currently available, namely micro hardness and depth-sensing nanoindentation instruments. The latter have the advantages of better data resolution, repeatability in the measurement in hardness and the ability to obtain information about the elastic and time-dependent plastic properties of the sample. Normally the measurement is done by applying one complete cycle of loading and unloading. Detailed explanation about the nanoidentation can be found in [72, 73].

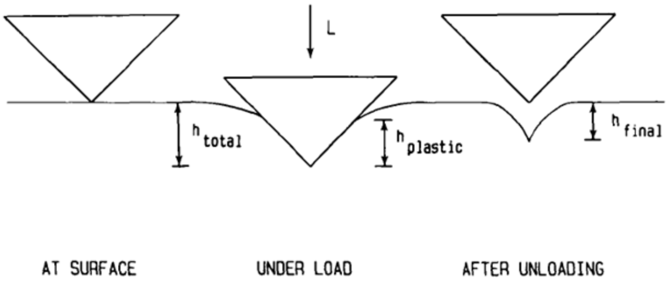

Figure 4.8 Schematic diagram of the indenting process [72].

As depth-sensing instrument, a commercial nanoidentation instrument from Nano Instruments Inc was used. As seen in figure 4.10, the nanoindenter consists of a triangular pyramid shaped indenter made of a diamond, whose position is determined by a capacitance displacement gauge. The capacitance displacement gauge permits the detection of displacement changes with a resolution of 0.2-0.3 nm [72]. All operations including indentation rate control and data recording are computer controlled.

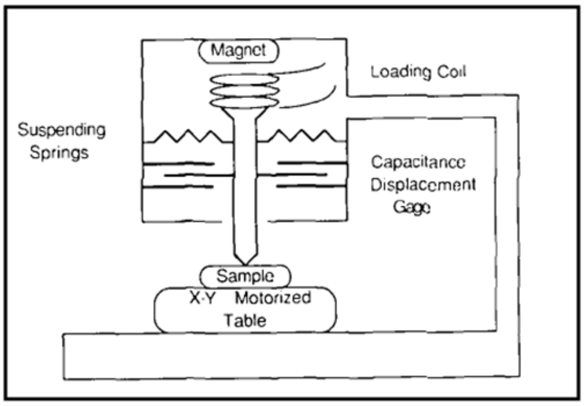

Figure 4.9 Schematic diagram of the nanoindentation [72].

Bulychev, Alekhin, Shorshorov, and co-workers have done the measurement with micro hardness in the early 1970’s. Based on their work, an elastic modulus can be calculated using the equation [74]:

$$E_r = \frac{\sqrt{\pi}}{2}\frac{S}{\sqrt{A}} \tag{4.2}$$

$$\frac{1}{E_r} = \frac{\left(1-v^2\right)}{E} + \frac{\left(1-v_i^2\right)}{E_i} \tag{4.3}$$

where S is the stiffness of the sample ν is Poisson's ratio and E is the elastic modulus of the sample and subscript i corresponds to the indenter. Furthermore, the hardness can be calculated using the following equation:

$$H = \frac{P_{\max}}{A} \tag{4.4}$$

where H is hardness, P_{max} is the maximum load and A is the contact area calculated from the corresponding contact depth with the tip area function.

In this work, a triboindenter from Hysitron Inc. with two different tips, Berkovich and cube corner, has been used. The first tip was used for elastic properties characterisation and the latter for surface roughness measurements. After the indentation, multiple load-unloading sequences were applied for drift correction. To avoid substrate effects [72], the contact depth was maintained to be ≤ 10% of the film thickness (1-2µm).

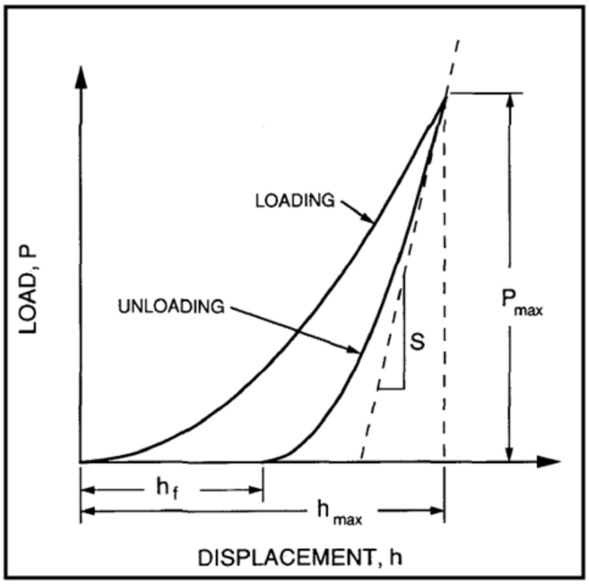

Figure 4.10 A schematic representation of load versus indenter displacement data for an indentation experiment [73].

The measured Young's modulus for Ti_2AlC film in this work is 266 ± 106 GPa and the corresponding bulk modulus approximated as isotropic is 145 ± 58 GPa. The Poisson's ratio value used for the calculations is 0.194 [60]. However, the standard deviation of the nanoidentation measurements is up to 40%, which to a great extent can reasonably be attributed to the surface roughness of the film. The root mean square (RMS) roughness value of the surface was measured to be 24 ± 5 nm, corresponding to 50% of the lower bound of the contact depths taken into consideration during the measurements. The measured hardness which was determined by the nanoindentation measurement is 9.8 ± 1.7 GPa.

From X-rays diffractograms of Cr_2AlC deposited thin films, it can be shown that polycrystalline thin film was successfully deposited at 650°C. Based on that initial result, we use this specimen for elastic property characterisation. The Young's and bulk modulus values are 298 ± 21 GPa and 189 ± 21 GPa, respectively. The Poisson's ratio used for the calculation is 0.236 [60]. The film has a low RMS surface roughness value of 7 ± 4 nm, corresponding to only ≈ 15% of the lower bound of the contact depth used in this present work. Figure 4.12 (a) and (b) show load-displacement curves of Ti_2AlC and Cr_2AlC respectively.

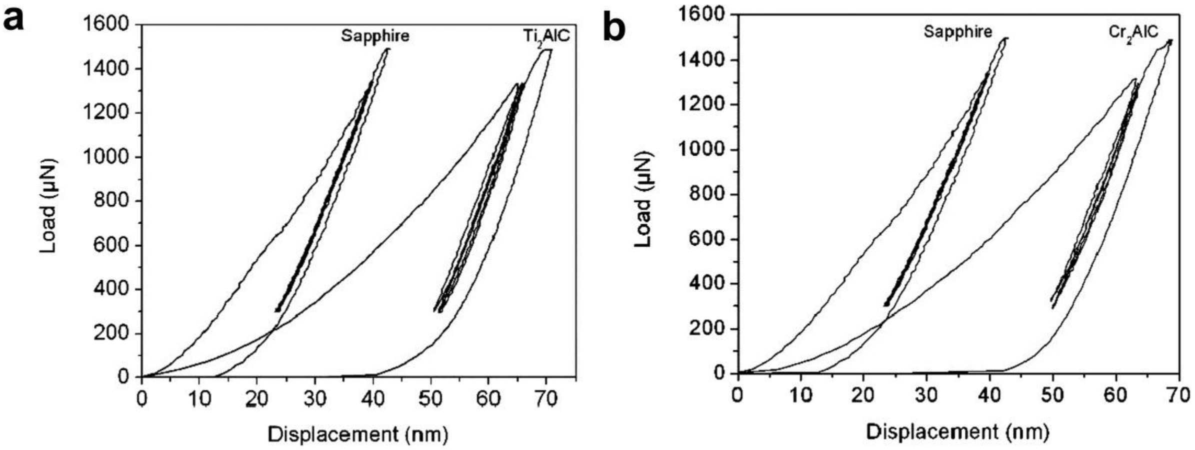

Figure 4.11 Load-displacement curve of the (a) Ti_2AlC + Ti target with ratio 3:1 and (b) Cr_2AlC thin film deposited on sapphire at 650°C. The load-displacement curve of sapphire is included as a reference.

This page is intended to be blank

5 Isothermal oxidation behaviour and microstructure evolution of high temperature oxidation resistant materials: Cr_2AlC thin films and Fe-Cr-Al model alloys

The oxidation resistance of materials is one of the primary requirements for their high-temperature application [75]. As reported by several investigators, MAX phases are known as promising candidate materials for advanced technologies and Ti_3SiC_2 is known as the best characterised MAX phase for this property. It has an activation energy in the range of 310-370 kJ/mol [76-79] and a parabolic rate constant, kp, ranging from 10^{-6} $kg^2m^{-4}s^{-1}$ [77] to 10^{-8} $kg^2m^{-4}s^{-1}$ [79] at 1200°C. On the other hand, Fe-Cr-Al as an iron base alloy is also known as a good material for high temperature applications. Frequently, reactive elements such as Y or Hf are added to improve the properties. For example, Naumenko et al. have reported that a high purity Fe-Cr-Al alloys with Y and Zr addition has a parabolic rate constant in the range 0.04-0.06 $mg^2 \cdot cm^{-4} \cdot h^{-1}$ [80].

5.1. Thermal properties of Cr_2AlC thin films

As explained in chapter 4, Cr_2AlC displays a unique combination of properties, including low density, high elastic modulus, easy machinability, excellent thermal shock resistance and damage tolerance. Unfortunately, only few descriptions about the oxidation behaviour of Cr_2AlC are reported in the literature. In bulk systems, Lin et al. [81] have reported that Cr_2AlC has a parabolic rate constant kp = 6.8×10^{-10} $kg^2m^{-4}s^{-1}$ at 1200°C, which is 2–4 times lower than Ti_3SiC_2 at 1200°C [76, 79, 82, 83] . Later on, several extensive investigations on the oxidation resistance of bulk Cr_2AlC were reported by Lin et al. [10] and Tian et al. [12] which cleary show that Cr_2AlC exhibits an excellent oxidation resistance. Although Ti_2AlC exhibits good high-temperature oxidation resistance in air, it could not resist serious Na_2SO_4 induced hot corrosion attacks at 900 and 1000°C [11]. Based on this information, it is clear that Cr_2AlC is a very promising candidate as a high-temperature material.

5.2. Oxidation of Cr_2AlC

In the selective oxidation of a material containing Cr and Al, both Al_2O_3 and/or Cr_2O_3 scales can be formed. Cr_2O_3 forming alloys generally contain less than 2-3% Al and 15% or more Cr. On the other hand, Al_2O_3 forming alloys can be found in material with as low as 5% Al. Environments also play an important role. It has been known that at high-temperatures (above 1000°C) Al_2O_3 will be formed more likely than Cr_2O_3 [84].

In bulk systems, Lee, et al. have showed that only a thin external Al_2O_3 oxide layer was formed after 336 h of oxidation at 1300°C in air [85]. They have also showed the Al-depletion and Cr-enrichment have occurred underneath the Al_2O_3 layer. Microstructure investigations have revealed that the surface grains of α-Al_2O_3 were fine but the inner grains were coarse and more columnar. The α-Al_2O_3 has grown very slowly and the measured oxide thickness was only ~ 27 µm.

5.3. Fe-Cr-Al alloys

Fe-Cr-Al alloys are high temperature materials with an increasing technological importance. The main reason for their importance is that their resistance against environmental attacks in the temperature range of 900 – 1300°C is better than of any other material. The formation of the alumina scale on the surface of Fe-Cr-Al during high temperature oxidation is believed to be the cause of this resistance. Fe-Cr-Al alloys are commonly used as construction materials in a large variety of industrial and domestic facilities, where the operating temperature is between 900 and 1300°C [86].

In domestic use, Fe-Cr-Al alloys are used as heating element foils and thin wires in cooking plates, radiation devices, toasters, microwave equipments, heaters in boilers and washing machines as well as glow plugs and precision resistors in cars. The Fe-Cr-Al-based heating elements are being applied for industrial use in furnaces for heat treatments and drying in e.g. paper-aluminium, semiconductor and coating industries.

One of the biggest constraints in Fe-Cr-Al application is the aluminium depletion, especially under temperature cycling conditions [87, 88]. If the depletion has reached a certain critical level, a continuous protective alumina layer can no longer be established [87, 88]. As a consequence, Fe-based oxides are formed and lead to a rapid “breakaway” oxidation of the whole alloy matrix and finally to failure of the component. One way to keep the aluminium concentration above the critical level is by adding more aluminium to the starting material [89].

Besides the need of saving raw material and primary energy sources as well as recycling costs, the need for more efficient energy conversion and reduction of hazardous emissions will cause the Fe-Cr-Al alloys to be operated at even higher temperature and in new designs, which often requires a decreased component wall thickness. The decreasing wall thickness will reduce the aluminium reservoir and later on will make the breakaway faster.

Another possibility to slow down the depletion process of Fe-Cr-Al alloy is by adding some reactive elements to the alloy. Zirconium, yttrium and hafnium are some of the reactive elements which can increase the life time of Fe-Cr-Al alloys [90].

5.4. Formation of Al_2O_3 scale

The overall chemical reaction for the formation of Al_2O_3 can be written as [89]:

$$2Al + \frac{3}{2}O_2 = Al_2O_3 \tag{5.1}$$

In thermodynamic equilibrium where ΔG=0, as described in chapter 3, the free energy and the equilibrium constant are given by:

$$\Delta G_o = -RT \cdot \ln K \tag{5.2}$$

where

$$K = \frac{a_{Al_2O_3}}{a_{2Al} \cdot P_{O_2}^{3/2}} \tag{5.3}$$

From Eq 5.2 and 5.3, the oxygen partial pressure at the scale/metal interface which is equal to the dissociation pressure of alumina, can be calculated by:

$$P_{O_2} = \frac{a_{Al_2O_3}^{2/3}}{a_{Al}^{4/3}} \exp\left[\frac{2\Delta G_o}{3RT}\right] \tag{5.4}$$

If depletion of the scale forming element, i.e. Al, occurs during oxidation, then its activity decreases with exposure time.

Based on experiments done by Quadakkers for commercial Fe-Cr-Al alloys, the experimentally determined oxide growth at temperature above 1000°C frequently shows a sub-parabolic time dependence with a value of n around 0.35 [91]:

$$x = k \cdot t^{n} \tag{5.5}$$

where x, k and tn are scale thickness, time and parabolic constant respectively.

At the beginning of the oxidation, oxygen uptake is caused by the growth of the alumina scale. During this stage, the alloy Al reservoir is only consumed for the scale formation. After some time the alumina scale starts to spall [91, 92]. Since there is still sufficient Al in the alloy, the protective alumina scale is successfully re-healed. This spalling/re-healing process contributes significantly to the consumption of the alloy Al-reservoir and continues until Al is depleted beneath a critical level. Breakaway oxidation occurs when this critical level has been reached.

The Al-reservoir can be defined as the amount of aluminium available for the formation of an external continuous alumina layer. Since the commercial Fe-Cr-Al alloys contain 4 to 6 mass % aluminium, one can increase the aluminium content to increase the Al-reservoir with the limitation up to 7% because of the deterioration of the alloy mechanical properties, especially the ductility and formability [93]. Another possibility to extend the material’s lifetime against oxidation is by increasing the wall thickness. Although it will increase the operating cost, it was shown that under the same experimental condition, thicker specimens due to the higher volume to surface ratio fail after much longer exposure time than the thinner ones [88].

5.5. Microstructural and protective properties of Al_2O_3 scale

In many Fe-Cr-Al high temperature alloys, the aluminium oxide formed on the surface adopts a wrinkled or convoluted morphology [94]. This morphology develops and changes with time during oxidation at high temperature and is not a result of the cooling process to room temperature. Observations of cross-sections reveal that the thickness of the oxide is more or less uniform, demonstrating that wrinkling is not caused by oxide intrusions or variations of the oxide growth rate from place to place. Several explanations about the wrinkling mechanisms can be found in literature [95-97]. Furthermore, a transient character of alumina lateral growth on the Fe-Cr-Al alloy, which the oxide-growth mechanism changes with time, has been observed by Tolpygo [98]. Tolpygo has also showed that the lateral growth of the detached scale appears to be the same as that of the adherent scale on the Fe-Cr-Al alloy, which means that the biaxial compression of the scale during oxidation does not suppress lateral growth, and conversely, when the stress is relieved in the detached oxide, this does not facilitate lateral growth. Furthermore, as discussed in chapter 3, both stable and metastable alumina have different microstructure. For example, Θ-Al_2O_3 scales are less dense than α-Al_2O_3 [43, 99] and the metastable alumina tend to form a bladelike morphology [44, 45].

5.6. Reactive element effect on growth mechanism and microstructure

The effect of reactive elements (RE) additions on the oxidation properties of chromia and alumina forming alloys has been studied extensively [100, 101]. In general, a small amount addition of RE, especially yttrium, will significantly increase the long term scale integrity. A finely dispersed yttria, for example, allows stabilising a very coarse alloy microstructure over long exposure time which at the end leads to excellent creep resistance up to much higher temperature. Quadakkers has reported that only a specific range amount of added RE concentration will reduce the oxidation rates. It has been proposed that the amount of Y-rich oxide particles on the alumina grains boundaries will form pores and microcracks. This condition will enhance molecular oxygen transport through the scale which causes the increase of oxidation rate [84, 91, 102].

The effect can be produced either by implanting the reactive elements into the surface alloys or by coating the surface with a thin layer of reactive element oxides [101]. Moreover, a detailed about the mechanisms of REE can be found in [103].

As mentioned above, it has also been reported that the most commonly used reactive element which is added to improve the properties of the alumina-based scale on Fe-Cr-Al alloys, is yttrium. One disadvantage of yttrium addition is the limited lifetime of Y-containing Fe-Cr-Al alloy in the temperature range of 1100-1300°C. Recently it was reported that addition of Zr might result in a substantial improvement of alumina scale adhesion, which was attributed to the prevention of Cr-carbide formation at the alloy grain boundaries and to the change of the oxide microstructure due to rapid Zr-incorporation into the scale [104, 105]. Microstructure oxide scale after addition of Zr to a Fe-Cr-Al-Y-based composition has been investigated. It has been shown that oxide morphology changes from columnar to small, equiaxed grains. The formation of zirconium's inclusion and in-scale porosity has also been identified [106].

5.7. Oxidation parameters calculation and experimental overview

5.7.1. Specimen fabrication

Compound Cr_2AlC target supplied by Kanthal [107] was used for the deposition Cr_2AlC thin films by magnetron sputtering. Polycrystalline α-Al_2O_3 substrate with 10x10 mm^2 size supplied by KERAFOL was used [108]. The substrate was cleaned in an ultrasonic bath prior to deposition. Deposition at a substrate temperature of 820°C was done for 5 hours at power density of 6.3 W/cm^2 under an Ar pressure of $6x10^{-3}$ mbar producing a film with 35 µm thickness. Before the deposition, the base pressure of approximately 10^{-7} mbar has been reached.

In the case of the Fe-Cr-Al model alloys, two batches of specimens were investigated. Both batches were manufactured by Armines [109]. High purity alloys (Fe+20%Cr+5%Al+Y+Zr) with defined elements addition, were prepared from pure elements by melting in a cold crucible under pure gas and solidification in the cold crucible. The alloys were forging and rolling down to 1.5 mm at 1000°C. The final annealing was performed at 1000°C followed by water quenching. Finally, sheets of alloys were quench annealed from 1000°C. The chemical compositions for both batches are similar with the only difference in the titanium contents which is higher in the J-batch specimens than the F-batch specimens. The detailed of the chemical composition can be found in appendix C, table C.1. Furthermore, the two kinds of oxidation test were performed for the batches. For the F-batch specimens, oxidation tests were performed in synthetic air at 1200°C with variation in the oxidation time. For this batch, the microstructure evolution due to the oxidation time was investigated. On the other hand, the J-batch specimens were oxidised for 100 h at the oxidation temperature of 1050 - 1200°C. All of the J-batch specimens were oxidised in laboratory air except those oxidised at 1200°C where the oxidation tests were performed in synthetic air. Additionally, there are two types of J- batch specimens which were investigated for every temperature oxidation: the thin and the thick specimens. In this work, the effect of specimen thickness was investigated. Table 5.1 shows the list of the specimen IDs for both batches. For convenience, we have changed the as received specimen ID to the new ID as shown in table 5.1.

Table 5.1. Specimen description ID for two batches of Fe-Cr-Al model alloys.

No	**Batch name**		**Description**
	As Received	**New**	
1	**FTJ32**	**F1H**	1200°C, 1 h, syn. Air, spec thickness: 1 mm
2	**FTJ31**	**F8H**	1200°C, 8 h, syn. Air, spec thickness: 1 mm
3	**FTJ2**	**F100H**	1200°C, 100 h, syn. Air, spec thickness: 1 mm
4	**JJG6**	**J1050-N**	1050°C, 100 h, lab air, spec thickness: 0.2 mm
5	**JJG5**	**J1050-K**	1050°C, 100 h, lab air, spec thickness: 1.3 mm
6	**JJG9**	**J1100-N**	1100°C, 100 h, lab air, spec thickness: 0.2 mm
7	**JJG10**	**J1100-K**	1100°C, 100 h, lab air, spec thickness: 1.3 mm
8	**JJG22**	**J1150-N**	1150°C, 100 h, lab air, spec thickness: 0.2 mm
9	**JJG21**	**J1150-K**	1150°C, 100 h, lab air, spec thickness: 1.3 mm
10	**JJG33**	**J1200-N**	1200°C, 100 h, syn. air (TG), spec thickness: 0.2 mm
11	**JJG34**	**J1200-K**	1200°C, 100 h, syn. air (TG), spec thickness: 1.0 mm

5.7.2. Oxidation parameter calculation

Although the corrosion process can be measured, repeated and predicted, the interpretation of the results under controlled conditions in high-temperature environments is often difficult. Together with temperature and time, the range of composition of the alloy, the protective coatings and the effect of corrosive gaseous environment make the prediction is further complicated. Pre-simulations are needed to achieve better results in determining the oxidation parameters. One parameter that has been deeply investigated is the shape of the test specimen. Metal alloy test specimens with different shapes (e.g., flat circular, cylindrical, or spherical) and sizes will give different corrosion rates. Romański has reported that the best reproducibility of the results is obtained with flat samples [110]. Corrosion studies usually use rectangular- or circular-shape flat specimens, with thickness not exceeding 1 mm and total surface area of a few square centimetres. To eliminate the effect of edges and corners on the corrosion process, these sample parts can be rounded. The corrosion process is additionally influenced by surface finishing (grinding, mechanical or electrolytic polishing, etc.) [111].

The most frequent method to measure the oxidation rate is thermogravimetric analysis. It consists of measuring the weight change of oxidised samples placed in the reaction zone (fig 5.1) with a precision as low as 0.1 µg of the mass change. The weight change taken from the TGA measurement, Δm(t), is caused by the additional weight of the oxidant taking part in the reaction with the metal, Δmox(t), and the weight of any volatile component of the corrosion products, Δmvol(t):

$$\Delta m(t) = \Delta m_{ox}(t) - \Delta m_{vol(t)} \tag{5.6}$$

The measuring errors in the TGA method, especially when the weight gains are small, may come from the weight change of the suspensions, which are usually made of thin platinum or platinum-rhodium wires, quartz fibres, or preoxidised Fe-Cr-Al wires covered with a protective film of alumina. High-temperature (over 1000°C) and high partial pressure of oxygen combined with prolonged test time (thousands of hours) would cause a volatile PtO_2 scale to form. At low temperature, on the other hand, using quartz suspension is not recommended because of the possibility of the formation of a volatile oxide, SiO_2. However, by weighing the suspension fixture before and after the experiment, it can be checked whether or not the weight change of the fixture due to the corrosion is negligible.

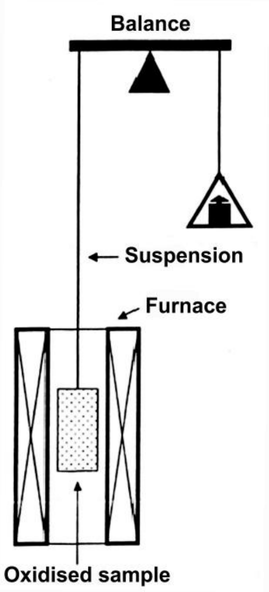

Figure 5.1 Schematic drawing of thermobalance for thermogravimetric analysis [112].

It should also be realised that the measured weight of the sample also includes that of gases that are dissolved in the metallic phase without taking part in the oxidation process. Because of its simplicity and high accuracy of measurement, the TGA method is the one most often encountered in corrosion studies.

In this work, all thermogravitric experiments were performed at IFF Jülich. For investigating Cr_2AlC thin films, the TGA was conducted in a vertical hot wall reactor with the sample being suspended with a Pt wire in the middle of the isothermal zone in an α-Al_2O_3 reaction tube. During the heating, the tube was evacuated to a pressure of approximately 10^{-2} mbar to avoid extensive oxidation of the sample. The mass gain was measured with a Linseis 4400 balance with a resolution of 10µg. The signal was recorded by a computer with a sampling rate of 1 s^{-1}. For Fe-Cr-Al alloys two different oxidation experiments were performed. The TGA experiment was conducted up to 500 h at temperatures between 1050°C and 1200°C and carried out in air (besides at 1200°C in synthetic air) with using a SETARAM® microbalance. The heating / cooling rate was 90 k/min. Additionally, isothermal experiments (up to 100 h) were carried out at temperature between 1050-1150°C in laboratory air.

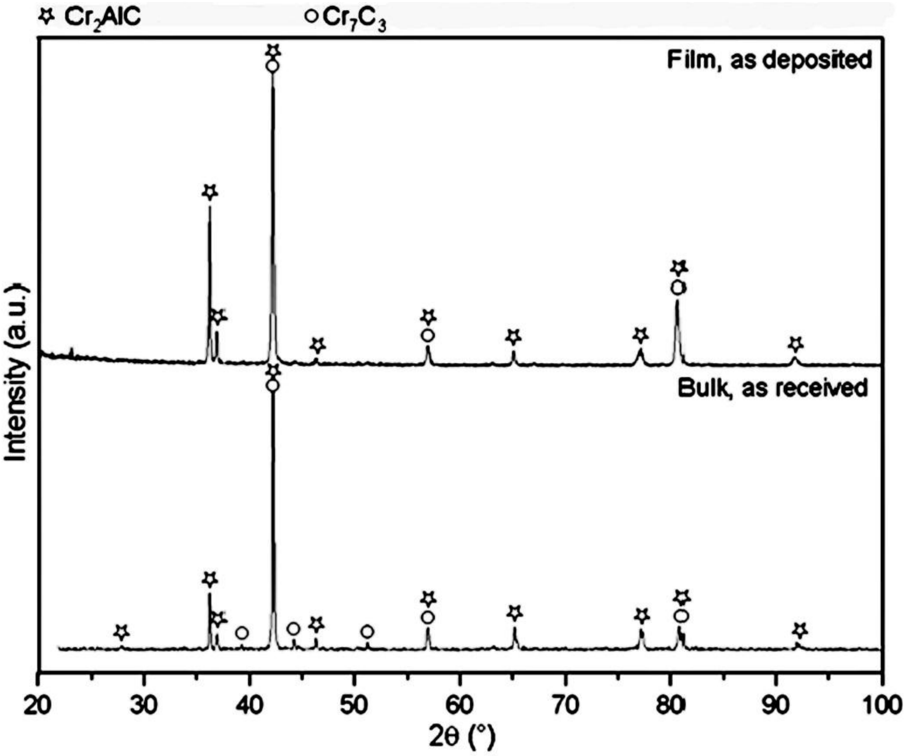

Figure 5.2 X-ray diffractograms of the as deposited film and bulk Cr_2AlC. In Cr_2AlC film only phase pure Cr_2AlC can be observed. On the other hand, small amounts of Cr_7C_3 phase (indicated by circle) in addition to Cr_2AlC is present in as received bulk Cr_2AlC [113].

Figure 5.2 shows the X-ray diffractograms of Cr_2AlC target materials and the as deposited Cr_2AlC films. Cr_2AlC was identified as the main phase present in the target material, together with a minor phase content of Cr_7C_3. In the as deposited films however, only the Cr_2AlC phase can be observed in the X-ray diffractograms, which tells us that the deposited films is a phase pure based on the diffraction data.

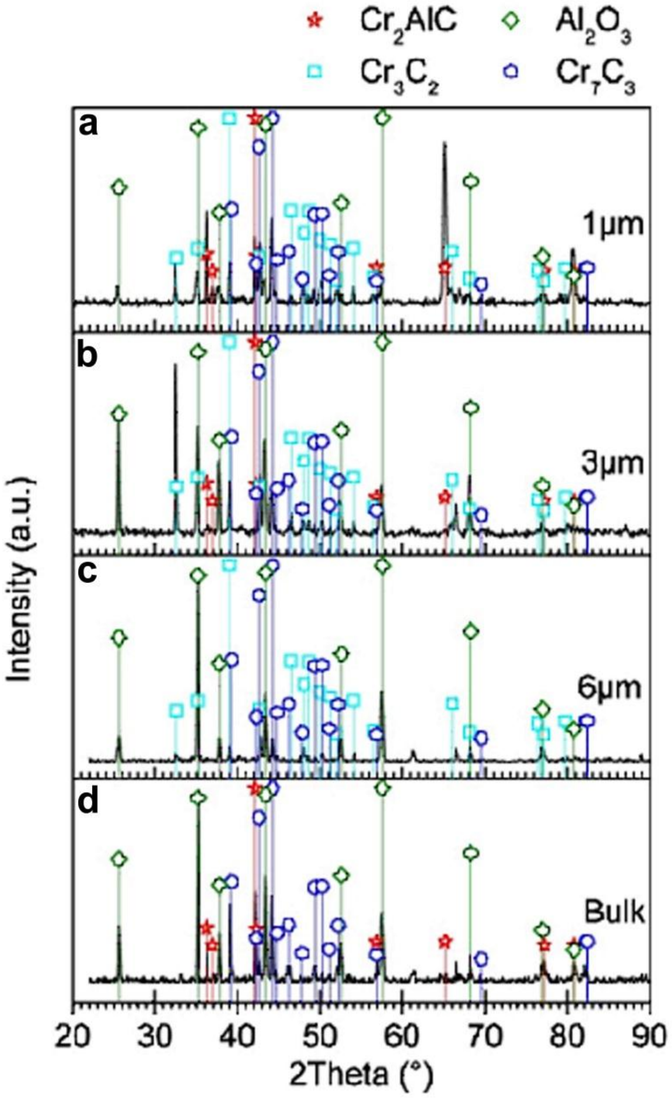

Figure 5.3 X-ray diffractograms of Cr_2AlC films with: a) 1 µm oxide scale, b) 3 µm oxide scale, c) 6 µm oxide scale and d) bulk Cr_2AlC with 6 µm oxide scale [113].

The X-ray diffractograms of oxidised Cr_2AlC films at 1320°C with different oxidation time are displayed in figure 5.2. On all oxidised films, only α-Al_2O_3 can be found as oxide scale. Furthermore, Cr_2AlC, Cr_3C_2 and Cr_7C_3 phases are found as additional phases in all thin film specimens. For comparison, figure 5.2 (d) shows X-rays diffractogram of oxidised bulk

Cr_2AlC with 6 µm oxide scale. In contrast to thin film with the same oxide scale thickness, in bulk Cr_2AlC only the Cr_7C_3 phase is present in addition to Cr_2AlC and the alumina oxide scale.

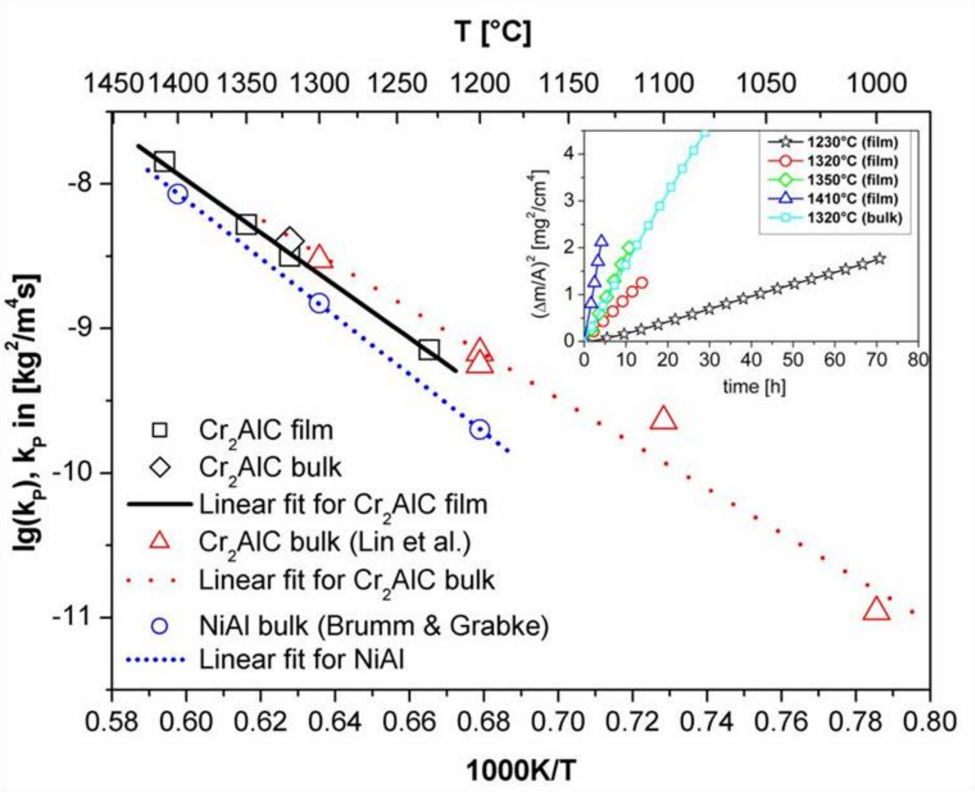

Figure 5.4 The temperature dependence of the parabolic rate constants for Cr_2AlC films (□) and bulk Cr_2AlC (◇) [113].

In the experiments, the TGA results as isothermal weight gain per unit area as a function of time for bulk Cr_2AlC and Cr_2AlC thin film samples at 1320°C, and for comparison, the Cr_2AlC thin film specimens at 1230, 1350 and 1410°C, were recorded. As mentioned before, a significant weight loss due to evaporation of Pt from the wire used to suspend the samples in the furnace was observed and corrected by adding corresponding weight losses at each time to the TGA data for each sample. The parabolic rate constant, kp, calculated from squared weight gain data increases from 7.1×10^{-10} $kg^2m^{-4}s^{-1}$ at 1230°C to 1.4×10^{-8} $kg^2m^{-4}s^{-1}$ at 1410°C. Figure 5.4 shows the logarithm of the parabolic rate constants kp as a function of the inverse temperature for the Cr_2AlC film (marked by □) and bulk Cr_2AlC (marked by ◇). As comparison, the parabolic rate constant values reported in the literature for Cr_2AlC after Lin et al. [10, 81] (marked byΔ) are added, which are consistent with the present work. Additionally, the logarithm of the parabolic constants, ln (kp), is also displayed as insert. The activation energy for oxidation of Cr_2AlC thin films, calculated by least square fit of a straight line through the ln kp values measured for the Cr_2AlC thin films is 384 kJ/mol compared to 298 kJ/mol for bulk Cr_2AlC [81].

Figure 5.5 shows weight change data for F-batch specimen of Fe-Cr-Al model alloys during isothermal oxidation at various temperatures.

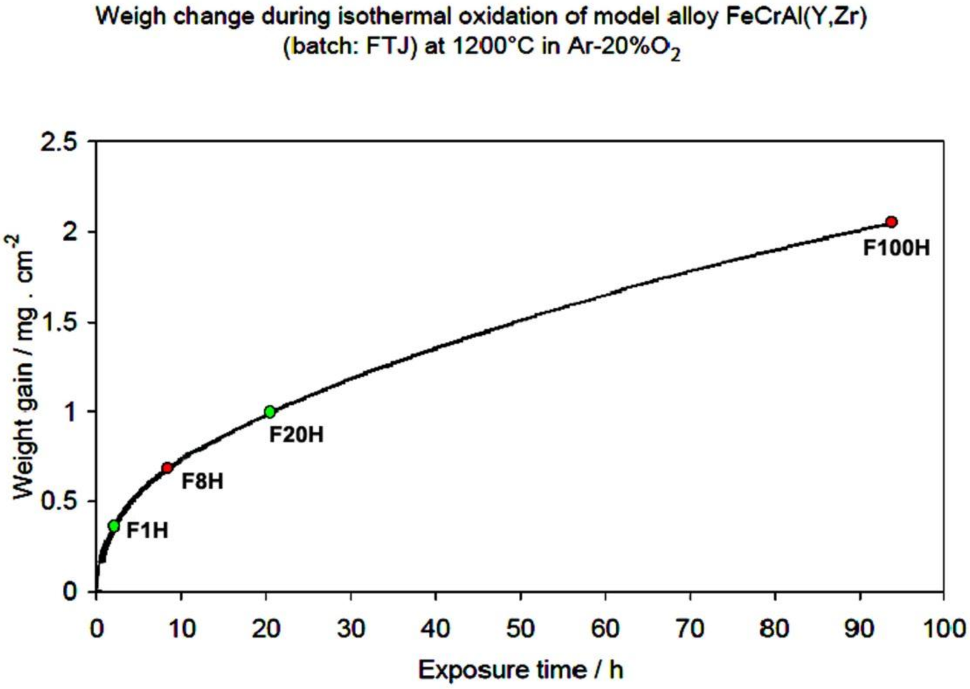

Figure 5.5 Mass change during isothermal oxidation of F-batch specimens at various temperature up to 100 h.

Weight change data for J-batch specimens of Fe-20Cr-5Al model alloys are displayed in figure 5.6. During isothermal oxidation at various temperatures in air, it was found that for short oxidation times of 100 h there was hardly any difference in the oxidation rate between thin and thick specimens. On the contrary, at higher temperature oxidation, e.g. at 1200°C, the difference in the oxidation rate between the thin and the thick specimens was clearer (see figure 5.7).

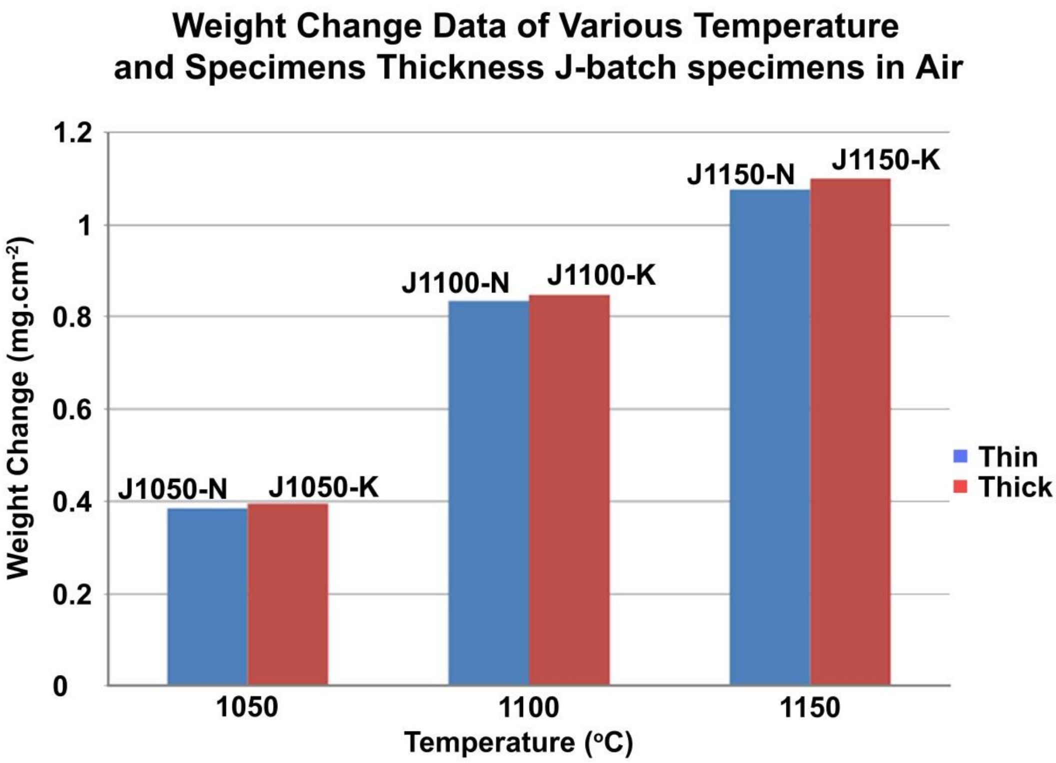

Figure 5.6 Mass change during isothermal oxidation of thin and thick J-batch specimens at various temperature for 100 h.

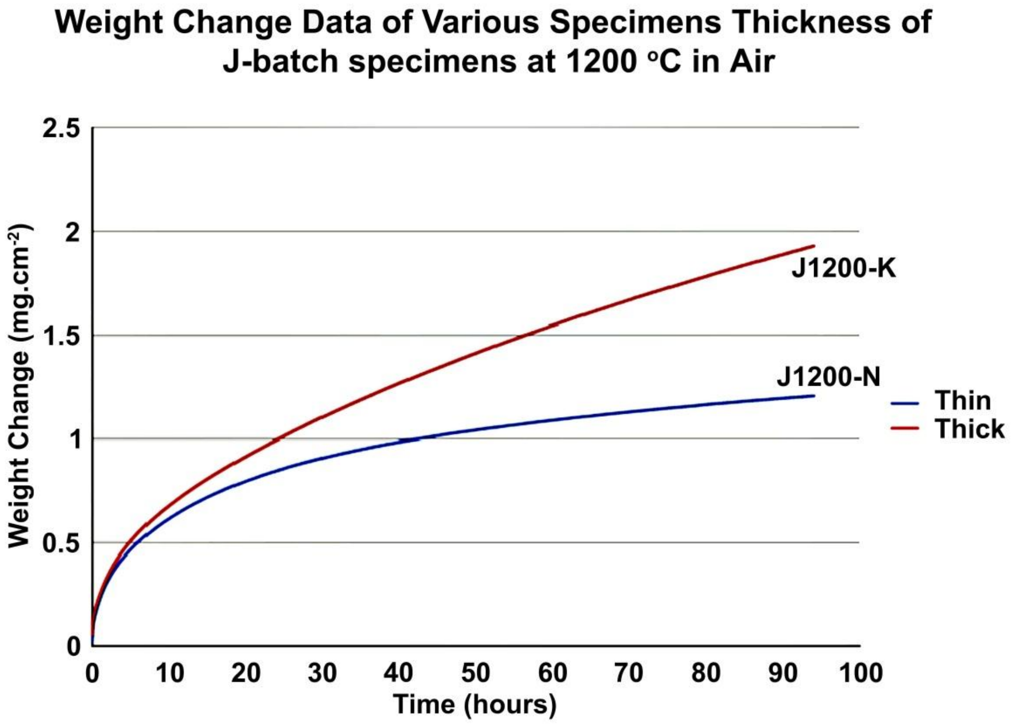

Figure 5.7 Mass change during isothermal oxidation of thin and thick J-batch specimens at 1200°C.

6 Experiments

Over the past years electron microscopes have become a very powerful tool for microstructural investigations. With recent achievements in transmission electron microscopy, for example, investigations with a resolution below 0.5 Å (50 pm) can be performed. This resolution is far beyond the resolution that can be achieved with light microscope which can separate distances only up to 300 nm ($3x10^5$ pm).

When an electron beam strikes the material, the electron can regenerate signals. Many of these signals are used for analytical analysis with transmission electron microscope. For example, reflected electrons can produce secondary and backscattered electrons which are mainly used for scanning electron microscope (SEM) investigations. On the other hand, transmitted electrons which consist of direct beam, elastic and inelastically scattered electrons are used in transmission electron microscope (TEM) investigations.

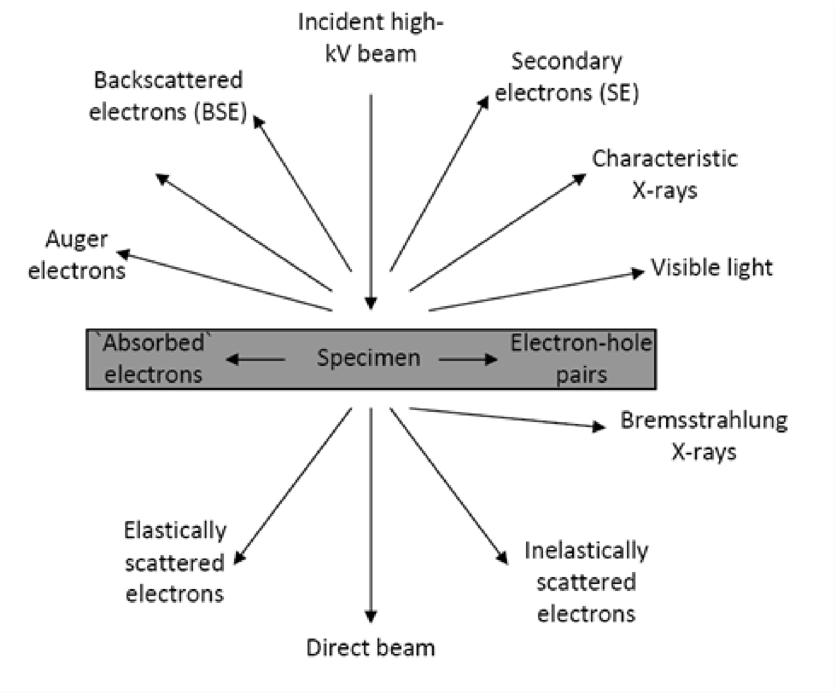

Figure 6.1 Electron beam interaction with the specimen [114].

6.1. Scanning Electron Microscopy (SEM)

The scanning electron microscope (SEM) is a powerful instrument for the examination and analysis of the microstructure characteristics of bulk materials. With a small electron probe, the investigation of a small area of material can be performed.

Basically, a SEM consists of an electron gun, lens system, electron collector, visual and recording cathode ray tubes (CRT). The use of CRT can be found in old SEM while nowadays all visualization and recording processes have been computerised. The electron gun, located on the top of the column, generates and accelerates electrons to energies in the range of 0.1 – 30 KV. There are several types of electron guns normally used: thermionic emitters (made of tungsten and LaB_6), cold and thermal or Schottky field emitters. The field emitters are being used especially in the modern SEMs due to their enhanced performance, reliability and lifetime.

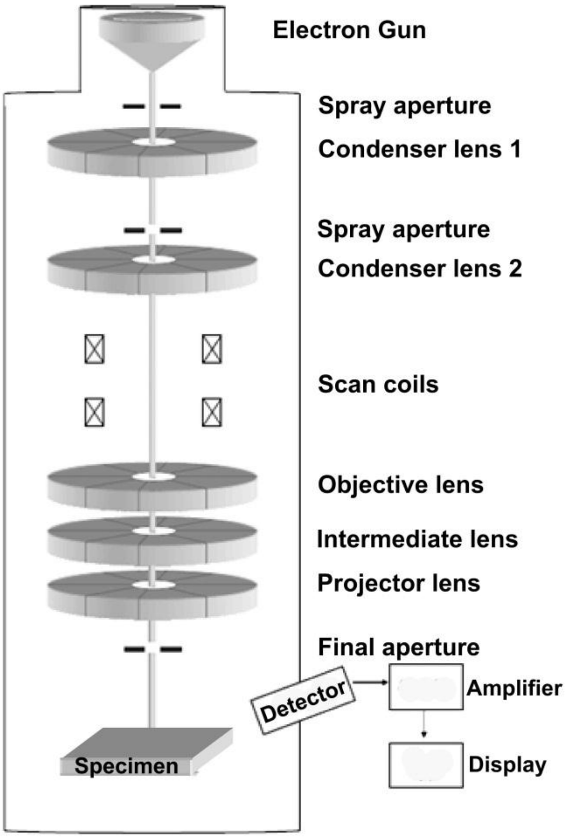

Figure 6.2 Schematic drawing of the electron column of a scanning electron microscope (SEM).

As its name says, the SEM produces the image by scanning the electron beam across the specimen point by point. In the imaging system there is a deflection system (see fig. 6.2) which causes the beam to move to a series of discrete locations along a line and then along another line below the first, and so on, until a rectangular “raster” is generated on the specimen.

In SEM investigations, secondary electrons and backscattered electrons are the most interesting electrons produced by the interaction with the specimen and are used to form the images. These two electron products vary as a result of differences in surface topography, as the electron beam scans across the specimen. The secondary electrons (SE) are produced when electrons from the specimen receive a small amount of kinetic energy by inelastic collisions with beam electrons and are emitted with energies in the range $0 \leq E_{SE} \leq 50$ eV. On the other hand, the backscattered electron (BSE) are the electron that escape the specimen as a result of multiple elastic/inelastic scattering through large angles and have an energy distribution of $E_{BSE} \geq 50$ eV. The most important contrast mechanism of BSE is the dependence of the backscattering coefficient on the mean atomic number Z, which allows phases with different value of Z to be recognised. More detailed information about SEM theory can be found in reference [115].

6.2. Cross Sectional TEM sample preparation: Focused Ion Beam (FIB)

Unlike in SEM investigations, very thin specimens are required to be investigated in a TEM. Although the word “thin” is a relative term, most people agree that it means “electron transparent”. Specimens below 100 nm thick should be used whenever possible, and in special cases for analytical investigation using electron energy loss spectroscopy (EELS) and high-resolution TEM (HRTEM), a thickness less than 50 nm is essential. There are several TEM specimen preparation techniques that have been known, namely ion beam thinning, mechanical polishing, ultramicrotomy, chemical and electro-polishing. Besides the duration of the preparation, which normally takes weeks, the main disadvantage of those preparation techniques is that they could not produce a very large thin area. The focused ion beam (FIB) techniques are used to overcome these problems. Besides the fact that it can produce a very large thin area, FIB can select the target area very precisely. Furthermore, compared to other methods, FIB preparation is fast and reliable. Last but not least, the FIB preparation techniques are virtually independent from the nature of the material, which means that most materials including ceramics, metals or even biological materials, can be prepared using this technique. With all those advantages, FIB preparation techniques have become the most powerful TEM sample preparation techniques over the last two decades. Nowadays FIB techniques can be used not only as preparation tools but also make material and failure analysis of isolated, sub-micron electrically tested structures possible [116-118].

The conventional FIB instrument consists of a vacuum system and a chamber, a liquid metal ion source (normally gallium), an ion column, a sample stage, detectors, gas delivery system, and a computer to run the complete instrument. A reservoir of gallium (Ga) is positioned in contact with a sharp Tungsten (W) needle. The Ga wets the needle and flows to the W tip. A high extraction field ($>10^8$ V/cm) is used to pull the liquid Ga into a sharp cone whose radius may be as small as 5-10 nm. Finally, ions are emitted as a result of field ionisation and post-ionisation and then accelerated down the FIB column [119]. As source, this liquid metal ion source (LMIS) of Ga is used because of two advantages: (i) it has a low melting point and therefore it exists in the liquid state near room temperature, and (ii) it can be focused to a very fine probe size (<10nm in diameter).

Conventional and lift out techniques are two common FIB-based sample preparation techniques. In the conventional technique, the specimens are picked up from the bulk specimen and then mounted on a cross section of Cu plate. Afterwards, it can be thinned and used as TEM specimens. Detailed explanation about conventional methods can be found in [120]. On the other hand, in the lift out technique the specimens will be milled to an electron-transparent membrane, and later on the membrane will be attached to a TEM grid using a manipulator. There are also two additional sub-techniques, Ex-situ and In-situ lifts out. In the Ex-situ lift out technique, the attachment process is done outside the FIB instrument while in the latter technique, it is done inside the FIB instrument [121-124].

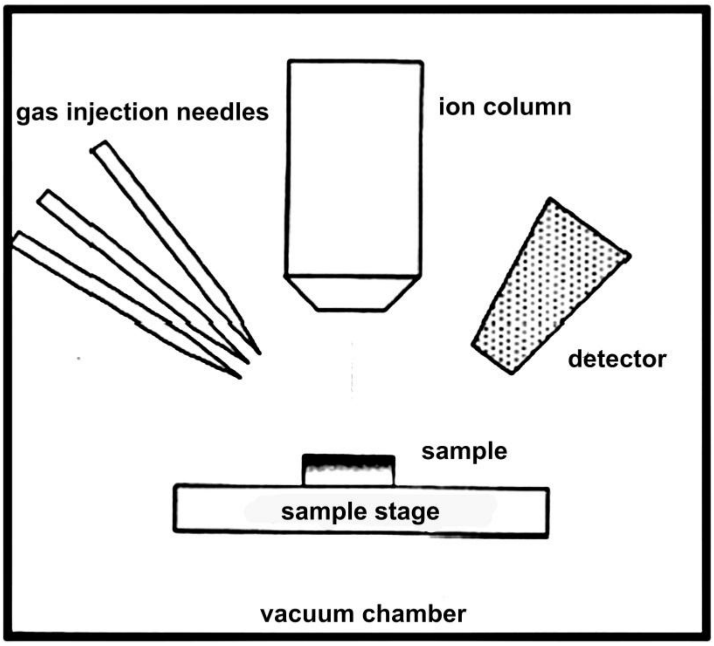

Figure 6.3 Schematic diagram of the FIB instrument [125].

All TEM specimens in this work were prepared by in situ lift out technique using FEI STRATA FIB 205. The process consisted of two steps; milling the specimens and re-thinning the attached lamella at TEM grid. The bulk material is first covered by tungsten with the size 20µm x 2µm x 3µm to protect the surface layer of the specimens from Ga ion bombardment. Next, the lamella is cut trace by trace on both sides using a special program. After the lamella reaches a thickness of about 500 nm, it is cut on the bottom and both left and right sides. At the right and the left sides small parts of the area are left to make sure the lamella is still fixed by the bulk specimen. The lamella is then tilted for 15 degrees by the user and one side of the lamella is attached to a micromanipulator. The lamella is made completely free from the bulk specimens by cutting all of the rest connected side and is attached to the micromanipulator to be transported to the TEM grid later on. In the second process, the lamella is attached to a special TEM grid, which is normally made of copper or molybdenum. Afterwards, the lamella is thinned on both sides until the thickness is less than 100 nm.

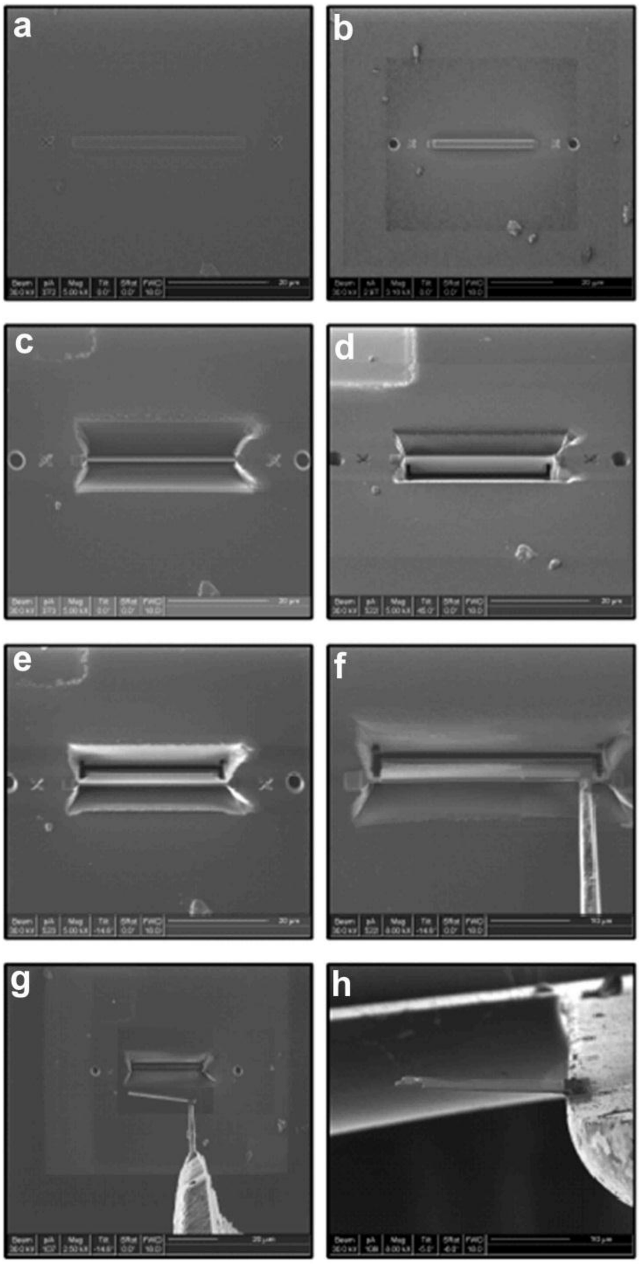

Figure 6.4 Step by step sequence of the FIB ex-situ lift out process as described in the text.

6.3. Transmission Electron Microscopy (TEM)

As seen in figure 6.1, electrons which pass through the specimen can be used in investigations by TEM. Back in 1932, the first TEM was developed by Knoll and Ruska and four years later the first commercial TEM was developed by Siemens and Halske in Germany in1939. After World War II, TEMs have become widely available from several commercial companies, namely Siemens, Zeiss, Hitachi, JEOL, Philips (now FEI) and RCA.

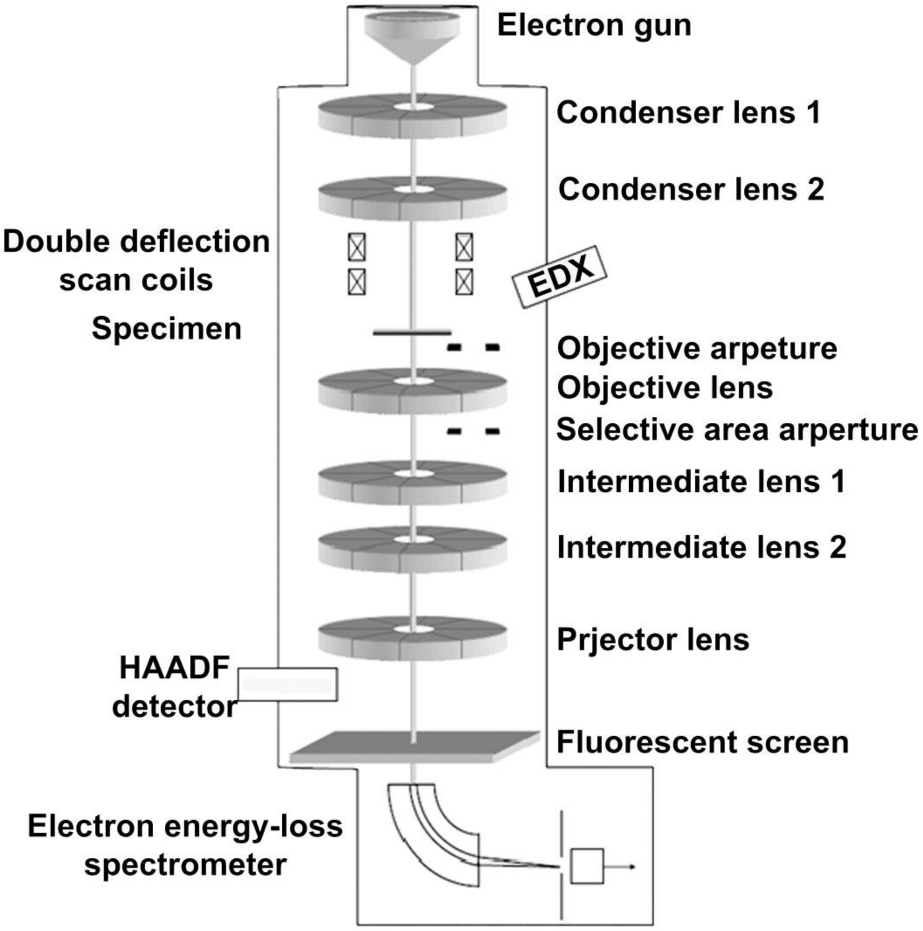

Figure 6.5 Schematic drawing of the electron column of a TEM with STEM capability.

A conventional TEM consists of an electron source, illumination system, specimen stage, imaging system, projection system and viewing screen to view the image. Furthermore, a modern TEM is equipped with analytical equipments such as energy dispersive X-rays and electron energy-loss spectroscopy. As in SEM, there are three types of electron emission guns in TEMs; thermionic, Schottky and field emission. In conventional TEM instruments, two-three condenser lenses (C1, C2) are located above the specimen. In normal TEM mode, those lenses are adjusted to illuminate the specimen with a parallel beam. Below the specimen, an objective lens will form images and also diffraction patterns. The next lens is an intermediate lens which is important to produce either the diffraction pattern or an image on the viewing screen. Since electrons cannot be “seen”, a viewing screen, normally coated with a material such as ZnS will translate electron intensity to light intensity ($\lambda \approx 550$nm). Furthermore, both the diffraction patterns and images, can be recorded onto photographic emulsion or Charge-Coupled Device (CCD) cameras with high sensitivity, which are available nowadays.

6.3.1. Selected Area Electron Diffraction (SAED)

SAED has been one of the powerful techniques used to identify the phases present in the materials. The phase identification can be performed by measuring the lattice-plane spacing from the diffraction patterns and comparing it with a database. Two databases which have been used in this work are ICSD [126] and JPDFWIN [127].

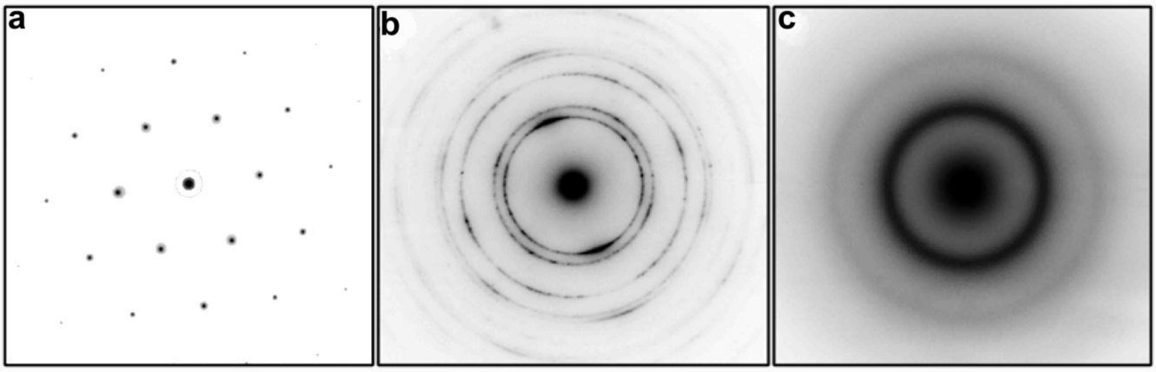

Figure 6.6 Selected area electron diffraction (SAED) pattern showing different materials (a) single crystal sapphire [0001] (b) Polycrystalline TiC and (c) amorphous Cr-C.

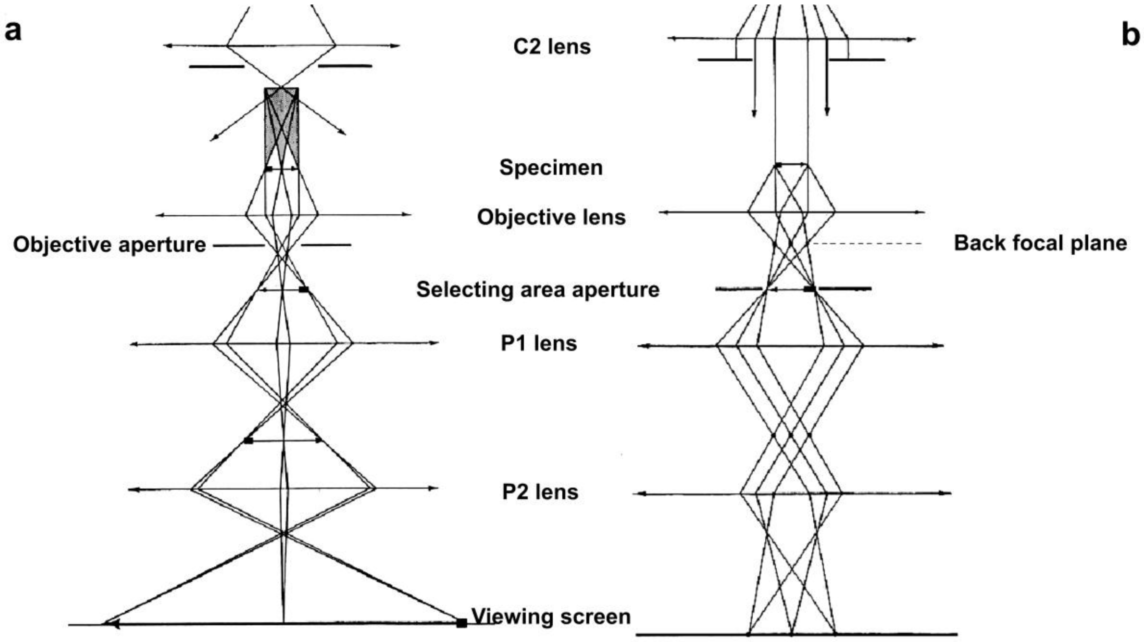

Figure 6.7 Image formation in the TEM (a) Bright-field image and (b) SAED [128].

Diffraction patterns differ based on the crystalinity of the material. Crystalline materials will have either spots or ring patterns. On the other hand, amorphous material will only show diffuse rings in the patterns. Additionally, extra spots and streaks can be used to investigate the presence of precipitates or faults.

Kossel and Möllenstedt were the first to announce the possibility to use electron diffraction in TEM [129]. The imaging system lenses are adjusted so that the back focal plane of the objective lens acts as the object plane for the intermediate lens. The diffraction pattern is then projected onto the viewing screen. The beam which is not diffracted by the specimens will be shown as an intense spot while the other spots are formed from diffracted beams. The diffraction pattern contains electrons from the whole area of the specimen that is illuminated with the beams. This condition is not very useful, since the direct beam is often so intense that it will damage the viewing screen. By using an aperture positioned in the image plane of the objective lens, a diffraction pattern from the selected area will show on the screen. This technique is called selected area electron diffraction (see fig. 6.7).

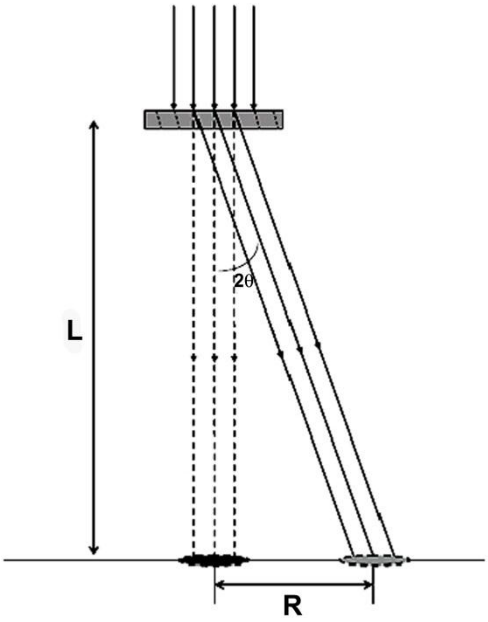

Figure 6.8 Schematic drawing of the SAED pattern geometry.

Figure 6.8 shows the scheme of SAED pattern formation in TEM. Patterns are solved by relating distances and angles in the crystal lattice. The relations for camera length (L), the distance of any spot from the centre of the pattern (R) and the diffracted angle (θ) can be written as

$$R = L \cdot \tan 2\theta \tag{6.1}$$

By assuming for electrons that λ is small, we can set tan $2\theta \approx 2\theta$

$$R = L \cdot 2\theta \quad or \quad 2\theta = \frac{R}{L} \tag{6.2}$$

Combining Eq. 6.2 with Bragg's relationship (Eq. 4.1)

$$\frac{R}{L} = \frac{n \cdot \lambda}{d} \tag{6.3}$$

for n = 1

$$R \cdot d = \lambda \cdot L \tag{6.4}$$

where

$\lambda \cdot L$ = camera constant
d = d-spacing of the set of lattice planes giving rise to that spot or ring

Values of R, L and λ for a particular diffraction spot or ring can be measured and the d-spacing can be determined. Detailed procedures of indexing diffraction patterns can be found in [128, 130]. Additionally, there are several programs that can be used to simulate and identify the phase present in material. Programs that have been used in this work are JEMS [131], CRISP [132] and DiffTools [133].

6.3.2. Bright Field (BF) and Dark Field (DF) Imaging

Two conventional imaging techniques in TEM are the bright-field (BF) and the dark-field (DF) imaging. Both transmitted and diffracted beam will make the specimen shows a little contrast. This condition rises because the diffracted intensity recombines with the transmitted intensity at the viewing screen and produces a little contrast. When the objective aperture is used to block all diffracted beam and allow only the direct transmitted beams, the BF image will be formed. When the direct transmitted beams are tilted and the objective aperture is used to block it, the formed image is called as the DF image (fig 6.9).

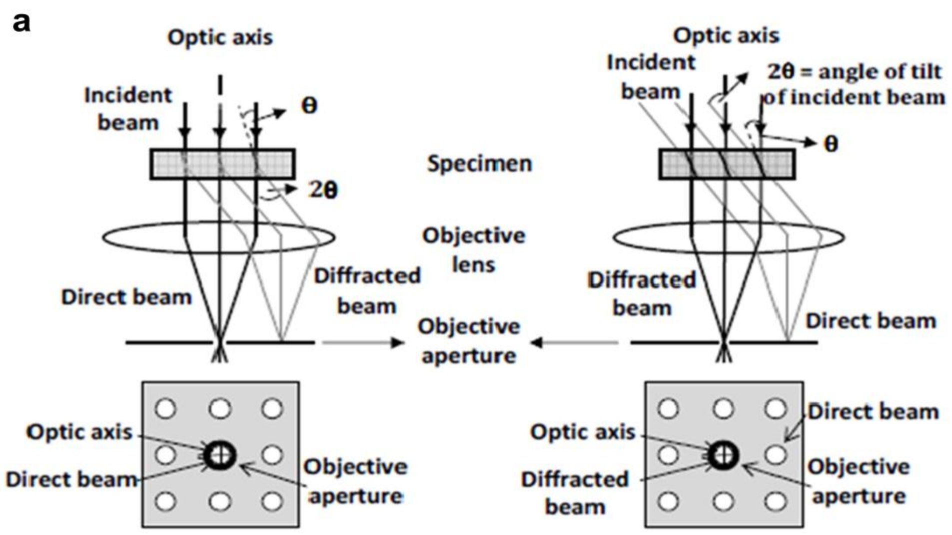

Figure 6.9 (a) Bright and (b) dark field image [114].

6.3.3. Scanning Transmission Electron Microscopy (STEM) and Energy Dispersive X-Ray (EDX) Analysis

A modern TEM can also have scanning capability, known as scanning TEM (STEM), which allows the specimen to be scanned point by point with a small probe. In order to obtain a small probe with a diameter of ≈ 0.2–5 nm, a large aperture angle α must be used. Two additional pairs of scan coils below the condenser lenses allow the raster process to be performed (see fig 6.5). Besides producing SE signal as in SEM instruments, the transmitted beam can also produce bright field, dark field and annular dark field (ADF) images. The latter mode is possible because of the presence of an annular detector which is positioned below the specimen that will collect electrons diffracted in large angles (see fig. 6.10).

The strong Coulomb interaction of the negatively charged electrons with the positive potential of an atom core, leads to high angle scattering as described in Rutherford scattering as follow:

$$\frac{d\sigma(\theta)}{d\Omega} = \frac{e^4 Z^2}{16(E_o)^2 \sin^4 \frac{\theta}{2}} \tag{6.5}$$

where

$\frac{d\sigma(\theta)}{d\Omega}$ = differential scattering cross sections as a function of scattering angle θ

E_0 = incident beam energy

e = electron charge

Z = atomic number of the scattering nucleus

As seen in Eq. 6.5, these diffracted electrons are very sensitive to increasing Z (atomic number) and the contrast is approximately proportional to Z^2. Based on that formula, heavier elements will be brighter in ADF STEM images compared to the lighter elements. This effect is even more pronounced when the electrons are diffracted in a very large angle (>50 mrad). The technique is known as high-angle annular dark-field or HAADF imaging, or Z-contrast imaging, which has been introduced by Crewe and co-workers [134].

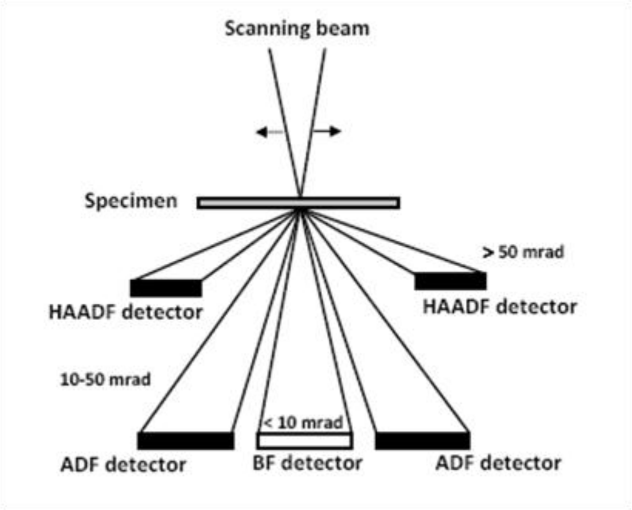

Figure 6.10 Arrangements of BF, ADF and HAADF detectors in STEM.

The electron beam also generates X-rays photons in the beam-specimen interaction, which have energies characteristic for the different elements in the specimen and can be used in STEM analysis. These characteristic X-rays are emitted from inner shell electrons of a specimen atom. They are referred to as characteristic X-rays since the energy of an emitted X-ray is related to the difference in the energy between the sharply defined levels of the atom. When the beam electron interacts with an inner-shell electron, it knocks out the bound electron, which leaves the atom in an excited state with a hole in the electron shell. During subsequent deexcitation, an electron transition involves a change in energy, and the energy released from the atom can manifest itself either in the form of an x-ray or an ejected (Auger) electron.

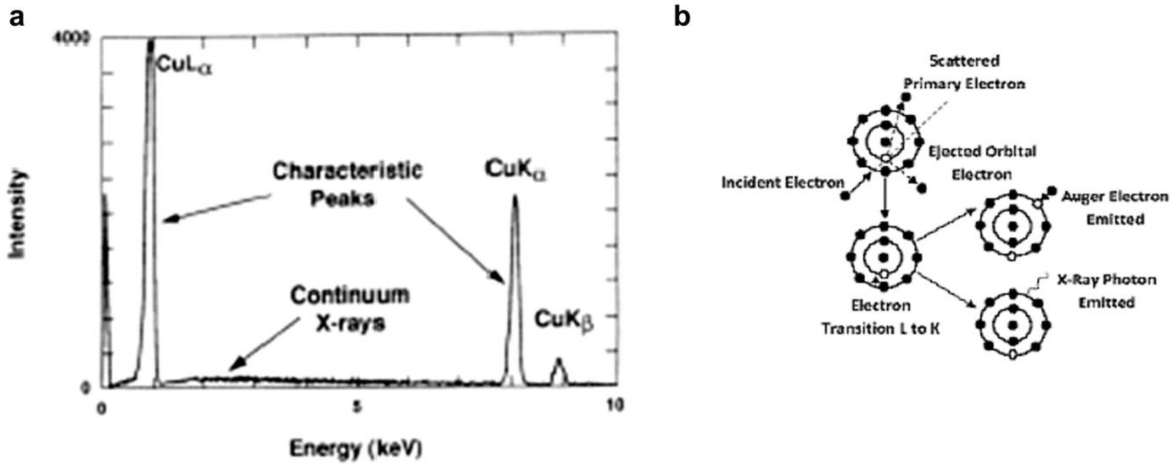

Figure. 6.11 (a) Characteristic X-ray and (b) excitation process [135].

These X-rays will be captured by energy-dispersive spectrometers (EDS). These spectrometers use lithium-drifted silicon Si(Li) solid state X-ray detectors or intrinsic or high-purity Ge (HPGe) EDS detectors . A detailed explanation about the principle of EDS can be found in literature [135].

6.3.4. Energy Filtered Transmission Electron Microscopy (EFTEM)

Unlike the conventional TEM, which uses all electrons that pass through the specimen, a new technique that allows image formation with electrons that have undergone selected energy losses in the specimen has emerged recently. The technique, energy-filtered TEM (EFTEM), detects “chemical contrast” in specimens by adjusting an energy filter to accept only electrons that have lost energy in core ionisations of selected elements. Furthermore, the energy filter can also pass the zero-loss electrons, i.e. electrons that do not experience inelastic scattering. As a result, all bright-fields and diffraction patterns taken with energy-filter will only use purely elastically-scattered electrons. As a consequence, the chromatic aberration for thicker specimens and the inelastic background are eliminated.

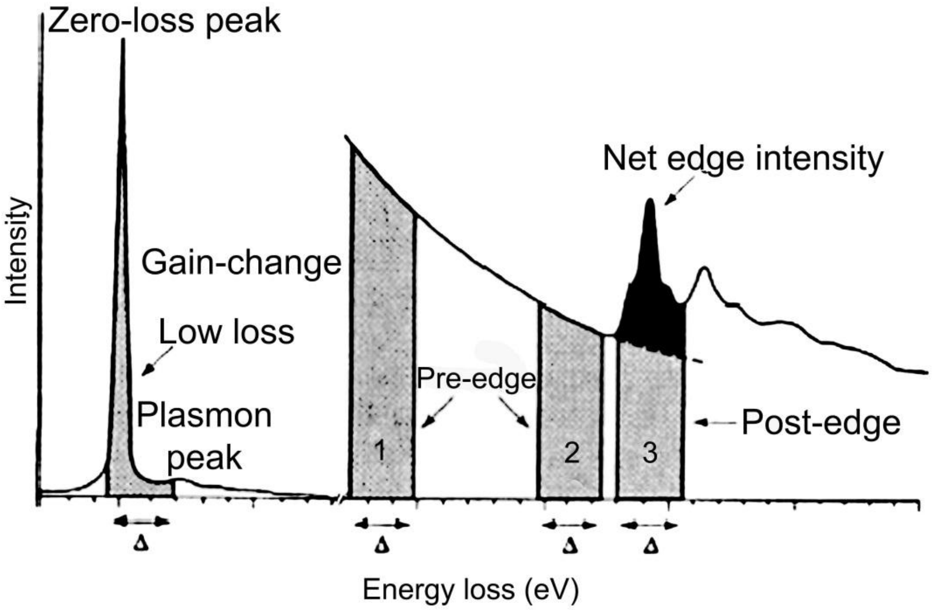

Figure 6.12 Electron energy loss spectrum showing a zero loss peak, a core loss edge position and energy windows which are used to form EFTEM images [136].

The chemical contrast can be used to map the element distribution in the specimen. There are two methods that are mainly used for elemental mapping, the jump ratio map or two windows technique [137] and the three windows technique [138]. The first technique is performed by recording two EFTEM images, one pre-edge and one post-edge, and then dividing the latter image to the first one (energy windows marked by 2 and 3 in fig 6.12). This technique is very useful especially when the element concentrations are very low. Moreover, the two windows method is faster than the three windows methods and it can also omit diffraction contrast.

On the other hand, the three windows uses three EFTEM images, two pre-edge images and a post-edge image (marked by pre-edge 1,2 and post-edge respectively in fig 6.12). The pre-edge images are used to estimate the background image with the help of a background model. The post-edge image is obtained from the edge energy region. At the end, the estimated background for each pixel is subtracted from the post-edge image resulting in the specific EFTEM image. This method allows making a quantitative image where the intensity is proportional to the EELS spectrum under a specific edge [136]. The signal in the maps is related to the concentration of the corresponding element. However, it also depends on a number of factors like crystal orientation, mass thickness, more drift problems and collection angle [139-141].

The EFTEM technique can also be used to measure the relative thickness of the specimens. Since the unfiltered image contains both the elastically- and inelastically-scattered electrons, while the zero-loss image contains only elastically-scattered electrons, it is possible to divide the unfiltered image by zero-loss image and take the logarithm of the result to obtain a thickness map in units relative sample thickness $\frac{t}{\lambda}$ [142]

$$\frac{t}{\lambda}=\left[\frac{\int I(E)dE}{\int I_Z(E)dE}\right] \tag{6.6}$$

where, $I_Z(E)$ is the zero loss intensity and I(E) total spectral intensity.

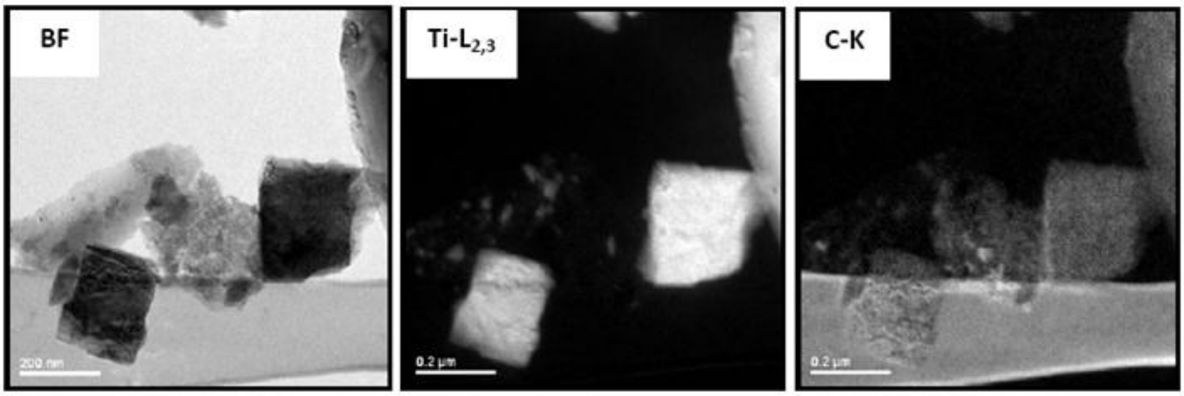

Figure. 6.13 EFTEM elemental maps showing the bright-field EFTEM image and element distributions of titanium and carbon of TiC particle on a carbon grid.

6.3.5. EFTEM – Spectrum Imaging (EFTEM-SI)

Although EFTEM elemental maps can be used as efficient tools for qualitative characterisation, they are not readily amenable to quantitative analysis. Another method, which is based on multi windows approach and known as ESI series has been proposed by Mayer et al. [143]. The technique acquires a series of ESI images around an inner-shell loss edge and in the low loss region for the quantification. There are at least three advantages of ESI series compared to the conventional EFTEM. First, information on the energy loss spectrum is obtained for each pixel in the image and the standard quantification methods developed for EEL spectra can be used for the analysis. Second, the background extrapolation and integration regions can be extended over a large energy loss range of up to 80 -100 eV below and above the edge, respectively. Third, the standard EELS methods for single scattering deconvolution and least squares fitting for overlapping edges can be used.

The data obtained by this method determine the intensities in a three dimensional data space, in which two coordinates are given by the position of x and y on the specimen and the third coordinate is given by the energy loss ΔE [137]. Mayer et al., showed that the quantification of the ESI series can result not only in the values for concentration ratios, but also in accurate values for number density of a specific element in a given sample area, specimen thickness and contamination layer thickness [143].

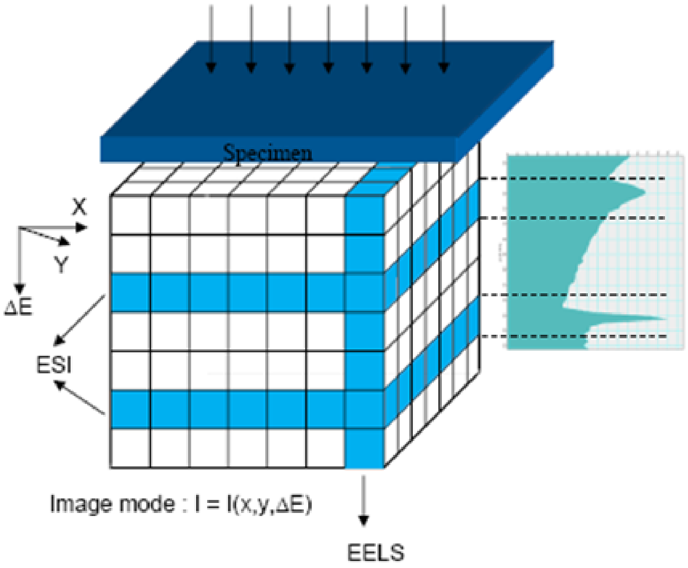

Figure. 6.14 The three-dimensional data space which represents the intensity distribution at the bottom surface of the specimen. It is assumed that the scattered intensity is integrated up to a maximum scattering angle which is defined by the collection aperture.

6.3.6. High Resolution Transmission Electron Microscopy (HRTEM)

By definition, high-resolution transmission electron microscopy (HRTEM) is an imaging mode of the TEM that allows the imaging of the crystallographic structure of a sample at an atomic scale. On contrast to the conventional imaging mode in CTEM which relies on a diffraction contrast, the image formation in HRTEM relies on phase-contrast resulting from an interference of several beams. In this case, to understand the image formation and the interpretation of the object structure on the atomic scale, one needs to understand the interactions of the electron beam with the crystal, the influenced of the lens aberrations and the wave transferred by microscope.

As mentioned before, the image formation in a high resolution electron microscope is an interference phenomenon. A parallel, coherent incident beam is diffracted by the thin crystal placed in the object plane of the objective lens. The aberrations of real lenses deform the electron waves and decrease the resolution of the microscope. These aberrations are defocus, spherical aberration, chromatic aberration, astigmatism and coma.

The spherical aberration (Cs) causes the electron parallel to, but distant from, the lens axis to be focused in a slightly different place than electron close to the axis (see fig. 6.15). The phase shift ($\chi(\theta)$) of the beam propagating under a different angle θ with respect to the optical axis is given by [144]:

$$\chi_1(\theta) = -\frac{2\pi}{\lambda} C_s \frac{\theta^4}{4} \tag{6.7}$$

The defocus presents since the focal distance of the electron lenses is variable dependent to excitation current. The defocus (Δz) results in another phase shift ($\chi(\theta)$):

$$\chi_2(\theta, \Delta z) = -\frac{2\pi}{\lambda} \Delta z \frac{\theta^2}{2} \tag{6.8}$$

If we assume the illumination condition as perfectly coherent, the both phase shifts play role in the coherent transfer function TC:

$$T_C = \exp i(\chi_1 + \chi_2) = \exp i\left\{ -\frac{2\pi}{\lambda}\left(C_S \frac{\theta^4}{4} + \Delta z \frac{\theta^2}{2} \right) \right\} \tag{6.9}$$

A detailed description about transfer function can be found in [145].

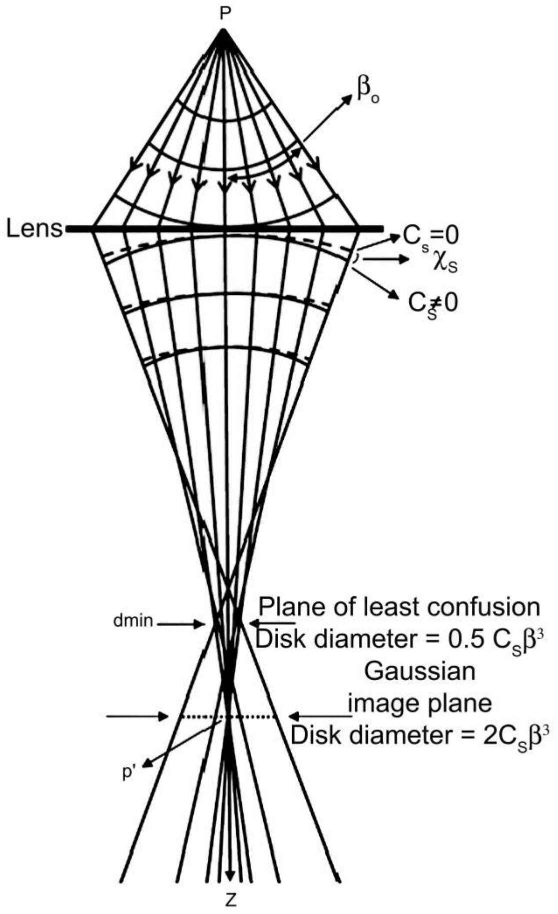

Figure 6.15 The spherical aberration of the electromagnetic lens leads to a blurring of the image in the Gaussian image plane.

Since the incident electron beam is only partially coherent, there are dispersion energy of electron and chromatic aberration (C_C) of the objective lens. The focal length of an electron lens difference depends on the energy dispersion of the electrons which is combination of the initial dispersion ΔE when the electrons leave the cathode, variations of the accelerating voltage ΔV, fluctuation of the lens current ΔI and the energy loss resulting from the interactions of the electron with the specimen. The focal length difference causes a point in the object plane is imaged as a disc of the radius Δr. We can write the focal length difference Δf as:

$$\Delta f = C_C \left[\left(\frac{\Delta V}{V} \right)^2 + \left(\frac{2\Delta I}{I} \right)^2 + \left(\frac{\Delta E}{E} \right)^2 \right]^{1/2} \tag{6.10}$$

Fejes has showed that a Gaussian distribution of this enlargement of the focal length gives an envelope function of the temporal coherence [146]:

$$E_T = \exp\left\{-\frac{\pi^2}{\lambda^2}\left(\Delta f\right)^2\theta^4\right\} \tag{6.11}$$

A detailed analysis of this envelope function is carried out in the work of Tanaka [147].

Additionally, the convergence of the incident beam also limits the resolution of the microscope as the chromatic aberration [148]. For a semi angle of convergence α, the envelope function is given by :

$$E_S = \frac{2\left(2\pi\alpha\left\{\Delta z\frac{\theta}{\lambda}+\left[\lambda C_S - i\pi\left(\Delta f\right)^2\right]\frac{\theta^3}{\lambda^2}\right\}\right)}{x} \tag{6.12}$$

Finally the real transfer function for both real and partial coherence is given by:

$$T_R = T_C \cdot E_T \cdot E_S \tag{6.13}$$

Besides receiving detailed crystallite structure in atomic scale such as defects, grains and crystal growth, the high resolution TEM image can also be used to inform the exact positions of atomic columns with respect to black and white contrast on the micrograph. But unfortunately, the direct interpretation is possible only where the final image correspondence to the projected potential of the whole specimen. In real crystal, the interaction of the crystal with the incident electron beam and also the transfer of the intensity of the image are not linear.

The position of the maxima and minima of interference with respect to the atomic columns depends on the crystal thickness and on the defocus of the objective lens, in which both values are often very difficult to determine. To overcome that problem, creating model of the corresponding crystal and simulating its interaction with the electrons and obtaining the wave function emerging from the crystals are necessary. Later, the image of this wave function is calculated and compared to the result form the experimental micrograph.

A detailed explanation about the high resolution TEM can be found in the literatures [145, 149-151].

7 Results

7.1. Growth mechanisms of Ti_2AlC and Cr_2AlC MAX phases

In this work, specific deposited thin films of Ti-Al-C and Cr-Al-C system have been chosen to be further investigated by means of electron microscope. The Ti-Al-C thin film deposited at deposition temperature of 850°C was investigated since the XRD diffractograms have reported that the crystalline Ti_2AlC was formed at that temperature. As for Cr-Al-C thin films, XRD diffractograms have informed that both the crystalline and phase present on the films were detected gradually at three different deposition temperatures: 450°C, 500°C and 650°C. Furthermore, the microscopic investigations were performed to give more detailed information about the elastic properties of the deposited film as reported in sub chapter 4.4.3. The microstructure investigations consist of the phase identifications using SAED together with analytical investigation and high-resolution TEM.

7.1.1. Ti-Al-C thin film

7.1.1.1. SEM and TEM investigation results

Figure 7.1 is a SEM image of the surface microstructure of a Ti-Al-C thin film. The image shows that the film consists of columnar grains with a size of 200 nm with random orientations. The SEM image also shows the presence of pores or voids, which could be the result of overlapping grains on the film surface.

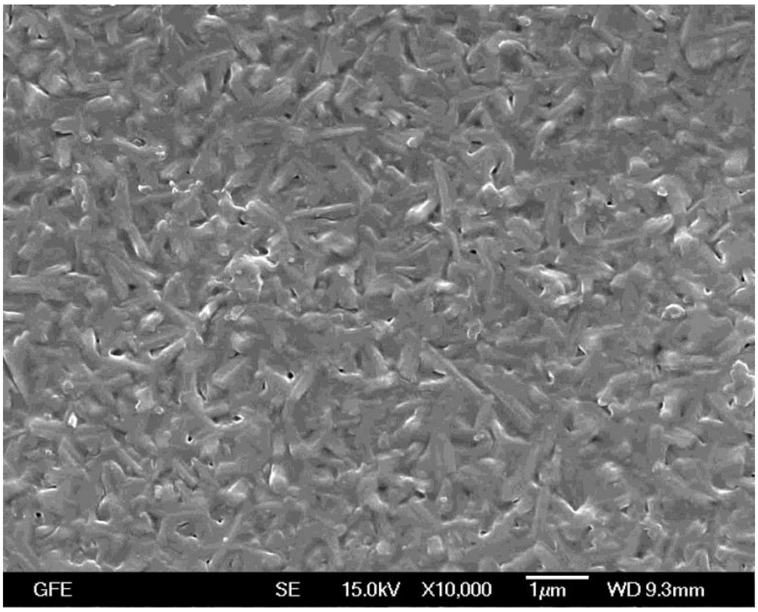

Figure 7.1 SEM image showing surface microstructure of Ti-Al-C thin film deposited at deposition temperature of 850°C which consists of columnar grain with random orientations.

TEM investigations of the cross-sections of the Ti-Al-C film have revealed more detailed information about the film microstructure. Bright field (BF) and magnified images show that the film is about 1600 nm thick (see fig. 7.2(a) and (b)). The film consists of columnar grains, several of which have grown from the interface of the substrate all the way to the top of the film without disturbance. Furthermore, at the interface no amorphous layer could be detected but unfortunately the film is not dense. Several bright areas, which indicate the presence of pores, are detected. Moreover, the dark field (DF) images (fig. 7.3) show that the textured crystal growth started right at the substrate interface. The images also show that the grains have about 100 - 300 nm in lateral size. The DF images indicate the presence of planar defects presumed to be stacking faults which are found throughout the film (marked by arrows).

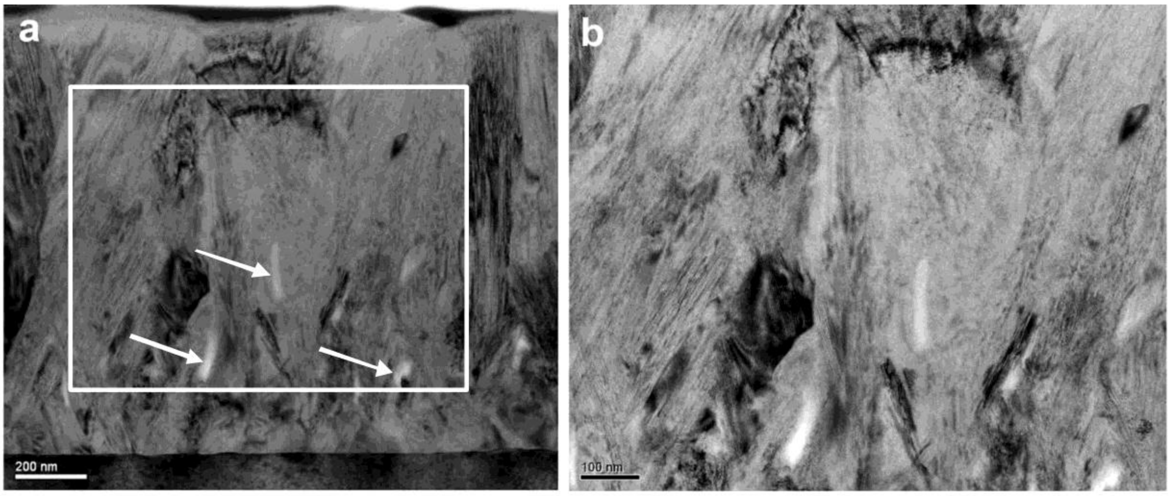

Figure 7.2 BF images showing the microstructure of the film. (a) The grains have grown directly from interface to the top of the film with no amorphous layer detected at the interface. (b) A magnified image of (a) showing that the film is not completely dense (marked by arrows in (a)).

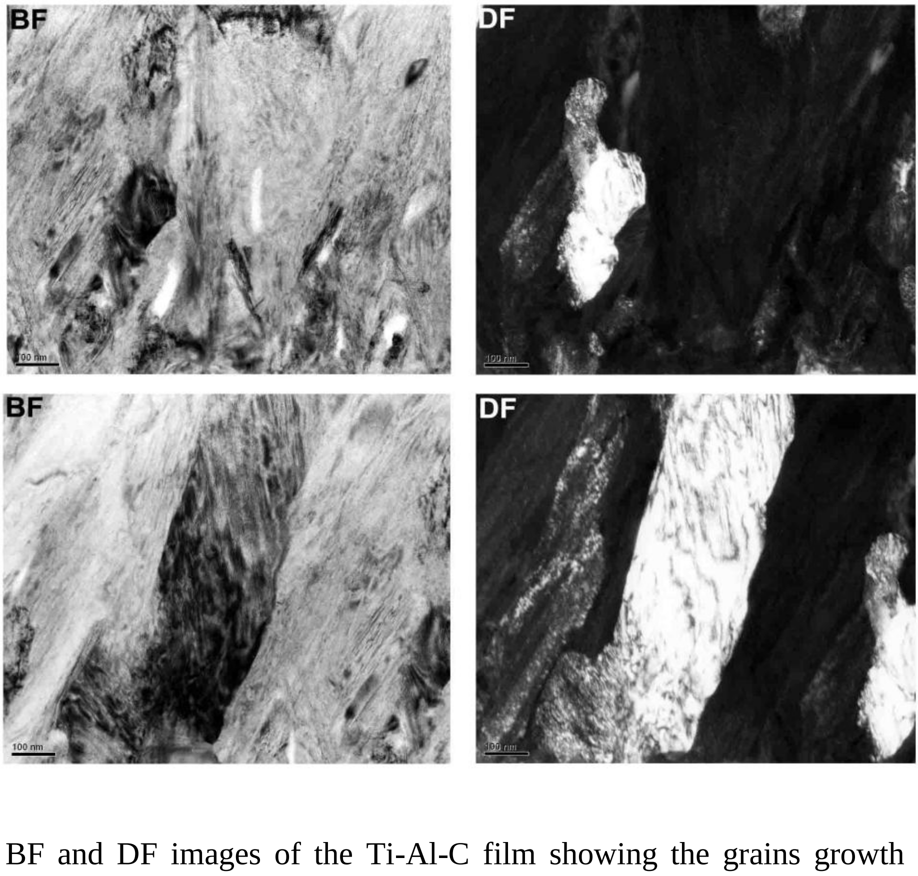

Figure 7.3 BF and DF images of the Ti-Al-C film showing the grains growth in different orientations. Planar defects are also detected in the film (marked by arrows).

The determination of the specimen structure, especially the phase identification, was done by analysing the SAED patterns of the film. As shown in figure 7.4 and presented in Appendix A, the film mainly consists of the Ti_2AlC and to a minor extent the Ti_3AlC_2 phases. The diffraction pattern which is formed by textured rings confirms the fact that the film contains extended grains. Linear streaks on the pattern indicate the presence of planar defects, which are also found in the DF images and presumed to be stacking faults.

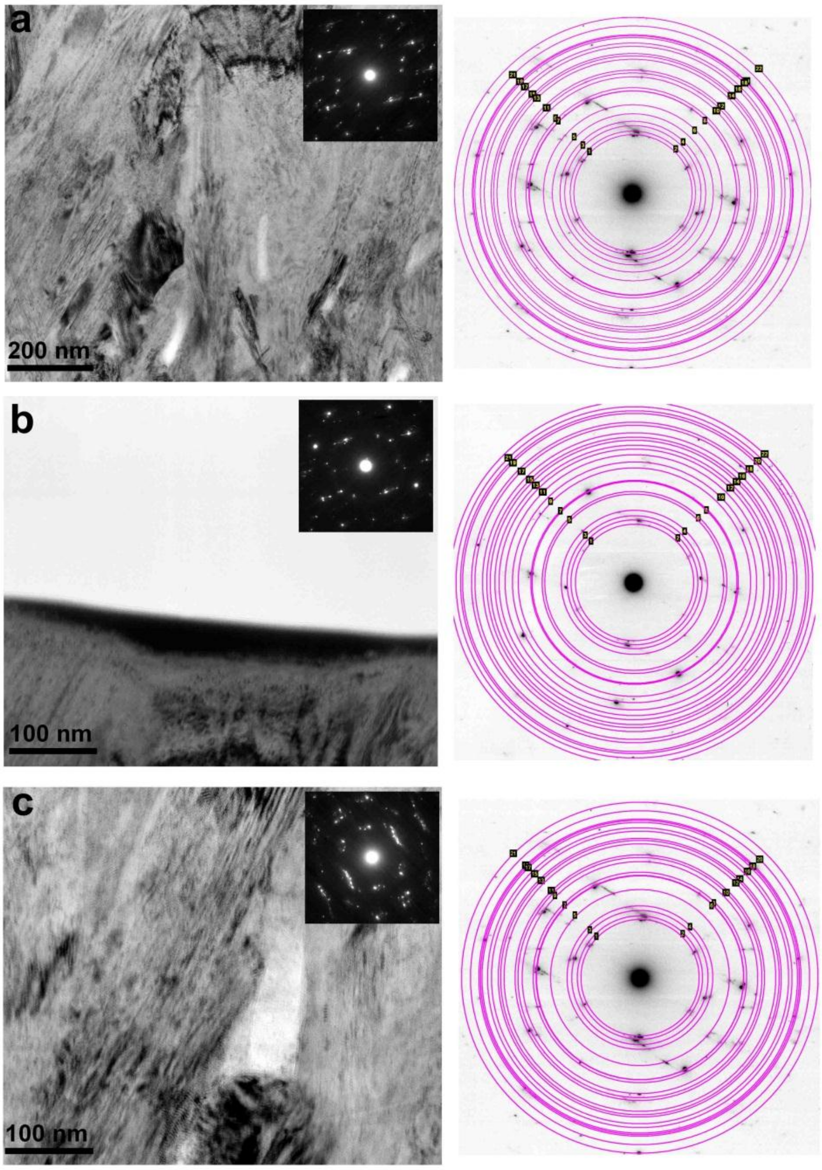

Figure. 7.4 BF images and SAED patterns taken from (a) middle, (b) upper part of the film and (c) area around the pore. The SAED patterns analysed for every area are shown on the right side of the image. The phase identification results have revealed that Ti_2AlC is found in whole film and a small amount of Ti_3AlC_2 is detected on upper part of the film (fig b).

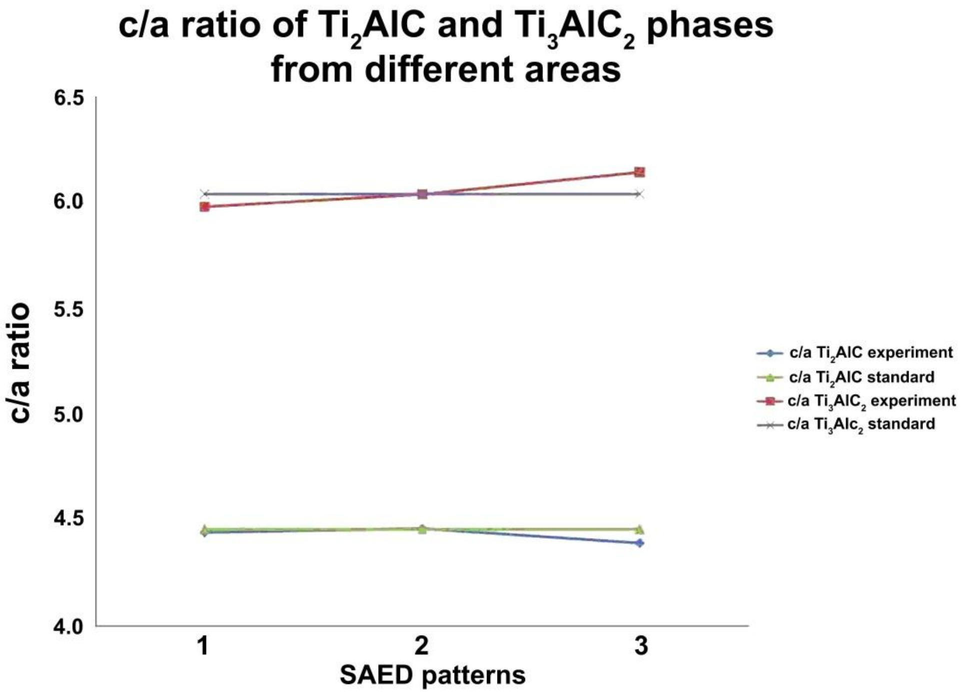

Figure 7.5 Summary of c/a ratio for Ti_2AlC and Ti_3AlC_2 phases present in three different areas on the film is as shown in figure 7.4.

The c/a ratio of both phases as presented in figure 7.5 gives an indication that Ti_2AlC is present in the whole area of the specimen. The presence of the Ti_3AlC_2 phase is mainly detected in the upper part of the film (position 2). Both c/a ratios of Ti_2AlC and Ti_3AlC_2 show large differences to the references in the area near the pores (position 3) which lead to the assumption that there is another phase, presumably the TiC phase, which exists in that area.

The BF and DF images also show some grains which have grown directly from the interface. SAED analysis has also been used to reveal the presence of the phase in one of those grains. Figure 7.6 shows the BF images of one grain with the corresponding SAED patterns taken from bottom (interface), the middle and the top part of the grain. Phase identification analysis for all these three parts reveals that the grain consists of a single Ti_2AlC phase which has grown in [2-1-10] orientation. At the interface, an epitaxial orientation relationship of [10-10] Al_2O_3 substrate and [2-1-10] Ti_2AlC grain has also been detected. This finding indicates that there is a grain with local epitaxy, which has grown almost perpendicular to the interface. Additionally as shown in fig 7.6.d, the phase identification analysis also shows that different orientations of the Ti_2AlC grain [0001] are present adjacent to the specific grains.

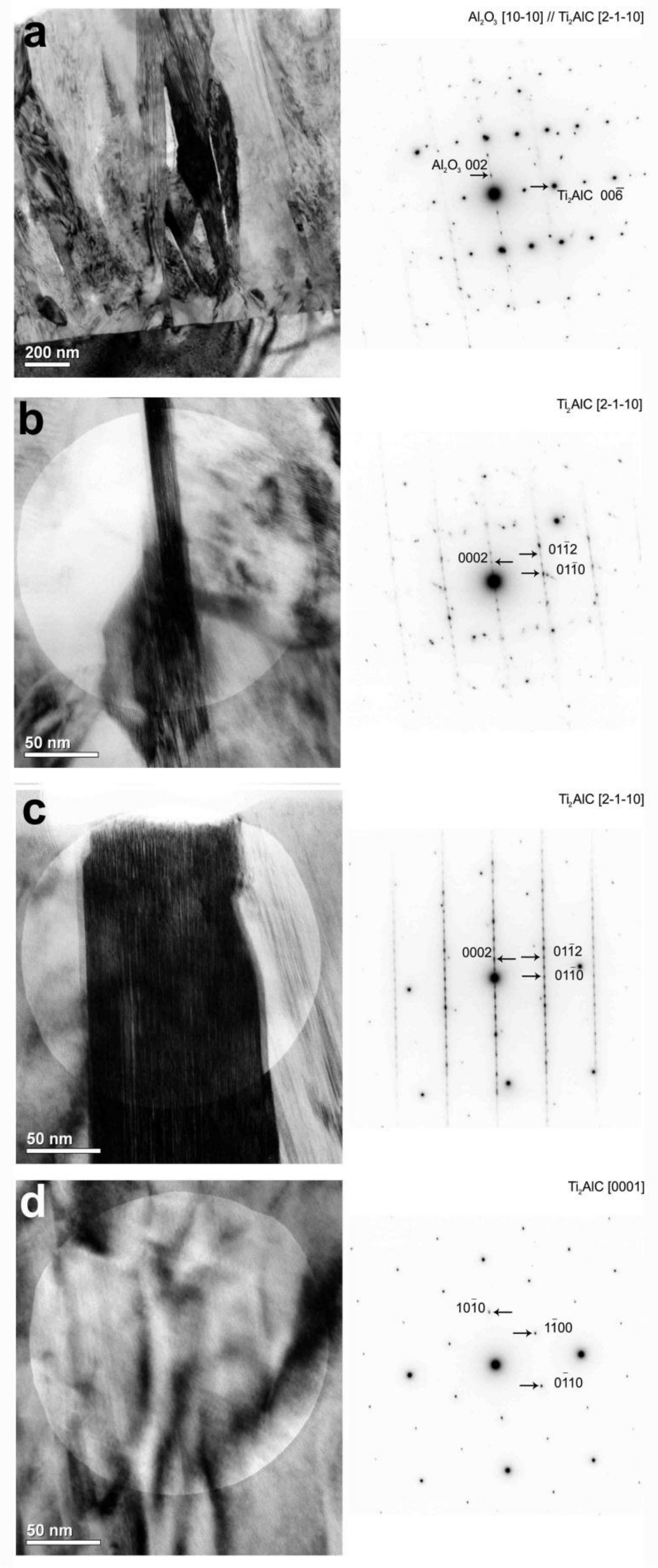

Figure 7.6 BF images and corresponding SAED patterns taken from a specific part of the grain which has grown directly from the interface to the top of the film. All SAED patterns indicate that the grain consists of Ti_2AlC phase. Additionally, a SAED pattern which is taken on the side of the grain also indicates the presence of the Ti_2AlC phase (fig d).

The STEM HAADF image in figure 7.7 shows more clearly two porous layers which are present in the film. The first layer started to grow perpendicularly to the interface at 200 nm and above, followed by the second layer which is located at about 600 nm above the substrate.

Furthermore, combining STEM HAADF and EDX line scans for the cross sections of the film shows that concentration gradients for several elements are present in the film. Since EDX could not detect carbon with a high accuracy, we were only taking into account the titanium and aluminium concentrations, which could be detected very well using EDX. The observed intensity variation divides the cross section of the film into several areas based on the titanium and aluminium concentrations (see fig 7.7). Moreover, the EDX line scan profiles have also revealed the presence of the pores by the decrease of both the titanium and aluminium signals. The intensity profiles also indicate that the Ti_2AlC has grown directly from interface. The EDX profiles demonstrate that there are three different areas containing different titanium and aluminium concentrations. The first area marked with a yellow rectangle shows that the concentration of aluminium increases while the titanium is constant. The second area shows that both titanium and aluminium concentrations are constant (marked by purple rectangle). The green rectangle shows the region where the titanium is rich and on other hand, the aluminium is lacking. This fact leads to the possibility that other phases, presumably TiC and/or Ti_3AlC_2, are present along Ti_2AlC on the film.

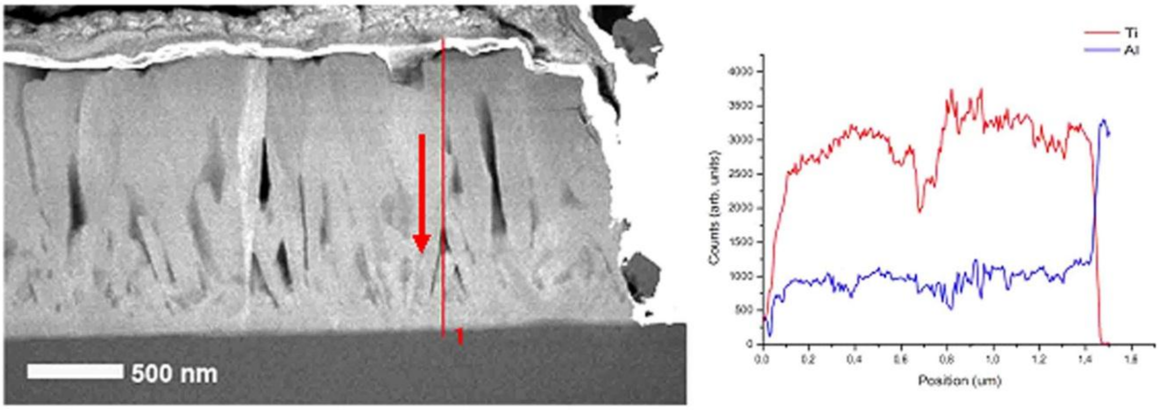

Figure 7.7 STEM HAADF image and EDX line profiles taken along the film showing the titanium and aluminium concentrations on the film.

To get more detailed information, especially on the distribution of carbon in the area near the pores, elemental maps for carbon, as addition to elemental maps of titanium and aluminium, were acquired. As seen from figure 7.8, the carbon elemental map clearly shows that the

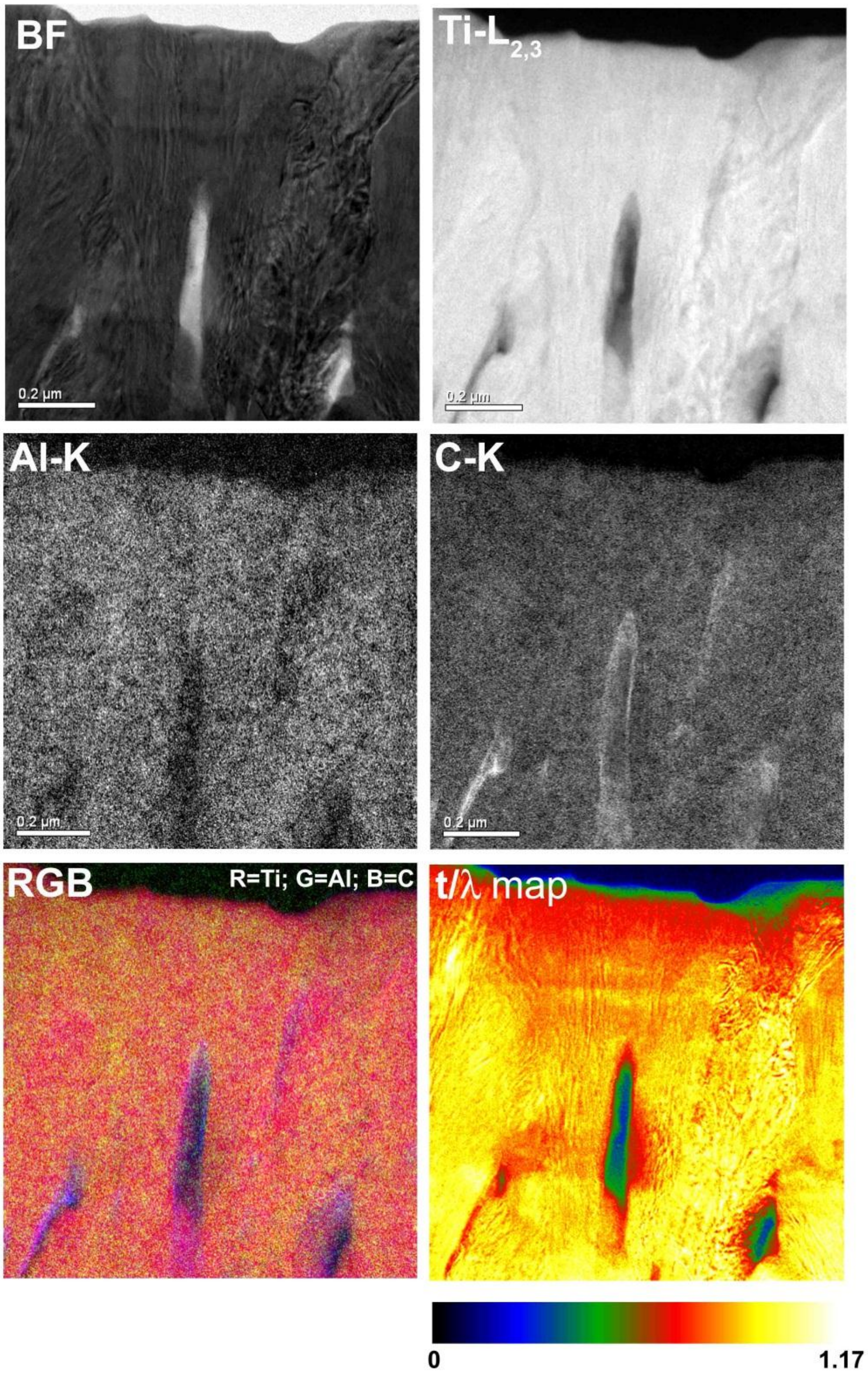

Figure 7.8 EFTEM-BF and elemental maps showing titanium, aluminium and carbon distribution in the film, respectively. In addition to the EDX line profile data, high carbon concentration near the pores increases the possibility of the presence of TiC and/ or Ti_3AlC_2 phase in that area. As additional information, the thickness map gives the t/λ value which is less than 1 and suitable for additional quantitative analysis.

carbon concentration in the pores is higher than in other part of the specimen. At that area, the aluminium content is also lower than in other parts of the specimen. It is suggested once again, at least from the element distributions, that different phases (TiC and/or Ti_3AlC_2) are present in both areas. Since the areas near the pores are quite small (10-50 nm size), EFTEM SI was used to get more detail information about the presence of the phases.

Figure 7.9 shows BF image and EFTEM SI spectra of the titanium and carbon edges extracted from five areas of the film. The spectra from area nearby the pores (position 3 and 5) show different profile shapes, which indicate that these areas contain different phases. Moreover, from the extracted EFTEM SI spectra, a concentration ratio from two elements can be calculated. In the area near the pores, the Ti/C ratio almost equals to 0.98 which could prove that the TiC phase is present in that area. From this result the possibility of the presence of the TiC phase is greater than that of Ti_3AlC_2.

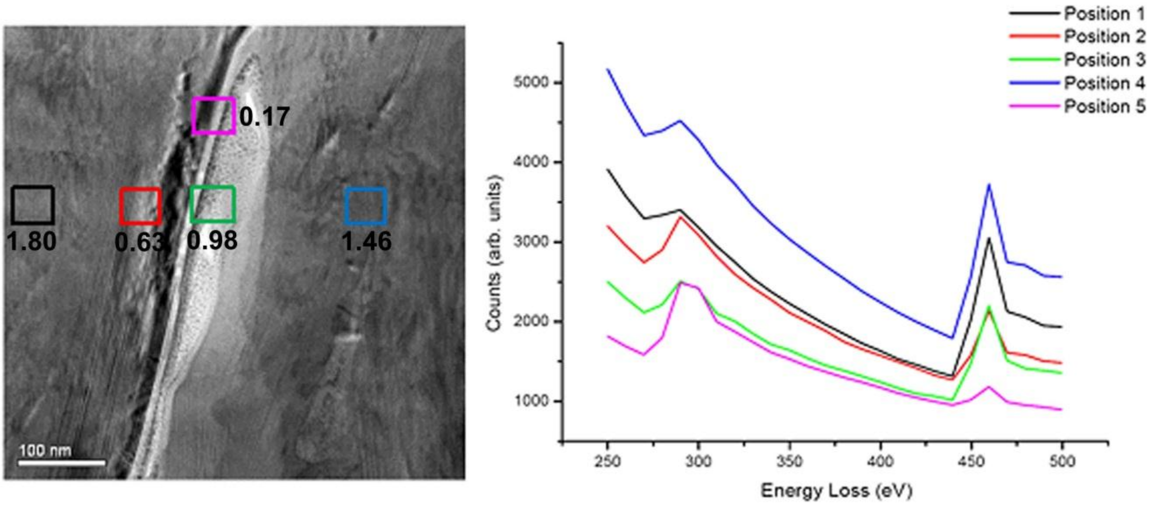

Figure 7.9 EFTEM-BF image (left) and EFTEM SI spectra (right) of the carbon and titanium edges peak taken from five different areas. Comparing both shape and Ti/C ratio from the spectra taken from the area near the pores to the other spectra, indicates the presence of different phases in the film.

To have more detailed information about crystallites on the atomic scale, high-resolution TEM (HRTEM) investigations have also been performed. Figure 7.10 shows a high-resolution image and a corresponding FFT patterns which were taken from the second porous layer (about 600 nm above interface). From the FFT pattern, a diffuse ring together with some reflections shows that the area actually consists of nano-crystalline materials instead of complete pores. Furthermore, the second FFT taken from the crystalline area shows that the reflections have a good agreement with the TiC phase. From this result, together with the Ti/C quantitative result from EFTEM-SI, we can conclude that the TiC phase is present at the area near the pores. Since the phase analysis yielded TiC, the aluminium presence in this area, as shown in the aluminium elemental map, indicates of aluminium in solid solution. Wilhemsons et al. have also reported in their experiment the presence of an aluminium solid solution leading to a mismatch of the TiC lattice constant, which is about 1 % smaller than the calculated parameter [147].

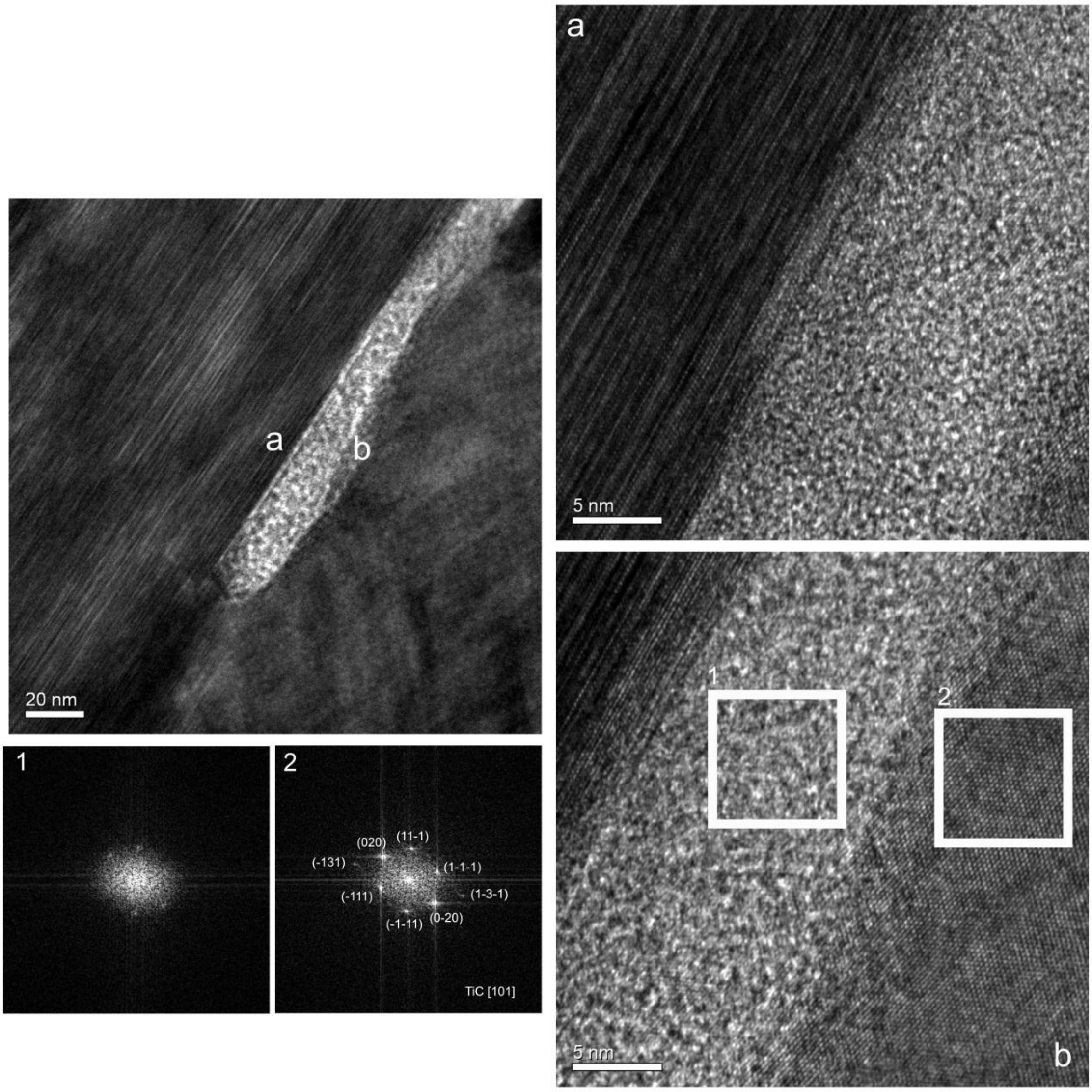

Figure 7.10 The pore contains nano-crystalls and it is also shown that TiC phase is present in areas near the pore.

Another HRTEM image was taken from an area 200 nm above the interface (see fig 7.11). On top of the pores crystalline grains which look like twins are also detected. Moreover, the FFT patterns from both areas indicate that there exist different grain orientations.

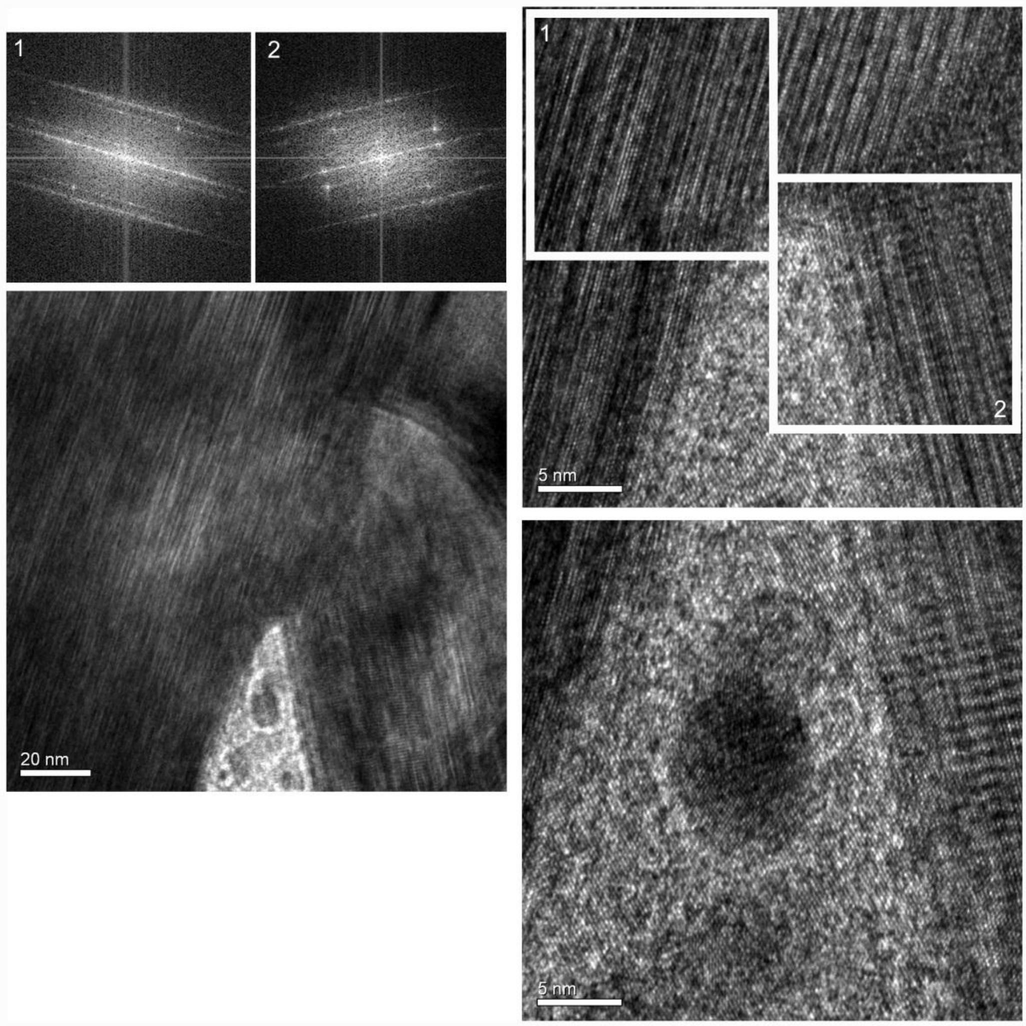

Figure 7.11 HRTEM images of a pore located at about 200 nm above the interface. Both corresponding FFT patterns show that the grains on the side of the pores have different orientations.

Figure 7.12 and 7.13 show HRTEM images taken from upper and middle parts of the film. In addition to an amorphous, some planar faults are also found (see fig. 7.12.b). Figure 7.13 shows high-resolution images taken from another area in the middle of the film with corresponding FFT pattern. From the FFT, a Ti_2AlC phase in the [0001] orientation was identified.

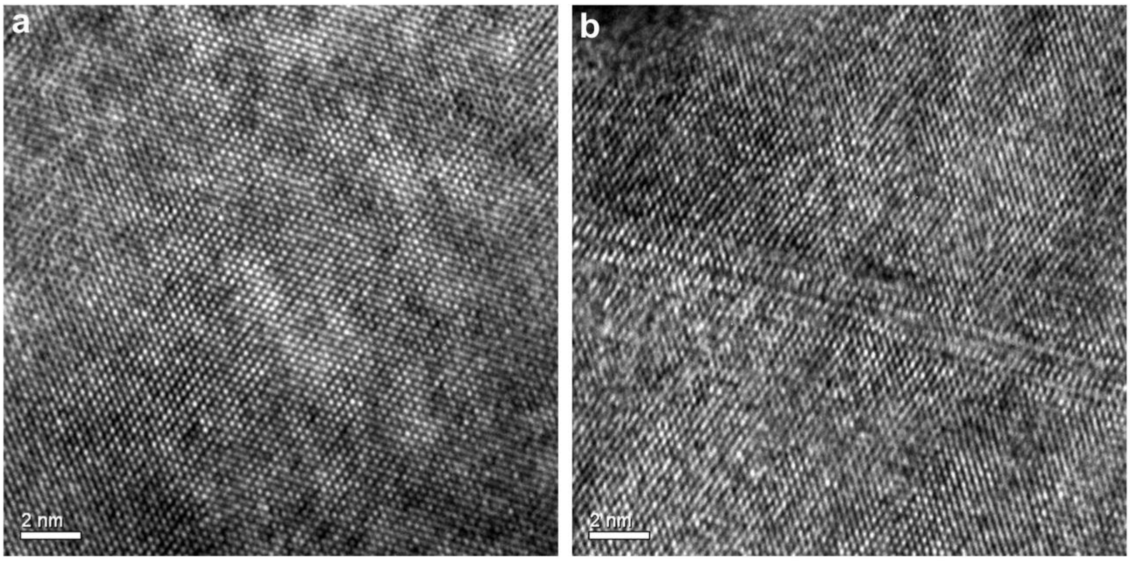

Figure 7.12 HRTEM image (a) taken from upper part of the film and (b) showing faults in the film.

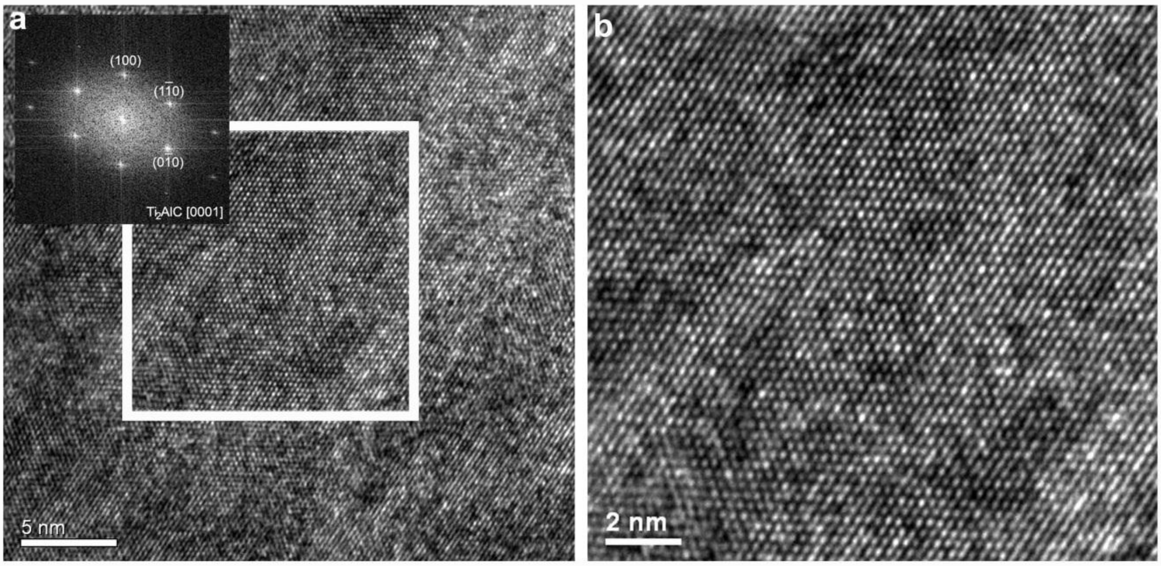

Figure 7.13 (a) HRTEM image with corresponding FFT pattern and (b) its higher magnification image. The FFT pattern indicates that the structure is Ti_2AlC in [0001] direction.

Previously, an orientation relationship has been revealed by SAED analysis for Ti-Al-C system (see fig 7.6). Once again, as seen from HRTEM image taken from the interface, an orientation relationship between sapphire and film can be measured as [10-10] Al_2O_3// [2-1-10] Ti_2AlC (see fig. 7.14). A higher magnification image on the right shows that in some areas the interface has some disordered crystallites but no amorphous phase can be observed.

In other areas, the initial local epitaxial growth has afterward changed to a polycrystalline growth about 500 nm above the interface.

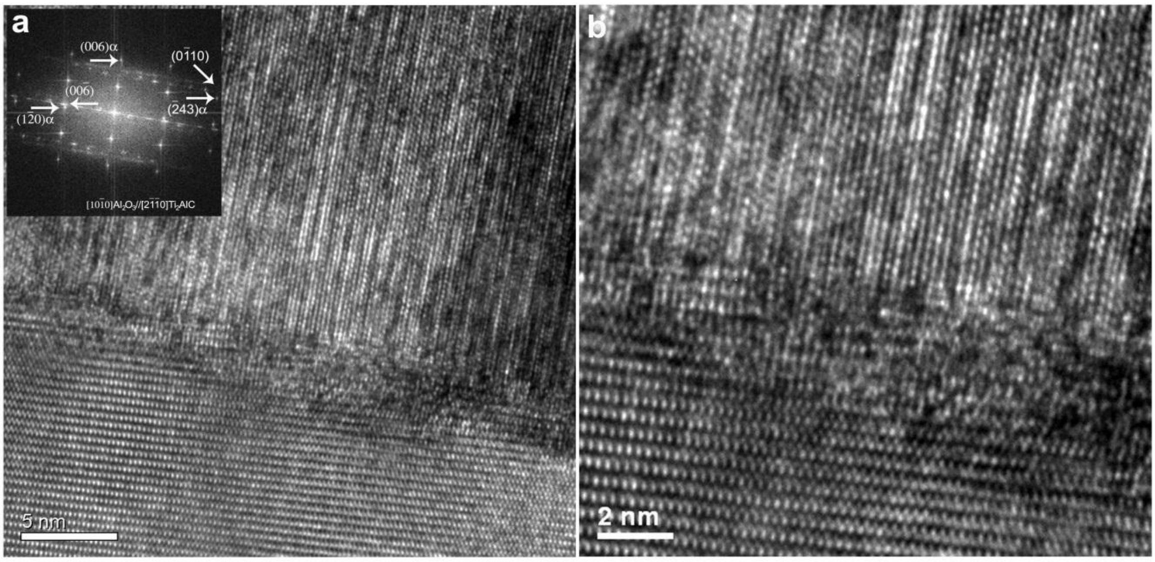

Figure 7.14 HRTEM image taken from area near the interface (left) and its magnified image (right). The high-resolution image clearly shows that no amorphous layer is present in that area. Additionally, the high-resolution image also shows the initial epitaxial growth which afterwards changes to polycrystalline growth behaviour. An FFT pattern taken from the interface shows the presence of Ti_2AlC with an orientation relationship of Al_2O_3 [10-10]//Ti_2AlC [2-1-10] and Al_2O_3(1-20)//Ti_2AlC(00-6).

7.1.1.2. Short summary of Ti-Al-C thin film growth

The TEM investigation results for Ti-Al-C film have revealed new information about the microstructure of the Ti-Al-C MAX-phases thin film. The TEM and STEM images of cross section of FIB lamella inform that the Ti-Al-C thin film is not dense and consists of many pores. Moreover the phase identification from SAED patterns shows the presence of Ti_2AlC with additional minor phases of TiC and Ti_3AlC_2. This finding has been supported by the analytical investigation results done by EDX and EFTEM. Furthermore, HRTEM images and corresponding FFT patterns also indicate the distribution of Ti_2AlC, Ti_3AlC_2 and TiC phases in the thin film. Based on these results, almost all area of the film which consist of Ti_2AlC and TiC and Ti_3AlC_2 have been found in the area near the pores and upper part the film respectively.

Table 7.1 Short summary of the TEM investigation results on the growth of Ti-Al-C MAX-phase thin films.

Ti-Al-C system	
Microstructure of the film	Pores are found in the film
Phase identification	Ti_2AlC and minor phase of TiC and Ti_3AlC_2
High-resolution TEM	The phase distribution in the film: • TiC is found near the pores • Ti_3AlC_2 on upper part of the film • The rest consists of Ti_2AlC

7.1.2. Cr-Al-C thin films

For the convenience, specimens deposited at 450°C, 550°C and 650°C are named as Cr450, Cr550 and Cr650 respectively.

7.1.2.1. SEM and TEM investigation results of Cr-Al-C thin film deposited at 450°C

Figure 7.15 shows the SEM image of surface microstructure of the Cr-Al-C thin film which was deposited at 450°C deposition temperature (Cr450). The surface morphology is rough and the grains are randomly oriented.

The cross sections of this deposited thin film were investigated in the TEM. The bright and dark field (BF and DF) images as presented in Figure 7.16 show the grains growth which is almost parallel to the substrate normal. The measured lateral grains size is about 200 nm. Moreover, as also shown in figure 7.16, there is amorphous layer at the interface. It has wavy morphology with the thickness approximately 200 nm. Another major difference compared to Ti-Al-C system is that no pores can be detected in the film.

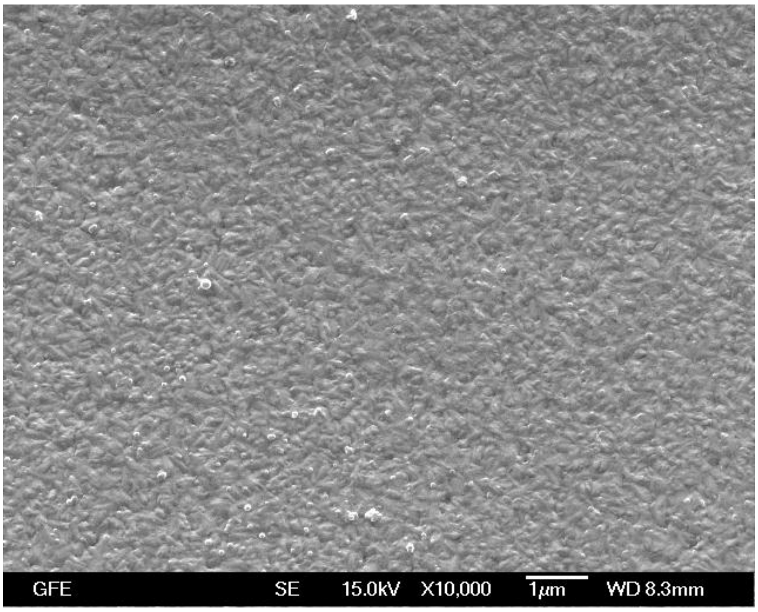

Figure 7.15 SEM image of surface microstructure of Cr450 specimen. The surface looks rough with randomly oriented grains.

The SAED patterns taken from the specimen contain reflections which are arranged on incomplete rings. This condition, which is also found in the Ti-Al-C film, exists due to the large number of grains which are present in the film. Additional streaks in the pattern also indicate that planar faults exist in the film. D-spacing measurements using the DiffTools software, as presented in appendix B, confirm that the Cr$_2$AlC phase is the main phase present in the film, with some additional Cr$_{23}$C$_6$.

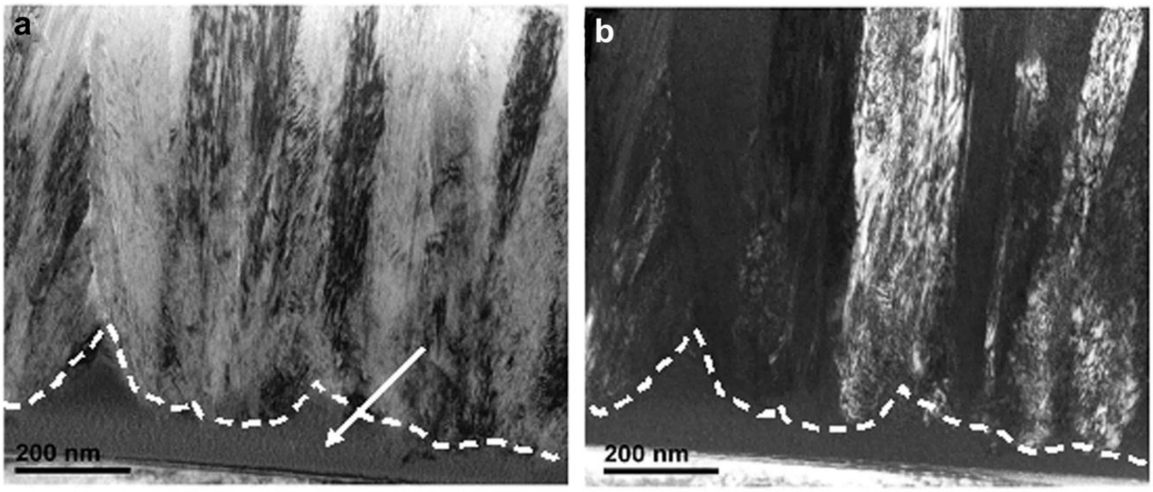

Figure 7.16 (a) BF and (b) DF images of Cr450 specimen. At interface a wavy amorphous layer is detected (marked by arrow). The grains have grown almost parallel to the substrate normal.

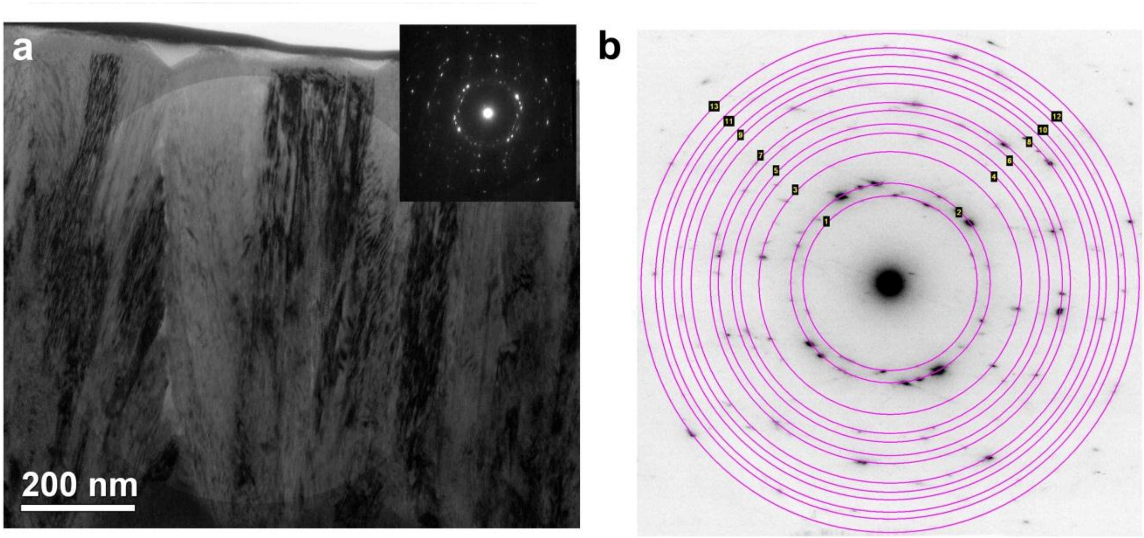

Figure 7.17 (a) BF image and SAED pattern taken from Cr450 specimen (inset) and (b) the corresponding d-spacing measurement of every ring of the film. The phase identification analysis have revealed that both Cr_2AlC and $Cr_{23}C_6$ are present in the film.

Since the phase identification from SAED patterns indicates that more than one phases are present in the film, analytical analysis was used to get a better understanding about the phase distribution in the film.

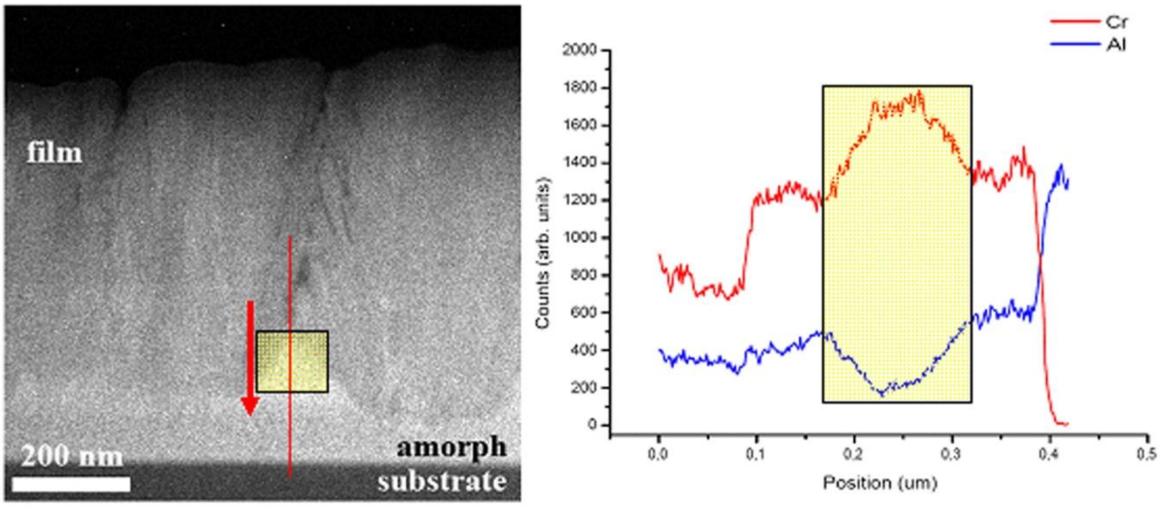

Figure 7.18 STEM HAADF image and its corresponding EDX line profiles of Cr450 specimen. At the top of the amorphous layer, EDX line scan shows the chromium concentration enrichment and also low concentration of aluminium.

Figure 7.18 shows STEM HAADF image and EDX line profiles for Cr450 specimen. The EDX line scan spectra show high concentration of chromium and low concentration of aluminium in the amorphous layer. This condition proposes the possibility that the minor $Cr_{23}C_6$ phase is present in the amorphous layer.

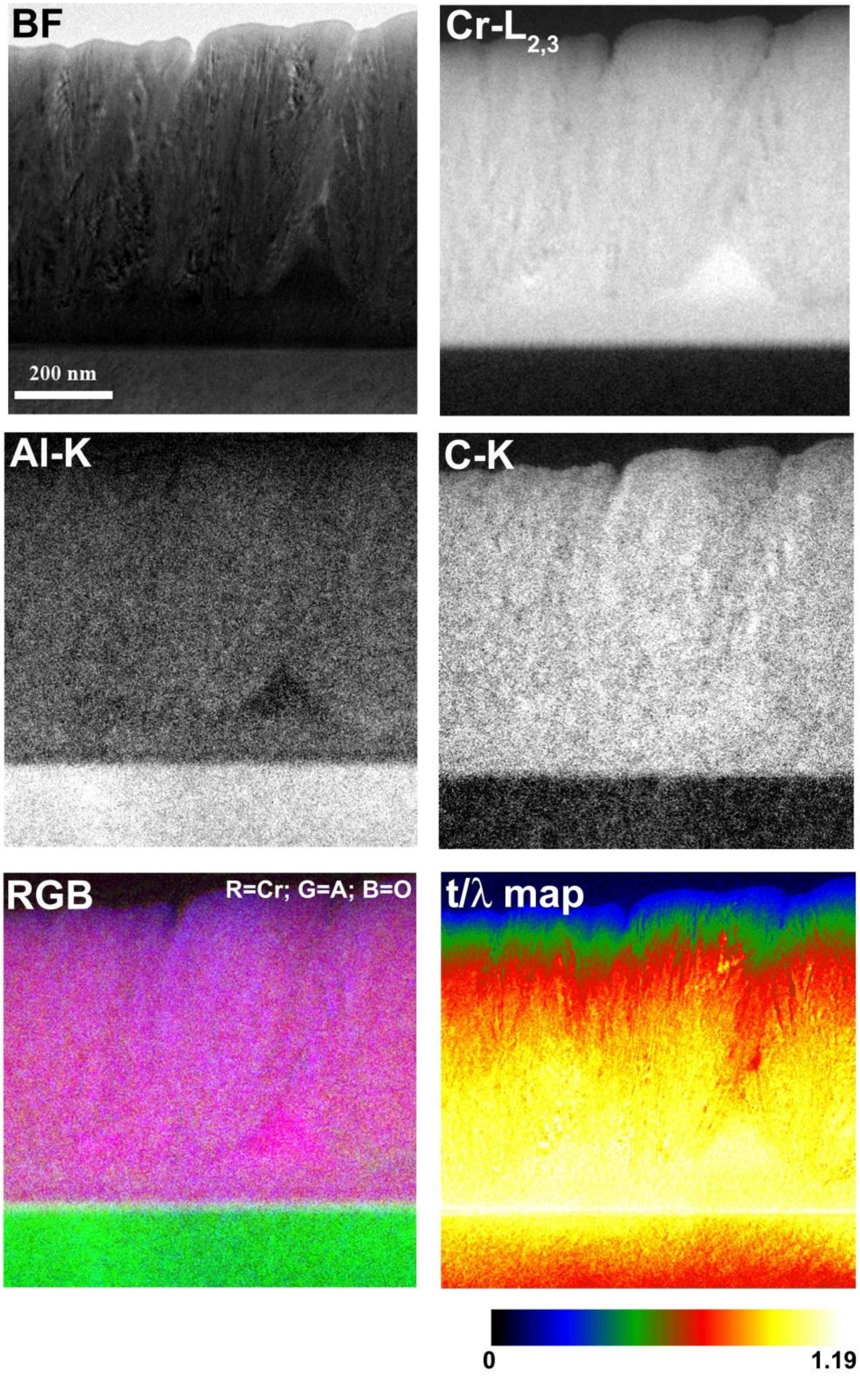

Figure 7.19 EFTEM elemental maps show chromium, aluminium, carbon and oxygen distribution on the Cr450 specimen respectively. A thickness map is also presented to give information about the thickness variation of the specimen.

EFTEM elemental mapping was used to add additional information especially about the carbon content in the film. As seen in figure 7.19, a high concentration of chromium and low concentration of aluminium in the amorphous layer were also revealed in the chromium and aluminium elemental maps. Furthermore, the carbon elemental map shows that the distribution of carbon is quite homogeneous, although its concentration is slightly increased in the same area where the chromium is also increased. Additionally, an oxygen elemental map is also presented, indicating the absence of oxygen contamination in the specimen.

In the Cr-Al-C system, high-resolution TEM (HRTEM) investigations were also performed to reveal the crystalline nature of the film. Figure 7.20 shows HRTEM images taken from the interface of the Cr450 specimen. An amorphous layer is confirmed once again from high-resolution image and the corresponding FFT pattern (see fig 2.20 (a)). On figure 2.20 (b) and (c), one can see the crystallites of the film and from the corresponding FFT, the phase present is known to be Cr_2AlC. Twins are also discovered in this film as seen in figure 2.20 (d).

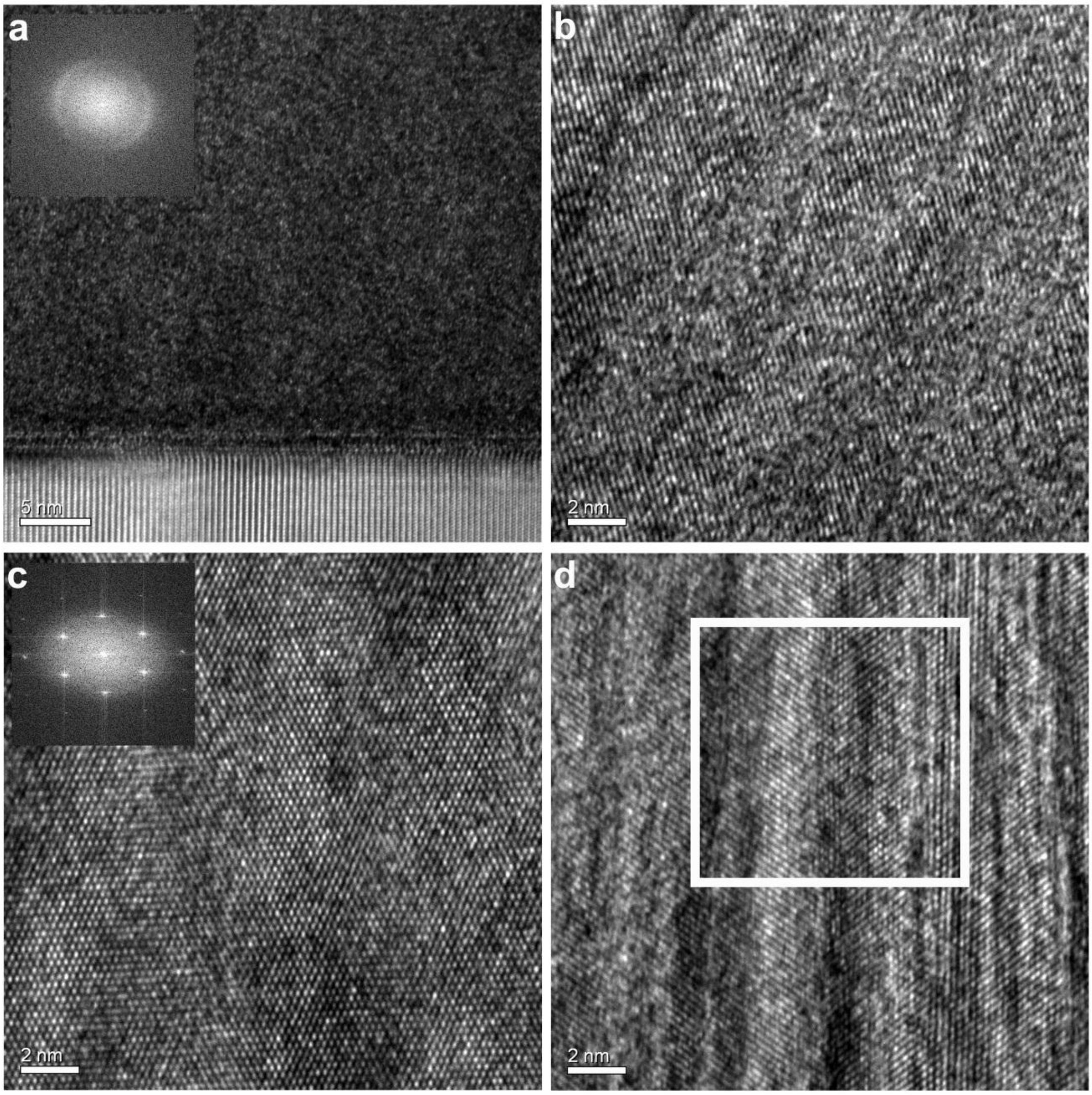

Figure 7.20 HRTEM images taken from (a) amorphous layer at interface, (b) and (c) crystalline part of the film and (d) an area which contains twins of the Cr450 specimen.

7.1.2.2. SEM and TEM investigation results of Cr-Al-C thin film deposited at 550°C

Figure 7.21 shows the SEM image of surface microstructure of the Cr-Al-C thin film deposited at 550°C (Cr550). The grains size is smaller than the Cr450 specimen.

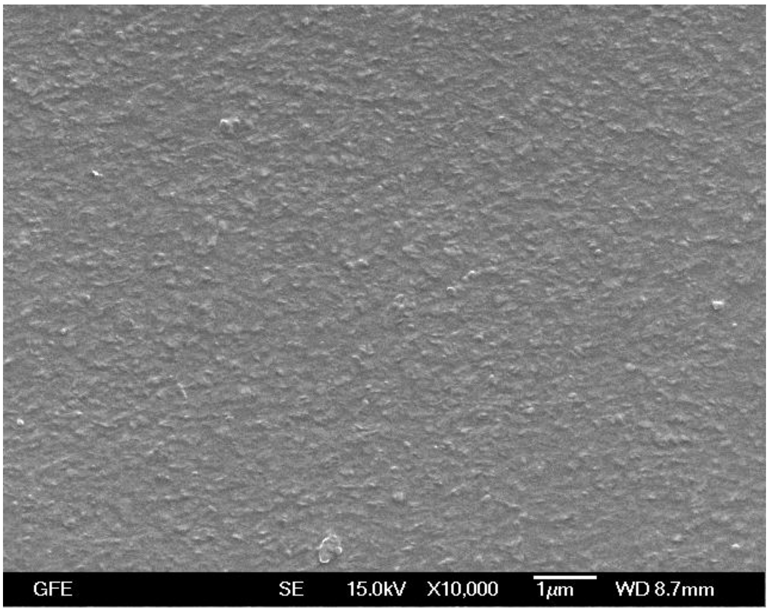

Figure 7.21 SEM image of surface microstructure of Cr550 specimen. The surface morphology is getting smoother than the Cr450 specimen.

The BF and DF images of Cr550 specimen have revealed that as addition to the grains which have grown parallel to the substrate normal, there are grains which have grown with some angle to the substrate normal (see figure 7.22). Furthermore, at the interface the amorphous layer is still detected with the thickness of the amorphous layer is thinner than the Cr450 (approximately 20 nm thick). Similar to the Cr450 specimen, there are no pores found on the film.

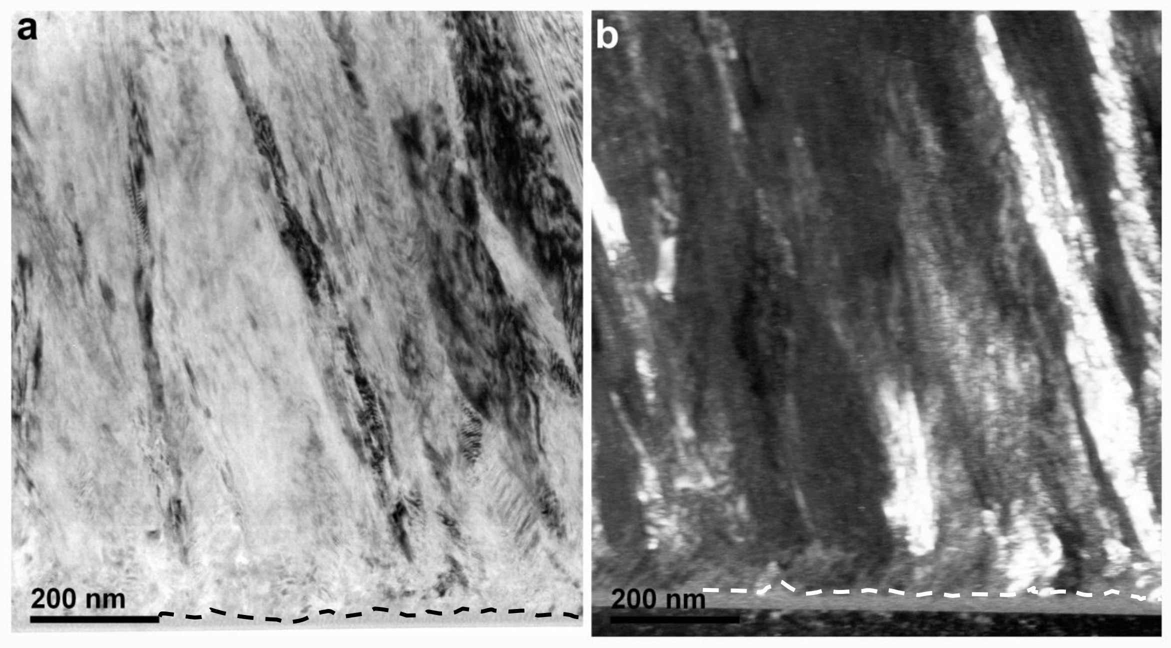

Figure 7.22 (a) BF and (b) DF images of Cr550 specimen. At interface a thinner amorphous layer compare to Cr-Al-C thin film is detected (marked by dash line). Besides the grains which have grown almost parallel to the substrate normal there are grains which have grown with an angle to substrate normal.

The phase identification from SAED patterns informs that as addition to Cr_2AlC, the $Cr_{23}C_6$ is still found in the Cr550 specimen (see figure 7.23). Moreover, the D-spacing measurements results using program DiffTools, as presented in appendix B, indicate that the lattice differences of Cr_2AlC from this experiment compared to the reference is smaller than the values from Cr450 specimen. This finding indicates that the phase present in the thin film tends to be single Cr_2AlC phase.

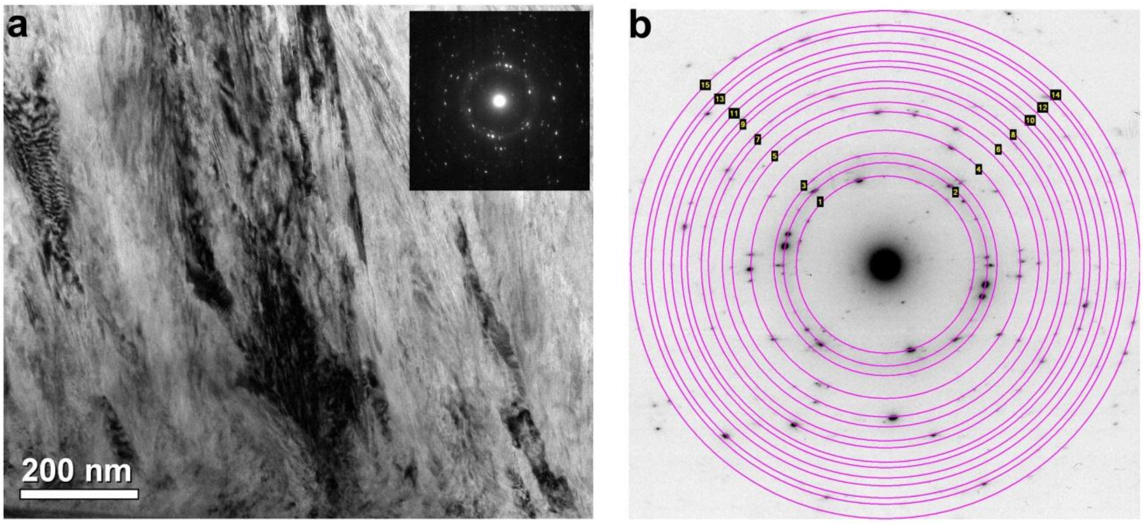

Figure 7.23 (a) BF image and SAED pattern taken from Cr550 specimen (inset) and (b) the corresponding d-spacing measurement of every ring of the film. The phase identification analysis have revealed that both Cr_2AlC and $Cr_{23}C_6$ are present in the film.

Figure 7.24 shows STEM HAADF image and EDX line profiles taken from Cr550 specimen. Although a slightly chromium enrichment is found in the Cr550 specimen, the concentration of aluminium in the amorphous layer at the interface tends to be constant.

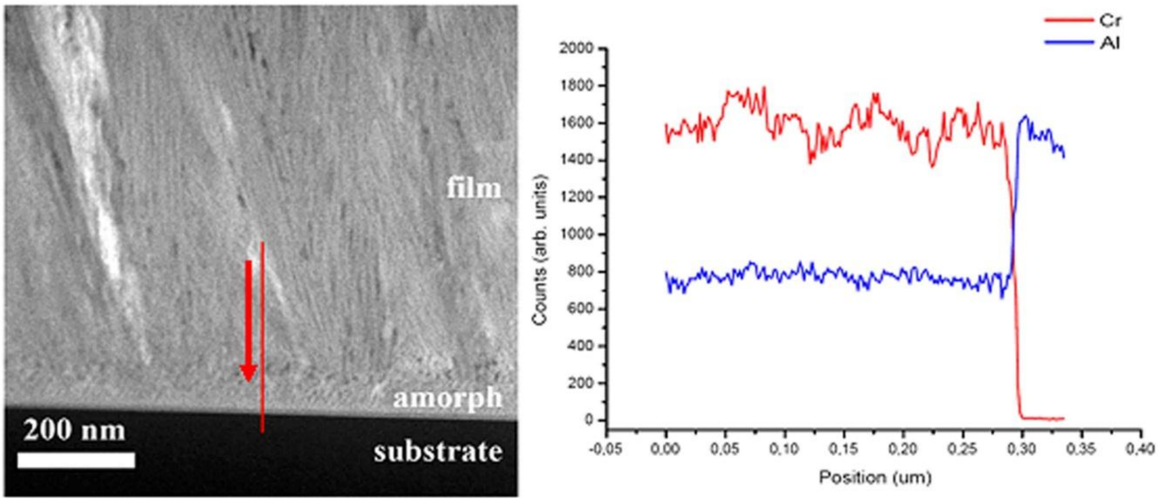

Figure 7.24 STEM HAADF image and its corresponding EDX line profiles of Cr550 specimen. There is a slightly chromium enrichment but the concentration of aluminium tends to be constant.

EFTEM elemental maps strengthen the EDX results. In the Cr550 specimen, as seen in figure 7.25, no concentration gradient for both aluminium and carbon can be detected. The elemental map of Cr-$L_{2,3}$ edge shows small concentration difference on several area on the film which is relevant with the EDX line scan results. Furthermore, the elemental map of oxygen shows no indication that oxygen contamination occurs in all areas of the specimen.

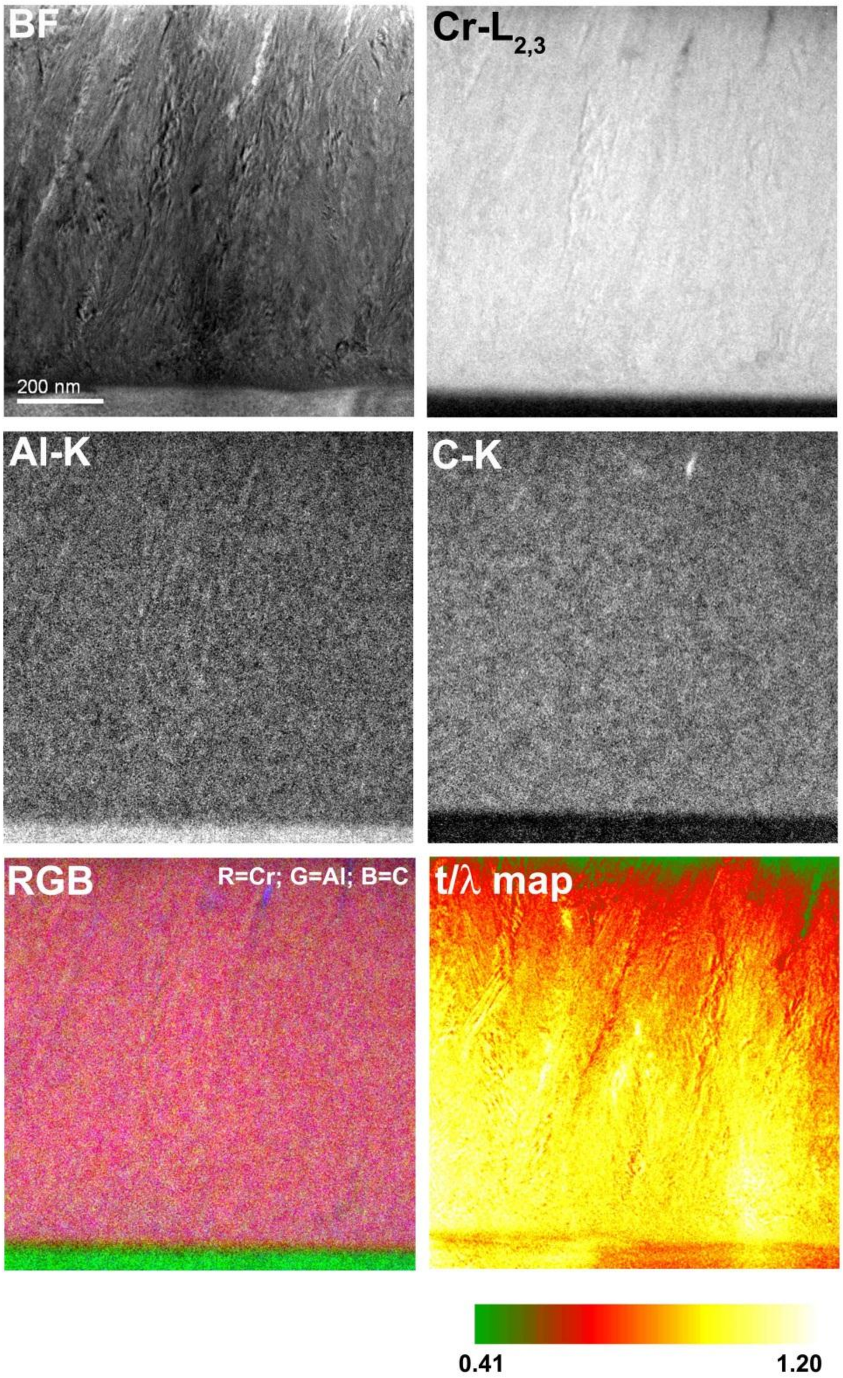

Figure 7.25 EFTEM elemental maps showing chromium, aluminium, carbon and oxygen distribution on the Cr550 specimen respectively. Additionally thickness map is also presented to give information about the thickness variation of the specimen.

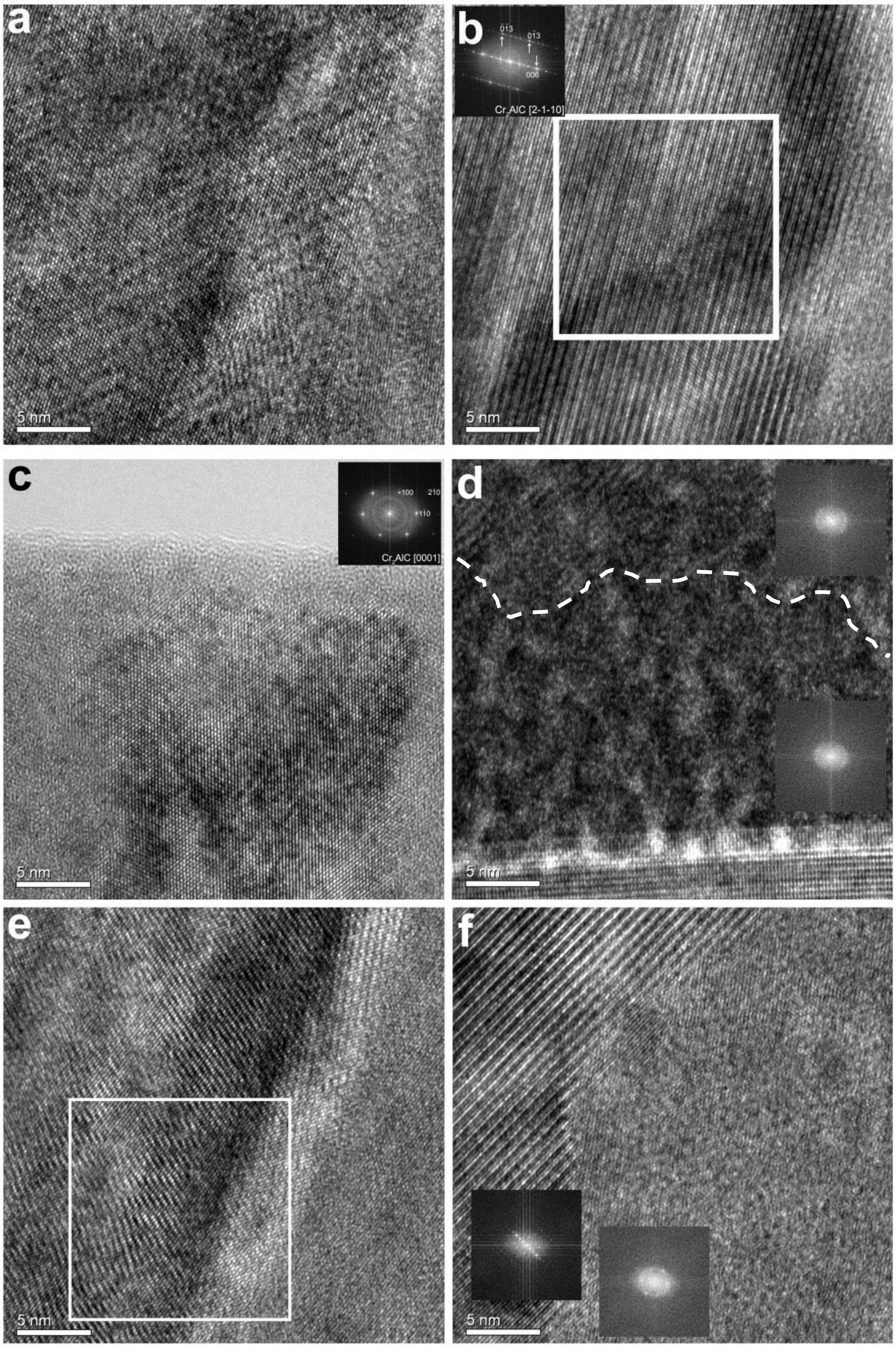

Figure 7.26 HRTEM images taken from the Cr550 specimen showing (a) – (c) crystallite of the film, (d) the amorphous layer at the interface followed by nano-crystalline order and (e) planar faults which are present in the film especially in the grain boundary (f).

HRTEM images taken from several parts of the Cr550 specimen show the atomic order of Cr_2AlC phase (see fig 7.26 (a)-(c)). Although it has been significantly reduced, the amorphous layer can still be seen in this film (see figure 7.26 (d) followed by nano-crystalline order.

Moreover, like the other MAX phases films, planar faults can be also detected in the film (fig 7.26 (d)). The typical stacking faults are mainly found in the grain boundary (figure 7.26 (e)).

7.1.2.3. SEM and TEM investigation results of Cr-Al-C thin film deposited at 650°C

The SEM image of Cr-Al-C thin film deposited at 650°C (Cr650) shows that the surface morphology of the film is the smoothest compared to the previous two Cr-Al-C thin films (see figure 7.27). Moreover, the SEM image also shows that the grains are less oriented compared to the other Cr-Al-C thin films.

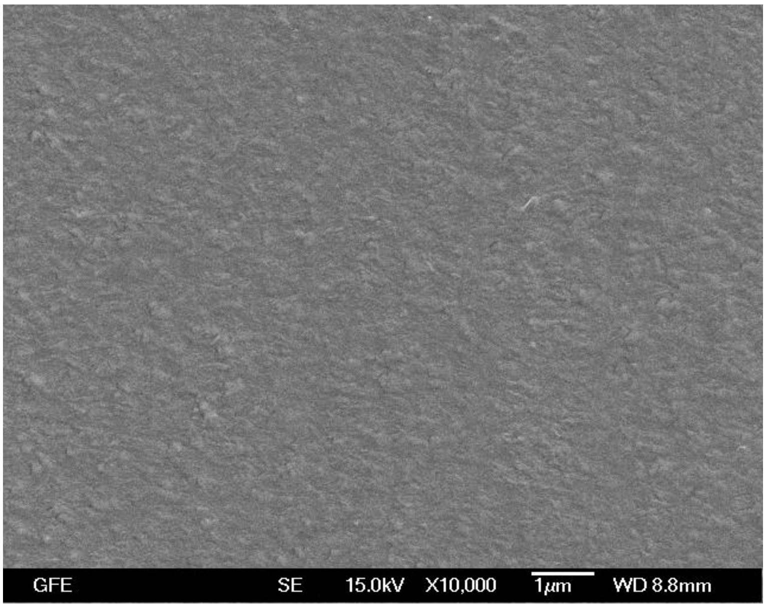

Figure 7.27 SEM image of surface microstructure of Cr650 specimen. The thin film has the smoothest surface and less oriented grains compared to other Cr-Al-C thin films.

Figure 7.28 shows BF and DF images of the Cr650 specimen. Unlike the other Cr-Al-C thin films, there is no amorphous layer detected on the thin film. The grains growth is also different from the other Cr-Al-C thin films. Here, besides the large grains which have grown directly from the interface, there are also small grains which have grown up to 300 - 400 nm above the interface. Moreover, those grains are more randomly oriented compared to other Cr-Al-C thin films.

The SAED patterns taken from Cr650 specimen have revealed that only Cr_2AlC phase is identified (see figure 7.29). The purity of the Cr_2AlC which is present in the film has also been indicated by the relative error of the lattice parameter of Cr_2AlC from this present work and reference based on the calculation with program DiffTools which is presented in appendix B.

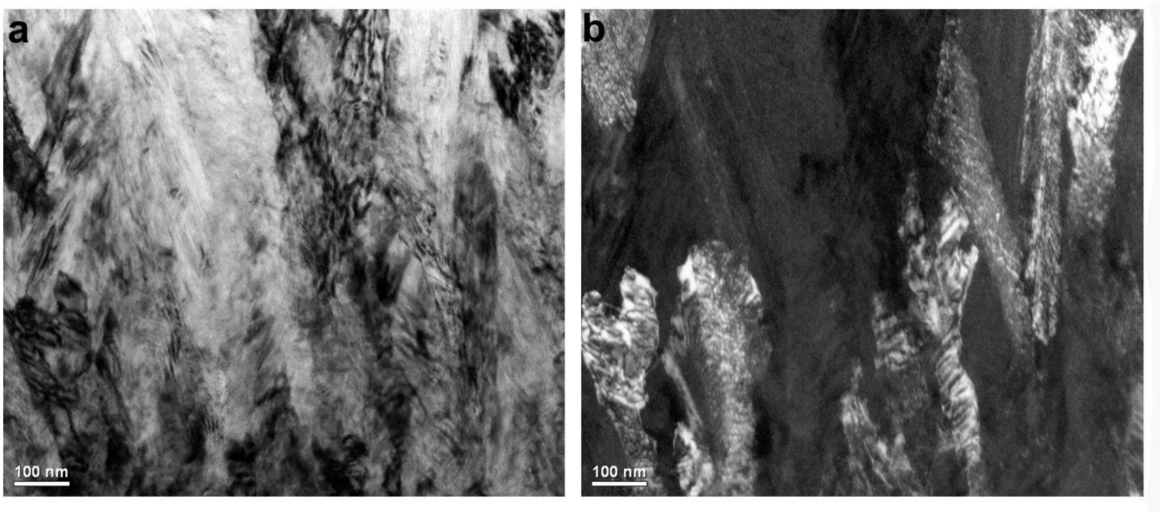

Figure 7.28 BF and DF images of Cr650 specimen. No amorphous layer is found. Besides the large grains which have grown directly from interface to top of the film, several small grains which oriented randomly and have grown up to 300 - 400 nm above the interface have also been found.

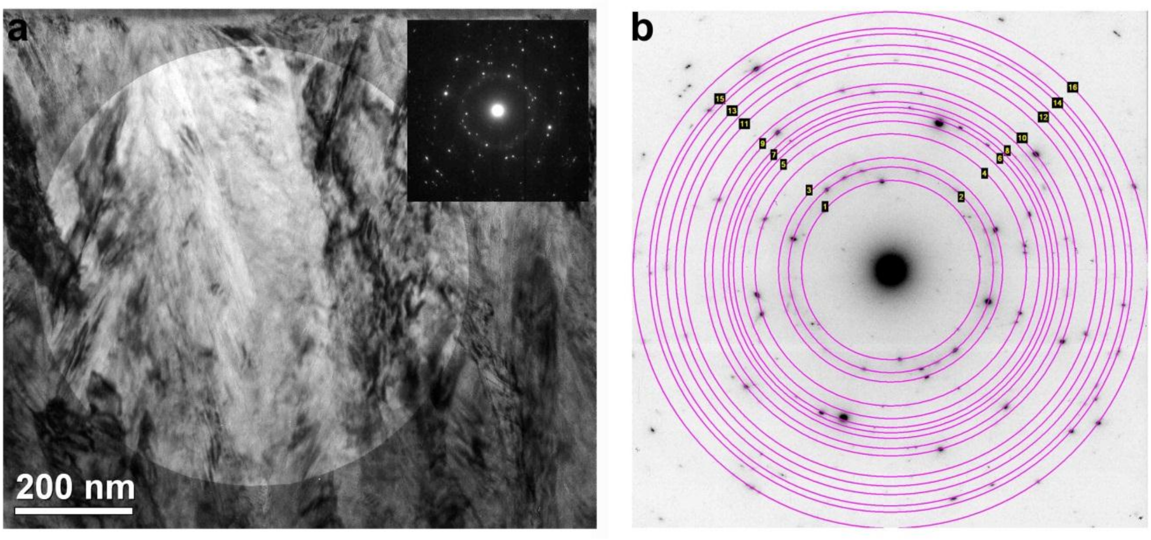

Figure 7.29 (a) BF image and SAED pattern taken from Cr650 specimen (inset) and (b) corresponding d-spacing measurement of every ring of the films. Only Cr_2AlC is identified from phase identification analysis.

As no amorphous layer found in the Cr650 specimen, STEM HAADF image and EDX line profiles indicate no significant concentration gradient for both chromium and aluminium (see figure 7.30). This condition proposes the possibility that the minor $Cr_{23}C_6$ phase is not present anymore in the thin film which agrees very well with the phase identification results from SAED patterns.

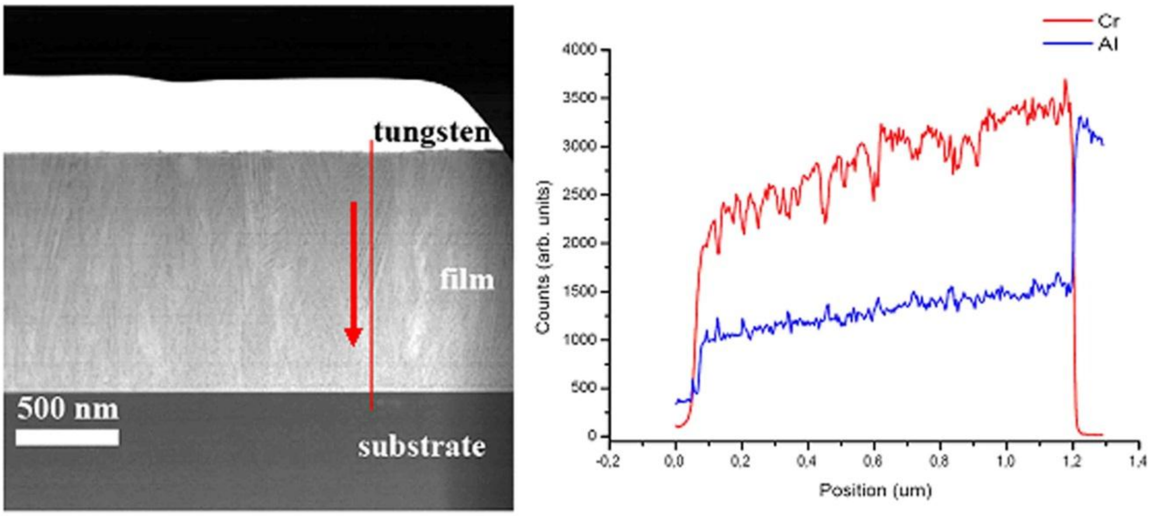

Figure 7.30 STEM HAADF image and its corresponding EDX line profiles of Cr650 specimen. No significant concentration gradient of both chromium and aluminium is detected.

HRTEM images taken from Cr650 specimen are presented in figure 7.31, 7.32 and 7.33 respectively. At the interface (figure 7.31) confirming other investigations, no amorphous layer is detected. The Cr_2AlC phase has grown directly from interface. Unfortunately there is no orientation relationship found in this specimen. Similar crystalline structures as those found on the Cr550 specimen are also found in this specimen (see fig 7.32). Furthermore, as seen in figure 7.33, stacking faults are also present in the film.

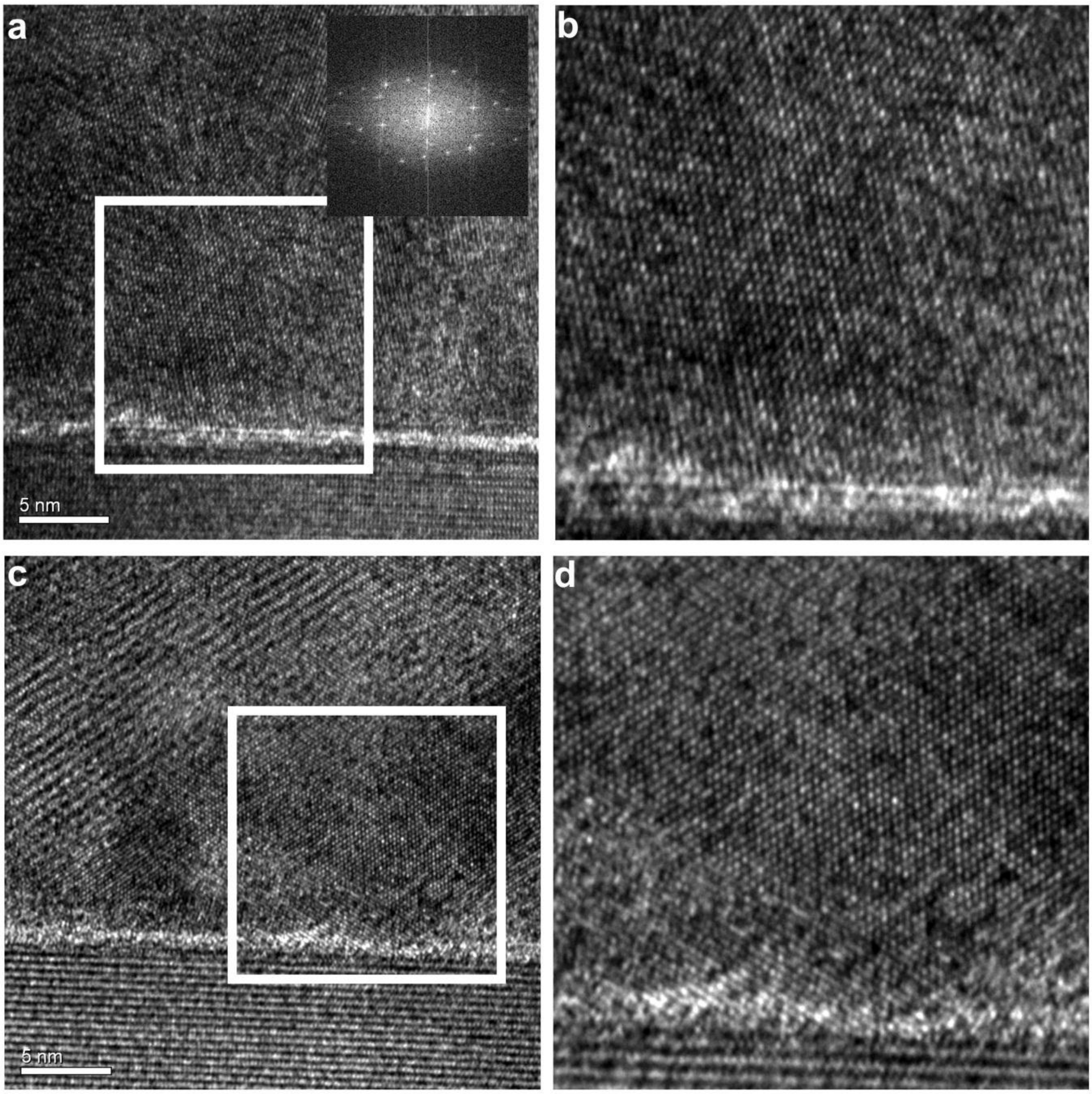

Figure 7.31 HRTEM images of interface taken from the Cr650 specimen (a and c) and their magnified images of selected area marked by white rectangular (b and d). No amorphous layer can be detected. Although the Cr_2AlC phase has grown directly from the interface, no orientation relationship is detected.

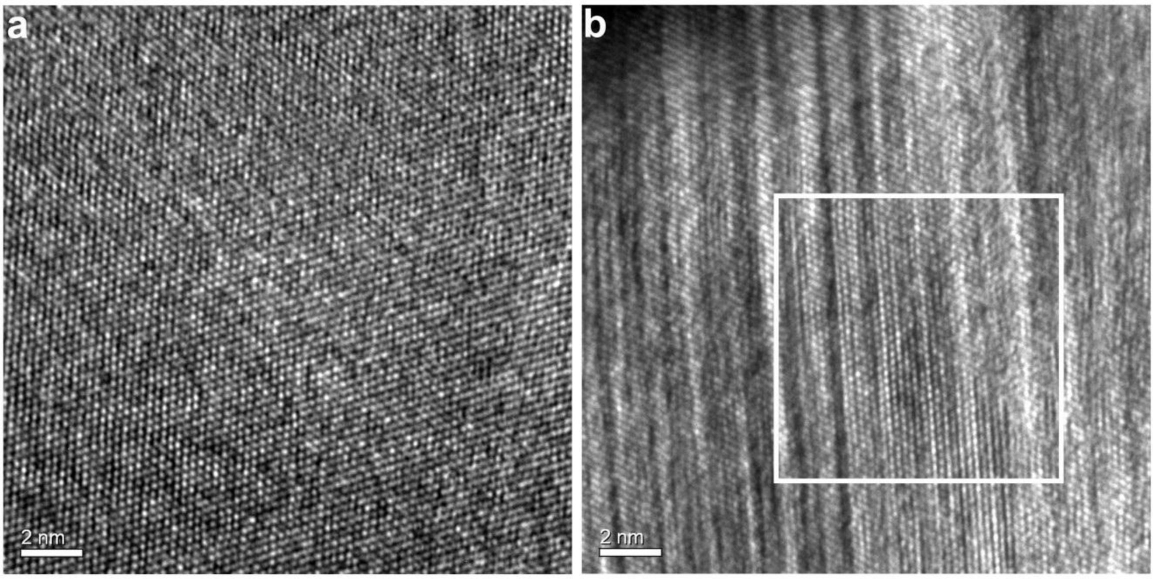

Figure 7.32 HRTEM images taken from Cr650 specimen showing the crystalline nature of the film.

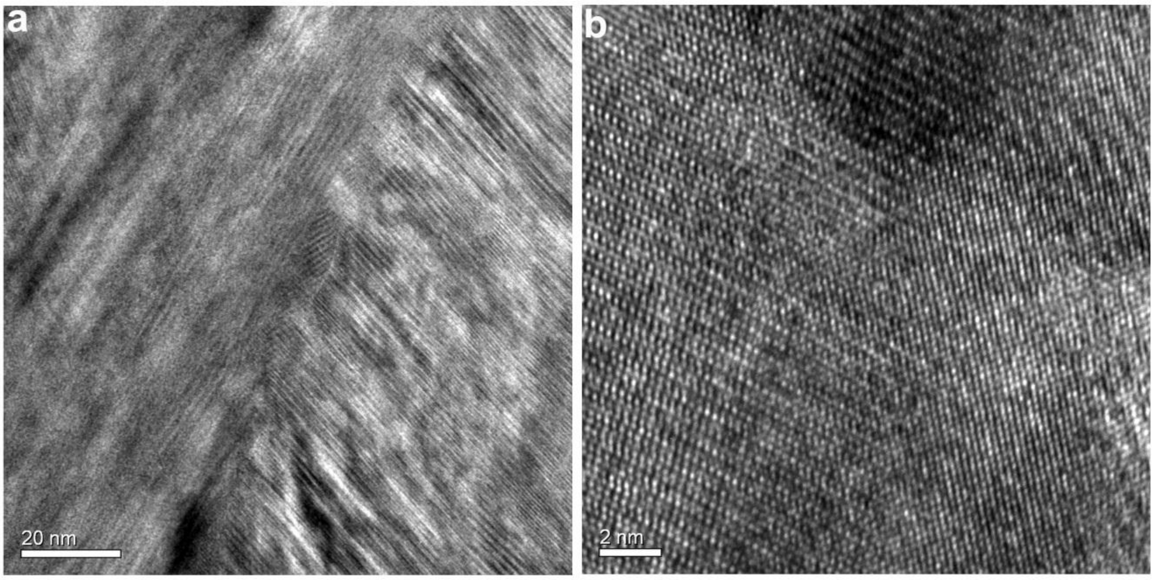

Figure 7.33 HRTEM showing stacking faults presence on the Cr650 specimen.

7.1.2.4. Short summary of Cr-Al-C thin films growth

The increasing deposition temperatures change the surface morphology to become smoother. Deposition temperature variations also reduce the thickness of amorphous layer until it has completely disappeared at 650°C. Moreover the phase transformation from multiphase

(Cr_2AlC and $Cr_{23}C_6$) found in the films become single phase at deposition temperature of 650°C. Figure 7.34 shows the summary of lattice difference for three different deposition temperatures. The presence of $Cr_{23}C_6$ in the specimen with 450°C deposition temperature causes the increase in the Cr_2AlC lattice parameter. The lattice parameter difference of the Cr_2AlC phase in the specimen deposited at 650°C, which is very small, leads to indications that only the Cr_2AlC phase is present in the specimen. Moreover, HRTEM images show that no orientation relationships can be found at the interface and the films consist of faults mainly stacking faults and twins.

Table 7.2 Short summary of the TEM investigation results on the growth of Cr-Al-C MAX-phase thin films.

Cr-Al-C system	
Microstructure of the film	On the film deposited at 450°C and 550°C amorphous layer are found at the interface
Phase identification	On thin film deposited at 450°C and 550°C minor phase of $Cr_{23}C_6$ are found. On thin film deposited at 650°C only Cr_2AlC film can be found
High-resolution TEM	Stacking faults and twins are found in the film
Increasing deposition temperature	• Reducing amorphous layer thickness • Forming single Cr_2AlC phase

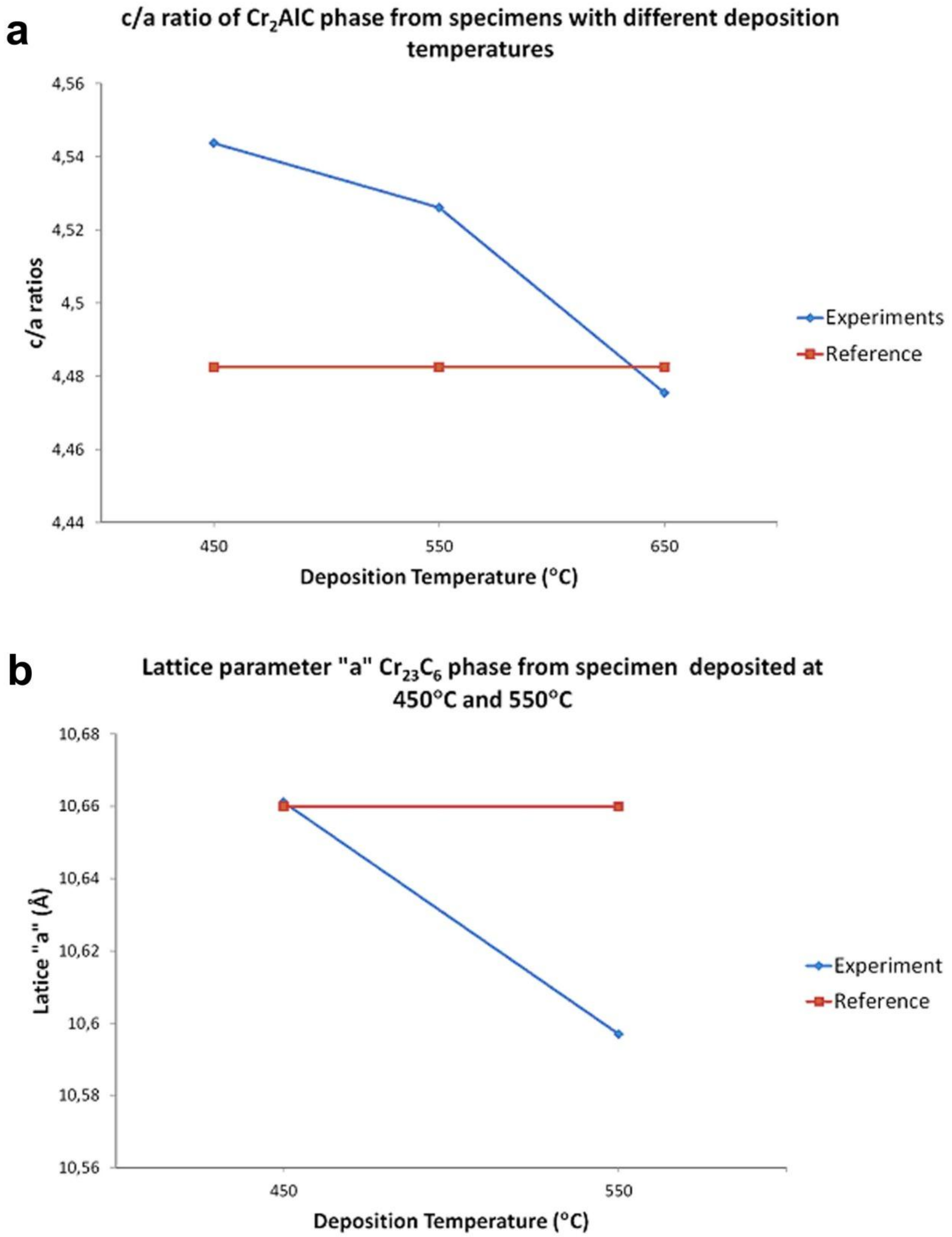

Figure 7.34 The summary of (a) c/a ratio for the Cr_2AlC phase and (b) lattice parameter “a” for the $Cr_{23}C_6$ phases from specimen deposited at 450°C and 550°C.

7.2. Isothermal oxidation behaviour and microstructure evolution of high temperature oxidation resistant materials: Cr_2AlC thin films and Fe-Cr-Al model alloys

In this present work, both Cr_2AlC and Fe-Cr-Al model alloys were investigated for their isothermal oxidation behaviour especially for their microstructure evolution. For SEM images, both SE and BSE techniques were used to give an overview about the cross section of the specimens. Furthermore, TEM investigations have been done to reveal microstructure evolution during the isothermal oxidation for all specimens.

7.2.1. Oxidation of Cr_2AlC thin films

The Cr_2AlC thin films were oxidised at 1320°C in TGA for three different total times: 4 min, 39 min and 282 min, with the resulting scale thicknesses of approximately 1 µm, 3 µm and 6 µm, respectively. The three specimens are named based on their thickness as Cr-1, Cr-3 and Cr-6 for oxidised Cr_2AlC thin films with oxide scale thickness of 1, 3 and 6 µm respectively. In the following sections, we present the microstructure investigation results for all specimens which are grouped based on their oxide scale thickness.

7.2.1.1. SEM and TEM investigation results of oxidised Cr_2AlC thin film with 1 µm oxide scale (Cr-1 specimen)

Figure 7.35 shows the SEM cross sectional image of the Cr-1 specimen. A dense and continuous alumina scale with the thickness approximately 1 µm oxide scale is observed. An additional interlayer, presumably consists of chromium carbide, has formed below the scale interface. Small voids are also found in the Cr_2AlC film.

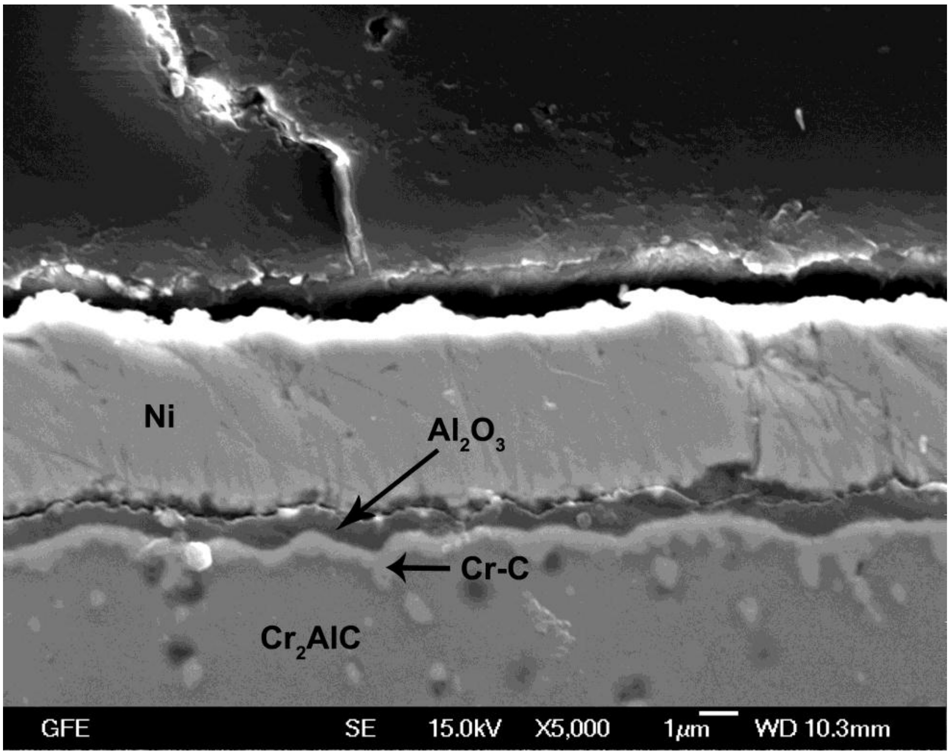

Figure 7.35 SEM-SE image of Cr_2AlC specimen oxidised at 1320°C with 1 µm (Cr-1 specimen). A dense and continuous alumina scale together with a thin interlayer below the scale is observed.

The BF image of the cross section of the Cr-1 specimen confirms the presence of a dense and continuous alumina scale, as well as the presence of the voids in the Cr_2AlC film. The BF image also indicates that the alumina scale has a wavy morphology. Phase identification analysis from SAED patterns from region 1 and 2 indicates the presence of Cr_2AlC and Cr_3C_2 in the specimen (see fig 7.36). Other phase identification analyses (not displayed here for brevity) confirm that the Cr_3C_2 is present as interlayer below the interface of the alumina scale.

Figure 7.37 shows EFTEM elemental maps of a specimen with 1 µm alumina scale. At 125 nm above the alumina scale interface, the presence of precipitates is observed. From EFTEM elemental maps, it is verified that the precipitates contain Cr and C. The chromium elemental map has also revealed that chromium was dissolved in the alumina scale.

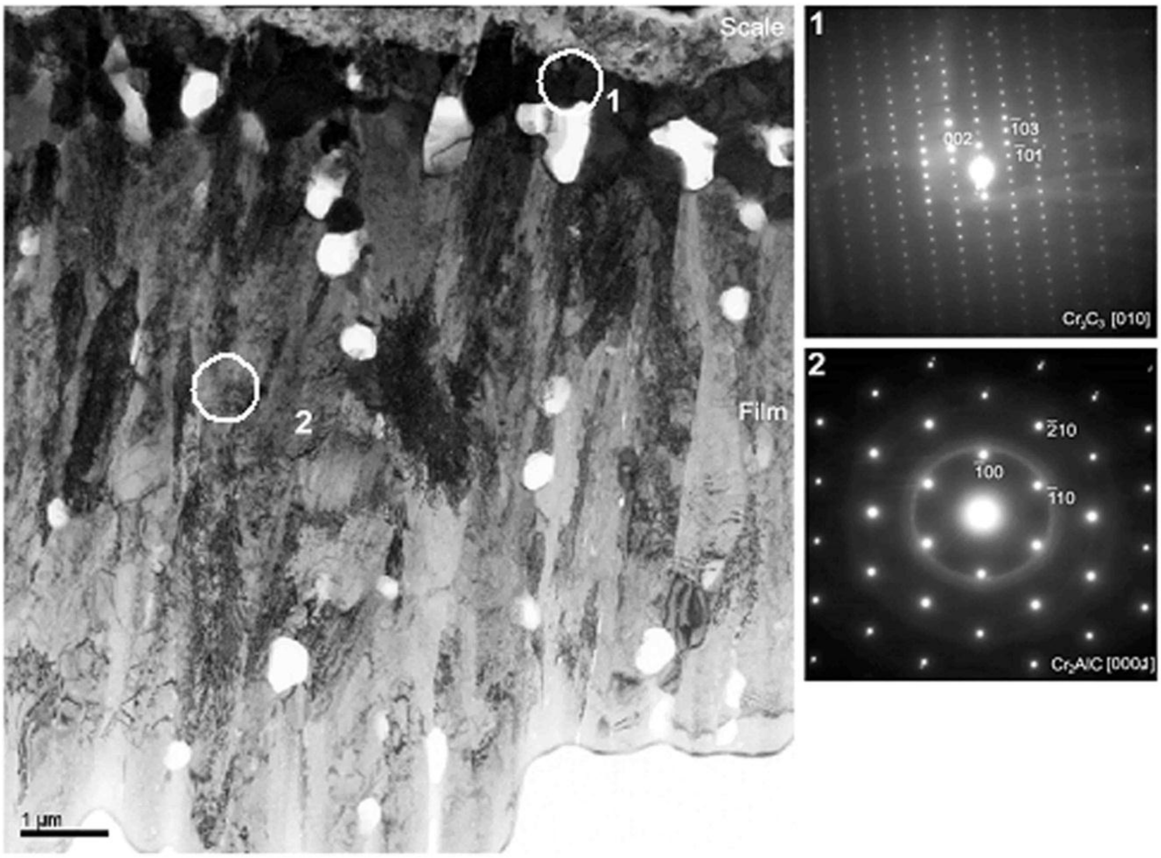

Figure 7.36 BF image of the Cr-1 specimen. SAED patterns from region 1 and 2 show that the specimen consists mainly of Cr_2C_3 and Cr_2AlC phases.

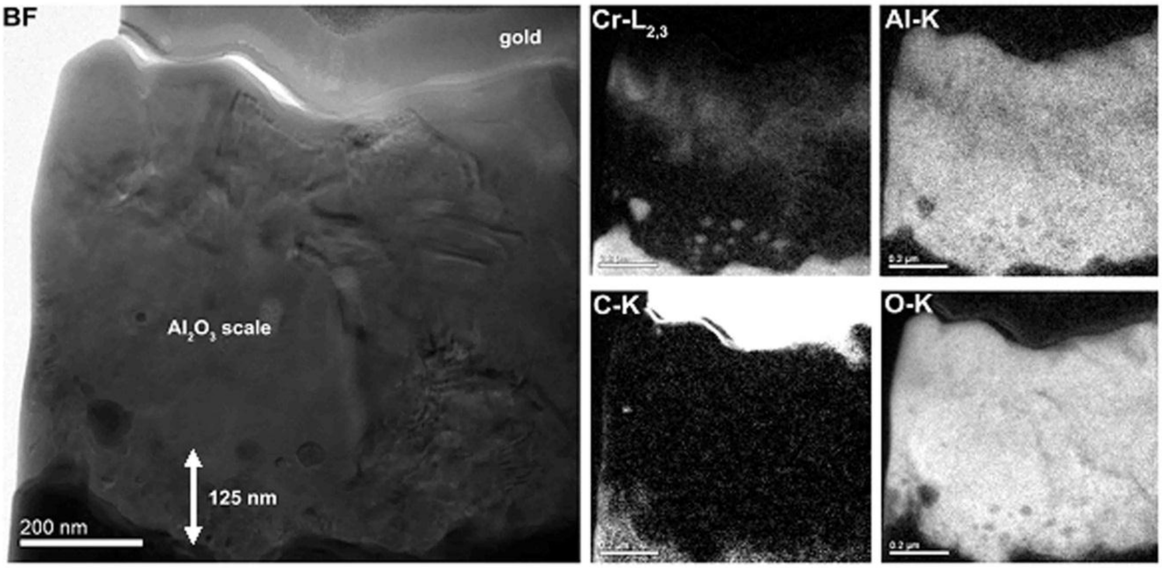

Figure 7.37 EFTEM elemental maps of the scale region of the Cr-1 specimen. A high concentration of Cr in the outer part of the scale can be observed. The elemental maps also indicate that the precipitates located close to the interface consist of Cr and C.

7.2.1.2. SEM and TEM investigation results of oxidised Cr_2AlC thin film with 3 µm oxide scale (Cr-3 specimen)

The SEM image of the cross section the Cr-3 specimen shows that the amount of porosity in the Cr_2AlC film increases (see figure 7.38). This condition decreases the density of Cr_2AlC film compared to the Cr-1 specimen.

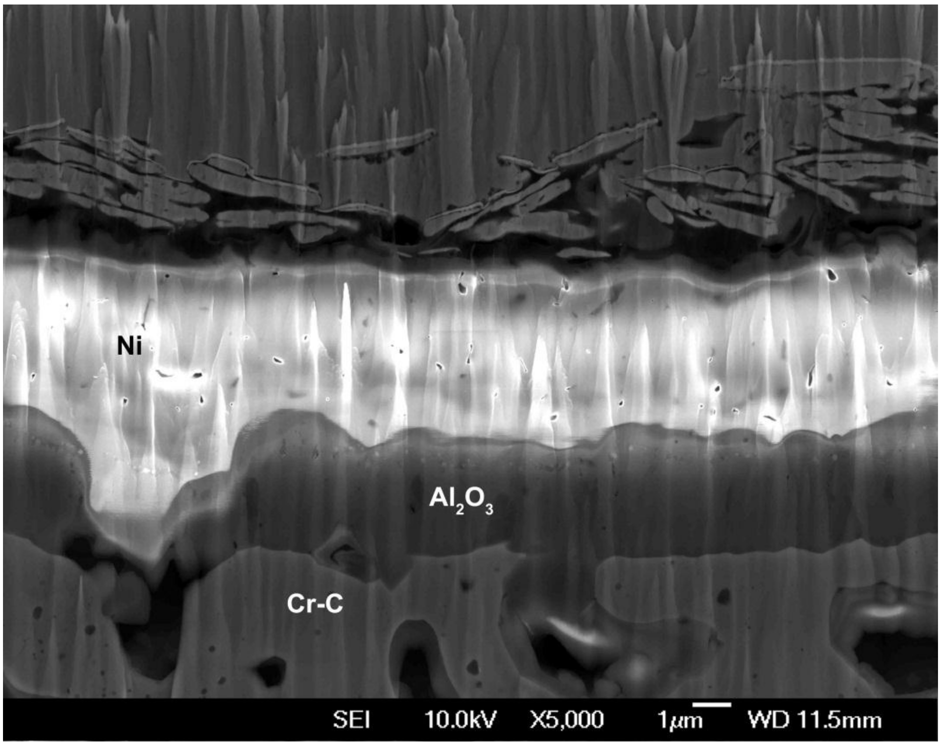

Figure 7.38 SEM-SE image of Cr_2AlC specimen oxidised at 1320°C with 3 µm (Cr-3 specimen). A dense and continuous alumina scale together with an interlayer below the scale is observed. Some pores are also observed in the interlayer.

Figure 7.39 shows a BF image and SAED patterns taken from region 1 and 2 of the Cr-3 specimen. The SAED phase identification has revealed the presence of Cr_2AlC and Cr_3C_2. It is observed that the amount of Cr_2AlC phase decreases compared to the Cr-1 specimen and the film now contains a significant amount of porosity. In contrast to the Cr-1 specimen, in which the voids concentrate only close to the interface, here, the voids distribution is found in the Cr-C interlayer. Moreover, the interface of alumina scale is also less wavy compared to the Cr-1 specimen.

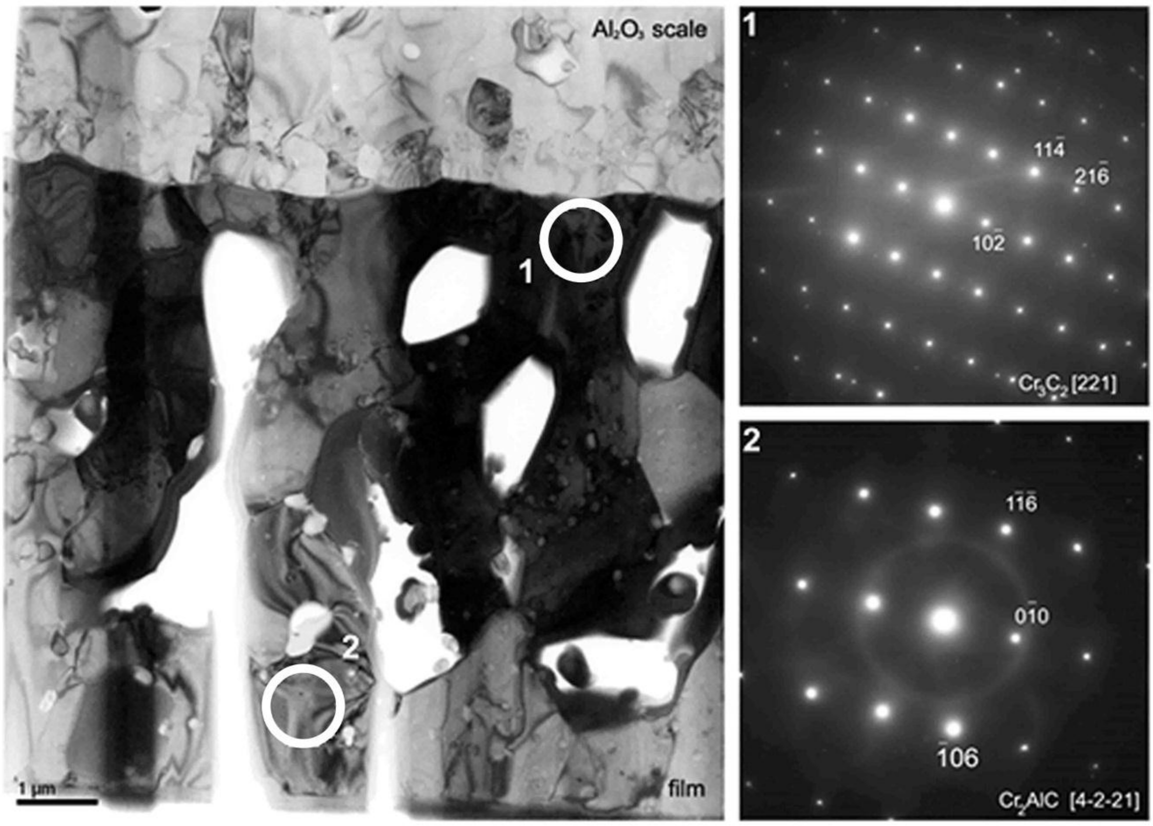

Figure 7.39 BF image of the Cr_2AlC specimen with 3 µm oxide scale and SAED patterns from location 1 and 2. Similar to the Cr-1 specimen, the presence of the Cr_2AlC and Cr_3C_2 phases are found in the specimen.

From the STEM-HAADF image and EFTEM elemental maps, the Cr-C precipitations are also found in the Cr-3 specimen (see fig 7.40). In contrast to the specimen with 1 µm alumina scale, there is no indication that chromium was dissolved in the scale.

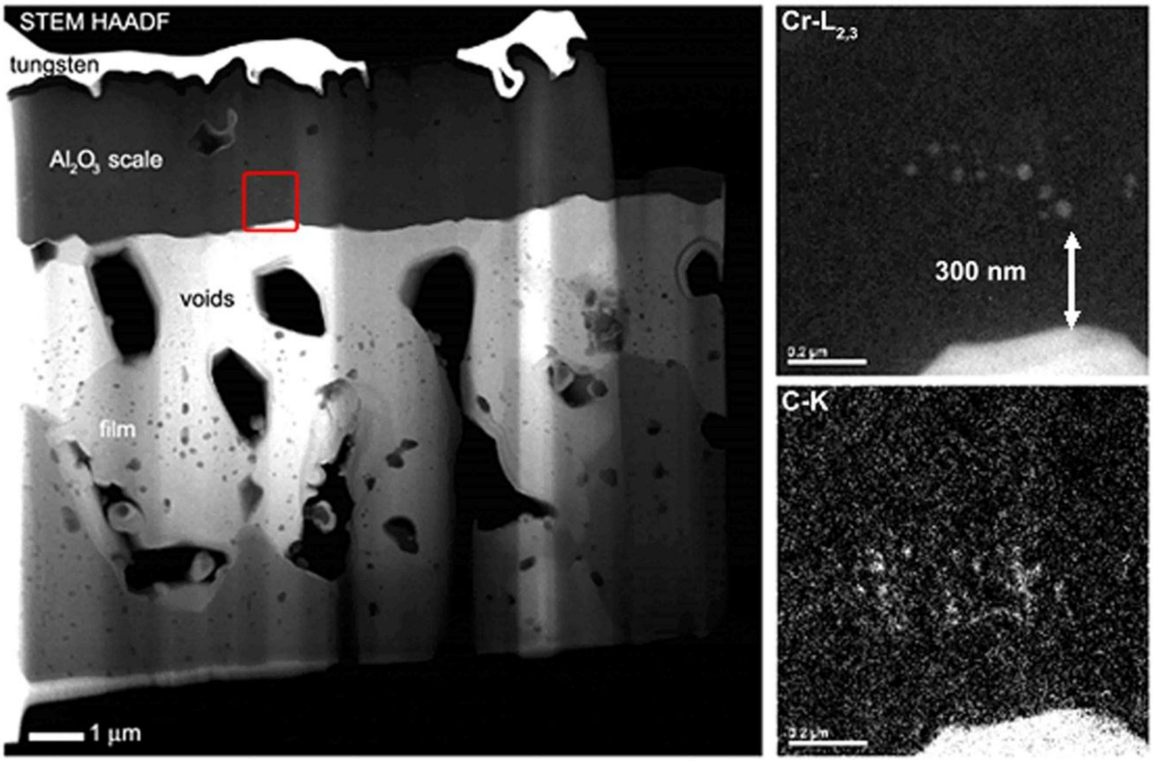

Figure 7.40 STEM-HAADF image (left) and EFTEM elemental maps (right) of the Cr-3 specimen. The Cr and C elemental maps show the Cr-C containing precipitates, which are formed in the scale.

7.2.1.3. SEM and TEM investigation results of oxidised Cr_2AlC thin film with 6 µm oxide scale (Cr-6 specimen)

Figure 7.41 shows the SEM image of the Cr-6 specimen. The density of the Cr_2AlC film is significantly decreased and a high porosity was formed. Compared to the other specimens, the amount of Cr_2AlC areas, which are transformed to Cr-C, increase significantly.

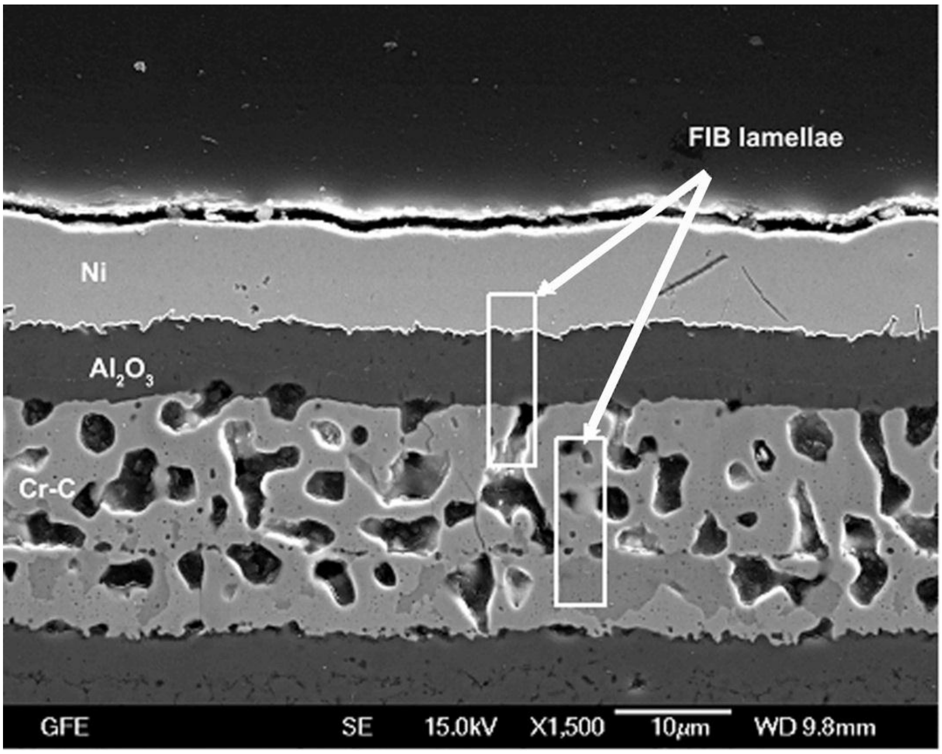

Figure 7.41 SEM-SE image of Cr_2AlC specimen oxidized at 1320°C with 6 µm (Cr-6 specimen). Similar to other specimens, a dense and continuous alumina is observed together with a large amount of voids below the scale. Additionally, the location where FIB lamellas were cut is also shown in the figure.

Since the Cr-6 specimen has a thick oxide sale, special location where the FIB lamellas were cut is shown in the SEM image. The Cr-6 specimen has a thicker Cr-C interlayer which contains porosity. A large amount of voids has been formed and additionally, some small precipitates and cracks in this interlayer have been also observed (see fig 7.42). Similar to the results of XRD, the phase identification analysis from SAED patterns confirms the presence of Cr_7C_3 in addition to Cr_2AlC and Cr_3C_2. From a detailed phase identification analysis, it can be concluded that the amount of Cr_2AlC decreases significantly and can only be found in small grains at the interlayer.

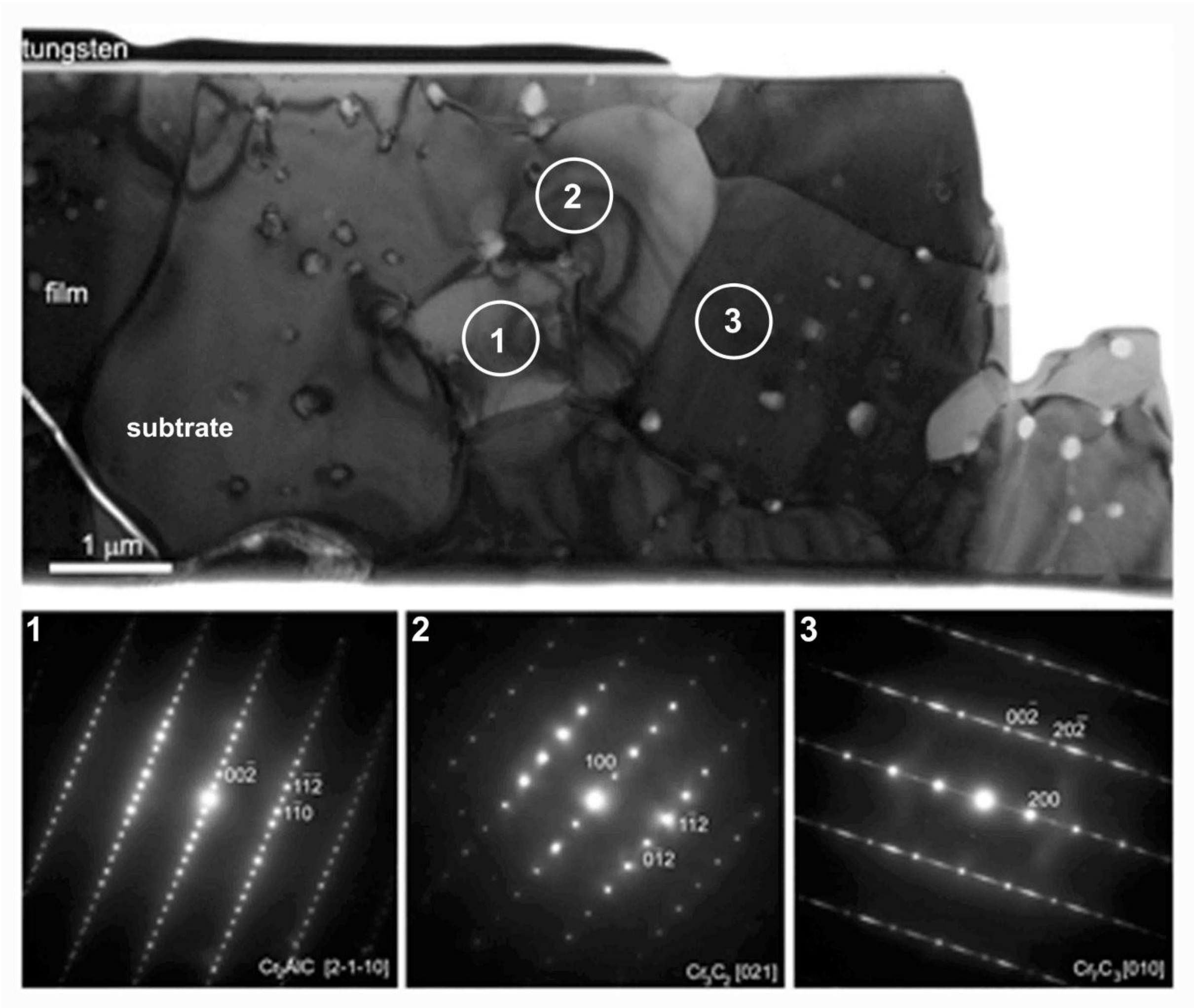

Figure 7.42 BF image of the Cr-6 specimen and SAED patterns from the corresponding positions. The single grains of Cr_2AlC phase and as addition to Cr_3C_2 phase, Cr_7C_3 phase can be found.

The EFTEM elemental maps of Cr-6 specimen also show the Cr-C containing precipitates in the scale (see figure 7.43). Similar to the Cr-3 specimen, there is no indication that chromium has been dissolved in the scale.

More information about the alumina scale of the Cr-6 specimen can be seen in figure 7.44 (a). A STEM-HAADF image shows that the scale is dense and contains continuous precipitates which have been identified by EFTEM as Cr-C precipitates, positioned higher than in the other specimens (approx. 3 µm above the interface). Near the interface, the bright contrast indicates that the Cr_2AlC phase is not present. This area contains either the Cr_2C_3 or Cr_3C_7 phases (see fig 7.44 (b)). In contrast, fig 7.44 (c) shows that at the lower part of the film the small grains, observed as darker areas, contain the Cr_2AlC phase. In fig 7.44 (d), elemental maps of the oxygen K-edge and the aluminium K-edge from the precipitates in the interlayer region (marked by white rectangles) indicate the presence of an inner oxidation zone.

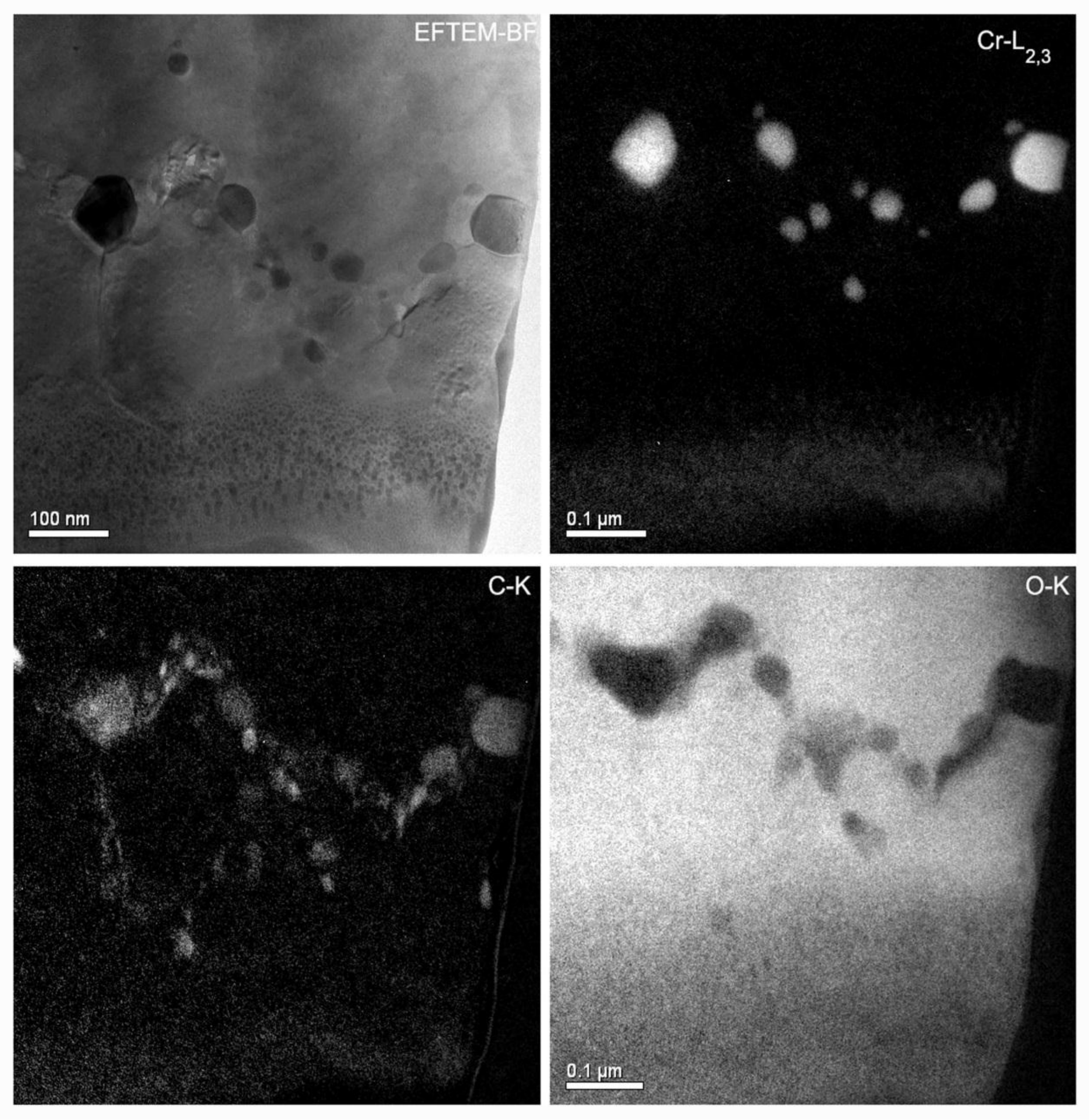

Figure 7.43 EFTEM elemental maps acquired from the Cr-6 specimen. Cr-C containing precipitates are observed in the scale.

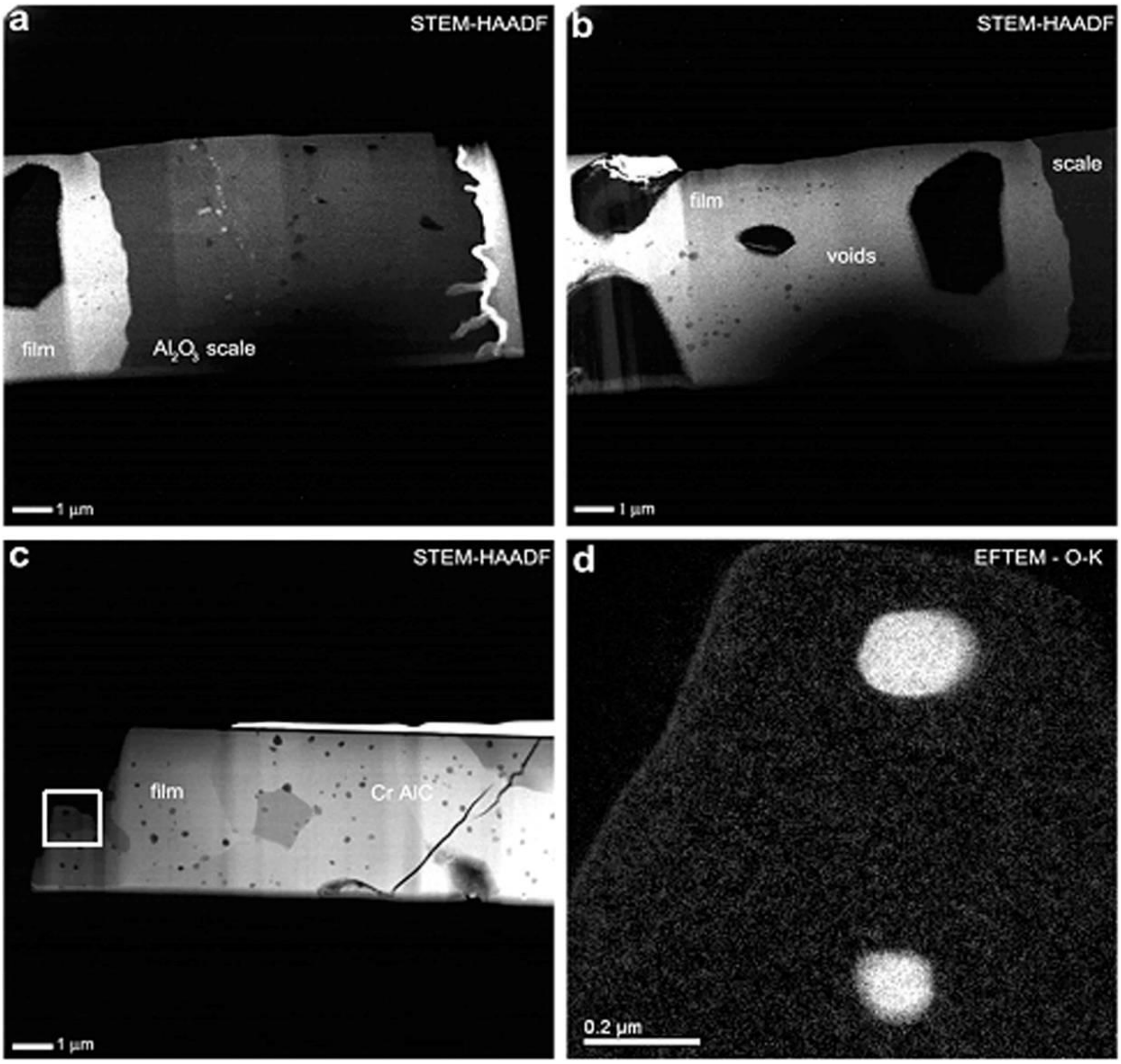

Figure 7.44 STEM HAADF images and O-K elemental map from two FIB lamellas of Cr-6 specimen. The first FIB lamella shows (a) the scale and (b) Cr-C interlayer below the alumina scale. The second FIB lamella shows (c) the Cr-C interlayer and the presence of internal oxidation on that interlayer which is indicated by oxygen elemental map. For brevity, the aluminium elemental map is not displayed here.

7.2.1.4. Short summary of oxidised Cr_2AlC thin films

With the increase in oxidation time, the dense alumina scale thickness also increases. No pores can be found in the scale. The pores formed below the scale together with Cr-C interlayer whose thickness also increases with the increasing oxidation time. Phase identifications have revealed the presence of Cr_3C_2 and Cr_7C_3 in the specimen.

Figure 7.45 shows the oxide scale of three specimens. Textured grain orientation is clearly seen at the upper part of the scale in the Cr-1 specimen (see fig 7.45 (a)). This condition on the other hand, is not observed at lower part of the scale (Fig 7.45 (b)). For Cr-3 specimen, the growth of the grains is observed directly from interface. In figure 7.45 (c), smaller grains near interfaces followed by larger grains at the upper part of the scale are observed on the Cr-6 specimen. These groups of grains are divided by a continuous precipitate.

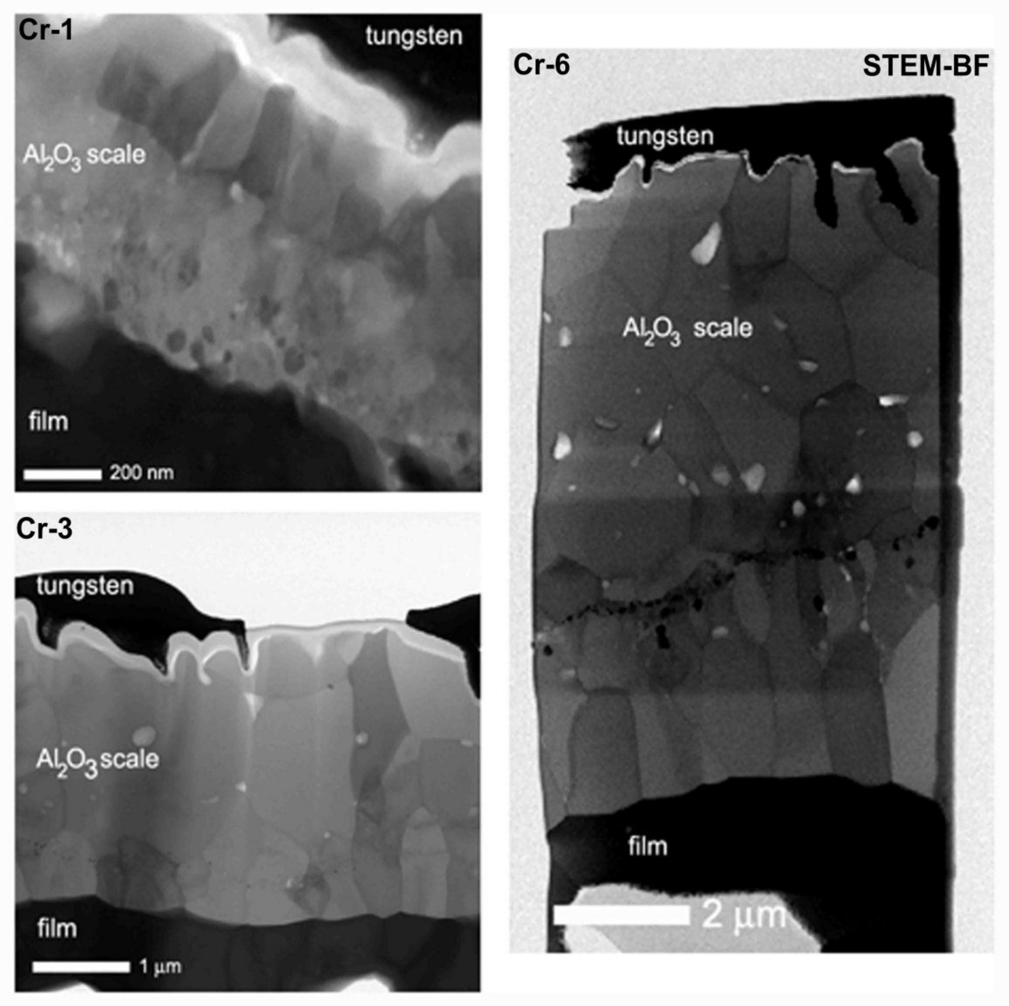

Figure 7.45 STEM BF images of the oxide scale on the Cr-1, Cr-3 and Cr-6 specimens.

A short summary of the investigation result for oxidised Cr_2AlC thin films is presented in table 7.3.

Table 7.3 Short summary of the investigation result for Cr_2AlC thin film oxidised at 1320°C in variations of oxidation time.

Oxidised Cr_2AlC thin Films	
Phase identification	Cr_2AlC and minor Cr_3C_2 are found in Cr-1 and Cr-3. Cr_7C_3 phase is also found in Cr-6
Disolved chromium	There is dissolved chromium in the alumina scale found in Cr-1
Cr-C precipitates	• Cr-C precipitates are found in oxide scale for all specimens • The Cr-C precipitates locations move higher with the increasing oxidation time
Pores in the film	Pores increase with the increasing oxidation time

7.2.2. Fe-Cr-Al model alloys

Two different Fe-Cr-Al model alloys specimens, the F and J-batches were investigated in this present work. The F-batch specimens were oxidised at 1200°C in variations of 1, 8 and 100 hours oxidation time. On the contrary, the J-batch specimens were oxidised in the same oxidation time but at different temperature at the range of 1050 – 1200°C. Moreover, there are two types of J-batch specimens which were investigated based on their specimen thickness, one with specimen thickness of 0.3 mm and the other with 1.3 mm thickness. A detail specimen description can be found in section 5.7. In this section, investigation results of microstructure and phase identification and also analytical investigations by means of microscope electron are presented.

7.2.2.1. SEM and TEM investigation results of F-batch specimens

Figure 7.46 shows SEM-BSE image of cross sections for the F-batch of Fe-Cr-Al model alloys. Since the specimens with oxidation time of 1 and 8 hours (F1H and F8H) have oxide scale of less than 1 µm and 3 µm respectively, the SEM cross-section image we present here is only for the specimen oxidised at 100 H (F100H). The cross section image shows that the oxide scale consists of pores and precipitates. The precipitates are distributed in the whole scale which has a wavy interface.

Furthermore, STEM dark-field (DF) images of the oxide scale from the F-batch specimens show that the oxide scales of those specimens have almost similar grain morphology (see figure 7.47). For specimen F1H and F8H, the grains are mainly columnar with small equaxial grains in the upper part of the scales. With the increasing oxidation time, the grains at lower part of the scales tend to be randomly oriented as seen in figure 7.47 (c). Pores (marked by black arrows) started to be found in scale of specimen F8H. The area marked by red rectangular shows that in the F8H specimen, the precipitates have not grown in the grain boundary but rather inside the grain (see figure 7.47 (c)).

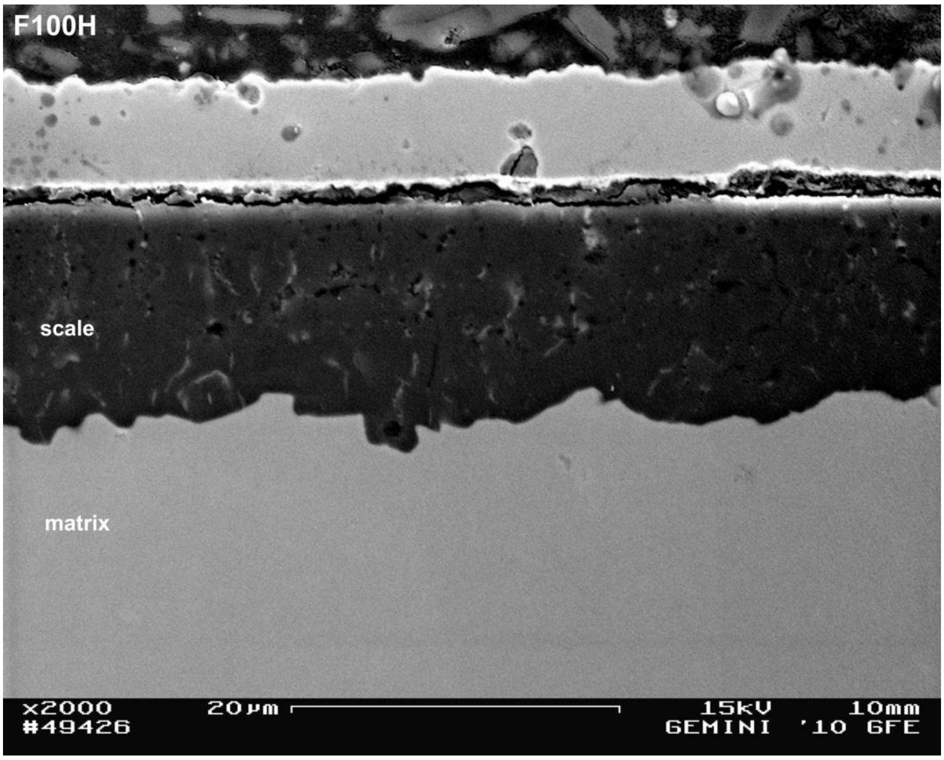

Figure 7.46 SEM-BSE image of cross section of batch F100H Fe-Cr-Al model alloys which was oxidised in air at 1200°C for 100 hours.

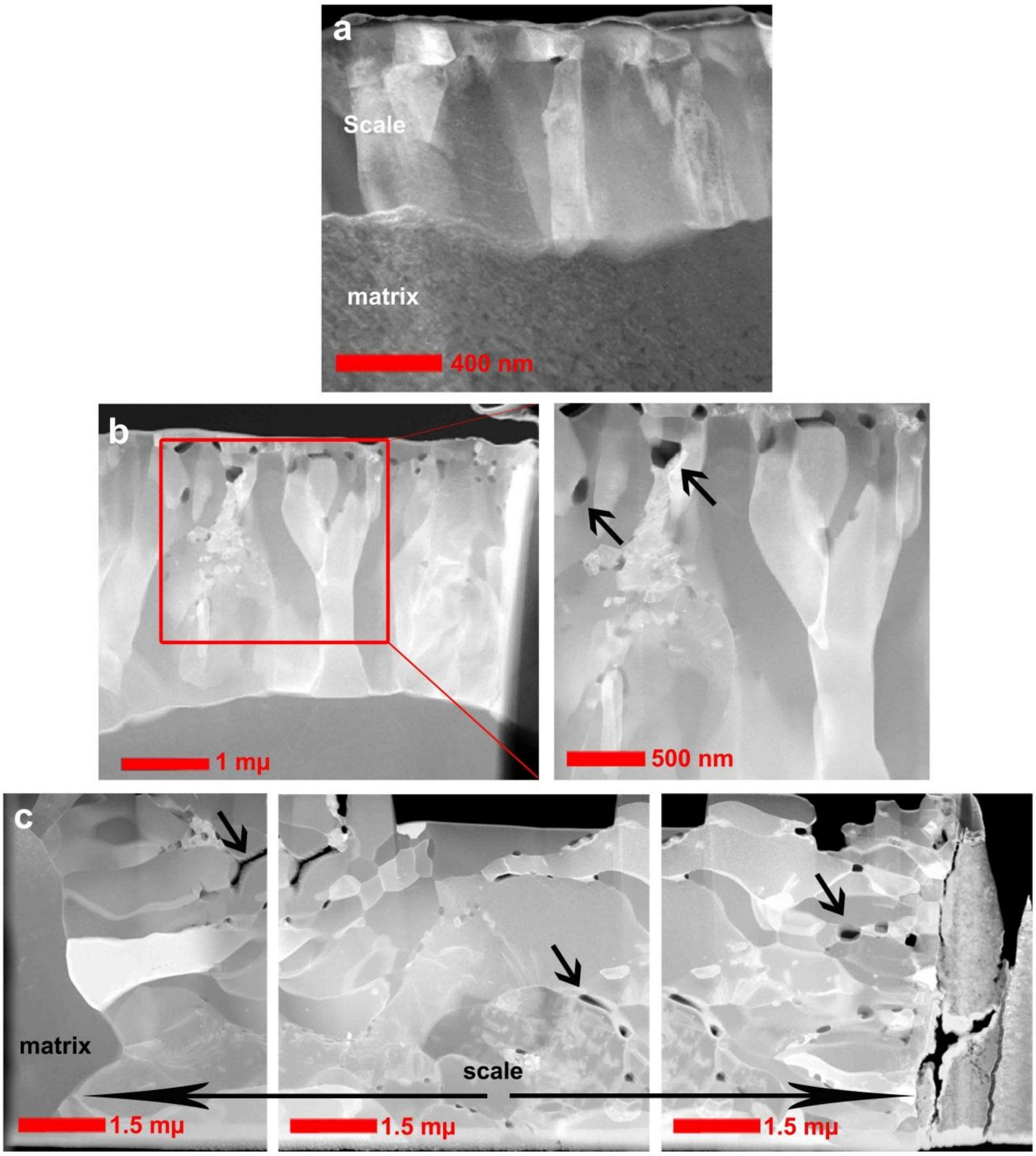

Figure 7.47 STEM-DF images of cross section (a) F1H, (b) F8H and (c) F100H for each specimen which were oxidised for 1, 8 and 100 hours. Red rectangular and arrows indicate the magnification area and pores respectively.

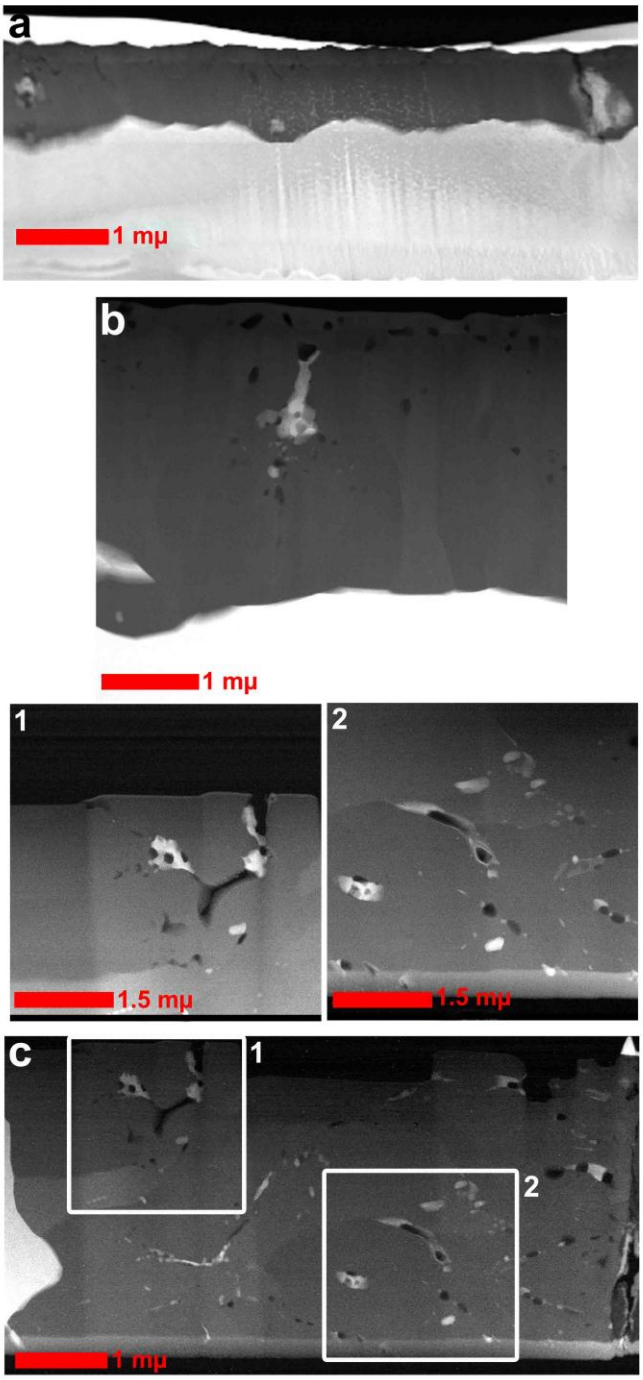

Figure 7.48 STEM HAADF images of specimens F1H, F8H and F100H showing the distribution of precipitates in alumina scale.

STEM-HAADF images in figure 7.48 show the precipitates distribution in the oxide scale. The F1H and F8H specimens consist of minor amount of precipitates and located mainly in the upper part of the oxide scale. For specimen 100 H, in the contrary, a number of precipitates and pores are found in the oxide scale. The precipitates are distributed in the upper and also inner part of the oxide scale. Naumenko et al. have reported from XRD patterns that the precipitates that could be present are either monoclinic or tetragonal ZrO_2 [148]. The STEM-HAADF images have also revealed that there are precipitates which have formed together with pores as well as without pores.

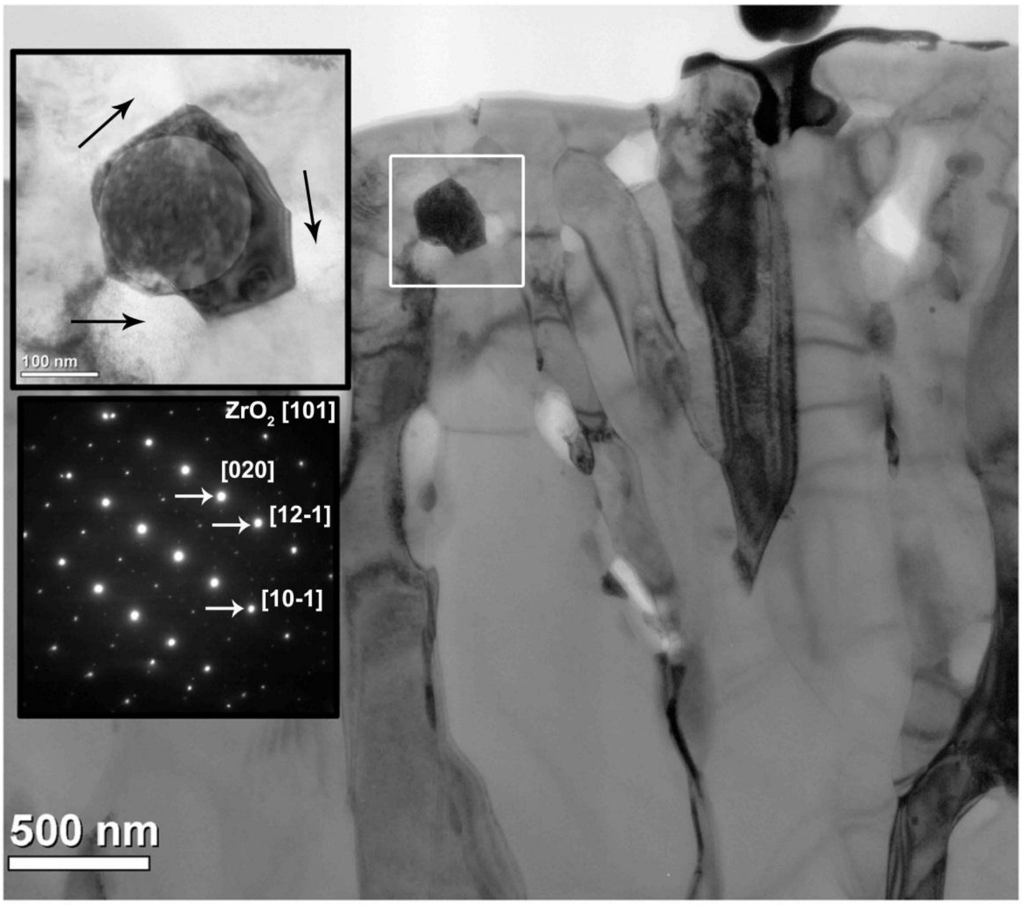

Figure 7.49 BF image of a cross section of F100H specimen and SAED pattern (inset) taken from precipitate located near the pores (marked by black arrows). Phase identification has revealed the tetragonal ZrO_2 presence in the precipitate.

The SAED patterns taken from precipitates locate near the pores show that the precipitates contain tetragonal ZrO_2 (see figure 7.49). Furthermore, in the SAED analysis for precipitates locate outside the pores, two possibilities of phase presence were identified, which are tetragonal ZrO_2 and/or Y_2O_3 (see figure 7.50).

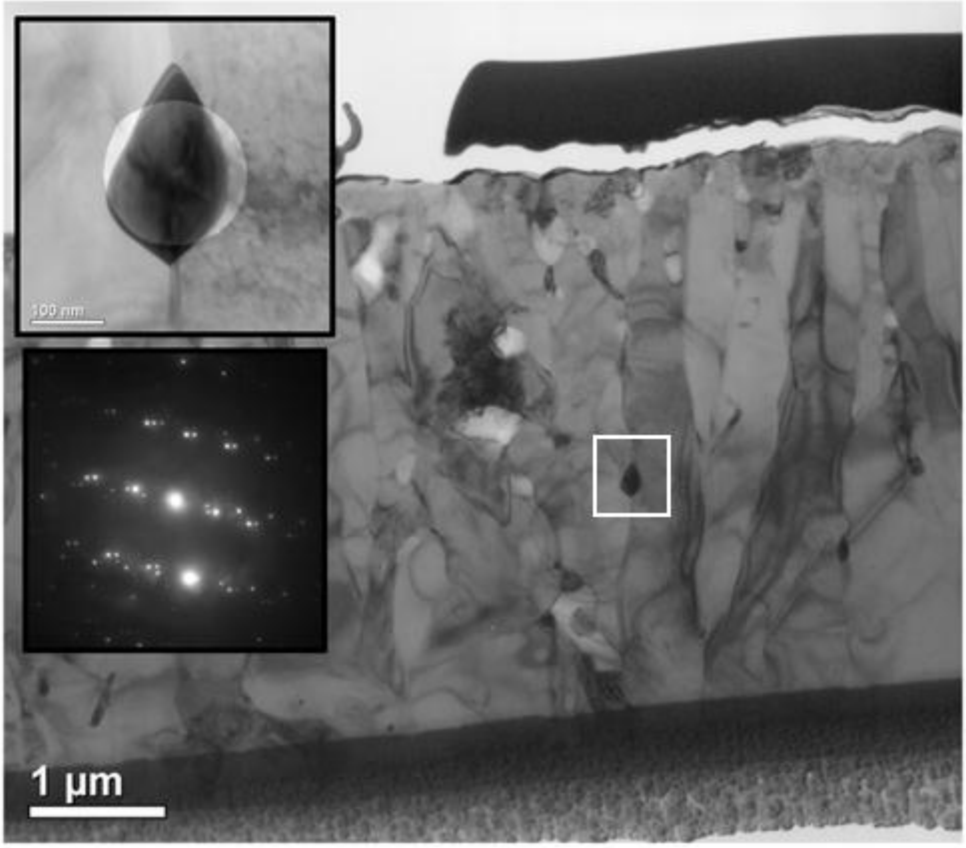

Figure 7.50 BF image of a cross section of F100H specimen and SAED pattern (inset) taken from precipitate marked by white rectangular.

For verification of the phase identification from SAED analysis, STEM-HAADF EDX line scans and elemental mapping have been used to disclose the phases present in the specimens. Figure 7.51 shows STEM-HAADF and EDX line scan results for F1H specimens which confirm that only Zr or together with a very small amount of Y is detected in the precipitates. At the matrix, the same precipitate is also found near the oxide scale interface. This information agrees very well with the phase identification results received by SAED.

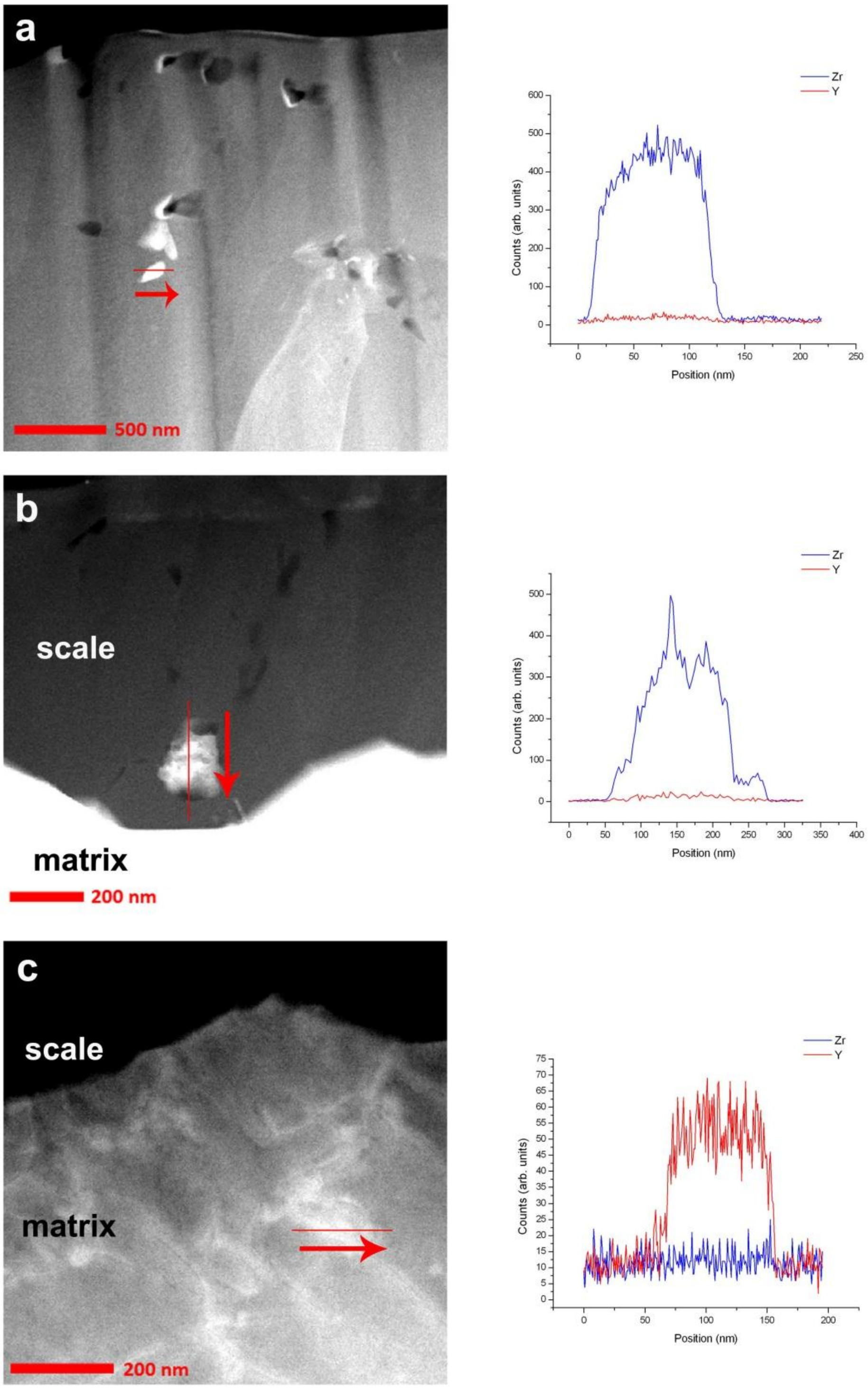

Figure 7.51 STEM-HAADF images and EDX line scan profiles of the precipitates located in the oxide scale ((a) and (b)) and in the matrix (c) for F1H specimens. Only Zr and small amount of Y are found in the precipitates.

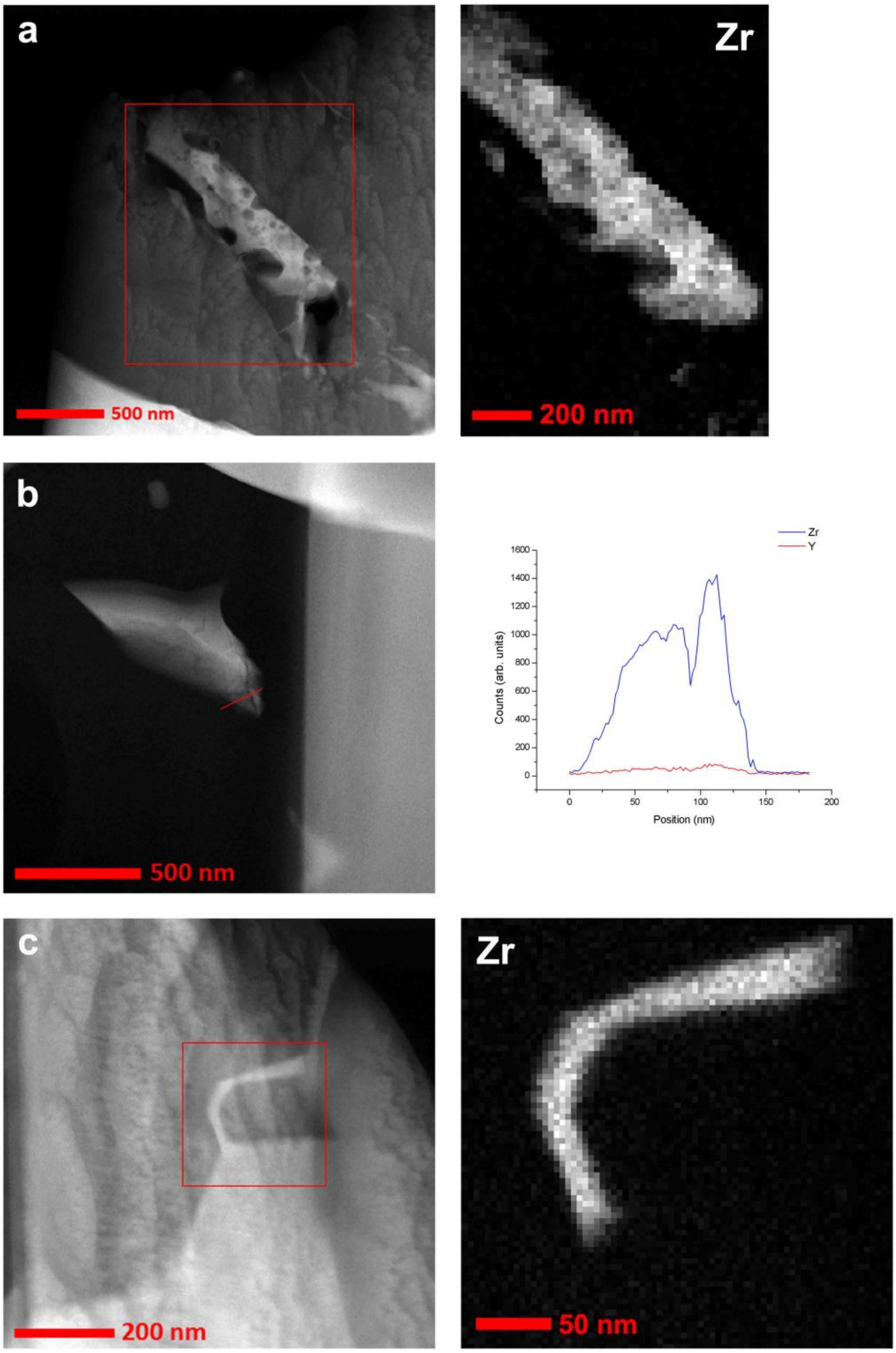

Figure 7.52 STEM-HAADF images with EDX line scan profiles and image mapping for corresponding images for the precipitates located in the oxide scale ((a) and (b)) and in the interface (c) for F8H specimen. Similar to the F1H specimen, only Zr and possibly Y are found in the precipitates.

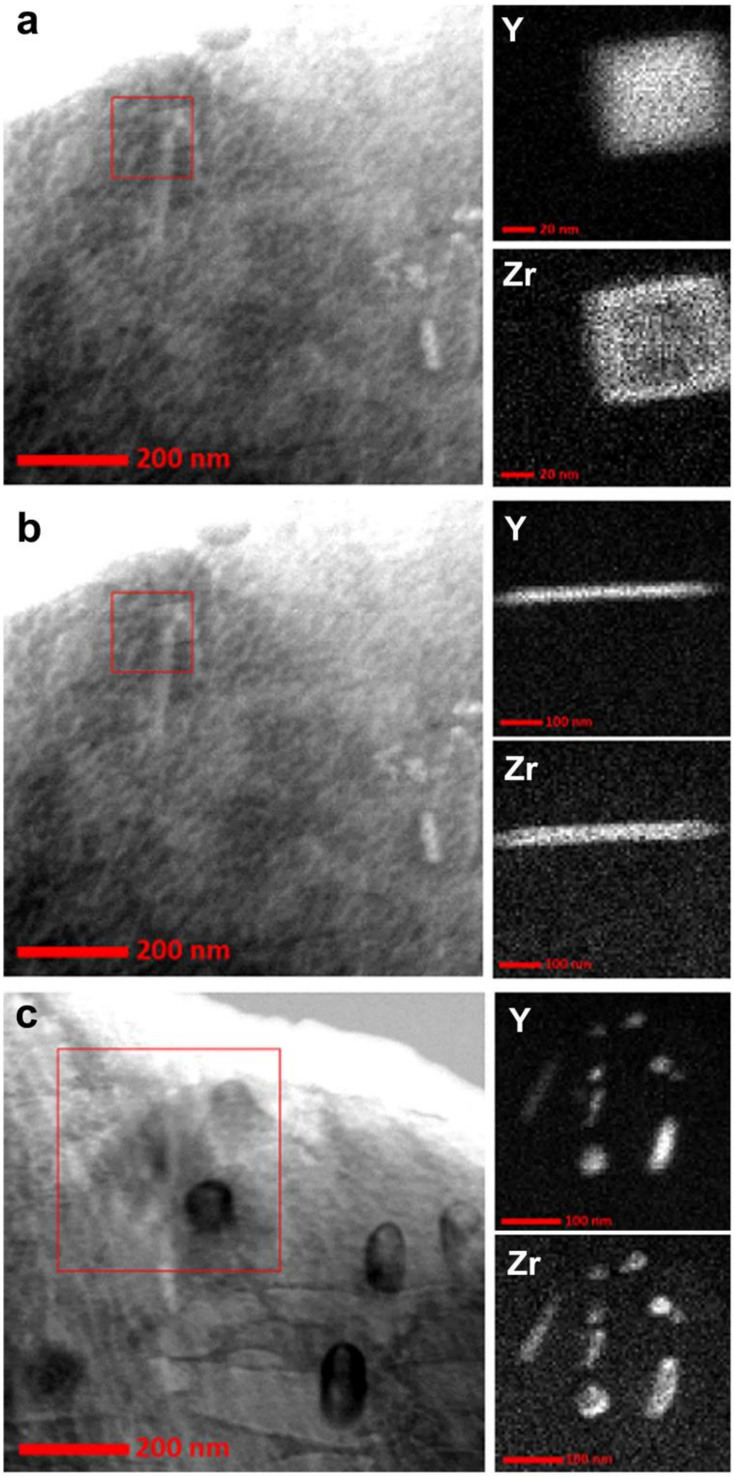

Figure 7.53 STEM-HAADF images and EDX elemental maps of the precipitates located in the matrix for F8H specimen. Similar to the F1H specimen, only Zr and possibly Y are found in the precipitates.

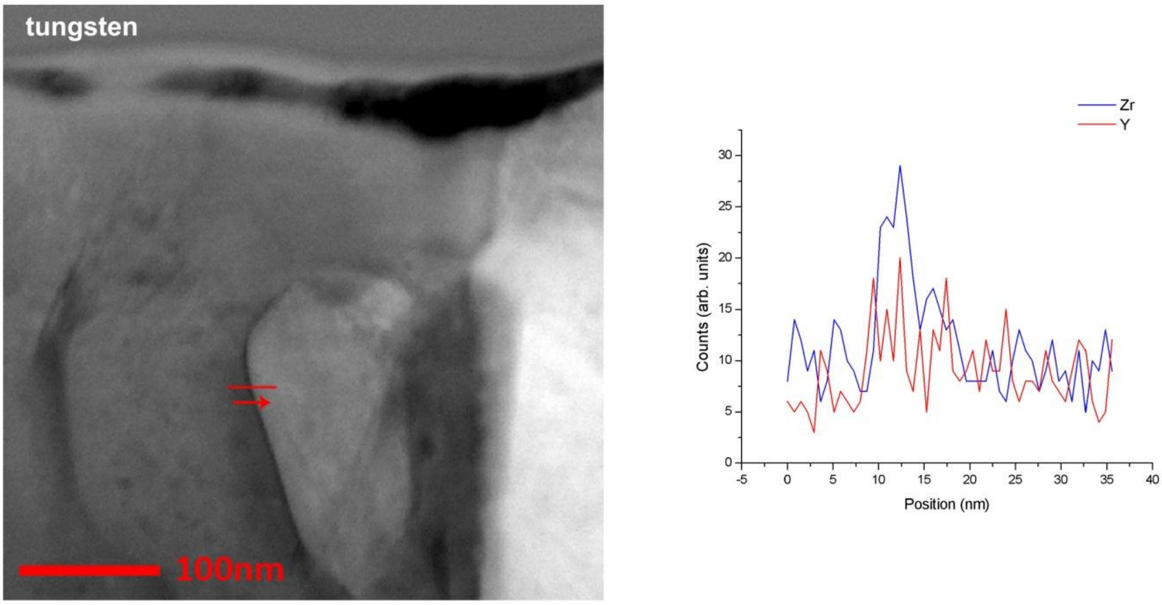

Figure 7.54 STEM-BF image and EDX line scan profiles across the grain boundary of F8H specimen. Both Zr and Y are detected on the grain boundary.

Figure 7.52 and 7.53 show the STEM and EDX analysis of specimen F8H. Similar to the precipitates which are found in F1H specimen, Zr containing precipitates with a possibility of small amount of Y are detected on the oxide scale. Moreover, in the matrix, significant Zr and Y containing precipitates are detected. This suggested the possibility for the formation of mixed Zr/Y oxide in the matrix. The Zr/Y precipitates are also found in the oxide scale grain boundary. As seen in figure 7.54, STEM-BF image of oxide scale grain with an EDX line scan has been performed across the grain boundary which has revealed that both Zr and Y elements are detected.

Figure 7.55 and 7.56 show STEM and EDX analysis of specimen F100H. Here, the Y concentration has clearly been seen in the precipitates with no pores around them (see figure 7.55 (c)). On the matrix, similar finding as in F8H specimen, the mixed of Zr/Y precipitates are detected by EDX elemental mapping and line scan.

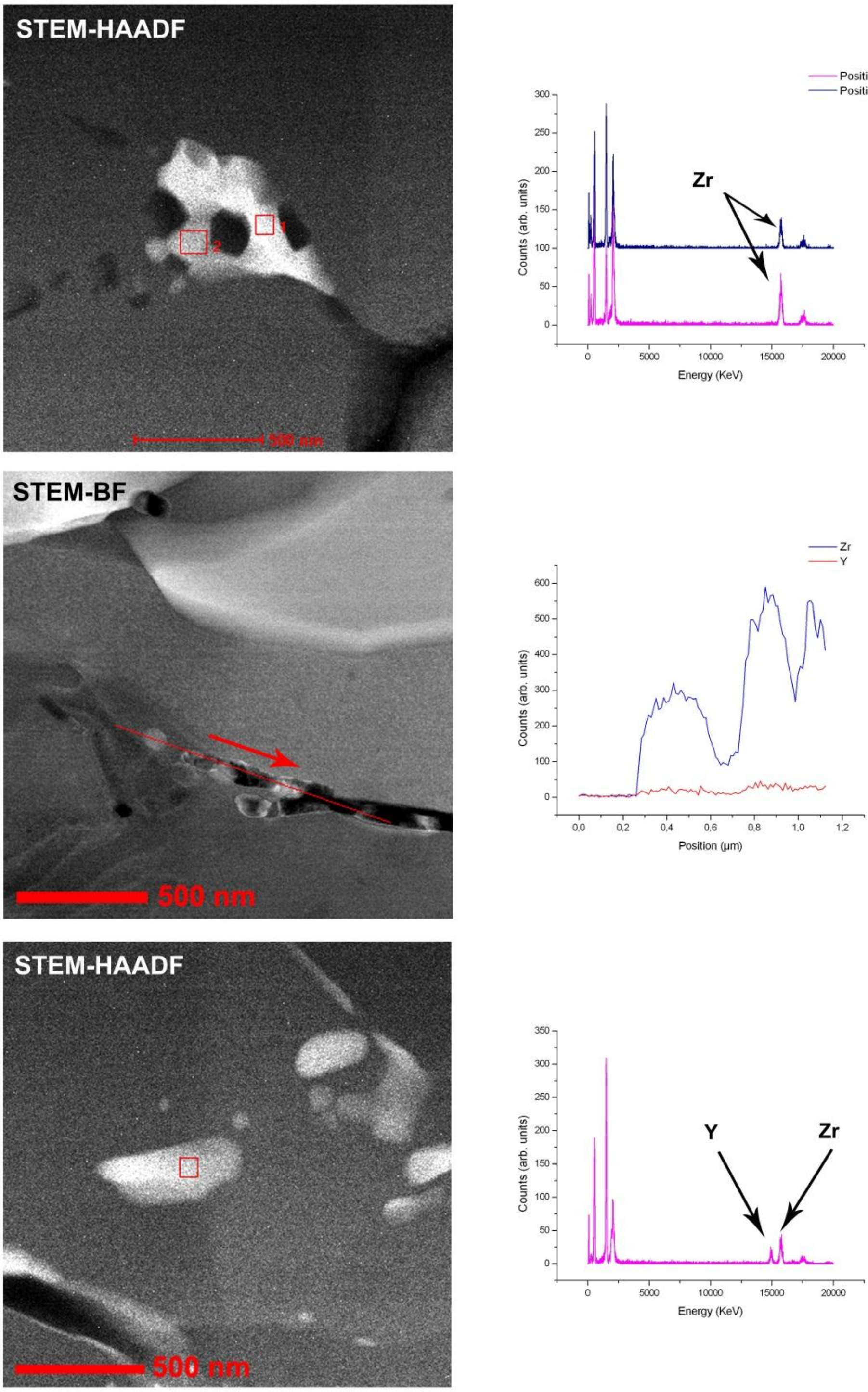

Figure 7.55 STEM-HAADF and BF images with the corresponding EDX analyses of the precipitates located in the oxide scale for F100H specimen. Different elements are detected by EDX analysis.

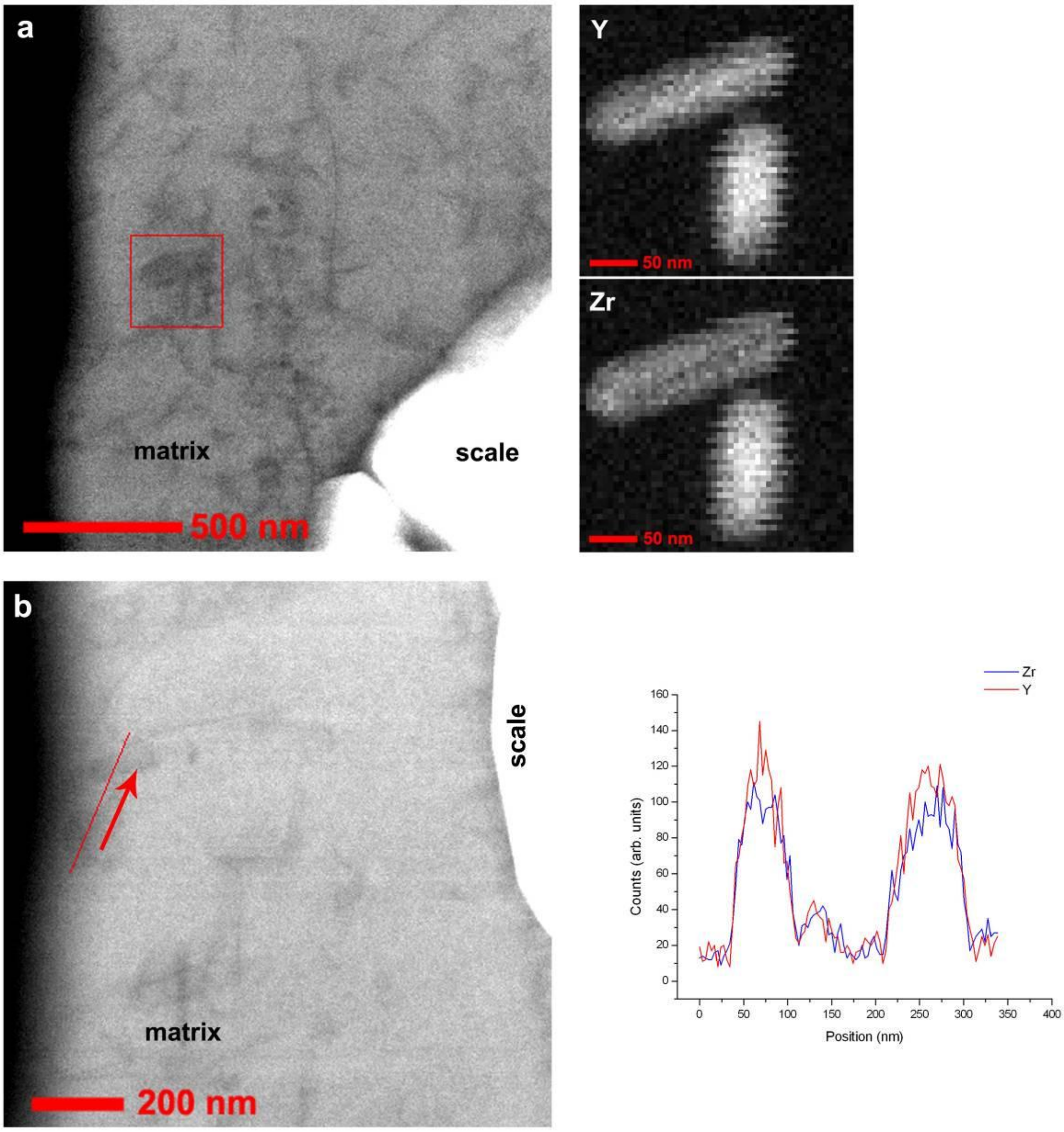

Figure 7.56 STEM-HAADF images, EDX line scan profiles and elemental maps of the precipitates locate in the matrix scale for F100H specimen. Both Y and Zr are detected in precipitates by EDX spectra.

7.2.2.2. SEM and TEM investigation results of J-batch specimens

The SEM-BSE images of cross sections of two types of J-batch specimens are presented in figure 7.57 and 7.58. In general, the thin specimens contain less precipitates than the thick specimens on their alumina scales. Furthermore, thick specimens have more precipitates near the interface than the thin specimens. Besides pores which are found on the scale, SEM-BSE images have also revealed morphological differences at the interfaces. The interfaces of the thick specimens are wavier than the thin specimens.

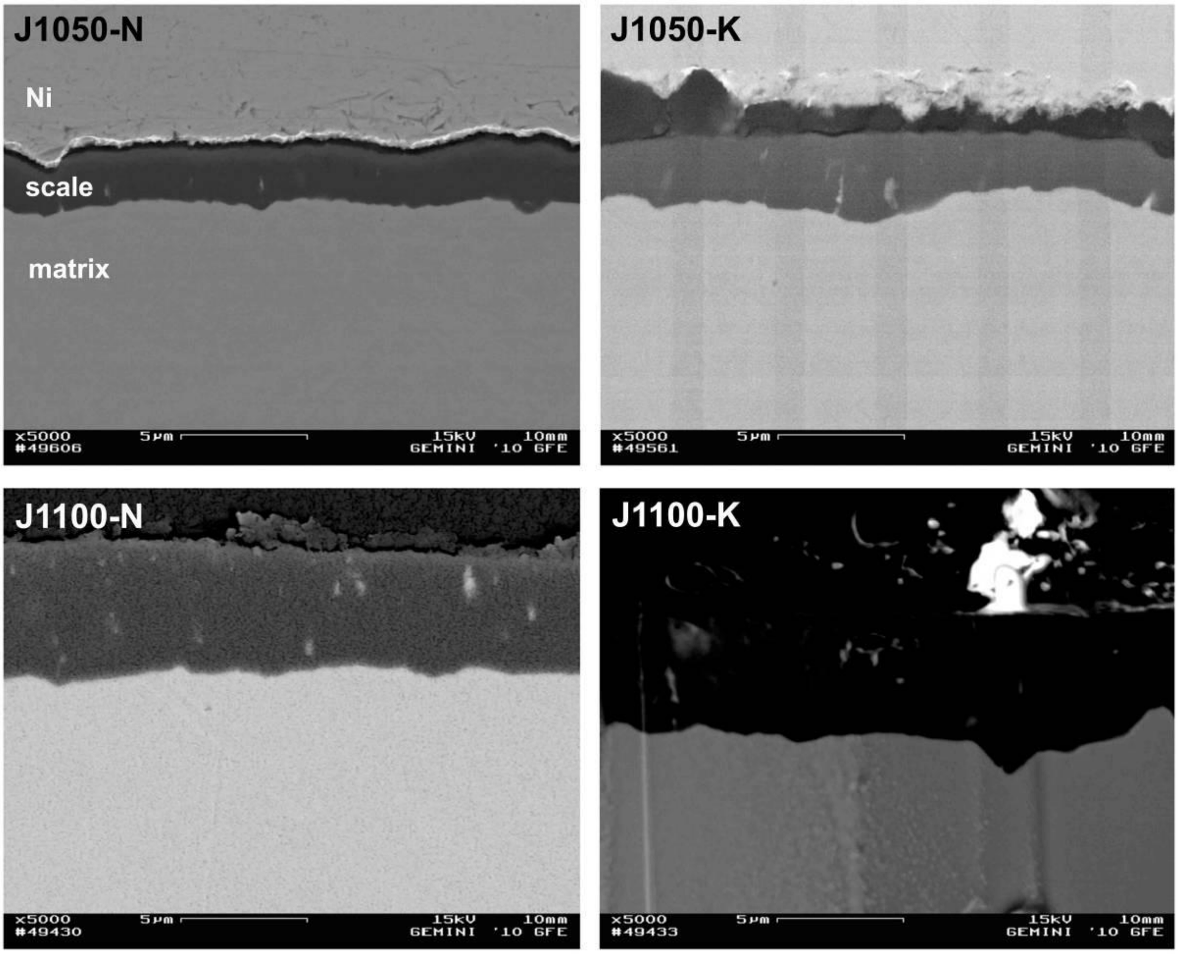

Figure 7.57 SEM-BSE images of cross section of thin and thick specimens oxidised at 1050 and 1100°C (J1050N/K and J1100N/K) for 100 hours.

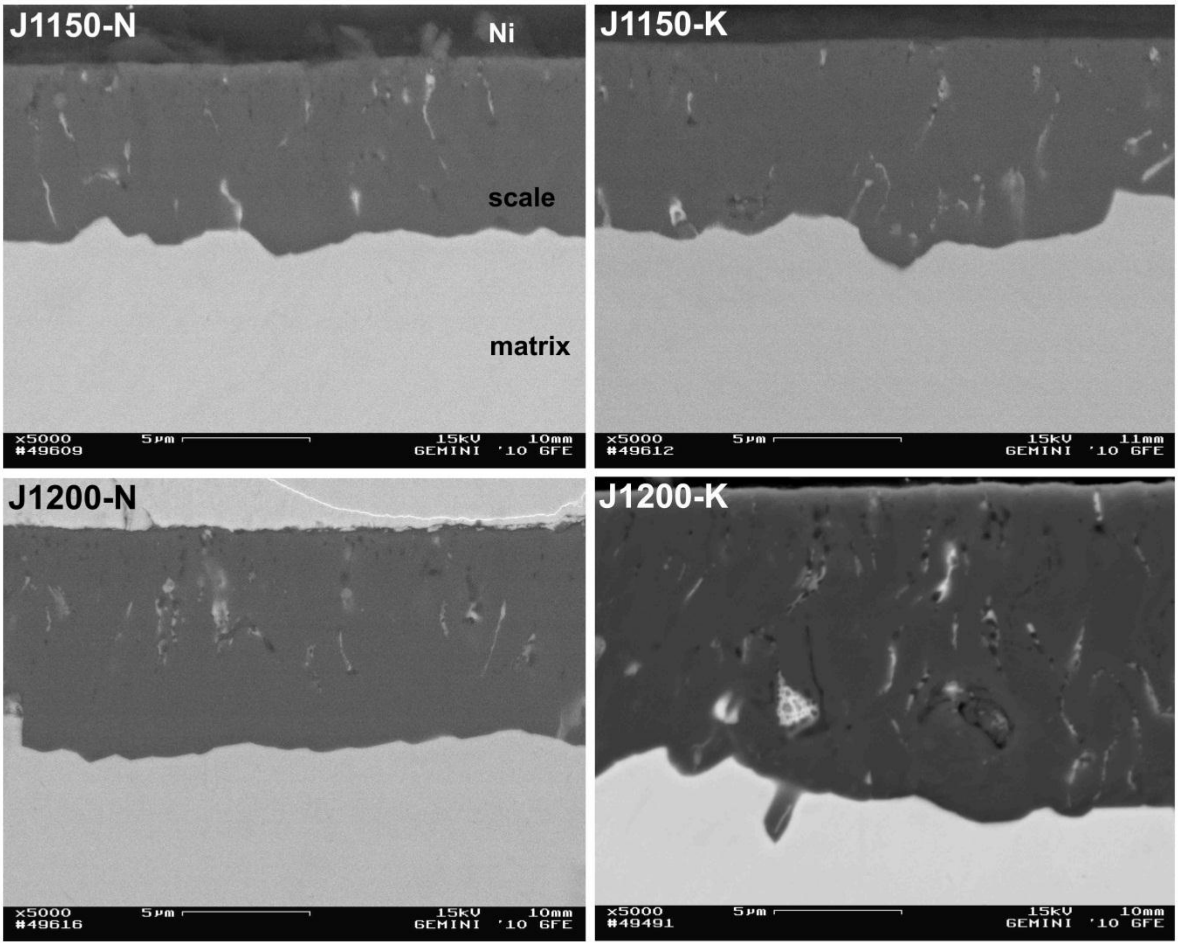

Figure 7.58 SEM-BSE images of cross section of thin and thick specimens oxidised at 1150 and 1200°C (J1150N/K and J1200N/K) for 100 hours.

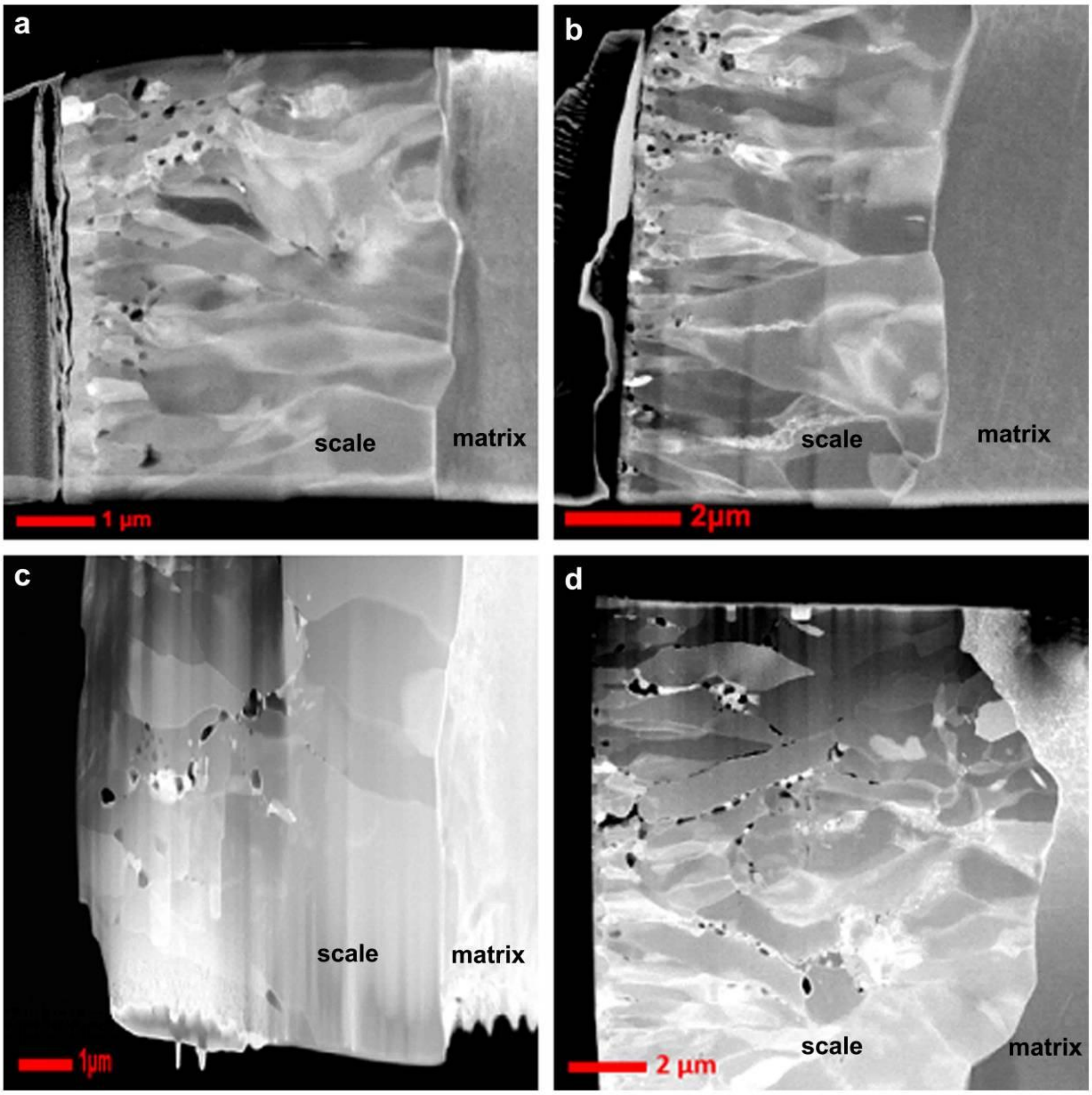

Figure 7.59 STEM-DF images of (a) J1100-N, (b) J1100-K, (c) J1200-N and (d) JJG1200-K. The grains have similar morphology to the F100 specimen.

Based on oxidation experiments and the microstructure overview showed by the SEM-BSE images, only selected J-batch specimens have been further investigated by TEM. Figure 7.59 shows STEM-DF images of the oxide scale from the J-batch specimens. The oxide scales of those specimens have almost similar grain structures with the F-batch specimens. Furthermore the STEM-HAADF images have also revealed precipitates distribution in oxide scale (see figure 7.60). The precipitates in thin specimens, J1100K and J1200K, look different from the thick specimens.

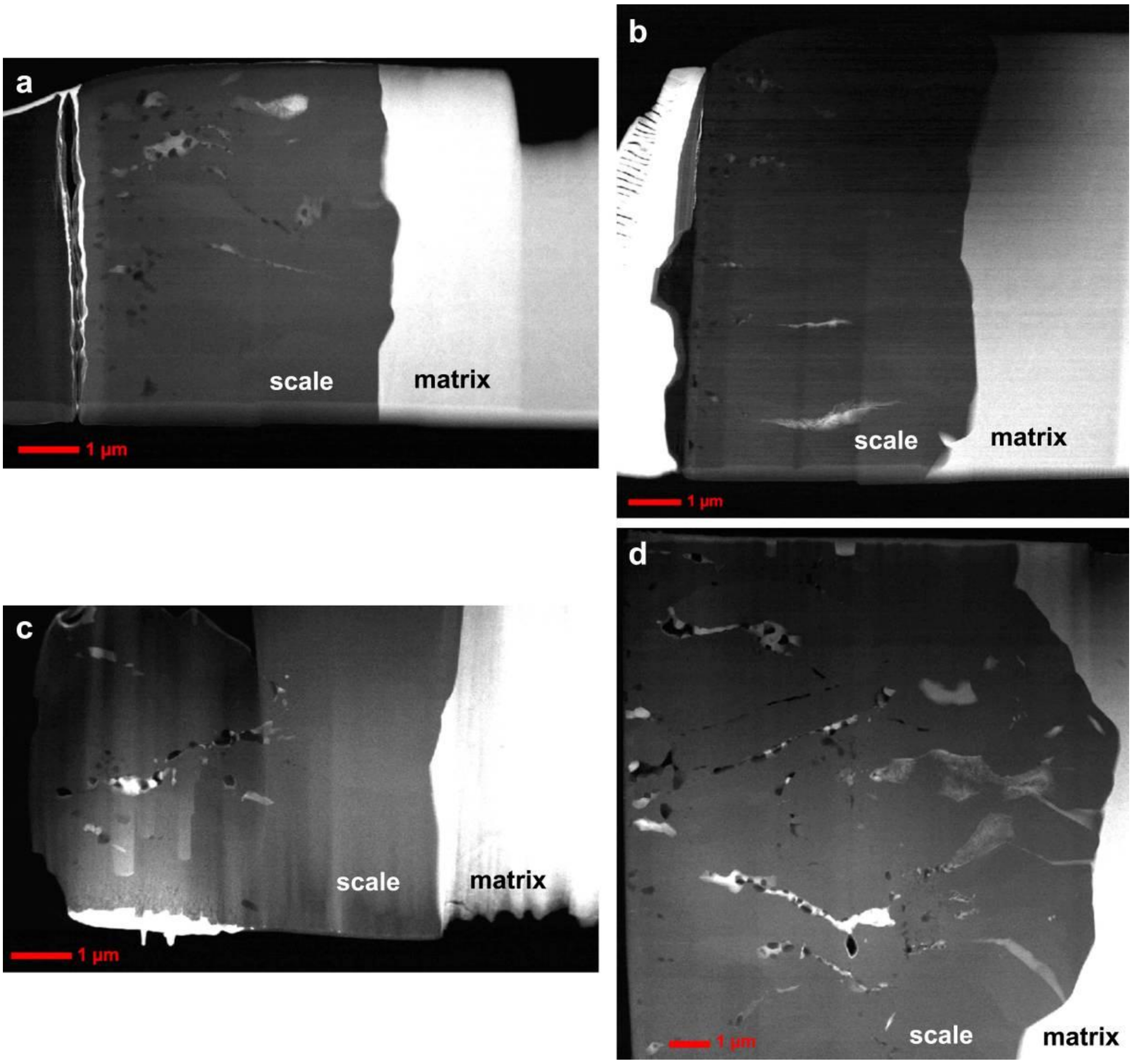

Figure 7.60 STEM-HAADF images of (a) J1100-N, (b) J1100-K, (c) J1200-N and (d) JJG1200-K showing the precipitations distribution in oxide scale.

Figure 7.61 shows BF images with SAED patterns as the insert from two different precipitates, base on the pores presence around the precipitates, in the oxide scale. Phase identification results have revealed that similar phases identified in the F-batch specimen have also been observed in the J-batch specimen (J1200-K).

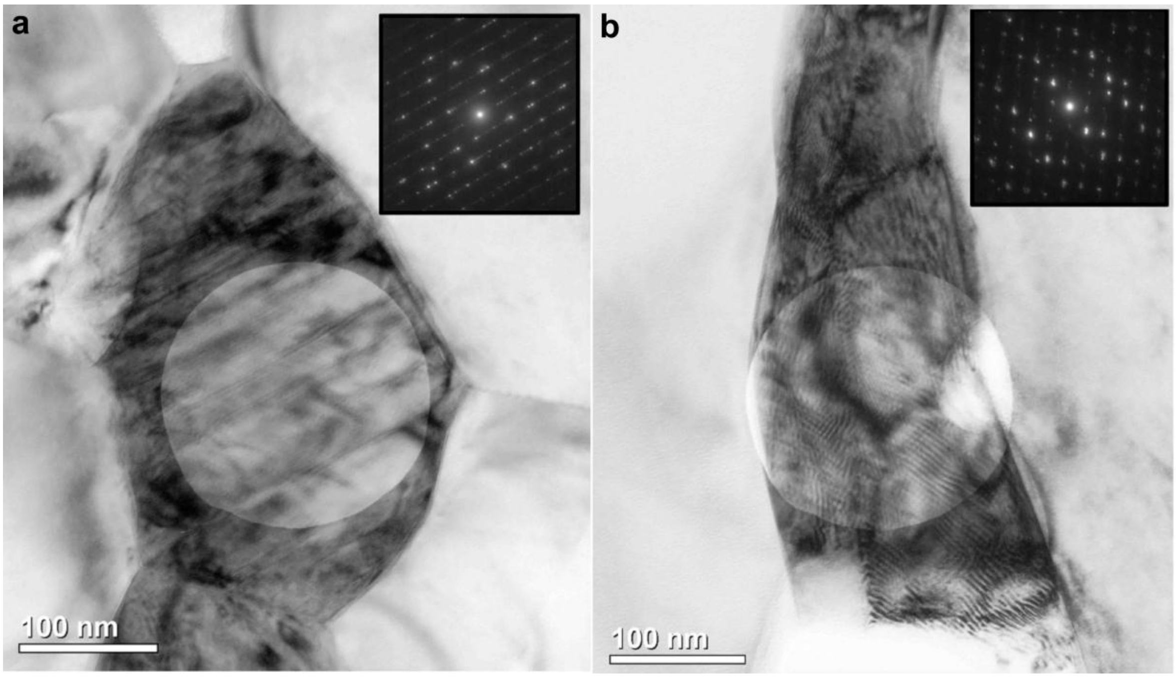

Figure 7.61 BF images of cross section and SAED patterns (insert) of J1200-K specimen taken from precipitates located near the pore (a) and (b) located on area without pores.

STEM-HAADF EDX elemental mapping of J-batch specimens has revealed that Zr dominates the precipitates found in the oxide scale. Furthermore, the EDX analysis shows that precipitates near the pores contain less Y than the precipitates located in the area without pores (see figure 7.62). Figure 7.63 shows the STEM-HAADF and EDX elemental maps of precipitates found in the matrix. The precipitates, which have needle-like morphology, contain yttrium and a small amount of zirconium.

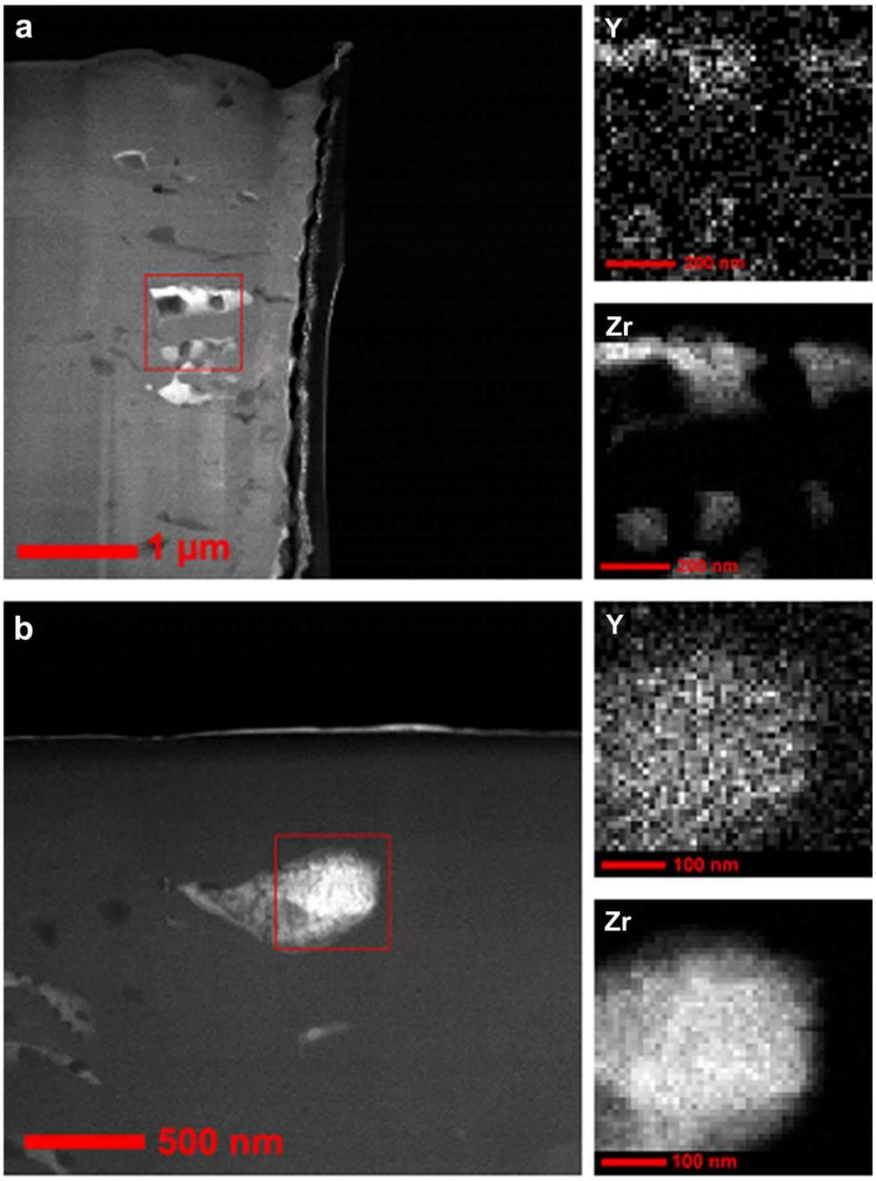

Figure 7.62 STEM-HAADF images and EDX elemental maps of precipitates located on the scale for J1100-N specimen.

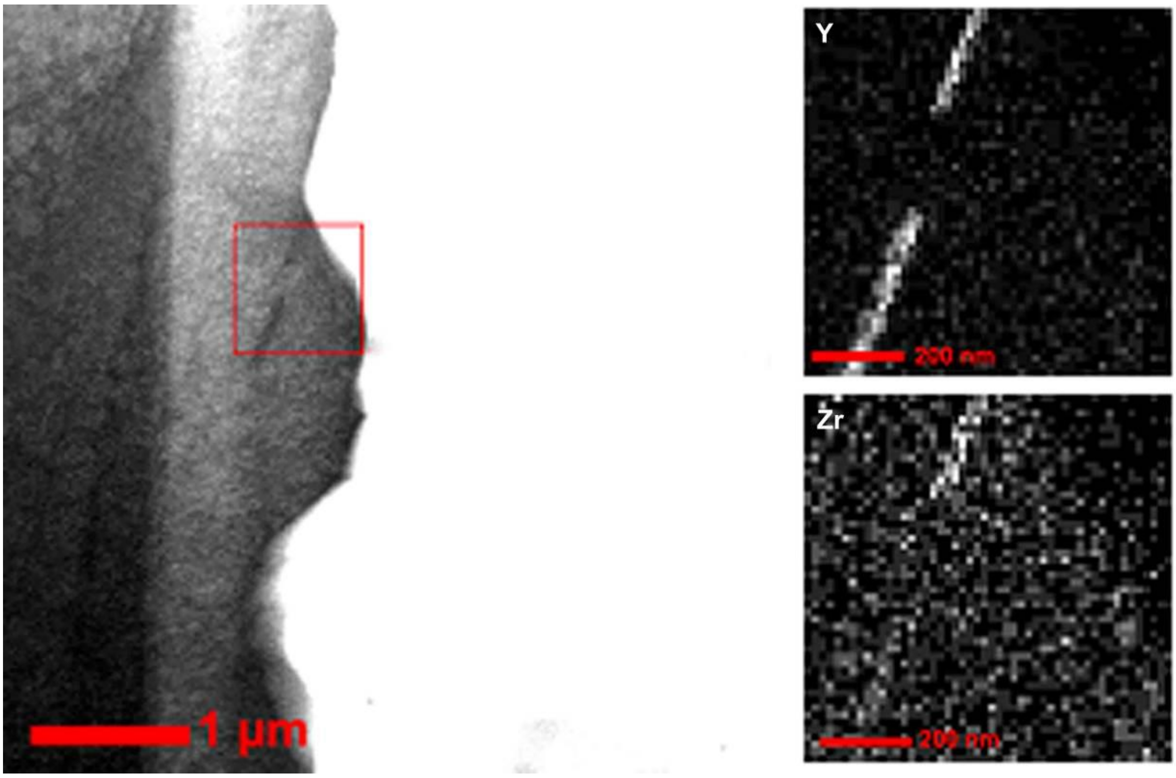

Figure 7.63 STEM-HAADF image and EDX elemental maps of precipitates located in the matrix of J1100-N specimen.

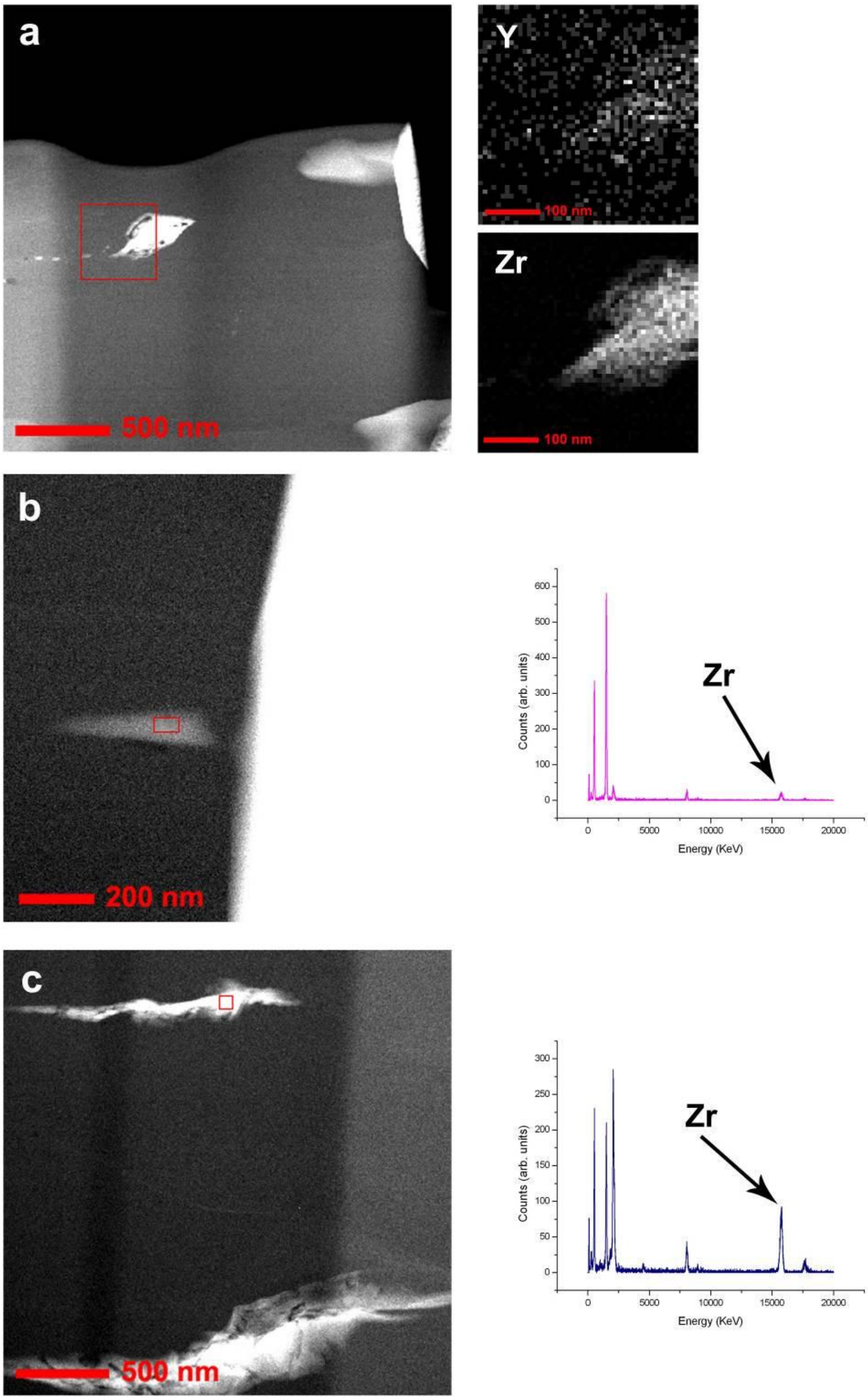

Figure 7.64 STEM-HAADF images and EDX analyses of precipitates located on the oxide scale for J1100-K specimen.

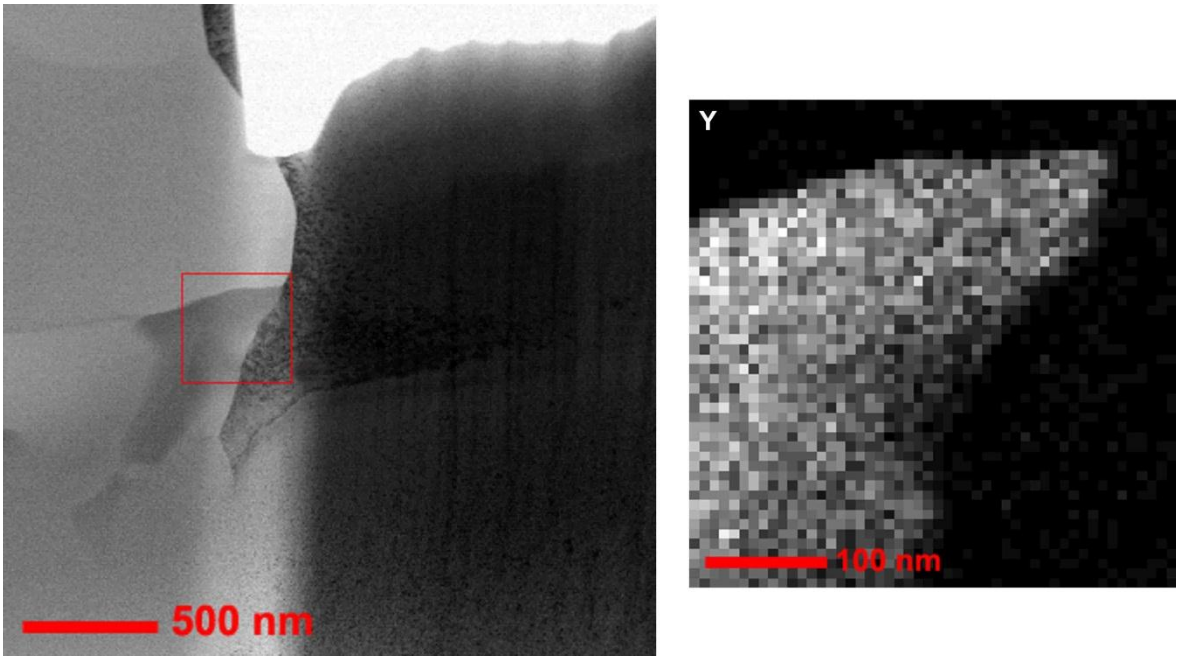

Figure 7.65 STEM-HAADF image and EDX elemental map of precipitates located on the interface for J1100-K specimen.

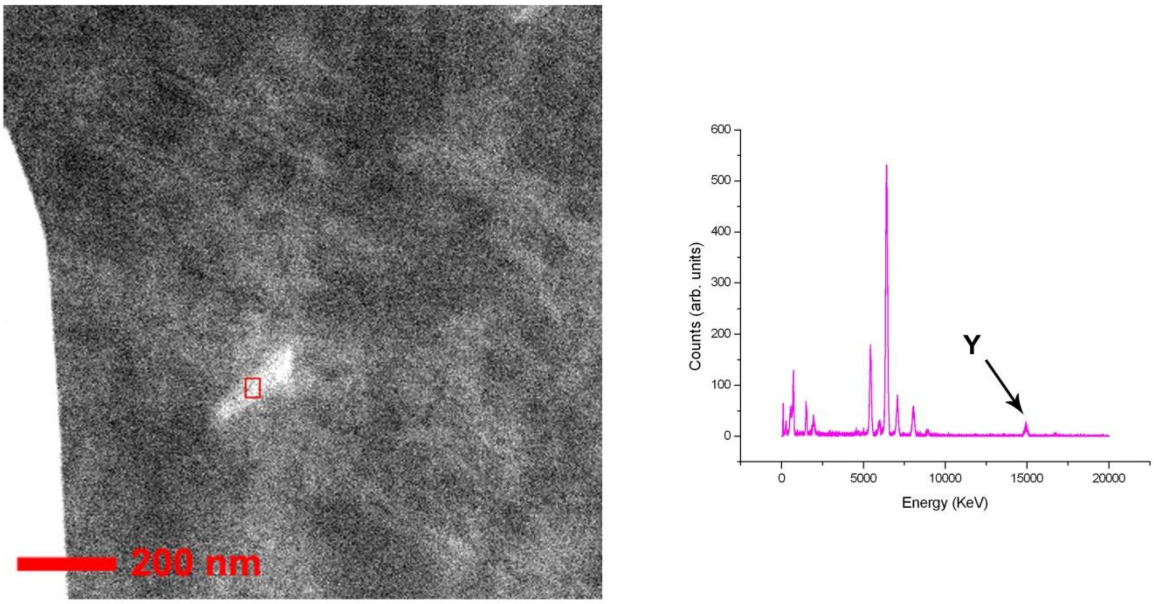

Figure 7.66 STEM-HAADF image and EDX spectrum of precipitates located on the matrix for J1100-K specimen.

Our EDX analysis on J1100-K specimen can only find Zr containing precipitates on the oxide scale (see figure 7.64). Similar to the thin specimen oxidised at 1100°C, the Y precipitates are found in scale interface and matrix (see figure 7.65 and 7.66).

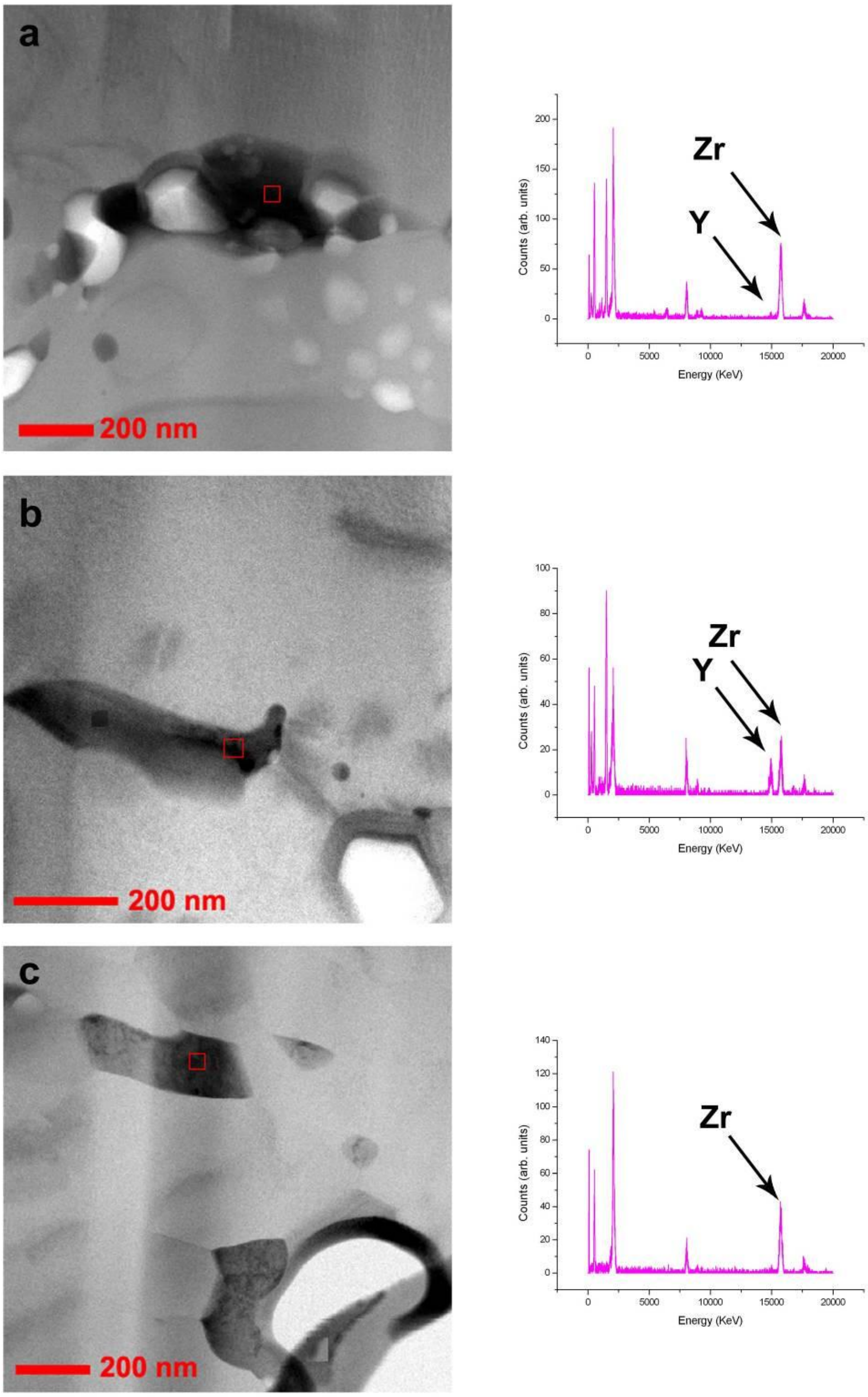

Figure 7.67 STEM-BF images and EDX spectra of precipitates located on the oxide scale for J1200-N specimen.

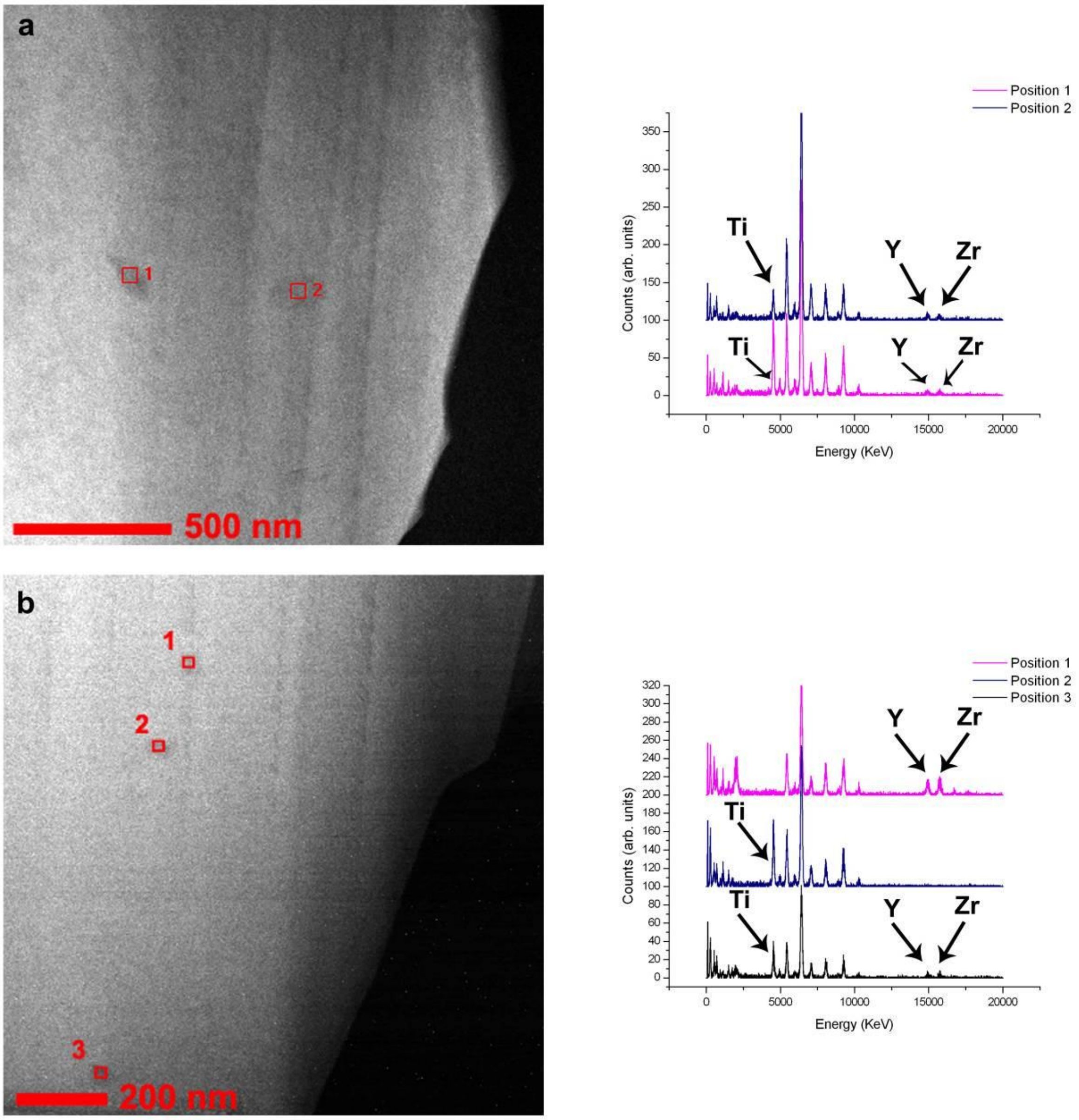

Figure 7.68 STEM-HAADF images and EDX spectra of precipitates located on the matrix for J1200-N specimen.

Similar EDX analysis results for J1200N specimen are found. Figure 7.67 shows the STEM-BF images and EDX spectra for precipitates found in oxide scale of the J1200N specimen. Based on this result, those precipitates contain Y and Y+Zr. Moreover, since the J-batch specimens contain more titanium than the F-batch specimen, EDX analyses have detected additional Ti in the precipitates found in matrix (see figure 7.68).

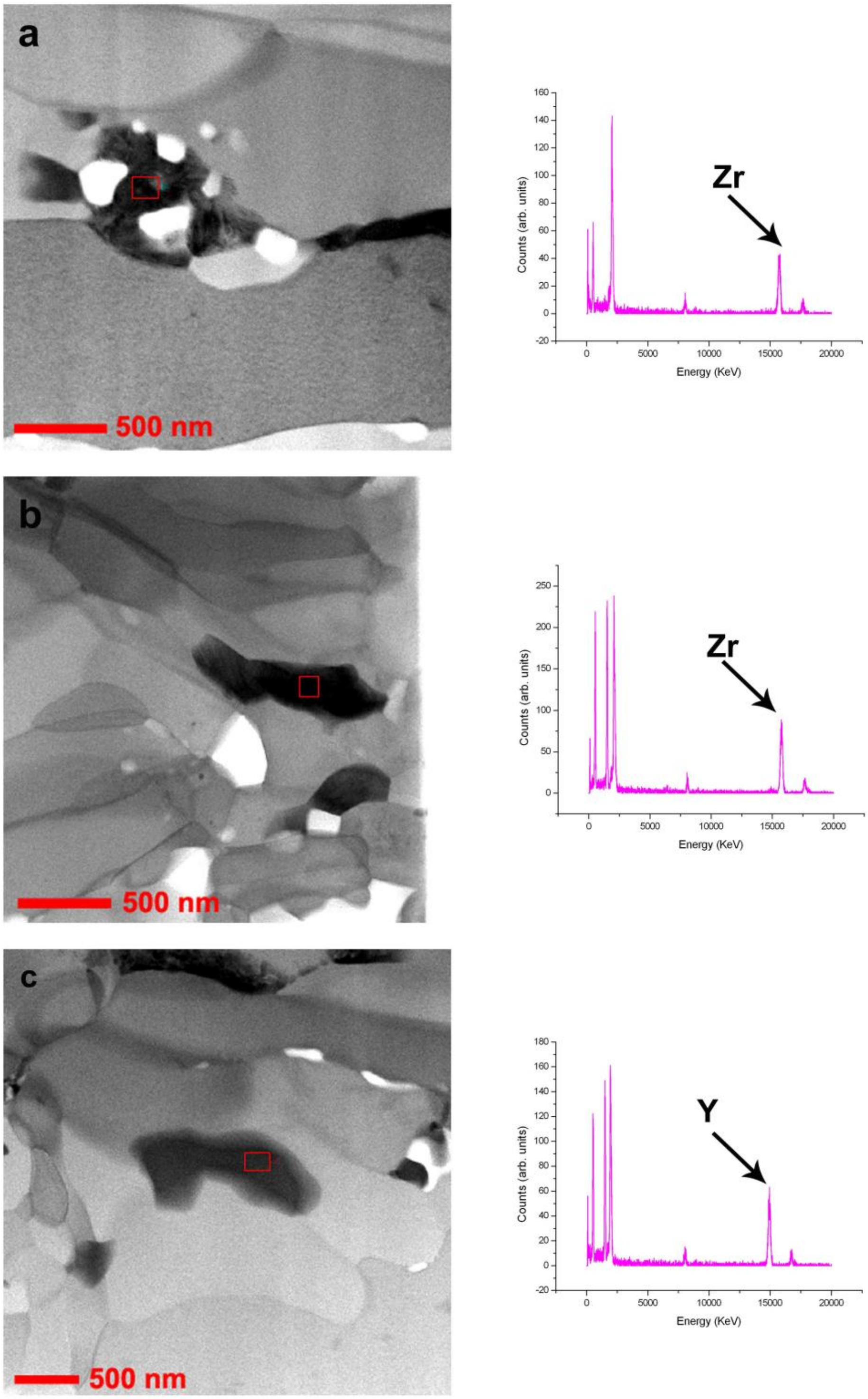

Figure 7.69 STEM-BF images and EDX spectra of precipitates located on the oxide scale for J1200-K specimen.

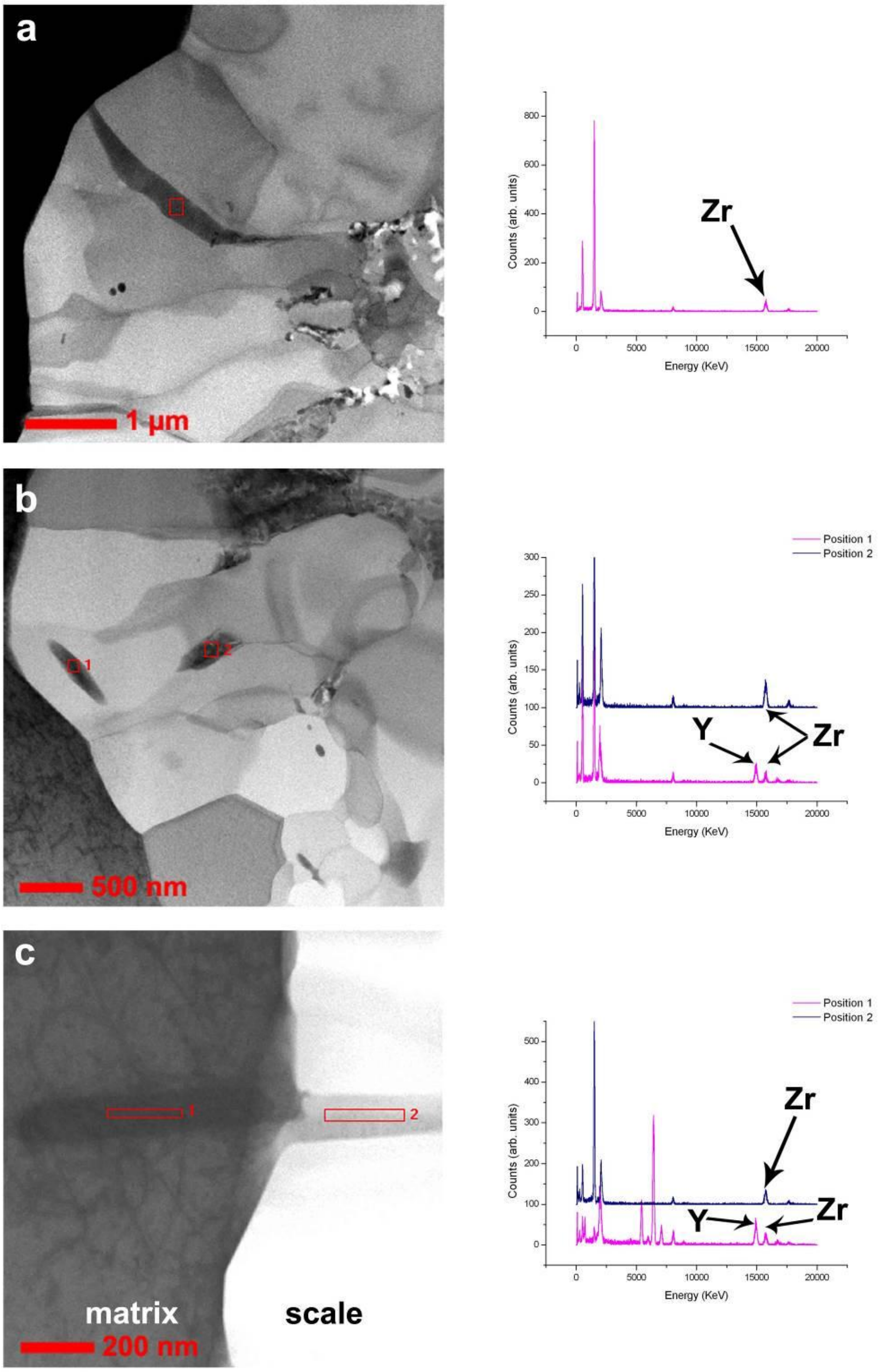

Figure 7.70 STEM-BF images and EDX spectra of precipitates close to scale-matrix interface for J1200-K specimen.

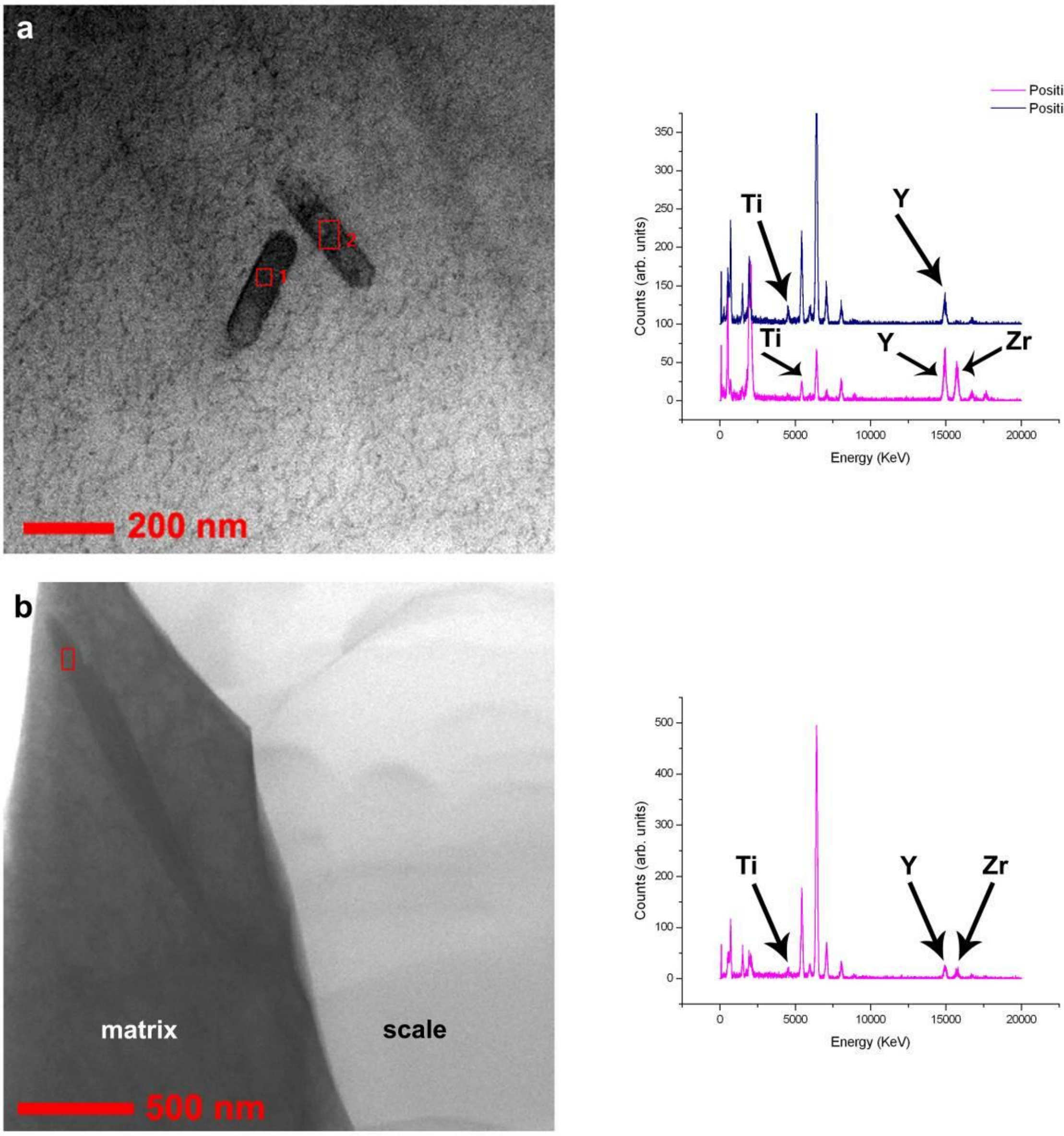

Figure 7.71 STEM-BF images and EDX spectra of precipitates located on the matrix for J1200-K specimen.

Figure 7.69, 7.70 and 7.71 show the precipitates found in oxide scale, interface and matrix of the J1200-K specimen respectively. In this specimen, needle-like precipitates which have grown from matrix to oxide scale are found. EDX analyses have revealed that these precipitates contain Zr (see figure 7.70). Interestingly, there are precipitates that have grown continuously from matrix to oxide scale. A part of the precipitates located in the matrix contain Y and Zr while in the part located in the oxide scale only Zr was detected by EDX (see figure 7.70 (c)). Similar to the J1200-N, titanium containing precipitates are found in the matrix together with Zr and Zr+Y precipitates.

7.2.2.3. Short summary of Fe-Cr-Al model alloys

Both SAED and analytical investigation results indicate the present of Zr and/or Y containing precipitates on the scale and matrix in both batch specimens. More detailed analysis have revealed that when there are pores around the precipitates in the oxide scale, significant Zr elements are detected. This condition is found especially in specimens with short oxidation time (F1H and F8H). At longer oxidation time (F100H) similar condition as found in J-batch specimens is also found in the present work. In this state, the precipitates in the oxide scale contain both Zr and Y.

On the matrix, different precipitates morphology between the two batches is observed. In the F-batch specimen, many morphology types of precipitates are found. On the contrary, most precipitates which are found in the matrix of J-batch specimens have needle-like morphology. Furthermore, since the J-batch specimens contains more titanium than the F-batch specimen, additional Ti containing precipitates are found in the matrix oxidised at 1200°C.

8 Discussion

In this chapter, the growth mechanisms of both Ti_2AlC and Cr_2AlC MAX phases will be discussed first based on the results from previous chapter. The discussion of the microstructure evolution due to the oxidation test of both Cr_2AlC thin films and Fe-Cr-Al model alloys will be presented in the next sub chapter.

8.1. The growth mechanisms of Ti_2AlC and Cr_2AlC MAX phases

8.1.1. Ti-Al-C thin film

The deposited Ti-Al-C thin film in this present work contains significant pores on the film (see figure 7.5). SAED and analytical investigations have revealed the presence of Ti_2AlC and minor phases of TiC and Ti_3AlC_2 which have a good correlation with the phase analysis from XRD diffractograms. Furthermore, high-resolution TEM images and the corresponding FFT patterns also show the possibility of phases distribution in the film which indicates that the Ti_2AlC is found through the film while the TiC and Ti_3AlC_2 phases are found in the area near the pores and the upper part of the film respectively.

We use the structure zone model proposed by Movchan & Demchishin and later modified by Thornton [152, 153]. The revised model by Thornton is based on morphologies developed in 20 to 250 µm thick magnetron sputtering coatings of Ti, Cr, Fe, Cu, Mo, and Al deposited at rates ranging from 50 to 20,000 Å/min. The microstructure depends on the substrate temperature and inert sputtering gas pressure which in Thornton experiment ranging from 1-30 mTorr.

At least there are two possibilities to explain the formation of pores during film growth based on the SZM model. First, since our Ti-Al-C thin film was deposited at 850°C (1,123.15 K), 5×10^{-3} mbar (3.75 mTorr) pressure and 270 Å/min of deposition rate, the T_s/T_m is approximately 0.52 (the melting point of Ti_2AlC is ≈ 1,625 ± 10°C [154]. It means, our thin film belongs to SZM 2 ($0.3 < T_s/T_m < 0.5$) although the T_s/T_m is a little bit higher. However, further investigation from Thornton has informed that for $T_s/T_m > 0.5$ and low deposition rate (~ 200 Å/min), large faceted grains separated by voids were frequently observed [155].

The second possibility that can explain the formation of pores during film growth is the surface substrate roughness. Figure 7.14 shows high-resolution TEM image of the Ti-Al-C film interface. From that figure, the substrate surface looks rough. It has been reported by several investigators that the surface roughness will produce more complex morphology and generally a less dense film than on a smooth surface [156-158]. Furthermore, Thornton has found that with substrate surface roughness, the shadowing effect as in Zone 1 could happen even at high values of T_s/T_m [153].

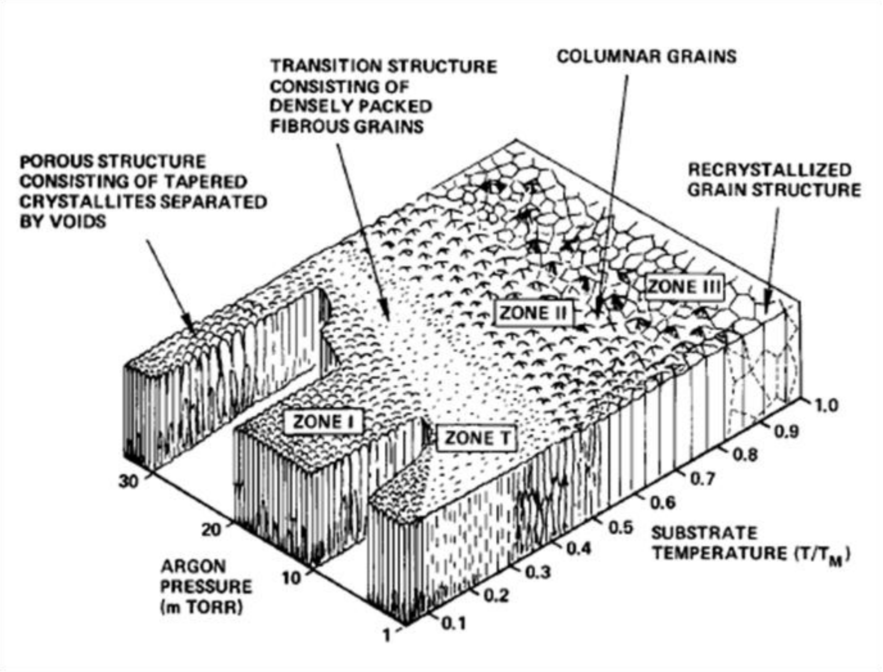

Figure 8.1 Structure zone model (SZM) proposed by Movchan & Demchishin and later modified by Thornton [153, 155]. Base on experimental setup, the structure of Ti-Al-C film which was deposited in this work belongs to SZM 2.

The elongated grains are also detected in the deposited film which could be explained by the infinite surface diffusion. As proposed by Drift, the surface diffusion redistributes the coating flux and removes any dependence on the condensation coefficient. The growth rate is assumed to be the same on all crystal planes. The direction of the fastest growth is from the centre to the remotest point on the crystal. Three dimensional crystals fill the available space and form a dense columnar Zone 2 structure [159]. Other possibility: the presence of intercolumnar defects is due the rotational substrate during the deposition. This condition is as reported by Bonne et al. [160].

The presence of TiC phase in this work has also been reported by other investigators. Schuster for example has reported the growth of TiC_{1-x} in bulk materials containing ternary $M_{n+1}AlC_n$ phases [62]. Previous researchers have also reported the similar condition for Ti_3SiC_2 [59, 161] and Ti_2AlC [3, 4, 162]. In our work, analytical investigation results and FFT pattern from HRTEM images inform that TiC is found near the pores. The EDX investigations show the presence of Al in that region which could consist of (Ti,Al)C, i.e. TiC with solid solution of Al at Ti sites. TiC has been known for its stability and Al solubility [163]. This metastable cubic solid solution may form in competition with the MAX phase since the Ti(C) layer in MAX phase structure continues to grow during the deposition process.

Although XRD do not indicate the presence of Ti_3AlC_2 in the film, FFT patterns of HRTEM images from the upper part of the film reveal that the film also consists of Ti_3AlC_2. This phase can be considered as an intergrown structure. In the bulk specimens Lin et al. have observed intergrowth of Ti_2AlC and Ti_3AlC_2 [164]. This condition could occur since both 211 and 312 MAX-phases have a related symmetry.

One interesting finding in this work is the presence of a local epitaxy of the Ti_2AlC at the substrate interface (see fig 7.14), although no seed layer was introduced as reported previously by other investigators [3, 4]. It has been known that seeding the substrate surface with oriented nuclei can enhance the oriented growth of the crystal i.e. to build an epitaxy growth [165]. The local epitaxy can happen when there is a large lattice misfit between the film and the substrate [166]. In our case, there is a misfit between sapphire with Ti_2AlC of approximately 4%. The SZM model can also be used to explain this phenomenon. When the T_s/T_m (in our case ≈ 0.52) is sufficient enough, it reduces the adatom surface density which leads to new crystal nucleation and the existing crystallites grow as columns by a localized epitaxial process [153].

Based on those results, we propose two scenarios for the growing model of Ti_2AlC thin film. In the first scenario, the high T_s/T_m and high deposition rate create large faceted grains together with pores. In the empty area, especially in the upper part of the film, intergrown Ti_3AlC_2 phase is formed. In the second scenario, due to the surface roughness, the shadowing effects cause a complex morphology and generates a less dense film which contains pores. For the local epitaxy, both the large misfits between the substrate and the film as well as the high energy to reduce the adatom surface density trigger the local epitaxy of Ti_2AlC. The metastable (Ti,Al)C forms near the pores due to the competition with Ti_2AlC MAX phase during the deposition. This growth model is presented in figure 8.2.

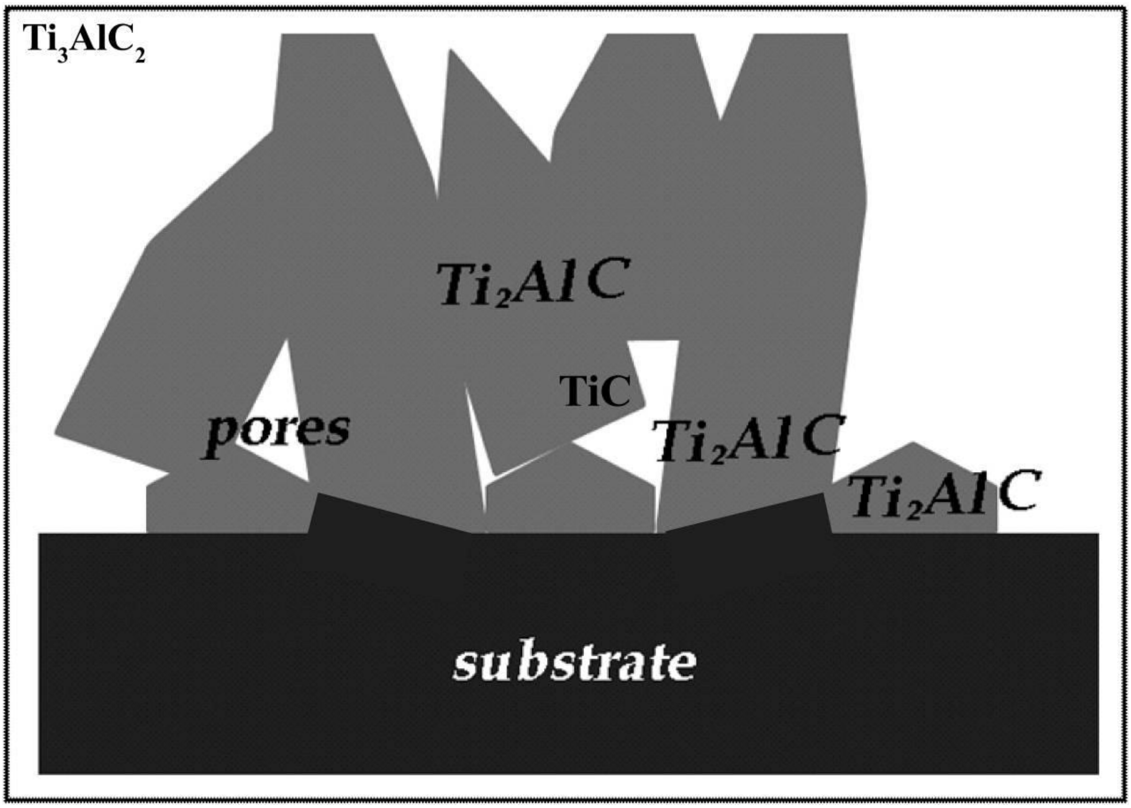

Figure 8.2 Ti_2AlC thin film growth model.

The presence of pores and additional TiC and Ti_3AlC_2 phases in the thin films have an influence on the mechanical properties of the Ti-Al-C thin film. The Ti-Al-C film grown in this work has a measured Young's modulus and a corresponding bulk modulus of 266 ± 106 GPa and 145 ± 58 GPa, respectively (see sub chapter 4.4.3). Although the Young's modulus values obtained in this work are slightly higher than the values previously reported for bulk Ti_2AlC, the bulk modulus values from this work are consistent with other reported values [21-25]. One reason for the difference is the presence of additional phases and pores in the film. TiC for example, has a much higher stiffness with a Young's modulus of 449 GPa which depends on the carbon concentration because of a wide solubility range [167]. The observed value for the hardness from our experiments is 9.8 ± 1.7 GPa. This value is also higher than the value reported for bulk Ti_2AlC specimens [3]. Besides the effect of the presence of pores, based on the Hall-Petch's rule, the strength of crystalline materials is proportional to the inverse of the square of crystallite size. The thickness of the thin film from this work is ≈ 1.6 µm, almost a factor of 25 smaller in comparison with the grain size of the bulk Ti_2AlC specimen, with which the hardness is compared to [3]. This might be the cause of the significantly higher hardness value reported in this work.

8.1.2. Cr-Al-C thin films

Unlike the Ti-Al-C thin film, there are no pores detected in the films but on the other hand the films deposited at temperature below 650°C contain amorphous layer at the interface. This amorphous layer could be consisted of $Cr_{23}C_6$ phase. Moreover, the HRTEM images have revealed that the films contain stacking faults and twins.

XRD patterns from specimens with three different deposition temperatures show that the crystalline phase of Cr_2AlC started to build up at 450°C. Peaks position of the Cr_2AlC phase are observed clearly at a deposition temperature of 650°C. TEM images of the specimen deposited at 450°C show additional information of the presence of an amorphous phase in the film. This information indicates that at 450°C the thin film is not entirely crystalline. The TEM images inform that no amorphous layer can be found at thin film deposited at 650°C.

Although XRD analyses have not indicated that other phases are present in the film, detailed analysis of SAED patterns shows that there are minor amounts of $Cr_{23}C_6$ phase with Al solid solution in the films deposited at 450°C and 550°C. This finding is confirmed by the EDX line scan results. The EDX line scans across the films show that from the upper part of the film through to the interface, the Cr/Al ratio at the amorphous layer starts to increase constantly from the boundary with the crystalline phase towards the substrate interface. Additionally, EFTEM elemental maps of carbon, which show a homogenous distribution of carbon, indicate that the amorphous areas have a chromium rich composition. This condition could not be found for film grown at a temperature at 650°C. Therefore, it can be assumed that the formation of the Cr rich amorphous layer must be temperature dependent. This fact once again agrees with the previous information as reported by Dirks and Leamy [168].

The SZM model can be used once again to explain the microstructure of the Cr-Al-C thin films. With the melting point of ≈ 1,450°C (1,773 K [63]) and the same deposition pressure with Ti-Al-C thin film, the T_s/T_m ratios for Cr450, Cr550 and Cr650 are ≈ 0.40, 0.46 and 0.52 respectively. All T_s/T_m values indicate the Cr-Al-C deposited thin film microstructure belongs to SZM 2. Unlike Ti-Al-C thin film, high-resolution images of all Cr-Al-C specimens inform that the substrate surface is smooth. This indicates, that the amorphous layers are not caused by the substrate surface roughness. The other possible cause is the deposition rate. All Cr-Al-C specimens were deposited at 500 nm/min, which was almost twice faster than Ti-Al-C specimen. This condition as reported by other investigators can produce less dense thin films, i.e due to the presence of amorphous layer. Furthermore, since the amorphous layer completely vanishes at 650°C deposition temperature, one can conclude that the surface mobility of adatoms increases with the increase of the substrate temperature during the film growth. This condition confirms the fact that a pure crystalline is formed in the thin films. Figure 8.3 shows a growth model of Cr-Al-C thin films. Although the T_m/T_s can produce microstructure of Zone 2, the lack of adatom surface mobility could prevent the growth of amorphous layer direct on the interface. The high deposition rate strengthens the amorphous layer growth. When the deposition temperature increases, the adatom surface mobility also increases and reduces the amorphous layer which at 650°C completely disappears.

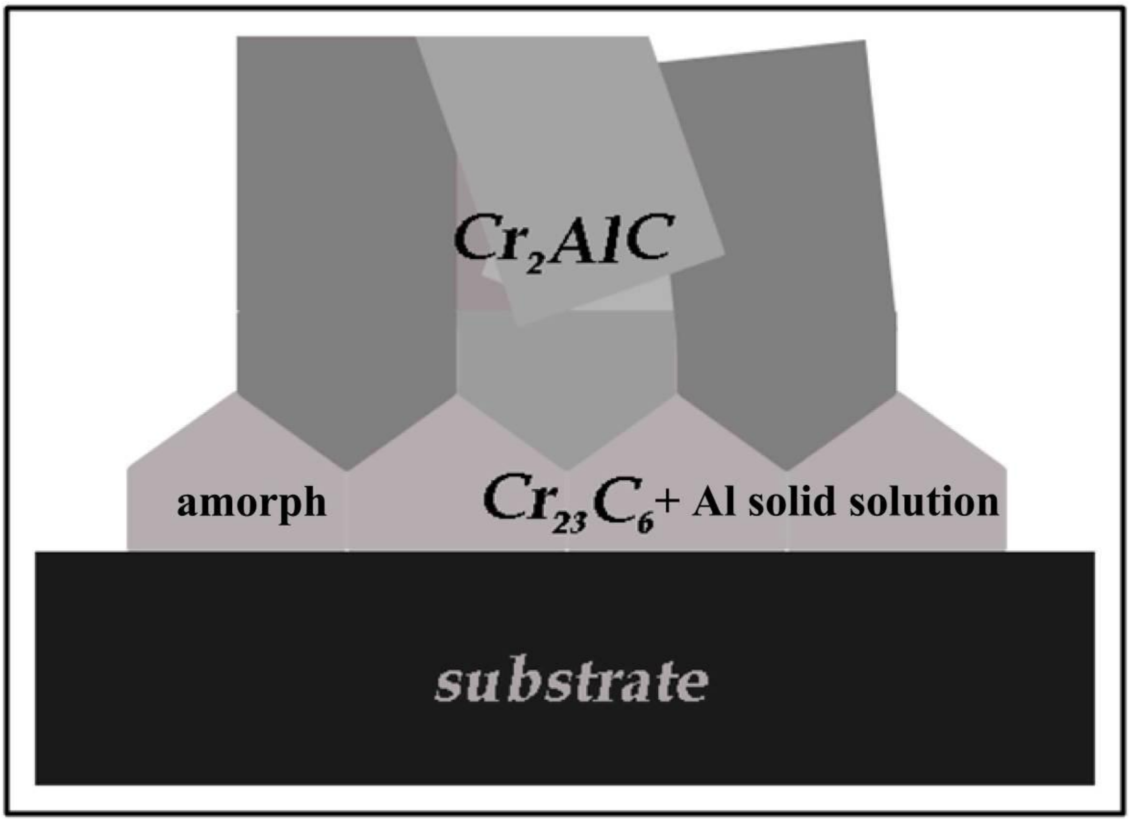

Figure 8.3 Cr-Al-C thin film growth model for deposited films.

The elastic modulus of the Cr_2AlC film grown at 650°C is 298 ± 21 GPa, which is approximately 17 ± 6% lower than the predicted value by ab initio data (see sub chapter 4.4.3) [169]. SEM cross section images show the thickness gradient of the film which could affect the measurement of elastic modulus (see figure 8.4). This thickness gradient is probably caused by the rotation during deposition.

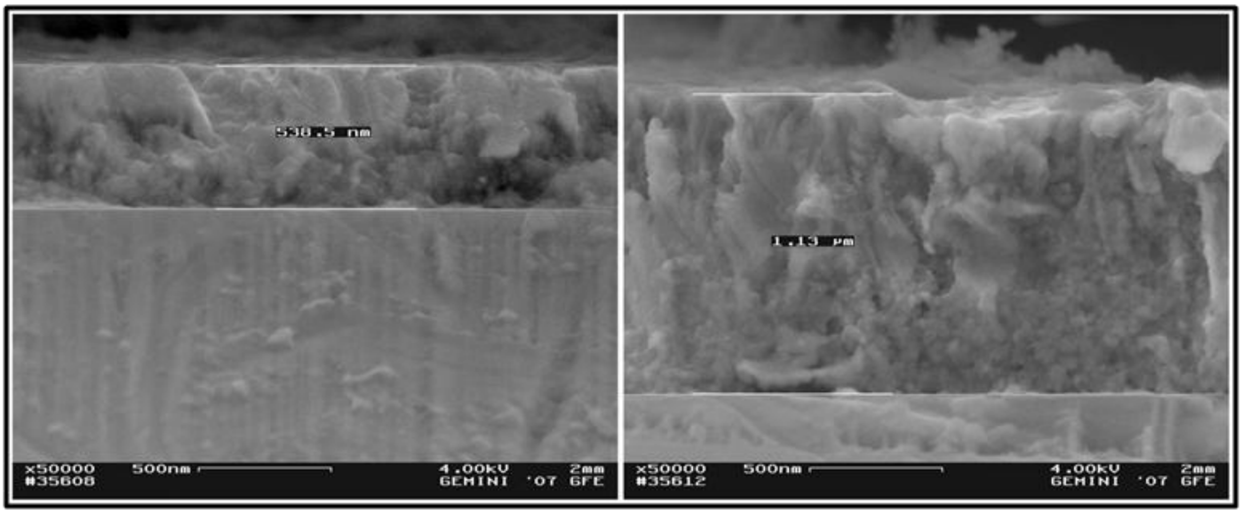

Figure 8.4 SEM cross section of specimen Cr650, showing the thickness gradient across the film (500 -1300 nm thick).

8.2. Isothermal oxidation behaviour and microstructure evolution of high temperature oxidation resistant materials: Cr_2AlC thin films and Fe-Cr-Al model alloys

8.2.1. Oxidation of Cr_2AlC thin films

In the investigated Cr_2AlC thin films, the oxide scale is dense without any pores detected. Furthermore, the oxide scale composition is not homogenous but contains non-homogeneously dissolved Cr and Cr carbide precipitates. When the dissolved Cr is found only in Cr-1, all oxide scales contain Cr carbide precipitates and its locations go higher to the upper part near the surface region. The phase identifications reveal the present of additional Cr_3C_2 in Cr-1 and Cr-2 and also Cr_7C_3 in Cr-6 specimen.

The dissolved Cr found in Cr-1 specimen and later disappeared indicates that the dissolved Cr is only present in the early oxidation stage. This finding has also been observed by other authors [12, 97, 170, 171]. The concentration of Cr increases with the increasing oxidation time.

Cr_7C_3 precipitates which can only be found in the film with 6 µm oxide scale with SAED, could be the product of the transformation of Cr_3C_2. This transformation also produced CO (g), CO_2 (g) and Cr_2O_3, which have been observed in other experiments [32, 34]. We believe that the CO_2 (g) should lead to the pores and at a higher temperature of $T \geq 1100°C$ CO_2 (g) formation becomes significant and as the result as observed in this work, cavities in the scale are formed [172]. The cavity formation can be explained as the result of the inward diffusion of oxygen, which reacts with Cr_3C_2 and forms CO gas which later diffuses outward to the solid/gas interface [171].

Beside the cavities, as seen in figure 7.37, at the last stage of oxidation, inner oxidation is also taking place. Our thermodynamic calculations indicate the same results. The local oxygen partial pressure would remain below 10^{-25} bar as long as Al is present. But when the Al supply is limited, the oxygen partial pressure may increase and the Cr-C carbides may start to oxidise [113].

For comparison, figure 8.5 shows BSE image of the cross section of bulk Cr_2AlC oxidised at 1320°C with approximately 6 µm oxide thickness [113]. Besides a dense and continuous α-Al_2O_3 scale which contains dissolved Cr, there are several differences between oxidised thin film and bulk Cr_2AlC that should be noted. First, there are only two kinds of contrast differences detected by BSE on the bulk Cr_2AlC which indicates that besides Cr_2AlC only one additional phase is present. The XRD results identify that phase as Cr_7C_3. Second, unlike the oxidised Cr_2AlC thin film, no precipitates containing Cr carbide is found in the α-Al_2O_3 scale. Third, there is spalling detected in the bulk Cr_2AlC specimens. The spalling of the scale is the result of a compressive growth stresses arising during oxidation. It reduces the elastic strains during oxidation due to the lateral expansion of the oxide scale parallel to the surface. Possible reasons for this elastic strain are the volume differences between the oxide and the base material, inward diffusion of oxygen and oxide formation at the grain boundaries within the oxide scale [95, 173].

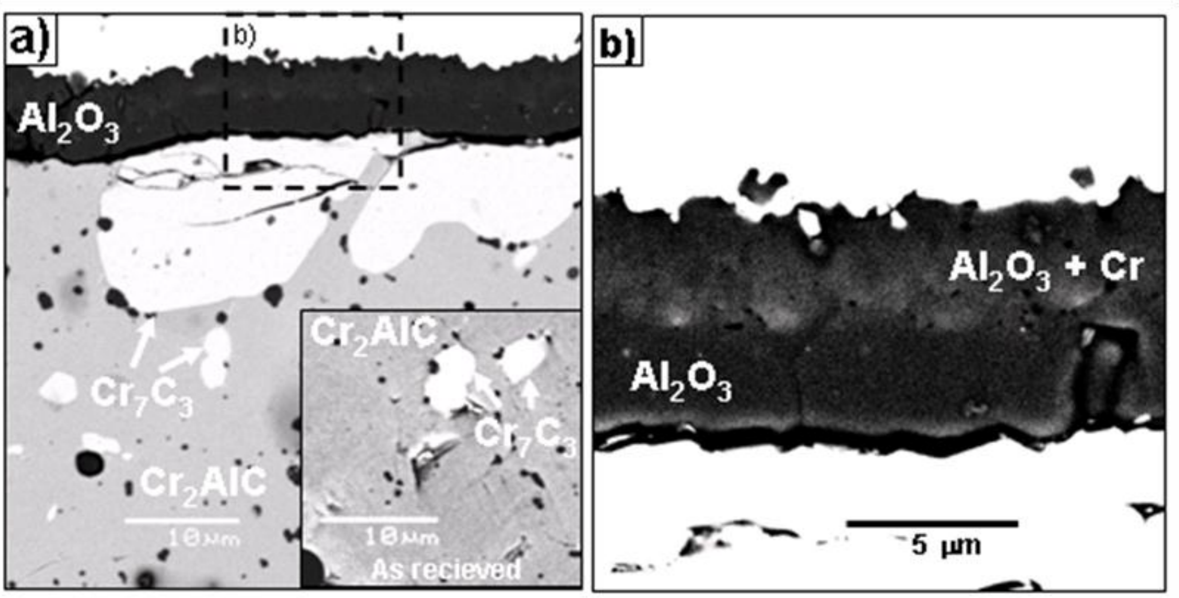

Figure 8.5. (a) A BSE image and (b) magnified image of a cross section of bulk Cr2AlC oxidised at 1320°C with approximately 6 µm oxide scale [113].

Based on these result we propose a model to explain the oxidation stage of the Cr_2AlC thin film as presented in figure 8.6. In the beginning of the oxidation process a dense continuous and heterogeneous α-Al_2O_3 scale forms on the surface of the film samples. The α-Al_2O_3 contains a thin Cr layer at the upper part and Cr-C precipitation close to the scale interface. Simultaneously, the other Cr carbides detected as Cr_3C_2 and Cr_7C_3 form as interlayer between the scale and the Cr_2AlC film. With the increasing oxidation time, both the scale and Cr carbide interlayer become thicker. At the longest oxidation time, significant pores formation can be observed in the Cr carbide interlayer together with an internal oxidation.

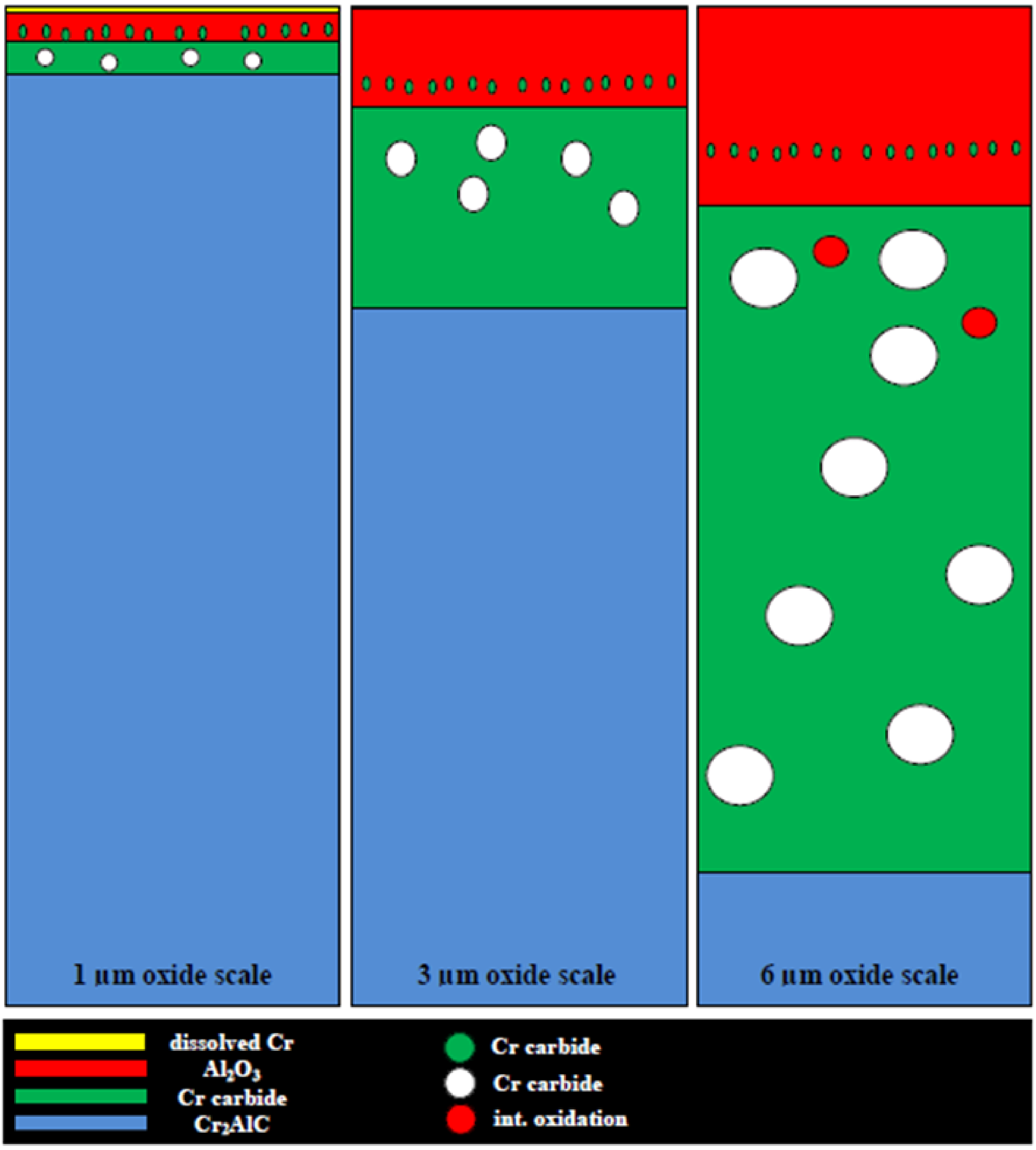

Figure 8.6 Model of oxidation behaviour of Cr_2AlC thin films with three different oxide scales thicknesses.

8.2.2. Fe-Cr-Al model alloys

The additional rare earth (RE) elements dopants have been added to grow internal oxide precipitates which can act as template for the incorporation of particles in the growing alumina layer. Together with oxidation test results, our detail microstructure study will help to understand the oxidation process of these materials.

Two batches specimens were investigated in this present work. The F-batch specimens were investigated to study the microstructure morphology of Fe-CR-Al-Y with Zr addition based on the increasing oxidation time. Small amount of the Zr precipitates, which from SAED and EDX are presumed to be Zr-oxides, together with pores started to be detected at 8 hours of oxidation time. At 100 hours oxidation time Zr-oxides are detected in a whole oxide scale suggesting that there is Zr incorporation.

The J-batch specimens were investigated to see the effect of Zr reservoir to the oxidation rate. The SEM images show that the amount of detected precipitates in oxide scale only differs on the specimens with highest oxidation time. In this case the thick specimens have thicker oxide scale for the same oxidation time. EDX analyses show that more Zr containing precipitates are found in the thin specimen than the thick specimen especially in the high temperature oxidation. These two evidences, the oxide scale thickness and the Zr precipitates, could indicate that the Zr reservoir plays a role in the oxidation rates of alumina scale. The Ti addition in the J-batch specimens formed mixed of Ti/Y/Zr precipitates in the matrix detected by EDX analyses. Naumenko et.al., reported that the Ti may decrease the mobility of Y, which prevents Y to become incorporated into the scale [174]. Although not really clear in this present work, the same effect could happen since the STEM-BF and EDX analyses show the same condition (see fig 7.69 or 7.70 c).

Based on these results, we modify a model proposed by Noumenko which can be used to illustrate the mechanism of Zr incorporation into the alumina scale during oxidation for a specimen with a finite thickness [105]. First, zirconia precipitates are formed at the surface alloys. With the growing of alumina scale, the internal zirconia is formed. In the next stage, due to the incorporation of Zr-oxides into the alumina scale, the oxidation rate increases. At the final stage, the zirconia is depleted from the alloy and causes the decreasing of the oxidation rate.

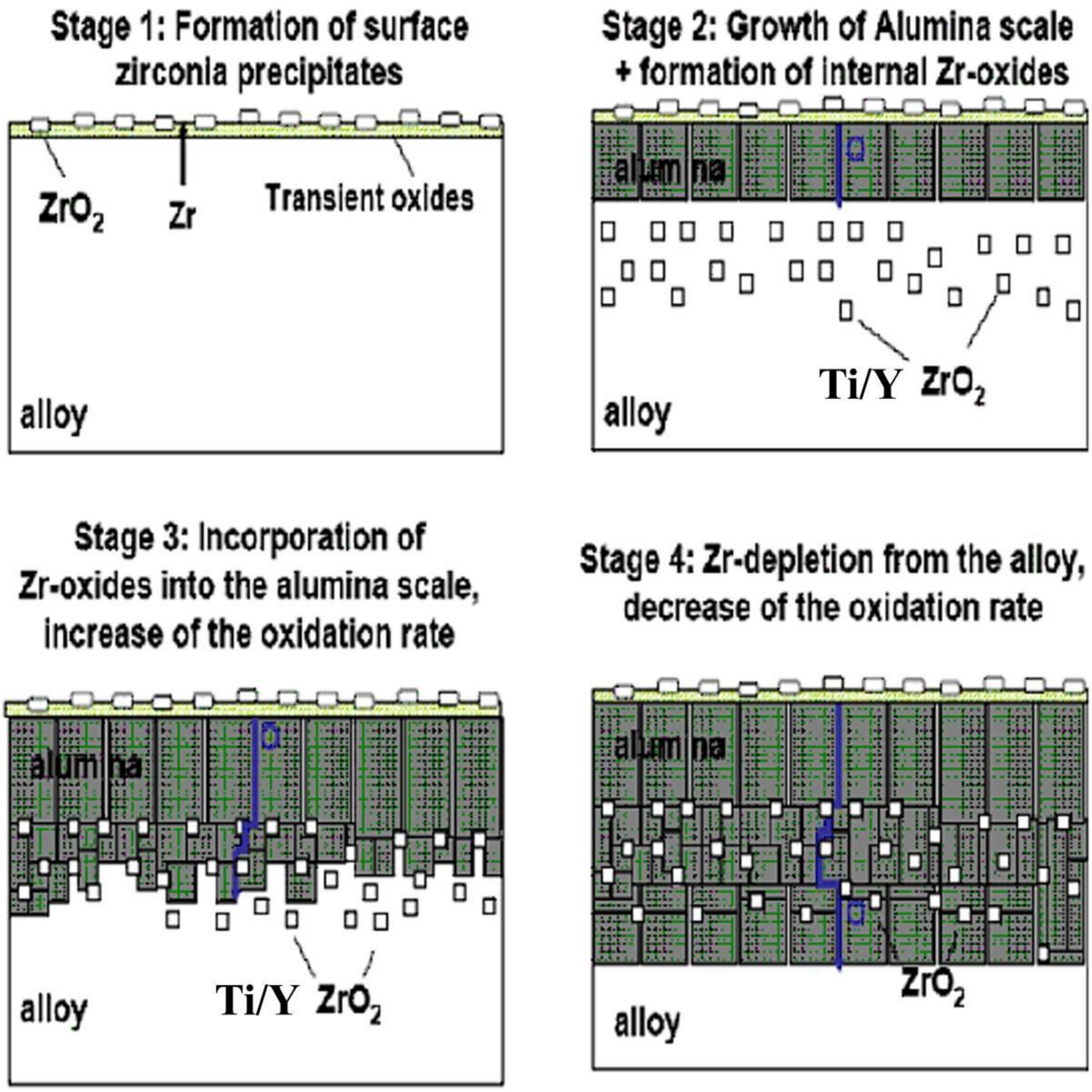

Figure 8.7 Schematic model of the mechanism of Zr incorporation into the alumina scale specimen, modified from [105]. Note that in the present work only up to stage 3 has been investigated.

This page is intended to be blank

9 Conclusions

The first objective of the present work was to develop a more detailed understanding of the MAX phase thin film growth processes, their microstructure and properties, and to obtain more insight in their physical and chemical properties. This research also prepares the basis for their technological application in industry, especially for high-temperature applications. For the industrial applications, at least there main objectives should be met:

- the thin films consist of a single phase,
- the films are homogenous over a large area,
- the films are deposited at low temperatures.

In order to fulfil these objectives and to optimise the film microstructure, detailed microscopic investigations on the growth mechanisms of polycrystalline Ti-Al-C and Cr-Al-C thin films which were synthesised by magnetron sputtering were performed. The observations made in the TEM studies of the MAX-phase films suggest a complex nucleation process. Ti_2AlC requires a higher deposition temperature than Cr_2AlC for crystalline growth. At 850°C, although no amorphous layer was detected, the Ti_2AlC film still contains pores and minor amounts of TiC and Ti_3AlC_2 phases.

In the Cr-Al-C system, although other means have indicated that a fully polycrystalline Cr_2AlC film has grown at 450°C, TEM investigations revealed that the film contains an amorphous layer at the interface. The amorphous layer disappears completely for a deposition temperature of 650°C. It can be concluded that the M element in the MAX-phases has a major influence on these deposition temperature differences. We have shown in the present work that the experimental setup in the deposition process was successful in growing both MAX-phases as thin films.

The second goal of the present work was to understand the microstructure evolution of high-temperature materials. We have studied the oxidation properties of Cr_2AlC thin films and also Fe-Cr-Al alloys. It has been demonstrated that Cr_2AlC thin films exhibit an excellent oxidation resistance. The oxidation mechanism has followed a parabolic rate law, which means that diffusion was the rate limiting mechanism. A dense continuous α-Al_2O_3 scale has formed on the surface of the film, which was accompanied by the formation of a Cr_3C_2

interlayer. The fraction of Cr_3C_2 has decreased with increasing oxidation time and at the longest oxidation time, the Cr_7C_3 phase and internal oxidation were found. Furthermore, the formation of CO_2 gas, together with the depletion of Al, C and Cr by outward diffusion, leads to the significant void formation observed in the Cr_3C_2 interlayer. There are still questions for the oxidation mechanisms especially at the early stage of oxidation which has not been resolved. This mechanism should be investigated in the future work.

The last part of this work was the microstructure investigation of the effect of the RE reservoir for the oxidation rate and life time of the Fe-Cr-Al alloys. A minor addition of Y+Zr into the Fe-Cr-Al alloys has successfully increased the oxidation life time of the alloy. The depletion of Zr has significantly reduced the oxidation rate of the alumina scale. In the future work, the need for stabilisation of the internal oxide precipitates to obtain a longer lasting effect in thinner components and at higher temperatures has to be systematically investigated.

This page is intended to be blank

References

[1] W. Jeitschko, *et al.*, "Kohlenstoffhaltige ternäre Verbindungen (H-Phase)," 1963.

[2] M. W. Barsoum, *et al.*, "The MAX Phases: Unique New Carbide and Nitride Materials," *American Scientist,* vol. 89, pp. 334-343, 2001.

[3] O. Wilhelmsson, "Deposition and characterization of ternary thin films within the Ti-Al-C system by DC magnetron sputtering," *Journal of Crystal Growth,* vol. 291, pp. 290-300, 2006.

[4] O. Wilhelmsson, "Deposition of Ti_2AlC and Ti_3AlC_2 epitaxial films by magnetron sputtering," *Applied Physics Letters,* vol. 85, pp. 1066-1068, August 2004.

[5] C. Walter, "Towards large area deposition of Cr_2AlC on steel," *Thin Solid Films,* vol. 515, pp. 389-393, 2006.

[6] J. M. Schneider and M. R. Iskandar. (2007) Elastic properties of Cr_2AlC thin flms probed by nanoidentation and ab initio molecular dynamics. *Scripta Materialia*. 1137-1140.

[7] J. M. Schneider. (2004) Ab initio calculations and experimental determination of the structure of Cr_2AlC. *Solid State Communications*. 445-449.

[8] D. Music. (2006) Electronic structure of M_2AlC (0001) surfaces (M=Ti,V,Cr). *J. Phys: Condens. Matter*. 8877-8881.

[9] Z. Sun, "Structure and bulk modulus of M_2AlC (M=Ti, V and Cr)," *Applied Physics Letters,* vol. 83, August 2003.

[10] Z. j. Lin, "High-temperature oxidation and hot corrosion of Cr_2AlC," *Acta Mater,* vol. 55, p. 6182, 2007.

[11] Z. Lin, "Hot corrosion and protection of Ti_2AlC againts Na_2SO_4 salt in air," *Journal of European Ceramic Society,* vol. 26, pp. 3871-3879, 2006.

[12] W. Tian, "Oxidation behaviour of Cr_2AlC ceramics at 1,100 and 1,250 C," *J. Mater. Sci,* vol. 43, pp. 2785-2791, 2008.

[13] D. Whittle and J. Stringer, "Improvements in high temperature oxidation resistance by additions of reactive elements or oxide disepresions," *Philosophical transactions of the Royal Soceity A London,* vol. 295, pp. 309-329, 1980.

[14] R. Prescott and M. Graham, "The formation of aluminum oxide scales on high temperature alloys," *Oxidation Metal,* vol. 38, pp. 233-253, 1992.

[15] B. Pint, "Experimental observation in suport of the dynamic segregation theory to explain the reactive element effect," *Oxidation Metal,* vol. 45, pp. 1-31, 1996.

[16] M. Ohring, *Material science of thin films, deposition and strucure,* 1991.

[17] R. F. Bunshah, "Evaporation: processes, bulk microstructures and mechanical properties," in *Handbook of deposition technologies for films and coatings, science, technology and applications*, ed Los Angeles, California: Noyes Publications, 1994.

[18] S. Schiller, *et al.*, "Proc. 7th Int'l. Vacuum Congress," in *R. Dobrozemsky,* Vienna, 1977, p. 1545.

[19] J.-O. Carlsson, "Chemical vapor deposition," in *Handbook of deposition technologies for films and coatings*, ed Los Angeles, California: Noyes Publications, 1994, p. 400.

[20] D. M. Mattox, *Handbook of physical vapour deposition (PVD) processing, film formation, adhesion, surface preparation and contamination control*. Westwood, New Jersey: Novel Publications, 1998.

[21] J. A. Thornton, *J. Vac. Sci. Technol.,* vol. 11, p. 666, 1974.

[22] J. A. Thornton. (1979, April) Recent development in sputtering, magnetron sputtering. *Metal Finishing*.

[23] J. A. Thornton and A. S. Penfold, "Cylindrical magnetron sputtering," in *Thin film processes*, ed: Academic Press, 1978.

[24] R. K. Waits, "Plannar magnetron sputtering," in *Thin Films Processes*, ed: Academic Press, 1978.

[25] A. S. Penfold, "Magnetron sputtering," in *Handbook of thin film process technology*, ed: Institute of Physics Publishing, 1995.

[26] R. K. Waits. (1978) *J. Vac. Sci. Technology*. 179.

[27] J. S. Chapin, US Patent #4,166,018, 1974.

[28] D. B. Fraser, "The sputter (gun)TM and s-gun TM manetrons," in *Thin Film Processes,* ed: Academic Press, 1978.

[29] D. B. Fraser and H. D. Cook, "Film deposition with sputter gun," *J. Vac. Sci. Tecnol.,* vol. 14, p. 147, 1977.

[30] P. Clarke, "Effect of anode bias on the index refraction of Al_2O_3 films deposited by DC s-gun magnetron reactive sputtering," *J. Vac. Sci. Tecnol.,* vol. 12(2), p. 594, 1994.

[31] O. Kubaschewski and B. E. Hopkins, *Oxidation of metals and alloys*: Butterworths, 1962.

[32] F. Richardson and J. Jeffers, *J. iron Steel Inst.*, vol. 171, p. 167, 1952.

[33] G. D. Smith, "High temperature, corossion test and standards, aplication and interpretation," *American Society of Testing and Materials,* p. 194, 1995.

[34] P. Kofstad. (1983) Oxidation mechanism for pure metals in single oxidant gases, high temperature corrosion 123-138.

[35] N. Cabrera and N. F. Mott, "Theory of oxidation of metals," *Rep. Prog. Phys.,* vol. 12, pp. 163-184, 1948-1949.

[36] K. Hauffe and B. Ilschner, "Defective-array states and transport processes in ionic crystals," *Zeitschrift für Elektrochemie,* vol. 58, p. 467, 1954.

[37] T. B. T. Grimley, B.M.W, "The Gas/Oxide Interface and the Oxidation of Metals," *Proceding Royal Society (London) A,* vol. A234, pp. 405-418, 1956.

[38] H. H. Uhling, "Initial oxidation rate of metals and the logarithmic equation," *Acta Metallurgica,* vol. 4, p. 541, 1956.

[39] C. Wagner, "Contributions to the theory of the tarnishing process," *Z. Phys. Chem,* vol. b21, pp. 25-41, 1993.

[40] N. M. Birks, Gerald H; Petit, Frederick S, *Introduction to the High-Temperature Oxidation of Metals,* 2nd ed.: Cambridge University Press, 2006.

[41] L. R. Scharfstein and M. Henthrone, "Testing at high temperatures," in *Handbook on corrosion testing and evaluation,* ed: John Wiley & Sons, 1971, pp. 291-366.

[42] M. Danielewski, "Kinetics of gaseous corrosion processes " in *ASM Handbook vol 13 A,* ed.

[43] G. C. Rybicki and J. L. Smialek, "Effect of the theta-apha Al_2O_3 transformation on the oxidation behaviour of beta-NiAl+Zr," *Oxidation of Metals,* vol. 31, pp. 275-304, 1989.

[44] B. Pint, *et al.*, "The oxidation mechanism of teta-Al_2O_3 scales," *Solid state ionics,* vol. 78, pp. 99-107, 1995.

[45] B. Pint and L. W. Hoobs, "Limitations on the use of ion implantation for the study of the reactive elements effect in beta-NiAl," *J. Electrochemical Soceity,* vol. 141, p. 2443, September 1994.

[46] C. S. Wukusick and J. F. Collins, "An iron-chromium-aluminum alloy containing yttrium, materials research standard," *American Society for Testing Materials,* vol. 4, p. 637, 1964.

[47] M. Barsoum. (2006) Physical properties of the MAX-phases. *Encyclopedia of Materials Science and Technology*.

[48] M. W. Barsoum and T. El-Raghy, *J.Am. Ceramic. Soc,* vol. 79, pp. 1953-1996.

[49] M. W. Barsoum, "The $M_{N+1}AX_N$ phases: A new class of solid; Thermodynamically stale nanolaminates," *Prog.Solid St. Chem,* vol. 28, pp. 201-281, 2000.

[50] S. Gupta*, et al.*, "Ambient and 550 C tribological behaviour of select MAX phases againts Ni-based superalloys," *Wear,* vol. 264, pp. 207-278, 2008.

[51] S. Gupta*, et al.*, "Ta_2AlC and Cr_2AlC Ag-based composites-- New solid lubricant materials for use over a wide temperature range againts Ni-based superalloy and alumina," *Wear,* vol. 262, pp. 1479-1489, 2007.

[52] V. I. Ivchenko*, et al.*, "Some Physical Properties of ternary compounds in the system Ti-Al-C," *Poroshkovaya Mettalurgiya,* vol. 5, pp. 45-48, May 1976.

[53] V. I. Ivchenko and T. Y. Kosolapova, "Conditions of preparation of ternary Ti-Al-C alloy powders," *Poroshkovaya Mettalurgiya,* vol. 6, pp. 1-4, June 1975.

[54] V. I. Ivchenko and T. Y. Kosolapova, "Abrasive properties of the ternary compounds in the systems Ti-Al-C and Ti-Al-N," *Poroshkovaya Mettalurgiya,* vol. 8, pp. 56-59, August 1976.

[55] M. Radovic, "On the elastic properties ad mechanical damping of Ti_3SiC_2, Ti_3GeC_2, $Ti_3Si_{0.5}Al_{0.5}C_2$ and Ti_2AlC in the 300-1573 K temperature range," *Acta Materialia,* vol. 54, p. 2757, 2006.

[56] X. H. Wang and Y. C. Zhou, "High-temperature oxidation behaviour of Ti_2AlC in air," *Oxidation of metals,* vol. 59, April 2003.

[57] X. H. Wang and Y. C. Zhou, "Intermediate-temperature oxidation behaviour of Ti_2AlC in air," *J. Mater. Res,* vol. 17, November 2002.

[58] C. Walter, "Towards large area MAX phase coatings on steel," *Steel Research Int.,* vol. 76, 2005.

[59] J. Emmerlich, "Systematic study on the pressure dependence of M_2AlC phases," *Physical Review B,* vol. 76, p. 224111, 2007.

[60] Z. Sun, "Calculated elastic properties of M_2AlC (M=Ti, V, Cr, Nb and Ta)," *Solid State Communications,* vol. 129, p. 589, 2004.

[61] H. Nowotny. (1971) Strukturchemie einiger verbindngen der ubergangsmetalle mit den elementen C, Si, Ge, Sn *Prog. Solid State Chem*. 27.

[62] J. C. Schuster, "The ternary system: Cr-Al-C, V-Al-C and Ti-Al-C and the behaviour of H-phases," *Journal of Solid State Chemistry,* vol. 32, p. 213, 1980.

[63] B. Hallstedt, "Thermodynamic evaluation of the Al-Cr-C system," *Int. J. Mat. Res (Z. Metallkd),* vol. 97, p. 5, 2006.

[64] R. Martens, "Effect of the composition on the structure of Cr-Al-C. Invesigation by combinatorial thin film synthesis and ab initio calculations," *Advanced Engineering Materials,* vol. 6, p. 903, 2004.

[65] S. E. Lofland, "Elastic and electronic properties of select M_2AlC phases," *Applied Physics Letters,* vol. 84, pp. 508-510, 2004.

[66] M. W. Barsoum, "Layered machinable ceramic for high temperature applications," *Scripta Materialia,* vol. 36, p. 535, 1997.

[67] M. W. Barsoum, "Processing and characterization of Ti_2AlC, Ti_2AlN and $Ti_2AlC_{0.5}N_{0.5}$," *Metalurgical and Material Transactions A,* vol. 31 A, p. 1857, 2000.

[68] W. Tian*, et al.*, "Synthesis and thermal and electrical properties of bulk Cr_2AlC," *Scripta Materialia,* vol. 54, pp. 841-846, 2006.

[69] C. Walter, "Simulation of diffusion processes in turbine blades and large area deposition of MAX phase thin films with PVD," 2005.

[70] D. P. Sigumonrong, Dr. Ing, Institute of Material Chemistry, RWTH Aachen University, Aachen, 2010.

[71] B. D. Culity, *Elements of X-rays difraction*. London: Addison-Wesley Publishing Company, Inc, 1978.

[72] M. F. Doerner and W. D. Nix, "A method for interpreting the data from depth-sensing indentation instruments," *J. Mater. Res,* vol. 4, pp. 601-609, 1986.

[73] W. C. Oliver and G. M. Pharr, "An improved technique for determining hardness and elastic modulus using load and displacement sensing indentation experiments," in *J. Matter. Res.* vol. 7, ed, 1992, pp. 1564-1583.

[74] S. I. Bulychev*, et al.*, "Determining Young's Modulus from the indentor Penetration diagram," *Industrial Laboratory,* vol. 41, pp. 1137-1140, 1975.

[75] R. Raj, "Fundamental research in structural ceramic for service near 200 degrees C," *J. Am Ceram Soc,* vol. 76, p. 2147, 1993.

[76] M. W. Barsoum*, et al.*, "Oxidation of Ti_3SiC_2 in air," *J. Electrochem. Soc.,* vol. 144, p. 2508, 1997.

[77] Z. Sun*, et al.*, "Oxidation behaviour of Ti_3SiC-based ceramic at 900-1300 degrees C in air," *Corros. Sci.,* vol. 43, p. 1095, 2001.

[78] A. Feng*, et al.*, "Field-activated pressure-assisted combustion synthsis of polycrystalline Ti_3SiC_2," *J. Mater Res,* vol. 14, p. 925, 1999.

[79] S. Li*, et al.*, "Oxidation behaviour of Ti_3SiC_2 at high temperature in air," *Mat. Sci. Eng A-Struct.,* vol. 341, p. 112, 2003.

[80] D. Naumenko*, et al.*, "Effect of combined Yttrium and Zirconium additions on protective alumina scale formation on high purity FeCrAl alloys during oxidation in the temperature range of 1200 to 1300 °C," *Materials Science Forum,* vol. 461-464, pp. 489-496, 2004.

[81] Z. j. Lin*, et al.*, "In-situ hot pressing/solid-liquid reaction synthesis of bulk Cr_2AlC," *Z. Metallkd,* vol. 96, p. 291, 2005.

[82] Z. Sun*, et al.*, "Cyclic-oxydation behaviour of Ti_3SiC_2-base material at 1100 degrees C," *Oxid. Met.,* vol. 57, p. 379, 2002.

[83] S. L. Yang*, et al.*, "Oxidation of Ti_3SiC_2 at 1000 degrees C in ar," *Oxid. Met.,* vol. 59, p. 155, 2003.

[84] W. J. Quadakkers and L. Singheiser, "Practical aspects of the reactive elements effect," *Materials Science Forum,* vol. 369-372, pp. 77-92, 2001.

[85] D. B. Lee*, et al.*, "Oxidation of Cr_2AlC at 1300 C in air," *Corrosion Science,* vol. 49, pp. 3926-3934, 2007.

[86] J. Klöwer*, et al.*, "Effect of aluminium and reactive elements on the oxidation behaviour of thin Fe-Cr-Al foils.," in *Metal-Supported Automotive Catalytic Converters, The international conference on metal-supported Automotove catalytic convertes (MACC'97),* 1997.

[87] F. Starr*, et al.*, "Pressurized heat exchangers for operation at 1100 °C, materials for advanced power engineering," 1994.

[88] W. J. Quadakkers and K. Bongartz, "Oxidation induced lifetime limits of thin waled, iron based, alumina forming, oxide dispersion strengthened alloy componnents," *Materials Sciences and Technology,* vol. 10, pp. 126-131, 1994.

[89] W. J. Quadakkers and K. Bongartz, "The prediction of breakway oxidation for alumina forming ODS alloys using oxidation diagrams," *Werkstoffe und Korrosion,* vol. 45, pp. 232-241, 1994.

[90] B. Pint, "Optimization of Reactive-Element Additions to Improve Oxidation Performance of Alumina-Forming Alloys," *J. Am. Ceram. Soc,* vol. 86, pp. 686-695, 2003.

[91] W. J. Quadakkers, "Growth mechanisms of oxide scales on ODS alloys in the temperature range 1000-1100 °C," *Werkstoffe und Korrosion,* vol. 41, pp. 659-668, 1990.

[92] M. J. Bennet*, et al.*, in *Proc. materials for advanced power engineering*, Liege, 1994, p. 1533.

[93] e. a. Gruappa, ""Factors governing breakway oxidation of FeCrAl-based alloys"," *Materials and corrosion,* vol. 51, pp. 224-235, 2000.

[94] F. H. Stott*, et al.*, "The influence of alloying elements on the developmet and maintanance of protective scales," *Oxid. Metals,* vol. 44, p. 113, 1995.

[95] F. A. Golightly*, et al.*, "The influence of yttrium additions on the oxide scale adhesion to an iron-chromium-aluminum alloy," *Oxid. Metals,* vol. 10, p. 163, 1976.

[96] Z. Suo, "Wrinkling of the oxide scale on an aluminum containing alloy at high temperatures," *Journal of the Mechanics and Physics of Solid,* vol. 43, p. 829, 1995.

[97] V. K. Tolpygo and D. R. Clarke, "Wrinkling of alpha-alumina films grown by thermal oxidation - I Quantitative studies on single crystals of Fe-Cr-Al alloys," *Acta. Mater.,* vol. 46, pp. 5153-5166, 1998.

[98] V. K. Tolpygo, "The morphology of thermaly grown alpha-Al_2O_3 scales on Fe-Cr-Al alloys," *Oxidation of Metals,* vol. 51, pp. 449-477, 1999.

[99] M. W. Brumm and H. J. Grabke, "The oxidation behaviour of NiAl -I. Phase transformation in the alumina scale during oxidation of NiAl and NiAl-Cr alloys," *Corros. Sci.,* vol. 33, p. 1677, 1992.

[100] E. Lang, *Proc. europ. colloqium on the role of active elements in the oxidation behaviour of high temperature materials and alloys*. London, England: Elsevier Applied Science, 1989.

[101] J. Stringer, "The reactive element effect in high-temperature corrosion," *Materials Science and Engineering,* vol. A 120, pp. 129-137, 1989.

[102] W. J. Quadakkers, "Oxidation of ODS alloys," *Journal de Physique IV,* vol. 3, pp. 177-186, December 1993.

[103] J. Stringer*, et al.*, "The high-temperature oxidation of nickel -20wt% chromium alloys containing dispersed oxide phases," *Oxidation of Metals,* vol. 5, pp. 11-47, 1972.

[104] D. Naumenko*, et al.*, "Effect of trace amounts of carbon and nitrogen on the high temperature oxidation resistance of high purity FeCrAl alloys," *Mater. Trans.,* vol. 43, pp. 168-172, 2002.

[105] D. Naumenko*, et al.*, "Effect of Zr addition on alumina sale formation durng oxidation of high purty FeCrAl-alloys," *Mater. Tech.,* vol. 7-9, pp. 63-69, 2003.

[106] E. Wessel*, et al.*, "Effect of Zr addition on the microstrucure of the alumina scales on FeCrAlY-alloys," *Scripta Materialia,* 2004.

[107] K. AB. Available: www.kanthal.com

[108] Kerafol. Available: www.kerafol.com

[109] Armines. Available: www.armines.net

[110] J. Romanski, "Geometrical factors in studies of kinetics of oxidaion of metals at high-temperatures," *Corrosion Science,* vol. 8, pp. 67-69, 1968.

[111] H. J. Grabke*, et al.*, "Points to be considered in thermogravimetry," *Werkstoff Korrosion,* vol. 44, pp. 345-350, 1993.

[112] A. Gil, *Methods for meassuring Gasseous Corrosion Rates*.

[113] D. E. Hajas*, et al.*, "Oxidation of Cr_2AlC coating in temperature range 1230 to 1410 °C," *Surface and Coatings Technology,* vol. 206, pp. 591-598, 2011.

[114] D. B. Williams and C. B. Carter, *Transmission electron microscopy, I*: Plenum Press, 1996.

[115] L. Reimer, *Scanning electron microscopy, physics of image formation and microanalysis*: Springer, 1998.

[116] T. Ishitani, *et al.*, "Transmission electron microscope sample preparation using a focused ion beam," *J. Electron. Microsc.,* vol. 43, pp. 322-326, 1994.

[117] A. Yamaguchi, *et al.*, "Transmission electron microscopy specimen preparation technique using focused ion beam fabrication: application to GaAs metal-semiconductor field effect transistor," *J. Vac. Sci. Technol.,* vol. B11, pp. 2016-2020, November/December 1993.

[118] J. Szot, *et al.*, "Focused ion beam micromachining for transmission electron microscopy specimen preparation of semiconductor laser diodes," *J. Vac. Sci. Technol.,* vol. B 10, pp. 575-579, 1992.

[119] L. A. Giannuzzi and F. A. Stevie, "A review of focused ion beam milling tcniques for TEM specimen preparation," *Micron.,* vol. 30, pp. 179-204, 1999.

[120] H. Sasaki, *et al.*, "Specimen preparation for high-resolution transmission electron microscopy using focused ion beam and Ar ion milling," *Journal of Electron Microscopy,* vol. 53, pp. 497-500, 2004.

[121] L. A. Giannuzzi, *et al.*, "FIB lift-out specimen preparation tecniques," in *Introduction to focused ion beams. Instrumentation, theory, tecniques and practice*, ed: Springer, 2005.

[122] L. A. Giannuzzi, *et al.*, "Application of the FIB lift-out for TEM specimen preparation," *Microscopy Research and Techniques*, vol. 41, pp. 285-290, 1998.

[123] M. H. F. Overwijk, *et al.*, "Novel scheme for the preparation of transmission electron microscopy specimen with a focused ion beam," *J. Vac. Sci. Tech,* vol. B11, pp. 2021-2024, November/December 1993.

[124] F. A. Stevie, *et al.*, "Aplication of focused ion beam lift-out specimen preparation to TEM, SEM, STEM, AES and SIMS anaysis," *Surface and Interface Analysis,* vol. 31, pp. 345-351, 2001.

[125] F. A. Stevie, *et al.*, "The focused ion beam instrument," in *Introduction to focused ion beams, intrumentation, theory, techniques and practice,* ed: Springer, 2005.

[126] G. Bergerhoff and I. D. Brown. *ICSD - Crystallographic Database*.

[127] (1997). *JCPDFWIN - JCPDS.*

[128] B. E. P. Beeston, *Electron diffraction and optical diffraction techniques, practical methods in electron microscopy* vol. 1: North-Holland Publishing Company, 1972.

[129] W. Kossel and G. Möllenstedt, "Elektroneninterferenze im konvergente bündel," *Annalen der Physik,* vol. 36, pp. 113-140.

[130] K. W. Andrews, *et al.*, *Interpretation of electron diffraction patterns*: Hilger and Watts LTD, 1967.

[131] P. Stadelmann. (2008). *Java electron microscopy software - JEMS.*

[132] S. Hovmöller, "CRISP: crystallographic image processing on a personal computer," *Ultramicroscopy,* vol. 41, pp. 121-135, 1992.

[133] D. R. G. Mitchell, "DiffTools: Software Tools for Electron Diffraction in DigitalMicrograph," *Microscopy Research and Technique,* vol. 71, pp. 588-593, 2008.

[134] A. V. Crewe and J. Wall, *J. Mol. Biol.,* vol. 48, p. 375, 1970.

[135] J. Goldstein, *et al.*, *Scanning electron microscopy and X-rays microanalysis*: Springer, 2003.

[136] R. Brydson, *Electron energy loss spectroscopy, microscopy handbook 48*: Taylor & Francis, 2001.

[137] O. L. Krivanek, *et al.*, "Elemetal mapping with energy selecting imaging filter," in *Proceding 51st Annual Meeting MSA*, San Fransisco, pp. 586-587.

[138] C. Jeanguillaume, "About the use of electron energy-loss spectroscopy for chemical mapping of thin foils with high spatial resolution," *Ultramicroscopy,* vol. 3, pp. 237-242, 1978.

[139] F. Hofer, *et al.,* "Imaging of nanometer-sized precipitates in solid by electron spectroscopic imaging," *Ultramicroscopy,* vol. 59, pp. 15-31, 1995.

[140] W. Jäger and J. Mayer, "Energy-filtered transmission electron microscopy of SimGen superlattice and Si-Ge heterostructures I. Experimental results," *Ultramicroscopy,* vol. 59, pp. 33-45, 1995.

[141] M. Schenner, *et al.,* "Diffraction effects in electron spectroscopic imaging," *Ultramicroscopy,* vol. 65, pp. 95-99, 1996.

[142] R. F. Egerton and S. C. Cheng, "Thickness measurement by EELS," in *43rd Ann. Proc. Electron Microsc. Soc. Ameri.*, San Francisco, pp. 389-390.

[143] J. Mayer, *et al.*, "Quantitative analysis of electron spectroscopic imaging series," *Micron.,* vol. 28, pp. 361-370, 1997.

[144] O. Scherzer, "The theoretical resolution limit of the electron microscope," *Journal of Applied Physics*, vol. 20, p. 20, 1949.

[145] L. Reimer and H. Kohl, *Transmission electron microscopy, Springer series in optical sciences 36*: Sprnger, 2008.

[146] P. L. Fejes, "Approximations for calculation of high-resolution electron-microscope images of thin films," *Acta Crystallographica Section A,* vol. 33, pp. 109-113, 1977.

[147] M. Tanaka, "Microscopie electronique a haute resolution experimentale at concept de coherence partielle," France, PhD Thesis1985.

[148] M. A. O'Keefe and J. V. Sanders, "n-Beam lattice images. VI. Degradation of image resolution by combination of incident-beam divergence and spherical aberration," *Acta Crystallographica Section A,* vol. 31, pp. 307-310, May 1975.

[149] M. De Graef, *Introduction to conventional transmission electronmicroscopy*. Cambridge: Cambridge University Press, 2003.

[150] J. C. H. Spence, *Experimental high-resolution electron microscopy*. Oxford: Oxford University Press, 1998.

[151] P. Buseck, *et al., High-resolution transmission electron microscopy and associated techniques*. Oxford: Oxford Unversity Press, 1988.

[152] B. A. Movchan and A. V. Demchishin, *Phys. Met. Mellagor,* vol. 28, pp. 83-90, 1969.

[153] J. A. Thornton, "High Rate Thick Film Growth " *Ann. Rev. Mater. Sci,* vol. 7, pp. 239-260, 1977.

[154] M. A. Pietzka and J. C. Schuster, "Phase Equilibria in the Quarternary System Ti-Al-C-N," *J. Am. Ceram. Soc,* vol. 79, pp. 2321-2330, 1996.

[155] J. A. Thornton, "Influence of substrate temperature and deposition rate on structure of thick Cu coatings," *J. Vac. Sci. Technol,* vol. 12, pp. 830-835, 1975.

[156] P. Bai, *et al.,* "Effect of substrate surface roughness on the columnar growth of Cu films," *J. Vac. Sci. Technol,* vol. 9, pp. 2113-2117, August 1991.

[157] J. W. Patten, "The influences of surface topography and angle of adatom incidence on growth structure in sputtered chromium," *Thin Solid Films,* vol. 63, pp. 121-129, 1979.

[158] K. Robbie, *et al.,* "Fabrication of thin films with highly porous microstructure," *J. Vac. Sci. Technol. A* vol. 13, pp. 1032-1365, 1995.

[159] v. d. Drift, *Philips Res. Rep.,* vol. 22, pp. 267-288, 1967.

[160] D. H. Bonne, *et al.,* "Some effects of structure and composition on the properties of electron beam vapor deposition deposite coatings for gas turbine supealloys," *J. Vac. Sci. Technologhy,* vol. 11, pp. 641-648, Juli / August 1974.

[161] J. Emmerlich, *et al.*, "Growth of Ti_3SiC_2 thin films by elemental target magnetron sputtring," *Journal of Applied Science,* vol. 96, pp. 4814-4825, November 2004.

[162] M. Magnuson, *et al.*, "Electronic struture investigation of Ti_3AlV_2, Ti_3GeC_2, and Ti_3GeC_2 by soft x-ray emission spektroscopy," *Physical Review,* p. 245101, 2005.

[163] J. Rosen, *et al., Journal of Applied Physics,* vol. 101, 2007.

[164] Z. j. Lin, *et al.*, "Microstructural characterization of layered ternary Ti_2AlC," *Acta Materialia,* vol. 54, pp. 1009-1015, 2006.

[165] K. T. Miller and F. F. Lange, "Highly oriented thin films of cubic zirconia on sapphire through grain growth seeding," *J. Mater. Res,* vol. 6, p. 2387, 1991.

[166] X. Jiang and C. L. Jia, "Direct local epitaxy of diamond on Si(100) and surface-roughening induced crystal misorietation," *Physical Review Letters,* vol. 84, p. 3658, April 2000.

[167] F. L. Meng, *et al., Scripta Materialia,* vol. 53, p. 1369, 2005.

[168] A. G. Dirks and H. J. Leamy, *Thin Solid Film,* vol. 47, pp. 219-233, 1977.

[169] J. Wang and Y. C. Zhou, "Dependence of elastic stiffness on electronic band structure of nanolaminate M_2AlC (M=Ti, V, Nb, and Cr) Ceramics," *Physical Review B,* vol. 69, p. 214111, 2004.

[170] N. Babu, *et al.*, "High-temperature oxidation of Fe_3Al-based iron aluminides in oxygen," *Corrosion Science,* vol. 43, pp. 2239-2254, February 2001.

[171] C. T. Fu and J. M. Wu, "Oxidation Behavior of Electroconductive Al_2O_3-Cr_3C_2 Composites," *British Ceramic Transaction*, vol. 94, pp. 112-117, 1995.

[172] V. A. Lavrenko, *et al.*, "Kinetics of formation of solid and gaseous Product of chromium carbide, Cr_3C_2, High Temperature oxidation n Oxygen," *Doklady Akademii Nauk SSSR,* vol. 21, p. 130, 1975.

[173] D. Caplan and G. I. Spoule, "Effect of oxidate grain structure on the high temperature oxidation of Cr," *Oxidation Metal,* vol. 9, p. 459, 1975.

[174] D. Naumenko, et.al., "Critical role of minor elemental constituents on the life time oxidation behaviour of FeCrAl-RE alloys," in *DECHEMA*, Frankfurt, pp. 1-19.

This page is intended to be blank

Appendix A

Here in appendix A, d-spacing values as a result measurement using program DiffTools are presented. The program was used to calculate the lattice constant. Crystallographic data from the inorganic crystal data base (ICSD) from KIZ Karlsruher have been used.

Table A. 1 D-spacing measurement with SAED taken from middle of Ti-Al-C film.

Rings	**d-measured (Å)**	**hkl**			**Reference (Å)**
		h	**k**	**l**	
1	2.620	1	0	0	2.570
2	2.470	1	0	3	2.445
3	2.270	1	0	4	2.308
4	2.125	1	0	5	2.163
6	1.733	1	0	8	1.749
7	1.498	1	1	0	1.484
8	1.492	1	1	2	1.516
9	1.451	1	1	2	1.448
10	1.316	0	0	10	1.322
11	1.271	2	0	2	1.262
12	1.243	2	0	5	1.253
13	1.141	2	0	5	1.156
14	1.113	2	0	6	1.110
15	1.095	2	0	7	1.063
16	1.043	2	0	11	1.045
17	1.019	2	0	8	1.015
18	0.983	1	1	10	0.987
19	0.972	2	1	0	0.972
20	0.963	2	0	9	0.967
21	0.915	2	1	5	0.912
22	0.87	2	0	11	0.878

Note : Ti_2AlC (black) and Ti_3AlC_2 (red)

Table A.2 Comparison of Ti_2AlC lattice constant from experiment and reference.

lattice constant	**d-measured**	**d-references**	**Δ lattice constant**	**Δ%**
a	2.987	2.968	0.019	0.634
c	13.112	13.224	-0.112	-0.846

Table A.3 Comparison of Ti_3AlC_2 lattice constant from experiment and reference.

lattice constant	**d-measured**	**d-references**	**Δ lattice constant**	**Δ%**
a	3.035	3.073	-0.038	-1.238
c	18.639	18.557	0.082	0.440

Table A.4 D-spacing measurement with SAED taken from upper part of Ti-Al-C film.

Rings	**d-measured (Å)**	**hkl**			**Reference (Å)**
		h	**k**	**l**	
1	2.616	1	0	1	2.634
2	2.440	1	0	3	2.445
3	2.294	1	0	4	2.308
4	2.118	1	0	5	2.163
5	1.730	1	0	8	1.749
6	1.677	1	0	6	1.673
7	1.512	1	1	2	1.516
8	1.495	1	1	0	1.484
9	1.335	0	0	10	1.322
10	1.269	1	0	8	1.262
11	1.197	0	0	10	1.198
12	1.145	2	0	2	1.155
13	1.112	2	0	4	1.110
14	1.074	2	0	7	1.063
15	1.051	2	0	11	1.045
16	1.021	2	0	8	1.015
17	0.973	2	1	0	0.972
18	0.953	2	1	3	0.949
19	0.903	2	1	9	0.904
20	0.892	2	1	6	0.889
21	0.87	2	0	11	0.878
22	0.843	3	0	2	0.850

Note : Ti_2AlC (black) and Ti_3AlC_2 (red)

Table A.5 Comparison of Ti_2AlC lattice constant from experiment and reference.

lattice constant	**d-measured**	**d-references**	**Δ lattice constant**	**Δ%**
a	2.968	2.968	0.000	0.008
c	13.236	13.224	0.012	0.094

Table A.6 Comparison of Ti_3AlC_2 lattice constant from experiment and reference.

lattice constant	**d-measured**	**d-references**	**Δ lattice constant**	**Δ%**
a	3.066	3.073	-0.007	-0.233
c	18.510	18.557	-0.047	-0.256

Table A.7 D-spacing measurement with SAED taken from area contains porous of Ti-Al-C film.

Rings	**d-measured (Å)**	**hkl**			**Reference (Å)**
		h	**k**	**l**	
1	2.590	1	0	0	2.570
2	2.460	1	0	3	2.445
3	2.289	1	0	4	2.308
4	2.130	1	0	5	2.163
5	1.832	1	0	5	1.843
6	1.741	1	0	8	1.749
7	1.521	1	0	7	1.522
8	1.515	1	1	2	1.516
9	1.500	1	1	2	1.448
10	1.394	1	0	8	1.390
11	1.319	0	0	10	1.322
12	1.266	2	0	2	1.262
13	1.143	2	0	5	1.156
14	1.049	2	0	7	1.063
15	0.997	1	0	12	1.013
16	0.978	1	1	10	0.987
17	0.972	2	1	0	0.972
18	0.967	2	0	9	0.967
19	0.914	2	1	5	0.912
20	0.87	2	0	11	0.878
21	0.852	3	0	0	0.857
22	0.827	0	0	16	0.827

Note : Ti_2AlC (black) and Ti_3AlC_2 (red)

Table A.8 Comparison of Ti_2AlC lattice constant from experiment and reference.

lattice constant	**d-measured**	**d-references**	**Δ lattice constant**	**Δ%**
a	2.962	2.968	-0.006	-0.219
c	13.151	13.224	-0.073	-0.552

Table A.9 Comparison of Ti_3AlC_2 lattice constant from experiment and reference.

lattice constant	**d-measured**	**d-references**	**Δ lattice constant**	**Δ%**
a	3.064	3.073	-0.009	-0.280
c	18.322	18.557	-0.235	-1.269

This page is intended to be blank

Appendix B

Table B. 1 D-spacing measurements for specimen Cr450.

Rings	d measured	References
1	2.456	2.445
2	2.146	2.143
3	1.631	1.626
4	1.430	1.430
5	1.350	1.333
6	1.244	1.256
7	1.189	1.188
8	1.074	1.071
9	1.026	1.026
10	0.991	0.994
11	0.939	0.935
12	0.911	0.915
13	0.860	0.856

Note : Cr_2AlC (black) and $Cr_{23}C_6$ (red)

Table B.2 Cr_2AlC lattice different between reference and experiment for specimen Cr450.

Lattice constant	d-measured	d-references	Δ lattice constant	Δ%
a	2.85119	2.86	-0.009	-0.308
c	12.95478	12.82	0.135	1.051

Table B.3 $Cr_{23}C_6$ lattice different between reference and experiment for specimen Cr450.

Lattice constant	d-measured	d-references	Δ lattice constant	Δ%
a	10.66112	10.6599	0.001	0.011

Table B.4 D-spacing measurements for specimen Cr550.

Rings	d measured	References
1	2.455	2.460
2	2.140	2.143
3	1.956	1.960
4	1.622	1.618
5	1.426	1.430
6	1.342	1.327
7	1.235	1.235
8	1.188	1.188
9	1.102	1.100
10	1.070	1.077
11	1.020	1.026
12	0.984	0.985
13	0.932	0.935
14	0.910	0.915
15	0.858	0.856

Note : Cr_2AlC (black) and $Cr_{23}C_6$ (red)

Table B.5 Cr_2AlC lattice different between reference and experiment for specimen Cr550.

Lattice constant	d-measured	d-references	Δ lattice constant	Δ%
a	2.84601	2.86	-0.014	-0.489
c	12.88121	12.82	0.061	0.477

Table B.6 $Cr_{23}C_6$ lattice different between reference and experiment for specimen Cr550.

Lattice constant	d-measured	d-references	Δ lattice constant	Δ%
a	10.59697	10.6599	-0.063	-0.590

Table B.7 D-spacing measurements for specimen Cr650.

Rings	**d measured**	**References**
1	2.459	2.477
2	2.143	2.143
3	1.961	1.960
4	1.618	1.618
5	1.48	1.430
6	1.398	1.396
7	1.354	1.345
8	1.309	1.306
9	1.235	1.235
10	1.184	1.188
11	1.066	1.072
12	1.02	1.026
13	0.98	0.981
14	0.934	0.935
15	0.911	0.915
16	0.853	0.856

Note : Cr_2AlC (black) and $Cr_{23}C_6$ (red)

Table B.8 Cr_2AlC lattice different between reference and experiment for specimen Cr650.

Lattice constant	**d-measured**	**d-references**	**Δ lattice constant**	**Δ%**
a	2.85918	2.86	-0.001	-0.029
c	12.79604	12.82	-0.024	-0.187

Appendix C

Table C.1 Chemical Composition of the Fe-Cr-Al F and J-batch model alloys.

Batch / Composition	**F-batch**	**J-batch**
Cr (wt%)	19.7	20.8
Al (wt%)	4.86	5.0
Y (ppm)	490	500
C (ppm)	90	110
S (ppm)	<10	30
O (ppm)	<10	16
N (ppm)	<10	6
P (ppm)	78	100
Zr (ppm)	290	310
V (ppm)	3.3	<50
Ti (ppm)	12	330
Cu (ppm)	5.0	<50
Ca (ppm)	<0.05	<50
Hf (ppm)	<0.005	<100
Mn (ppm)	1.5	<20
Si (ppm)	18	<50
Nb (ppm)	<50	<100
Mg (ppm)	<0.005	<20
Mo (ppm)	0.85	<50

Curriculum Vitae

Personal Data

Name: Mohamad Riza Iskandar

Place/ Date of Birth: Jakarta, 25.05.1976

Nationality: Indonesian

Marital Status: Married

Education

10/2006 – 05/2011 Doktoral Student at RWTH Aachen University, Central Facility for Electron Microscopy (Gemeinschaftslabor für Elektronenmikroskopie)

/2000 - /2003 Master student at Universitas Indonesia, Jakarta, Indonesia

- Major: Physics with a main focus on materials physics
- Degree: Master of Science

/1994 - /1999 Undergraduate Student at Universitas Indonesia, Jakarta, Indonesia

- Major: Physics with a main focus on materials physics
- Degree: Sarjana Science (Bachelor of Science)

06/1991 – 05/1994 High school student at SMUN 34 – Jakarta, Indonesia